Modeling radiative transfer of Sun-Induced Fluorescence, thermal emission and radiative budget of 3D vegetation canopies : towards a comprehensive 3D SIF model

Omar Regaieg

Université Fédérale
Toulouse Midi-Pyrénées

THÈSE

En vue de l'obtention du

DOCTORAT DE L'UNIVERSITÉ DE TOULOUSE

Délivré par l'Université Toulouse 3 - Paul Sabatier

Présentée et soutenue par

Omar REGAIEG

Le 12 janvier 2023

Modélisation du transfert radiatif de la fluorescence induite par le soleil, de l'émission thermique et du bilan radiatif des couverts végétaux 3D : vers un modèle SIF complet

---

Ecole doctorale : **SDU2E - Sciences de l'Univers, de l'Environnement et de l'Espace**

Spécialité : **Surfaces et interfaces continentales, Hydrologie**

Unité de recherche :
CESBIO - Centre d'Etudes Spatiales de la BIOsphère

Thèse dirigée par
Jean philippe GASTELLU ETCHEGORRY

Jury

M. Roberto COLOMBO, Rapporteur
M. José SOBRINO, Rapporteur
M. Zbynek MALENOVSKY, Examinateur
Mme Valérie LE DANTEC, Examinatrice
M. Tiangang YIN, Examinateur
M. Jean-Louis ROUJEAN, Examinateur
Mme Karine ADELINE, Examinatrice
M. Jean-Philippe GASTELLU-ETCHEGORRY, Directeur de thèse
M. Philippe MAISONGRANDE, Invité
M. Ferran GASCON, Invité

Modeling Radiative Transfer of Solar-Induced Fluorescence, Thermal Emission and Radiative Budget of 3D Vegetation Canopies: Towards a Comprehensive 3D SIF Model

by

Omar REGAIEG (عمر الرقـيّق)

A thesis submitted for the degree of

Doctor of Philosophy

2023

“In the darkness, all the ordinary colors of our daylight world disappear. Only the intensely glowing hues of fluorescent substances touched by the ultraviolet beam shine out with striking clarity.”

Sterling Gleason, 1960

Acknowledgements

At the end of my PhD journey, I realize how fruitful this experience was on all scales, and also the good and tough times I went through before reaching this distinguished moment. During this journey, I had always persons there for helping and supporting me, to whom I would like to address my sincere expressions of gratitude.

I would firstly like to express my deepest appreciation to my PhD advisor Jean-Philippe Gastellu-Etchegorry. I appreciated a lot working under his supervision. His passion and dedication to keep improving the DART model and to conduct high quality and upstanding research work have been a source of inspiration and motivation for me, he can perfectly find the sweet spot between giving steady guidance and according decent autonomy, he is always available for conveying his knowledge and for discussion, not to mention his numerous personal qualities and his valuable moral support especially during the quarantine periods.

I am also extremely grateful to the computer scientists of the DART team Nicolas Lauret, Eric Chavanon and Jordan Guilleux. Nicolas was always available to give precious coding assistance, advice and ideas. Eric was always there to find mysterious bugs and to provide useful scripts. Jordan was ready to modify the GUI whenever I needed. Thanks should also go to all current and past DART team members including my officemate Yingjie Wang, with whom I enjoyed discussing, Quang-Thang Nguyen, Paul Boitard, Najmeddine Ben Romdhane, Antony Delavois, Zhijun Zhen, Xuebo Yang and Zhu Tao.

I would like to extend my sincere thanks to our international collaborators. I had the pleasure of working with Tiangang Yin (Hong Kong University) who was always happy to share his data and work, Zbyněk Malenovský (Bonn University, Germany), I learned a lot from his expertise about vegetation biology and SIF, Ronan Paugam (Barcelona University, Spain) who tested the thermal part of my work and helped to find bugs, Abdelaziz Kallel (CRNS, Sfax, Tunisia) to whom I owe thanks for recommending me to work with the DART team, and also Bruce Cook and Douglas Morton at NASA GSFC (USA).

I am also thankful to CNRS (Centre National de la Recherche Scientifique) for funding my PhD through the 80|Prime program, to CESBIO for providing a nice research environment for doing my PhD and for helping me in administrative matters, and to our collaborators Jean-Louis Roujean and Valérie Le Dantec in CESBIO.

Lastly, I would be remiss in not mentioning my family and all my friends. Although we are hundreds of miles apart, their perpetual care and emotional support have kept my motivation always high even during the hardest times.

List of publications

Journal articles

1. **Regaieg, O**., Yin, T., Malenovský, Z., Cook, B. D., Morton, D. C., & Gastellu-Etchegorry, J.-P. (2021). Assessing impacts of canopy 3D structure on chlorophyll fluorescence radiance and radiative budget of deciduous forest stands using DART. Remote Sensing of Environment, 265, 112673. https://doi.org/10.1016/j.rse.2021.112673

2. **Regaieg, O.**, Lauret, N., Wang, Y. Guilleux, J., Chavanon, E., Gastellu-Etchegorry, J-P. (2022). DART 3D bi-directional Monte-Carlo modelling of solar-induced chlorophyll fluorescence images of vegetation canopies. (Sumbitted)

3. Malenovský, Z., **Regaieg, O.**, Yin, T., Lauret, N., Guilleux, J., Chavanon, E., Duran, N., Janoutová, R., Delavois, A., Meynier, J., Medjdoub, G., Yang, P., van der Tol, C., Morton, D., Cook, B. D., & Gastellu-Etchegorry, J.-P. (2021). Discrete anisotropic radiative transfer modelling of solar-induced chlorophyll fluorescence: Structural impacts in geometrically explicit vegetation canopies. Remote Sensing of Environment, 263, 112564. https://doi.org/10.1016/j.rse.2021.112564

4. Wang, Y., Kallel, A., Yang, X., **Regaieg, O.**, Lauret, N., Guilleux, J., Chavanon, E., & Gastellu-Etchegorry, J.-P. (2022). DART-Lux: An unbiased and rapid Monte Carlo radiative transfer method for simulating remote sensing images. Remote Sensing of Environment, 274, 112973. https://doi.org/10.1016/j.rse.2022.112973

5. Yang, X., Wang, Y., Yin, T., Wang, C., Lauret, N., **Regaieg, O.**, Xi, X., & Gastellu-Etchegorry, J. P. (2022). Comprehensive LiDAR simulation with efficient physically-based DART-Lux model (I): Theory, novelty, and consistency validation. Remote Sensing of Environment, 272, 112952. https://doi.org/10.1016/j.rse.2022.112952

Conference articles

1. **Regaieg, O.**, Wang, Y., Malenovský, Z., Yin, T., Kallel, A., Duran, N., Delavois, A., Qi, J., Chavanon, E., Lauret, N., Guilleux, J., Cook, B., Morton, D., & Gastellu-Etchegorry, J. P. (2020). Simulation of Solar-Induced Chlorophyll Fluorescence from 3D Canopies with the Dart Model. IGARSS 2020 - 2020 IEEE International Geoscience and Remote Sensing Symposium, 4846–4849. https://doi.org/10.1109/IGARSS39084.2020.9323616

2. Gastellu-Etchegorry, J.-P., Wang, Y., **Regaieg, O.**, Yin, T., Malenovsky, Z., Zhen, Z., Yang, X., Tao, Z., Landier, L., Bitar, A. A., Deschamps, Lauret, N., Guilleux, J., Chavanon, E., Cao, B., Qi, J., Kallel, A., Mitraka, Z., Chrysoulakis, N., Morton, D. (2020). Recent Improvements in the Dart Model for Atmosphere, Topography, Large Landscape, Chlorophyll Fluorescence, Satellite Image Inversion. IGARSS 2020 - 2020 IEEE International Geoscience and Remote Sensing Symposium, 3455–3458. https://doi.org/10.1109/IGARSS39084.2020.9323458

3. Gastellu-Etchegorry, J.-P., Wang, Y., **Regaieg, O.**, Yin, T., Malenovsky, Z., Zhen, Z., Yang, X., Tao, Z., Landier, L., Bitar, A. A., Deschamps, Lauret, N., Guilleux, J., Chavanon, E., Cao, B., Qi, J., Kallel, A., Mitraka, Z., Chrysoulakis, N., … Morton, D. (2020). Why To Model Remote Sensing Measurements In 3d? Recent Advances In Dart: Atmosphere, Topography, Large Landscape, Chlorophyll Fluorescence And Satellite Image Inversion. 2020 5th International Conference on Advanced Technologies for Signal and Image Processing (ATSIP), 1–6. https://doi.org/10.1109/ATSIP49331.2020.9231884

4. Gastellu-Etchegorry, J. P., Lauret, Tavares, L., Lamquin, N., Bruniquel, V., Roujean, J. L., Hagolle, O., Zhen, Z., Wang, Y., **Regaieg, O.**, Guilleux, J., Chavanon, E., & Goryl, P. (2022). Correction of Directional Effects in Sentinel-2 and -3 Images with Sentinel-3 Time Series and Dart 3D Radiative Transfer Model. IGARSS 2022 - 2022 IEEE International Geoscience and Remote Sensing Symposium, 4563–4566. https://doi.org/10.1109/IGARSS46834.2022.9883522

Abstract

The photosynthetic activity of vegetation is of major interest given current environmental concerns such as climate change and water resources. In this process, chlorophyll molecules excited by absorption of photosynthetically active radiation (PAR), dissipate some of the energy not used for photosynthesis in the form of heat and fluorescence radiation (SIF) which turns out to be a reliable and instantaneous indicator of photosynthetic activity. However, many factors complicate the interpretation of remote sensing measurements in terms of SIF and thus photosynthetic activity. In particular, the 3D architecture of the vegetation greatly affects radiation propagation, and thus PAR absorption, SIF emission in the canopy, and the remote sensing measurement. Accurate modeling of SIF emission and remote sensing measurements is therefore essential to accurately interpret these measurements in terms of SIF emitted *(i.e.*, photosynthetic activity) by the vegetation. Moreover, it must be adapted to complex landscapes of large dimensions, at least larger than the resolution of the relevant satellite sensors (*e.g.*, 300 m for the upcoming ESA FLEX satellite mission to measure SIF). Given the number, complexity and diversity of terms to be taken into account, this modeling uses strong approximations that often lead to significant errors in the interpretation of remote sensing measurements. The model developed in this thesis deals mainly with the radiative aspect. It is based on the DART radiative transfer model (https://dart.omp.eu). Based on the discrete ordinate method, DART-FT, the initial mode of DART, simulates the SIF emission and the remotely sensed SIF signal, but has computational requirements (*i.e.*, memory, computational time) that are prohibitive for the simulation of large landscapes. The new mode of DART, called DART-Lux, solves this problem with a very efficient two-way Monte Carlo algorithm. To complement the functionality of DART-Lux, four original models have been designed and implemented. (1) Modeling of landscapes with turbid volumes and facets, as the "turbid" representation is often useful for simulating large landscapes. (2) Modeling of SIF emission and the SIF signal that is measured by satellite, airborne and in-situ sensors. It takes into account local bioclimatic conditions via a coupling with the SCOPE energy balance model. Applied to

eight forest plots realistically reconstructed with LiDAR measurements, this modeling allowed one to study the impact of the 3D structure of the vegetation on the SIF emission and on the SIF observed by a sensor at nadir, from morning to evening. It highlighted that the relative error made by neglecting the 3D architecture of the canopies, as in the 1D models, is often greater than 30%, especially in the morning and evening when the solar direction is very oblique. (3) Modeling of remote sensing images corresponding to the thermal emission of the landscape. As DART is not an energy balance model, the 3D temperature distribution is imported or approximated via short-wave illumination. (4) 3D radiation balance modeling with the ability to simulate it by sub-scene and feature type. All of these modeling, with the exception of the radiation balance modeling, were found to be very accurate and efficient in terms of computation time and memory volume, with gains often greater than 100. The resulting new DART model opens very interesting perspectives for the study of land surfaces using remote sensing observations in the visible to thermal infrared range. This work is currently being pursued in order to take into account the multiple biophysical interactions within the canopies that condition their SIF emission and their 3D temperature.

Résumé

L'activité photosynthétique de la végétation revêt un intérêt majeur compte tenu des préoccupations environnementales actuelles comme le changement climatique et les ressources en eau. Dans ce processus, les molécules de chlorophylle excitées par absorption de rayonnement photosynthétiquement actif (PAR), dissipent une part de l'énergie non utilisée pour la photosynthèse sous forme de chaleur et de rayonnement de fluorescence (SIF) qui ainsi est un indicateur fiable et instantané de l'activité photosynthétique. Cependant, de nombreux facteurs compliquent l'interprétation des mesures de télédétection en termes de SIF et donc d'activité photosynthétique. En particulier, l'architecture 3D de la végétation affecte beaucoup la propagation du rayonnement, et donc l'absorption du PAR, l'émission de SIF dans le couvert végétal, et la mesure de télédétection. Une modélisation précise de l'émission SIF et des mesures de télédétection est donc essentielle pour interpréter avec précision ces mesures en termes de SIF émis (i.e., activité photosynthétique) par la végétation. De plus, elle doit être adaptée aux paysages complexes de grandes dimensions, du moins plus grands que la résolution des capteurs satellites concernés (*e.g.*, 300 m pour la prochaine mission satellite FLEX de l'ESA pour mesurer la SIF). Vu le nombre, complexité et diversité des termes à prendre en compte, cette modélisation utilise de fortes approximations qui induisent souvent de grandes erreurs lors de l'interprétation des mesures de télédétection. La modélisation développée dans cette thèse traite principalement de l'aspect radiatif. Elle s'appuie sur le modèle de transfert radiatif DART (https://dart.omp.eu). Le mode initial, DART-FT, de DART, basé sur la méthode des ordonnées discrètes, simule l'émission SIF et le signal SIF mesuré par télédétection, mais a des besoins informatiques (*i.e.*, volume mémoire, temps de calcul) prohibitifs pour simuler de grands paysages. Le nouveau mode, appelé DART-Lux, résout ce problème via un algorithme bidirectionnel Monte Carlo très efficace. Pour compléter les fonctionnalités de DART-Lux, quatre modélisations originales ont été conçues et implémentées. (1) Modélisation de paysages avec des volumes turbides et des facettes, car la représentation "turbide" est souvent utile pour simuler de grands paysages. (2) Modélisation de l'émission et mesure satellite de la SIF, en

tenant compte des conditions bioclimatiques locales via le couplage avec le modèle de bilan d'énergie SCOPE. A partir de huit parcelles forestières reconstruites de manière réaliste avec des mesures LiDAR, cette modélisation a permis d'étudier l'impact de la structure 3D de la végétation sur la SIF émise et observée par un capteur au nadir, du matin au soir. Ainsi, l'erreur relative commise en négligeant l'architecture3D des couverts, comme dans les modèles 1D, est souvent supérieure à 30%, surtout les matins et soirs quand la direction solaire est très oblique. (3) Modélisation des images de télédétection correspondant à l'émission thermique du paysage. DART n'étant pas un modèle de bilan d'énergie, la distribution3D des températures est importée ou calculée de manière approchée via un éclairement dans les courtes longueurs d'onde. (4) Modélisation du bilan radiatif 3D avec possibilité de le simuler par sous scène et par type d'élément. Toutes ces modélisations, excepté la modélisation du bilan radiatif, se sont avérées très précises et efficaces en termes de temps de calcul et de volume mémoire, avec des gains souvent supérieurs à 100. La modélisation implémentée dans DART ouvre donc des perspectives très intéressantes pour l'étude des surfaces terrestres avec l'aide d'observations de télédétection visible à infrarouge thermique. Ce travail est actuellement poursuivi, pour tenir compte des multiples interactions biophysiques qui au sein des couverts conditionnent leur émission SIF et température 3D.

Contents

List of figures

List of tables

General introduction

Photosynthesis is a biochemical process consisting in transforming carbon dioxide (CO_2) molecules captured from the atmosphere and water molecules absorbed from the soil into carbohydrates and dioxygen molecules by green vegetation. This endothermic reaction uses the solar radiation as a source of energy. It is a fateful process for the human kind and for life on Earth in general. Indeed, it is the main process used by primary producer organisms to produce organic compounds necessary to provide energy to all the elements of the food chain. Moreover, it plays a crucial role in the carbon cycle on Earth as it makes green vegetation work as a carbon sink that uptakes atmospheric CO_2 released by natural phenomena (*e.g.*, respiration of living organisms, fires, etc.) and especially by anthropogenic activities (*e.g.*, industrial activities, fossil fuels burning, etc.), then to store it as biomass. Therefore, it reduces the impact of human carbon footprint on the atmospheric CO_2 concentration which continues to increase at an alarming rate since the 19^{th} century. The global warming and climate change, caused by greenhouse gases including CO_2 that prevent the heat received by the Earth surface through the sun radiation from escaping to external space, are seriously impacting and even threatening human life. They are causing an increase in the average temperature of the planet and in the frequency of extreme weather events such as droughts (Cogato et al., 2019) and thus are becoming major concerns for contemporary human societies. Furthermore, the world population is increasing and therefore there is an increasing demand on food that needs to be satisfied. Consequently, in the recent years, the scientific community has become increasingly interested in studying the photosynthetic process at different spatial and temporal scales, both for agricultural and forest canopies, in order address these urgent and critical challenges of humanity.

Earth surfaces emit and scatter electromagnetic radiation over the entire spectrum, with differences depending on the spectral domain (*e.g.*, optical and microwave domains). The measurement of this radiation by active and passive remote sensing can provide information on

the characteristics of these surfaces. In particular, multispectral and hyperspectral optical sensors onboard Earth observation satellites are very useful for large scale vegetation monitoring. Indeed, they provide high spatial and temporal resolution observations in different spectral domains (*e.g.*, visible, near-infrared, thermal infrared) used for inferring biophysical and biochemical information about vegetation (*e.g.*, LAI, biomass, chlorophyll content, water content, etc.). However, they generally cannot provide real-time information on the photosynthetic process of vegetation, which is essential for detecting eventual stresses, and in particular water and temperature stress. For instance, retrieved information such as current pigments content (*e.g.*, chlorophyll, carotenoid) of vegetation generally results from past bioclimatological conditions (*e.g.*, photosynthesis inhibited by water or temperature stress) that influence vegetation optical properties sometime later, when these changes can be irreversible. Presently, only two types of remote sensing measurements can provide real-time information on plant responses to stress. 1) Reflection of sun radiation at 0.531 µm and 0.570 µm, used to define the photochemical reflectance index (PRI), can indicate short-term changes in the xanthophyll cycle (Gerhards et al., 2019; Suárez et al., 2009). 2) Thermally emitted radiation can indicate changes in temperature that can allow early stress detection (Costa et al., 2013; Gerhards et al., 2019).

Solar-induced chlorophyll fluorescence (SIF) is a spontaneous re-emission of radiation by vegetation excited by photosynthetically active solar radiation. Together with the photochemical and heat dissipation processes, they form the three possible ways for an excited chlorophyll molecule to dispose of the excess of energy. These three processes are in competition, which makes the SIF correlated with photosynthetic activity and gross primary production. Because its response to the inhibition of photosynthesis due to stress is instantaneous, SIF is a real-time indicator of the photosynthetic process, and therefore a potentially very useful signal for monitoring the vegetation functioning state and for stress detection.

SIF represents a small fraction of the sun radiation scattered by vegetation and it is spectrally overlapping with it. Hence, except for some absorption bands (*e.g.*, atmospheric oxygen O_2A and O_2B absorption bands, Fraunhofer lines of solar radiation), it is impossible to dissociate it from the total radiation outgoing from the vegetation at the top of canopy (TOC) or at the top of atmosphere (TOA) levels. Indeed, in these absorption bands, the solar incident radiation and therefore the scattered radiation are small enough such that the SIF can be detected and

measured. We usually observe small peaks of the TOC reflectance spectrum at these bands. This is explained by the fact that the radiation absorbed at a given wavelength gives rise to fluorescence at other wavelengths, and therefore increases the apparent reflectance at these bands. In recent years, many techniques for retrieving the SIF signal from in-situ, airborne and spaceborne sensors within the oxygen O_2A and O_2B absorption bands and the Fraunhofer lines were developed. The European Space Agency (ESA) has shown a particular interest in SIF and its potential to monitor vegetation functioning from space using these techniques and has selected the Fluorescence Explorer (FLEX) satellite as its eighth Earth Explorer mission.

Nevertheless, the interpretation of SIF measurements remains challenging. Indeed, although the atmospheric oxygen allows to measure the SIF because it attenuates the incident radiation, it also attenuates the SIF signal before reaching the sensor especially for spaceborne sensors. Therefore, accurate atmospheric corrections are needed to retrieve the TOC signal. Moreover, TOC SIF directly measured by TOC sensors or retrieved from TOA sensors is solely a part of the total SIF emitted within the canopy that escapes from it, directly or after being scattered, to the observation direction. Most of the SIF radiation escapes to other directions, or is absorbed by the canopy elements (*e.g.*, leaves, woody elements, soil, etc.). Besides, in addition to the instantaneous photosynthetic activity, the SIF measurements are influenced by several other confounding factors, such as the photosynthetically active radiation absorption, the canopy structure, the optical properties of canopy elements, the sun-canopy-sensor configuration, etc.

For these reasons, models that simulate SIF emission and observations stand out as essential tools to help in retrieving and interpreting the SIF signals from measurements and to disentangle the effect of each influencing factor. Ideally, these models should take into account all the parameters that affect the SIF emission and observation including the local climatological conditions that affect the temperature dependent photosynthetic rate and therefore the leaf-level SIF emission, the canopy's 3D structure and optical properties and the experimental configurations that affect the radiation propagation. Hence, the full energy balance should be simulated including all the radiative and non-radiative processes with an accurate 3D representation of the canopy. Radiative energy exchanges include the absorption of solar radiation and the emission of thermal radiation, while non-radiative energy exchanges include sensible and latent heat exchanges with the atmosphere and the soil.

Currently, the canopy SIF models developed by the scientific community can be classified into two major groups: 1) 1D models that simulate the full energy balance by taking into account all the major physical processes that cause SIF emission. They include a leaf-level photosynthesis model and a 1D radiation canopy model. However, they neglect the 3D architecture of canopies. The reference models are SCOPE and its multilayer version mSCOPE. 2) 3D radiative transfer models that accurately simulate the propagation of radiation within the canopy. They also include a leaf-level SIF model. However, they do not simulate the non-radiative processes. Among these models, the Discrete Anisotropic Radiative Transfer (DART) model is one of the most comprehensive 3D radiative transfer models. It is developed by CESBIO since 1992. It includes the Fluspect leaf SIF model and therefore simulates canopy SIF emission as well as TOC and TOA SIF observations since 2017. Its initial version, DART-FT, is based on an adapted discrete ordinates method. A more efficient Monte Carlo based mode, called DART-Lux, has been developed since 2018 for simulating remote sensing images. An initial objective was to include all the functionalities of the DART-FT mode. The approach is not straightforward because DART-Lux uses a modeling approach very different from that of DART-FT.

DART simulates any type of urban or natural landscapes. It can simulate vegetation canopies represented using imported realistic 3D objects, schematic 3D objects created internally by DART or canopies represented using 3D turbid medium. In this thesis, the modeling implementations, including SIF emission, are introduced and tested for the two DART modes (*i.e.*, DART-FT and DART-Lux) and for the two vegetation representation methods (facets, turbid). The SIF introduction in DART allowed to evaluate the impact of 3D structure on a deciduous forest's SIF, using a realistic forest scene reconstructed from LiDAR data. Moreover, the thermal emission and the radiation budget are two important components of the energy budget that quantify the energy exchange of vegetation through radiation. They need to be accurately simulated before the consideration of the energy exchange via non-radiative processes. In this thesis, we also introduce the modeling of thermal emission and radiative budget in DART-Lux. The aim of this work is to provide radiative transfer building blocks towards the development of a comprehensive 3D SIF model.

This thesis is organized in five chapters:

Chapter 1 is an introductory chapter that presents general theoretical concepts about fluorescence, solar-induced fluorescence and its use for monitoring vegetation functioning with remote sensing. It also presents the DART model with a special focus on DART-Lux which will be the most considered in the following chapters.

Chapter 2 presents the SIF modeling in DART-FT for vegetation simulated as facets and as 3D turbid medium.

Chapter 3 presents the SIF modeling in DART-Lux for vegetation simulated as facets and as 3D turbid medium. A novel method was developed to introduce the SIF emission for the bi-directional path tracing. Moreover, the turbid vegetation was introduced in DART-Lux including SIF emission.

Chapter 4 shows the impact of vegetation structure on both the SIF emission and observation. The work is a theoretical study with LiDAR reconstructed forest scenes.

Chapter 5 presents the modeling of the thermal emission and radiative budget in DART-Lux for scene elements simulated as facets and as volumes (turbid medium, fluids).

Introduction générale

La photosynthèse est un processus biochimique consistant à transformer les molécules de dioxyde de carbone (CO_2) captées de l'atmosphère et les molécules d'eau absorbées du sol en hydrates de carbone et en molécules de dioxygène par la végétation verte. Cette réaction endothermique utilise le rayonnement solaire comme source d'énergie. Il s'agit d'un processus fatidique pour l'espèce humaine et pour la vie sur Terre en général. En effet, il s'agit du principal processus utilisé par les organismes producteurs primaires pour produire les composés organiques nécessaires pour fournir de l'énergie à tous les éléments de la chaîne alimentaire. En outre, il joue un rôle crucial dans le cycle du carbone sur Terre, car il permet à la végétation verte de fonctionner comme un puits de carbone qui absorbe le CO_2 atmosphérique libéré par des phénomènes naturels (*e.g.*, la respiration des organismes vivants, les incendies, etc.) et surtout par les activités anthropiques (*e.g.*, les activités industrielles, la combustion des hydrocarbures fossiles, etc.). Il réduit donc l'impact de l'empreinte carbone humaine sur la concentration de CO_2 dans l'atmosphère, qui continue d'augmenter à un rythme alarmant depuis le XIX^{e} siècle. Le réchauffement de la planète et le changement climatique, causés par les gaz à effet de serre, dont le CO_2, qui empêchent la chaleur reçue par la surface de la Terre par le biais du rayonnement solaire de s'échapper vers l'espace extérieur, ont un impact sérieux, voire menaçant sur la vie humaine. Ils provoquent une augmentation de la température moyenne de la planète et de la fréquence des événements climatiques extrêmes tels que les sécheresses (Cogato et al., 2019) et deviennent ainsi des préoccupations majeures pour les sociétés humaines contemporaines. En outre, la population mondiale augmente et il y a donc une demande croissante de produits alimentaires qui doit être satisfaite. Par conséquent, au cours des dernières années, la communauté scientifique s'intéresse de plus en plus à l'étude du processus de photosynthèse à différentes échelles spatiales et temporelles, pour les canopées agricoles et forestières, afin de répondre à ces défis urgents et critiques de l'humanité.

Les surfaces terrestres émettent et diffusent du rayonnement électromagnétique sur l'ensemble du spectre, avec des différences en fonction du domaine spectral (*e.g.*, les domaines optique et micro-ondes). La mesure de ce rayonnement par télédétection active et passive peut fournir des informations sur les caractéristiques de ces surfaces. En particulier, les capteurs optiques multispectraux et hyperspectraux à bord des satellites d'observation de la Terre sont très utiles pour le suivi de la végétation à grande échelle. En effet, ils fournissent des observations à haute résolution spatiale et temporelle dans différents domaines spectraux (*e.g.*, visible, proche infrarouge, infrarouge thermique) utilisées pour déduire des informations biophysiques et biochimiques sur la végétation (*e.g.*, LAI, biomasse, teneur en chlorophylle, teneur en eau, etc.). Cependant, ils ne peuvent généralement pas fournir d'informations en temps réel sur le processus photosynthétique de la végétation, ce qui est essentiel pour détecter d'éventuels stress, et en particulier les stress hydriques et thermiques. Par exemple, les informations récupérées telles que la teneur actuelle en pigments (*e.g.*, chlorophylle, caroténoïde) de la végétation résultent généralement de conditions bioclimatologiques passées (*e.g.*, photosynthèse inhibée par un stress hydrique ou thermique) qui influencent les propriétés optiques de la végétation quelque temps plus tard, lorsque ces changements peuvent être irréversibles. Actuellement, seuls deux types de mesures de télédétection peuvent fournir des informations en temps réel sur les réponses des plantes au stress. 1) La réflexion du rayonnement solaire à 0,531 µm et 0,570 µm, utilisée pour définir l'indice de réflectance photochimique (PRI), peut indiquer des changements à court terme dans le cycle des xanthophylles (Gerhards et al., 2019; Suárez et al., 2009). 2) Le rayonnement émis thermiquement peut indiquer des changements de température qui peuvent permettre une détection précoce du stress (Costa et al., 2013; Gerhards et al., 2019).

La fluorescence chlorophyllienne induite par le soleil (SIF) est une réémission spontanée de rayonnement par la végétation excitée par le rayonnement solaire photosynthétiquement actif. Avec les processus photochimique et de dissipation de chaleur, ils constituent les trois moyens possibles pour une molécule de chlorophylle excitée de se débarrasser de l'excès d'énergie. Ces trois processus sont en compétition, ce qui fait que la SIF est corrélée à l'activité photosynthétique et à la production primaire brute. Parce que sa réponse à l'inhibition de la photosynthèse due au stress est instantanée, la SIF est un indicateur en temps réel du processus photosynthétique, et donc un signal potentiellement très utile pour suivre l'état de fonctionnement de la végétation et pour la détection du stress.

La SIF représente une petite fraction du rayonnement solaire diffusé par la végétation et elle se chevauche spectralement avec celui-ci. Par conséquent, à l'exception de certaines bandes d'absorption (*e.g.*, les bandes d'absorption O_2A et O_2B de l'oxygène atmosphérique, les lignes de Fraunhofer du rayonnement solaire), il est impossible de la dissocier du rayonnement total sortant de la végétation en haut de la canopée (TOC) végétale ou en haut de l'atmosphère (TOA). En effet, dans ces bandes d'absorption, le rayonnement solaire incident et donc le rayonnement diffusé sont suffisamment faibles pour que la SIF puisse être détectée et mesurée. On observe généralement des petits pics du spectre de réflectance TOC dans ces bandes. Cela s'explique par le fait que le rayonnement absorbé à une longueur d'onde donnée donne lieu à une fluorescence à d'autres longueurs d'onde, et augmente donc la réflectance apparente à ces bandes. Ces dernières années, de nombreuses techniques ont été développées pour récupérer le signal SIF à partir de capteurs in situ, aéroportés et spatiaux dans les bandes d'absorption de l'oxygène O_2A et O_2B et dans les lignes de Fraunhofer. L'Agence Spatiale Européenne (ESA) a montré un intérêt particulier pour la SIF et son potentiel pour suivre le fonctionnement de la végétation depuis l'espace à l'aide de ces techniques et a choisi le satellite Fluorescence Explorer (FLEX) comme sa huitième mission d'observation de la Terre.

Néanmoins, l'interprétation des mesures de la SIF reste difficile. En effet, bien que l'oxygène atmosphérique permette de mesurer la SIF car il atténue le rayonnement incident, il atténue également le signal SIF avant d'atteindre le capteur, surtout pour les capteurs spatiaux. Par conséquent, des corrections atmosphériques précises sont nécessaires pour récupérer le signal TOC. De plus, le signal SIF en TOC directement mesuré par les capteurs TOC ou déduit à partir des capteurs TOA ne représente qu'une partie du signal SIF total émis à l'intérieur de la canopée, qui s'en échappe, directement ou après avoir été diffusé, vers la direction d'observation. La plupart du rayonnement SIF s'échappe vers d'autres directions, ou est absorbé par les éléments de la canopée (*e.g.*, feuilles, éléments ligneux, sol, etc.). En outre, en plus de l'activité photosynthétique instantanée, les mesures de la SIF sont influencées par plusieurs autres facteurs de confusion, tels que l'absorption du rayonnement photosynthétiquement actif, la structure de la canopée, les propriétés optiques des éléments de la canopée, la configuration soleil-canopée-capteur, etc.

Pour ces raisons, les modèles qui simulent l'émission et les observations de la SIF sont des outils essentiels pour aider à récupérer et à interpréter les signaux SIF à partir des mesures et pour démêler l'effet de chaque facteur d'influence. Idéalement, ces modèles devraient prendre

en compte tous les paramètres qui affectent l'émission et l'observation de la SIF, y compris les conditions climatologiques locales qui affectent le taux de photosynthèse dépendant de la température et donc l'émission de la SIF au niveau des feuilles, la structure 3D et les propriétés optiques de la canopée et les configurations expérimentales qui affectent la propagation du rayonnement. Par conséquent, le bilan énergétique complet doit être simulé, y compris tous les processus radiatifs et non radiatifs, avec une représentation 3D précise de la canopée. Les échanges d'énergie radiative comprennent l'absorption du rayonnement solaire et l'émission de rayonnement thermique, tandis que les échanges d'énergie non radiative comprennent les échanges de chaleur sensible et latente avec l'atmosphère et le sol.

Actuellement, les modèles de SIF de canopée développés par la communauté scientifique peuvent être classés en deux groupes principaux : 1) les modèles 1D qui simulent le bilan énergétique complet en prenant en compte tous les processus physiques majeurs qui causent l'émission de la SIF. Ils comprennent des modèles de photosynthèse et de SIF au niveau des feuilles. Cependant, ils négligent l'architecture 3D des canopées. Les modèles de référence sont SCOPE et sa version multicouche mSCOPE. 2) Le modèles de transfert radiatif 3D qui simulent avec précision la propagation du rayonnement dans la canopée. Ils comportent un modèle de SIF au niveau des feuilles. Cependant, ils ne simulent pas les processus non radiatifs. Parmi ces modèles, le modèle de Transfert Radiatif Anisotrope Discret (DART) est l'un des modèles de transfert radiatif 3D les plus complets. Il est développé par le CESBIO depuis 1992. Il inclut le modèle SIF foliaire Fluspect et simule donc l'émission SIF de la canopée ainsi que les observations SIF TOC et TOA depuis 2017. Sa version initiale, DART-FT, est basée sur une méthode adaptée des ordonnées discrètes. Un mode plus efficace basé sur la méthode Monte Carlo, appelé DART-Lux, a été développé depuis 2018 pour simuler les images de télédétection. Un objectif initial était d'inclure toutes les fonctionnalités du mode DART-FT. La démarche n'est pas évidente car DART-Lux utilise une approche de modélisation très différente de celle de DART-FT.

DART simule tout type de paysages urbains ou naturels. Il peut simuler des couverts végétaux représentés par des objets 3D réalistes importés, des objets 3D schématiques créés en interne par DART ou des couverts représentés par un milieu turbide 3D. Dans cette thèse, les approches de modélisation et les implémentations de l'émission de SIF sont introduites et testées pour les deux modes de DART (*i.e.*, DART-FT et DART-Lux) et pour les deux méthodes de représentation de la végétation (facettes, turbide). L'introduction de la SIF dans DART a permis

d'évaluer l'impact de la structure 3D sur la SIF d'une forêt à feuilles caduques, en utilisant une scène forestière réaliste reconstruite à partir de données LiDAR. De plus, l'émission thermique et le bilan radiatif sont deux composantes importantes du bilan d'énergie qui quantifient l'échange d'énergie de la végétation par le rayonnement. Ils doivent être simulés avec précision avant de considérer l'échange d'énergie via des processus non-radiatifs. Dans cette thèse, nous introduisons également la modélisation de l'émission thermique et du bilan radiatif dans DART-Lux. L'objectif de ce travail est de fournir des éléments de base du transfert radiatif en vue du développement d'un modèle SIF 3D complet.

Cette thèse est organisée en cinq chapitres :

Le chapitre 1 est un chapitre introductif qui présente les concepts théoriques généraux sur la fluorescence, la fluorescence induite par le soleil et son utilisation pour le suivi du fonctionnement de la végétation avec la télédétection. Il présente également le modèle DART avec un accent particulier sur DART-Lux qui sera le plus considéré dans les chapitres suivants.

Le chapitre 2 présente la modélisation SIF dans DART-FT pour la végétation simulée comme des facettes et comme un milieu turbide 3D.

Le chapitre 3 présente la modélisation de la SIF dans DART-Lux pour la végétation simulée en tant que facettes et en tant que milieu turbide 3D. Une nouvelle méthode a été développée pour introduire l'émission SIF pour le traçage de chemin bidirectionnel. De plus, la végétation turbide a été introduite dans DART-Lux en incluant l'émission SIF.

Le chapitre 4 montre l'impact de la structure de la végétation sur l'émission et l'observation de la SIF. Il s'agit d'une étude théorique avec des scènes forestières reconstruites à partir du LiDAR.

Le chapitre 5 présente la modélisation de l'émission thermique et du bilan radiatif dans DART-Lux pour des éléments de scène simulés comme des facettes et comme des volumes (milieu turbide, fluides).

Chapter 1

Context: Solar-Induced Fluorescence and DART model

This thesis is centered on the modeling of chlorophyll solar-induced fluorescence in the DART model. In addition to the presentation of DART, this chapter introduces the context and associated questions: what is the chemical process behind the fluorescence emission and does it only happen for chlorophyll molecules? When was the fluorescence and particularly the chlorophyll fluorescence discovered? What about the correlation between chlorophyll fluorescence and photosynthesis? Why is it important to have models that simulate the SIF? What is the state of the art of fluorescence modeling?

1.1 Fluorescence

Fluorescence is considered as a photoluminescence phenomenon among others like phosphorescence and delayed fluorescence. Photoluminescence is the type of luminescence (*i.e.*, emission of photons from electronically excited chemical species) of which the excitation is due to the absorption of light. The first reported observation of fluorescence was as early as 1565 when the Spanish medical practitioner Nicolás Monardes described the blue color of the water infusion of a type of wood known as Lignum nephriticum under certain conditions. The

term fluorescence was introduced by Stokes, (1852), from "fluorspar" analogously to "opalescence" which was also derived from the name of a mineral. He found that the emitted light has a longer wavelength than the absorbed light when he illuminated a solution of quinine sulfate with ultra-violet light and observed a blue light (Valeur, 2012b).

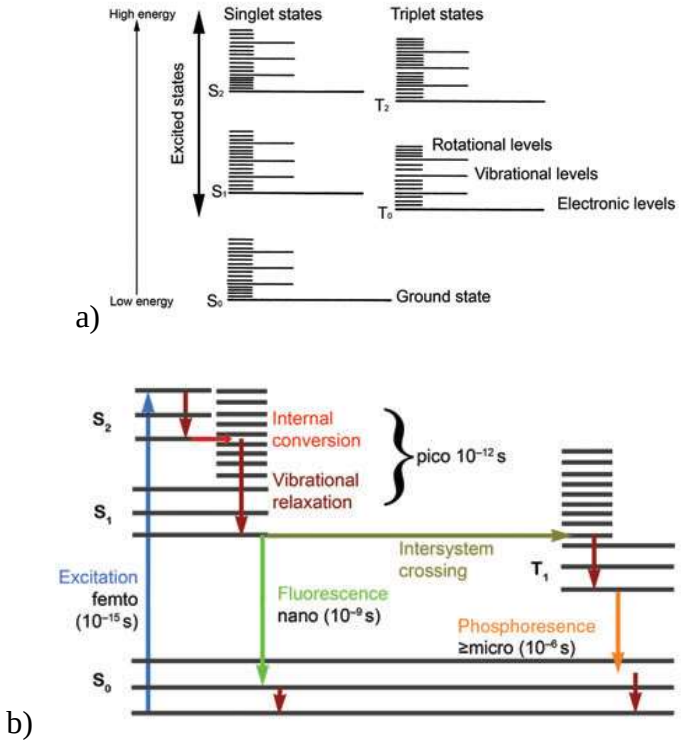

Figure 1-1: Jablonski diagram: a) Energy states, b) Possible transitions and their time lapses. (Lichtman & Conchello, 2005)

After absorbing a quantum of light, a fluorescent molecule passes to a vibrational level associated to a higher electronic state. The excited state is unstable and the molecule needs to dispose of its excess of energy. First, the excited molecule can lose energy through non-radiative (*i.e.*, without photon emission) state transitions (*e.g.*, internal conversion, vibrational relaxation) that occur in a time lapse in the order of 10^{-12} s allowing the molecule to pass to the lowest vibrational level of an electronic state by transferring energy to other molecules and generating heat. Then, in a time lapse in the order of 10^{-9} s, it can release the remaining energy by emitting a photon, and this emission is called fluorescence. Because the loss of energy due non-radiative state transitions is faster than fluorescence emission, the latter usually occurs at wavelengths larger than the incident light and therefore having less energy. This is called the

Stokes' Law. However, the emission can, with a low probability, be at a lower wavelength. This may seem to contradict the energy conservation principle, nevertheless, it happens because a small fraction of molecules have a vibrational level higher than 0 at normal temperature, and can emit a photon with higher energy than that of the absorbed photon (Valeur, 2012a). The electronic states and the transitions between them are usually illustrated with a Jablonski diagram (Jabłoński, 1935) as shown in Figure 1-1.

1.2 Solar-induced chlorophyll fluorescence (SIF)

The chlorophyll molecule has also shown to be fluorescent. The first reported observation of chlorophyll fluorescence induced by solar radiation was made by Brewster (1834) who noticed that the color of an alcoholic extract of chlorophyll hit by sunlight was a brilliant red. The photosynthetic process (photochemical quenching), the heat dissipation (non-photochemical quenching) and the fluorescence emission are three processes in competition over the absorbed energy by a chlorophyll molecule. Hence, the chlorophyll fluorescence emission is closely linked with photosynthetic activity. This link was first noticed by Müller (1874) and confirmed by Kautsky & Hirsch (1931) who noted the correlation between the variation of fluorescence emission and CO_2 assimilation. This correlation was further studied by McAlister & Myers (1940), Kautsky & Zedlitz (1941) and Kautsky et al. (1960). Since then, the fluorescence emission is considered as a proxy for photosynthetic activity (Baker, 2008).

1.3 Remote sensing of SIF

Being an electromagnetic radiation, the passive chlorophyll fluorescence of canopies induced by sunlight can be studied via remote sensing. Chlorophyll solar-induced fluorescence emission spectral range [640-850 nm] is spectrally overlapping with sunlight reflected by vegetation canopies. Moreover, because of its small quantum yield which is typically between 0.5 and 3% and usually does not exceed 10% in vivo (Porcar-Castell et al., 2014), it represents a small fraction of the light reflected by vegetation canopies (*e.g.*, 2-6% at 740 nm (Campbell et al., 2008)). Nevertheless, the retrieval of SIF is possible in absorption bands of the incident radiation, where the SIF has a larger relative contribution to the total signal from the canopy.

Some techniques use the atmospheric oxygen O_2A and O_2B absorption bands located inside the SIF spectrum around 760 nm and 687 nm respectively, to quantify the SIF observed in these bands (Fournier et al., 2012; Moya et al., 2004). Other techniques utilize the Fraunhofer lines of the solar spectrum to retrieve the SIF (Frankenberg et al., 2011; Guanter et al., 2012). The development of these techniques allowed accurate retrievals of SIF from in situ (Cogliati et al., 2015; Fournier et al., 2012), airborne (Rossini et al., 2015) and even spaceborne (Guanter et al., 2012) sensors. This enabled to use SIF remote sensing for monitoring the functional state of vegetation, by early stress detection (Ač et al., 2015), tracking photosynthetic activity and estimating the gross primary production (Campbell et al., 2019; Guanter et al., 2014; X. Liu et al., 2019; Z. Liu et al., 2019; P. Yang et al., 2021). This potential of SIF led the European Space Agency (ESA) to select a satellite dedicated for SIF observation Fluorescence Explorer (FLEX) as its 8th Earth Explorer mission (Drusch et al., 2017).

1.4 Modeling of SIF emission and observations

Although SIF emission is highly correlated with instantaneous photosynthetic activity and gross primary production, it is also highly impacted by several other confounding factors. Indeed, it is directly linked with the PAR absorption, which depends on the sun direction, the atmospheric conditions and also the 3D architecture and optical properties of the canopy. Besides, the SIF emitted within the canopy interacts with all canopy elements and can undergo wavelength-dependent phenomena such as scattering and re-absorption by the different canopy elements or the soil. Therefore, only a small fraction of the emitted SIF can escape from the canopy into the upward hemisphere and is measured by remote sensing sensors. These interactions greatly depend on the canopy 3D architecture of the canopy and on the wavelength. In addition, the SIF signal above the canopy (*i.e.*, canopy SIF radiance) is anisotropic, which makes it more complex to extrapolate the SIF emission of the canopy from a single remote sensing observation. Therefore, for an accurate interpretation of SIF remote sensing observations, a comprehensive and deep understanding of three consecutive processes is essential. 1) Interception and absorption of photosynthetically active radiation by leaf pigments directly or after interacting with the atmosphere and all canopy elements. 2) Emission of SIF at photosystem level based on the absorbed PAR with a certain quantum efficiency that depends on photosynthetic and

heat dissipation efficiencies which in turn depend on local climatological conditions. 3) Propagation of SIF radiation through the canopies and its interaction with all canopy elements including leaves, soil, woody elements etc. until reaching the sensor.

Models that accurately simulate SIF emission and observations are essential tools for understanding and interpreting the SIF measurements, and extracting useful information from them. For this objective, models should consider each of the many parameters (*e.g.*, 3D architecture and optical properties of the canopy, illumination conditions, environmental parameters) that influence SIF emission. Second, models should accurately simulate the measured SIF signal as a function of the emitted SIF, the canopy properties and the observation configuration. Third, models should help in understanding the links between the within canopy SIF emission, the photosynthetic activity and the gross primary production of vegetation. Finally, models should allow performing sensitivity studies difficult or even impossible to do on real canopies. They should also allow the generation of synthetic databases or look-up tables that can be used by inversion algorithms to estimate SIF related parameters (*e.g.*, fluorescence quantum efficiency) and other vegetation functional state parameters (*e.g.*, CO_2 assimilation rate, gross primary production). In short, they should allow to link the SIF measurements to the real-time photosynthetic activity. Among these models, we can distinguish leaf-level SIF models that simulate radiative transfer within the leaf to provide leaf-level SIF emission, and canopy level models that upscale the leaf-level SIF models to the canopy level by simulating within-canopy radiative transfer.

1.4.1 Leaf-level modeling

Leaf-level SIF models include semi-empirical models such as FluorMODleaf (Pedrós et al., 2010) and Fluspect (Vilfan et al., 2016, 2018) that are based on the PROSPECT model (Jacquemoud & Baret, 1990). They simulate leaf hemispherical spectral optical properties and leaf SIF emission using the leaf biochemical properties and photosystem level fluorescence quantum efficiency as input parameters. Figure 1-2 shows an example of the output of the widely used leaf-level SIF model Fluspect. (Input parameters: chlorophyll content: 30 $\mu g.cm^{-2}$, carotenoid content: 10 $\mu g.cm^{-2}$, dry matter content: 0.01 $g.cm^{-2}$, equivalent water thickness: 0.012 cm, structure coefficient: 1.8, fluorescence yields: PSI: 0.002, PSII: 0.01). These are four excitation-emission fluorescence matrices. An element $f_{i,j}$ of each matrix multiplied by the leaf irradiance E_i at the spectral band i, gives the emitted SIF exitance $F_{i,j}$ at

the spectral band j induced by E_i. The leaf SIF exitance F_j emitted at spectral band j is the sum of the SIF exitance $F_{i,j}$ due to all the N_{exc} excitation bands:

$$F_j = \sum_{i=1}^{N_{exc}} E_i . f_{i,j} \tag{1.1}$$

The row vector of spectral SIF for the N_{em} emission bands $\left(F_j\right)_{j\in\{1..N_{em}\}}$ can be written as the product of the row vector spectral irradiance $(E_i)_{i\in\{1..N_{exc}\}}$ by the SIF excitation-emission matrix $\left(f_{i,j}\right)_{\substack{i\in\{1..N_{exc}\}\\ j\in\{1..N_{em}\}}}$ for the corresponding excitation and fluorescent bands. According to the Stokes' Law, if $N_{exc} = N_{em}$, these matrices should be upper triangular (*i.e.*, $f_{i,j} = 0, \forall\, i > j$). However, they can have non-null very low values below the diagonal. This is not in contradiction with the energy conservation principle as explained in Section 1.1.

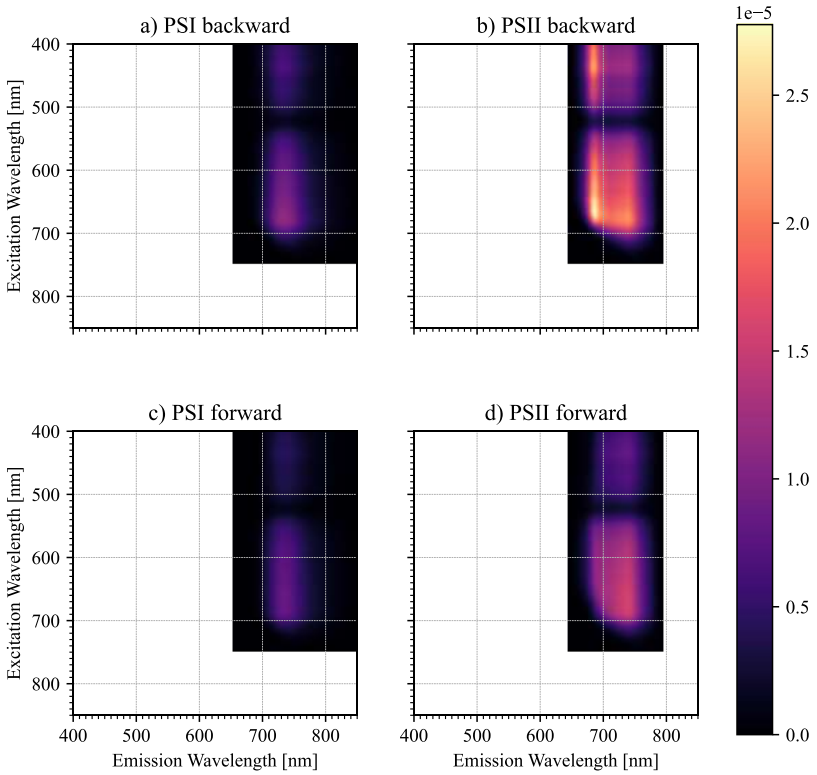

Figure 1-2: Image representations of four fluorescence excitation-emission matrices at 1 nm spectral resolution simulated by the Fluspect model. White pixels represent exact 0 values, black pixels represent positive values close to 0.

Leaf SIF models also include 3D radiative transfer models that use accurate (Kallel, 2020b) or less accurate (Sušila & Nauš, 2007) 3D descriptions of the leaf to simulate within leaf radiative

transfer and to compute leaf spectral reflectance, transmittance and fluorescence. Leaf SIF models are usually combined with canopy radiative transfer models to upscale the SIF emission from leaf to canopy level.

1.4.2 Canopy level modeling

Ideally, a canopy-level SIF model should simulate accurately all the radiative and non-radiative processes that impact the SIF signal. Considering the accurate 3D architecture of vegetation canopies, it should simulate the propagation of sunlight to quantify the absorbed PAR, and the propagation of SIF radiation to estimate the measured signal. Moreover, it needs to compute the leaf-level SIF emission based on the absorbed PAR, possibly using a leaf-level SIF model, and considering the local parameters that influence SIF emission (*e.g.*, leaf temperature). To this end, the full energy balance needs to be modeled with its radiative (*i.e.*, full radiative budget from visible to thermal infrared domain), and non-radiative (*e.g.*, photosynthesis, turbulence, heat exchanges) components. The existing SIF models that simulate the full energy balance are 1D only. They make a very limiting assumption of horizontally homogenous canopies, neglecting the actual 3D structure of vegetation canopies. They represent the canopy by homogeneous turbid layers characterized by a Leaf Area Index (LAI) and a Leaf Angular Distribution (LAD). This is the case of the SCOPE model (van der Tol et al., 2009) and its multi-layered version mSCOPE (P. Yang et al., 2017). They use the Fluspect model to simulate dark-adapted leaf fluorescence, and then weight the SIF emission by multiplicative factors derived from a 1D energy balance algorithm in order to consider the effect of local climatology on SIF emission. These models are, to some extent, adapted for homogeneous and closed crop canopies, but they are much less adapted for forest heterogeneous covers and crop canopies with a clear row distribution that can provoke important effects related to 3D structure both for radiation absorption and remote sensing observations. They also neglect some canopy elements such as woody elements and local topography. In recent years, several 3D canopy SIF models have been developed. They usually result from already existing 3D radiative transfer models combined with a leaf-level SIF model. For instance, FluorFLIGHT (Hernández-Clemente et al., 2017) is based on the FLIGHT model (North, 1996), FLiES-SIF (Sakai et al., 2020) and FluorFLiES (Gao et al., 2022) are based on the FLiES (Kobayashi & Iwabuchi, 2008) model, the FluLCVRT (Kallel, 2020b) is based on the LCVRT model (Kallel, 2020a) and FluorWPS (Zhao et al., 2016) is based on the WPS model (Zhao et al., 2015). However, none of these

models simulate the full 3D energy balance. Hence, they cannot compute the multiplicative factors to get the steady state leaf SIF from the dark-adapted leaf SIF based on the local climatology. It is left up to the user to input directly the steady state fluorescence quantum efficiency, which is challenging to measure for all the leaves. This is also the case for the DART model. However, the latter offers the possibility to import fluorescence multiplicative factors computed by other models (*e.g.*, the η factors computed by SCOPE) to weight the leaf SIF emission according to the local climatology. Obviously, importing information from a 1D model (SCOPE) to a 3D model (DART) is only an approximation. For example, the η factor can have a large horizontal variation depending on the local conditions of each individual leaf.

1.5 DART model

DART (Discrete Anisotropic Radiative Transfer) is one of the most comprehensive 3D radiative transfer models in optical remote sensing domain. It is developed in CESBIO (Centre d'Etudes Spatiales de la BIOsphère) since 1992. It simulates the 3D radiative budget and remote sensing observations from ultraviolet to thermal infrared of any natural or urban 3D landscape for any experimental configuration (*e.g.*, sun direction, atmosphere, etc.) and instrumental configuration (e.g., viewing direction, spatial resolution, etc.) for spaceborne, airborne and in situ imaging spectro-radiometers (scanners, cameras, etc.) and LiDAR (Light Detection And Ranging). To this end, DART has four main modules: 1) "Directions" is used for subdividing the 4π space into a finite number N of discrete directions Ω_n having solid angles $\Delta\Omega_n$and P ($P \leq N$) angular sectors. 2) "Phase" is used for computing the optical properties, temperature properties and phase functions for the user defined surfaces and volumes, and for the specified spectral bands. 3) "Maket" is used to create the mock-up from the user-defined scene elements. A Python toolbox, called "DAO" is also provided with DART to allow the automatic creation of mock-ups directly from external data such as 3D LAI information derived from LiDAR data. It can replace the "Maket" module that is in general used with the graphical user interface. 4) "Dart" is the module that simulates radiative transfer in the scene using geometric and optical information generated by the three pervious modules in order to generate the user-selected radiative products (*e.g.*, 3D radiative budget and / or remote sensing signal). Each DART spectral band can have any of three radiation modes: 1) R mode: the sun is the only source of

radiation. 2) T mode: thermal emission of scene elements and the atmosphere is the only source of radiation. 3) R + T mode: both the solar radiation and thermal emission are considered. Moreover, three modes (i.e., DART-FT, DART-RC and DART-Lux) are used to simulate radiative transfer in the 3D scenes. These modes are presented in the next sub-sections.

1.5.1 DART-FT

DART-FT is the standard mode of DART. It is called FT, as Flux Tracking, because it tracks radiation using an adaptation of the discrete ordinates method in a finite number N of discrete directions (Ω_n, $\Delta\Omega_n$) over the 4π space (Yin et al., 2013) in a scene made of voxels (Figure 1-3). This approach is iterative: radiation intercepted at iteration i is scattered at iteration $i+1$. Using the pure discrete ordinates method, each ray intercepted at a given iteration would give rise to N scattered rays at the following iteration, which would result in an exponential growth of the number of tracked rays, and therefore a huge and unmanageable number of rays. To avoid this exponential growth, pragmatic approximation approaches such as the use of barycenters of scattering points on surfaces and in voxels are used, which greatly reduces the number of scattering points, and consequently the number of scattered rays. The DART-FT mode has two major limitations. 1) It is not efficient in terms of computation time and memory usage for image simulation. It spends computation resources to track and to store every single ray even if this ray has not a real contribution to the signal of interest. 2) The discretization of the 4π space into a finite number of discrete directions and the inevitable use of approximations to limit the number of rays is a source of inaccuracies and discretization artefacts. On the other hand, since all the radiation is tracked inside the scene, it is possible to know the amount of radiation that is intercepted, scattered or absorbed everywhere in the scene. Therefore, DART-FT is efficient for simulating the radiation budget of canopies. Moreover, because of its iterative approach, a single simulation can provide products at different scattering orders. In addition, an iterative process extrapolates the last iteration orders to the infinite scattering order.

The initial version of DART was only adapted to 3D vegetation canopies made of voxels either empty or filled with turbid medium, and to radiation in the shortwaves (Gastellu-Etchegorry et al., 1996). Other modelling processes were introduced later: use of facets to simulate surface elements in the voxelized scene (Gastellu-Etchegorry et al., 2004), radiative transfer in the atmosphere (Gascon et al., 2001), thermal emission for simulating the remote sensing signal

and radiative budget in the thermal infrared domain (Guillevic et al., 2003), and solar induced fluorescence (Gastellu-Etchegorry et al., 2017).

1.5.2 DART-RC

DART-RC is the DART radiative transfer mode for simulating the LiDAR signal of 3D scenes (Gastellu-Etchegorry et al., 2015) simulated by an array of voxels. It tracks radiation using a combination of the discrete ordinates method and forward Monte Carlo ray tracing. Its products include several types of LiDAR products (*e.g.*, waveforms, point clouds, photon counting).

1.5.3 DART-Lux

Since 2018, DART includes a new mode called DART-Lux (Wang et al., 2022). It is a bi-directional Monte Carlo radiative transfer method based on the open-source rendering engine LuxCoreRender (https://luxcorerender.org). DART-Lux uses Monte Carlo integration techniques to solve the Light Transport Equation. Monte Carlo integration is an integration method that allows to estimate the integral of a given function using only random sampling of points in the definition domain of this function and the evaluation of the function in these points. The naïve Monte Carlo estimator for the integral $I = \int_a^b f(x).dx$ of the 1D function f is:

$$\hat{I} = \frac{b-a}{N}\sum_{i=1}^{N} f(x_i) \tag{1.2}$$

with $\{x_1, \dots, x_N\}$ are points uniformly sampled over the interval $[a, b]$.

This estimator is not biased: its expected value is the real value I of the integral (cf. Appendix 1-1). Therefore, it converges towards the real value when the number of samples is large enough.

The sampling of x_i can be done using any probability distribution function (PDF) $p(x)$, apart from the uniform distribution. In this case, the Monte Carlo estimator becomes:

$$\widehat{I_p} = \frac{1}{N}\sum_{i=1}^{N} \frac{f(x_i)}{p(x_i)} \tag{1.3}$$

Ideally, the PDF should be chosen such that it has a similar shape to f. This technique is called "Importance Sampling" and is used to reduce the variance of Monte Carlo estimators.

The Monte Carlo integration method can easily be extended to estimate integrals over high dimensional integration domains. Its algorithmic complexity does not change with the dimension of the domains as it only depends on the number of sampled points. Therefore, it can be used to compute the radiance measurement $L^{(j)}$ of pixel j of a simulated image given by the integral form of the Light Transport Equation:

$$L^{(j)} = \int_{\mathcal{D}} C^{(j)}(\bar{p}).dA(\bar{p}) \tag{1.4}$$

- $\bar{p}$: light transport path. $\bar{p}_k=(p_0,...,p_k)$ is a path of length k (*i.e.*, k segments and $k+1$ vertices p_i with $i\in[0, k]$).
- $\mathcal{D}$: set of all possible light paths. $\mathcal{D}=\bigcup_{k=1}^{\infty}\mathcal{D}_k$, with $\mathcal{D}_k$ the set of all paths $\bar{p}_k$ of length k.
- $dA(\bar{p})$: area product for path $\bar{p}$; *e.g.*, $dA(\bar{p}_k)=dA(p_0)...dA(p_k)$ with area $dA(p_i)$ at vertex i.
- $C^{(j)}(\bar{p})$: contribution function of path $\bar{p}$ to the measurement $L^{(j)}$ of pixel j.

When sampling random light paths for the Monte Carlo estimator of pixel radiance using the importance sampling technique, paths with higher contribution to the pixel radiance have higher chances to be sampled. The light path sampling starts from the light source (*i.e.*, forward direction) and from the sensor (*i.e.*, backward direction). Forward tracing is more efficient for sampling light sources with narrow solid angle of illumination and backward tracing for sensors with narrow fields of view (FOV) (Disney et al., 2000). The bi-directional tracing combines the forward and backward tracing and allows to benefit from the advantages of the two methods. Unlike the discrete ordinates method that spends computational resources to track all radiation over the scene even if it has a negligeable impact on the simulated observation, the bi-directional path tracing (BDPT) algorithm, by sampling with higher probability light paths that have higher contribution to the image, it allows to preferentially track rays that contribute most to the required observations which makes it more computationally efficient for images simulation. Moreover, because its algorithmic complexity does not depend on the scene complexity, it is more and more efficient for large and complex scenes. DART-Lux takes advantage of the development of rendering algorithms in computer graphics. The BDPT algorithm implementation of the physical renderer LuxCoreRender has been selected and adapted to the remote sensing field, in the comprehensive and user-friendly framework of DART. The initial goal of the DART team was to introduce most of the functionalities of DART-FT and DART-RC into DART-Lux, with improved accuracy and lower computer and memory requirements, within the framework of DART and with the ability to switch seamlessly

between modes. To this end, many physical and technical improvements and adaptations had to be made. Ten major modelling developments are listed here. 1) To overcome the hard coded 3-channel RGB limit in LuxCoreRender for simulations with any number of spectral bands. 2) To simulate radiance and reflectance remote sensing images (Wang et al., 2022; Wang & Gastellu-Etchegorry, 2021). 3) To support input and output formats of the DART framework. (DAO, SQL databases, images, etc.). 4) To implement radiative transfer modelling in the atmosphere in order to simulate BOA and TOA images. 5) To simulate LiDAR signal (X. Yang et al., 2022). 6) To simulate polarization mechanisms. 7) To implement the modeling of radiative transfer in scenes made of volumes filled with turbid medium and fluids. 8) To model solar-induced fluorescence. 9) To model thermal emission by the scene elements and the atmosphere. 10) To model the 3D radiative budget of 3D scenes.

Compared to DART-FT, DART-Lux greatly reduces computation time and memory needs for image simulation of large and complex scenes. It also usually improves accuracy and avoids artefacts due to discretization as it eliminates processes such as discretizing the 4π space, voxelizing the 3D scene (Figure 1-3) and combining rays to reduce their number.

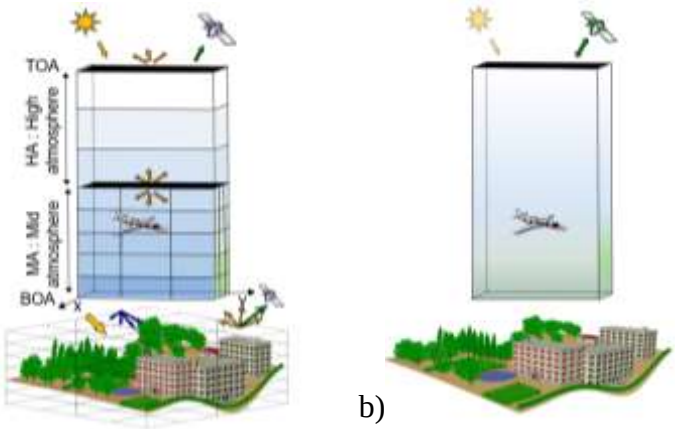

a) b)

Figure 1-3: a) DART-FT voxelized scene b) DART-Lux scene: voxels are no more needed

1.6 Conclusion

This chapter presented historical and theoretical aspects about the fluorescence, and in particular chlorophyll solar-induced fluorescence and its great potential for monitoring real-time vegetation functioning status. It also presented the DART model, and in particular the DART-Lux mode and its BDPT algorithm which will be of interest in the next chapters.

Appendix 1-1: Expected values of $\hat{I}$ and $\widehat{I_p}$

$$E[\hat{I}] = \frac{b-a}{N}\sum_{i=1}^{N} E[f(x_i)]$$

$$= \frac{b-a}{N}\sum_{i=1}^{N} \frac{1}{b-a}\int_a^b f(x).dx$$

$$= \int_a^b f(x).dx = I$$

$$E[\widehat{I_p}] = \frac{1}{N}\sum_{i=1}^{N} E\left[\frac{f(x_i)}{p(x_i)}\right]$$

$$= \frac{1}{N}\sum_{i=1}^{N} \int_a^b \frac{f(x)}{p(x)}.p(x)dx$$

$$= \int_a^b f(x).dx = I$$

Appendix 1-2: Nomenclature

Symbol	Description	Unit
E_i	Irradiance at the spectral band i	$W.m^{-2}.\mu m^{-1}$
F_j	SIF exitance at the spectral band j	$W.m^{-2}.\mu m^{-1}$
$f_{i,j}$	Fluorescence matrix element for excitation band i and emission band j	-
$F_{i,j}$	SIF exitance at the spectral band j due to the excitation at the spectral band i	$W.m^{-2}.\mu m^{-1}$

$\hat{I}$	Monte Carlo estimator of the integral I using the uniform probability density function.	-
$\widehat{I_p}$	Monte Carlo estimator of the integral I using the probability density function p.	-
$L^{(j)}$	Radiance measurement of pixel j	$W.m^{-2}.\mu m^{-1}.sr^{-1}$
N_{em}	Number of emission bands	-
N_{exc}	Number of excitation bands	-

Chapter 2

SIF modeling in DART-FT

DART-FT is the initial DART mode that simulates radiative transfer based on the discrete ordinates method. It has two possible representations of vegetation: facets-based 3D objects representation and 3D voxelized turbid representation. In this chapter, the two approaches used for modeling the SIF emission and radiation propagation in DART-FT for the facets and turbid representations are presented. The first section is dedicated to the facets-based SIF simulation. It was the subject of a publication included in this thesis in which I am the second author. My main contribution was to design and prepare DART and SCOPE/mSCOPE simulations for comparing their simulations of the SIF signal, using the 1D models as reference models, as are generally accepted in the community. The second section presents SIF modeling in vegetation simulated as turbid medium. I participated in the design of this new modelling and implemented it in DART.

2.1 Vegetation simulated as facets

2.1.1 Modeling approach

The implementation of SIF emission in DART-FT for vegetation simulated as facets consisted in imbedding the leaf-level SIF model Fluspect into DART-FT. Fluspect gives SIF excitation-emission matrices at 1 nm spectral resolution that are resampled to the user-specified spectral

bands of the DART simulation. It is important to note that the excitation spectral bands should cover all the excitation spectral interval (*i.e.*, [400 – 750 nm]) otherwise the SIF will be underestimated, and should not overlap otherwise the SIF will be overestimated. To include the SIF radiation, radiation fluxes vectors have 3 components: total flux components, and two SIF components for the photosystems PSI and PSII, respectively. Radiation fluxes with these 3 components are mechanistically tracked in the forward direction within the scene. Intercepted by a non-fluorescent or a fluorescent surface, the total, PSI and PSII radiation flux components are scattered or absorbed in the same way as the total flux. If the interacting surface is fluorescent, SIF radiation is added to the scattered PSI and PSII radiation components. This added SIF radiation is simulated by multiplying the total leaf irradiance by the relevant SIF excitation-emission matrix (PSI or PSII, backward or forward). The article of Malenovský et al. (2021) in Section 2.1.3 gives further details about SIF modeling in DART-FT for vegetation simulated as facets.

2.1.2 Results

Ideally, a radiative transfer model should be compared to real field measurements to assess its consistency. However, this comparison is very challenging in general, especially for 3D models. In order to be consistent with the very tiny and anisotropic SIF signal, a relevant comparison of a 3D SIF radiative transfer model with field measurement requires: 1) accurate 3D scene reconstruction that accounts for the field geometry and the plants 3D architecture, 2) bottom of atmosphere spectral irradiance with a good spectral resolution (*i.e.*, ≤ 1 nm), or accurate atmosphere parameters to simulate radiative transfer in the atmosphere, 3) steady-state fluorescence quantum efficiency at photosystems level or dark-adapted fluorescence quantum efficiency along with η multiplicative factors computed by a 3D energy balance model, 4) scene elements optical properties including leaves optical properties (*i.e.*, spectral reflectance and transmittance) that need to inverted to retrieve the Fluspect input parameters to compute the leaf level fluorescence matrices. Most of these input parameters are not straightforward to obtain and require long processes. For instance, the fluorescence quantum efficiency, a major key parameter that drives SIF emission, is highly variable in time and space and is challenging to measure. Hence, although several SIF measurements are available at different levels (in-situ, airborne, satellite), a complete dataset ready to use for comparison with 3D radiative transfer models was not available. Therefore, in order to assess the accuracy of DART-FT SIF modeling,

we performed a model-to-model comparison with a model that is considered as a reference SIF model in the community. The agreement of two models that use completely different approaches can be a first assessment of the models' consistency provided that they are tested in exactly the same conditions. Unfortunately, the only reference model is 1D only. This approach does not replace the need of comparisons with real field SIF measurements. Bearing this in mind, we have compared the SIF modeling in DART-FT with SCOPE (van der Tol et al., 2009) and its multi-layered version mSCOPE (P. Yang et al., 2017). They are 1D models and are considered as a "reference" for SIF modeling. They represent vegetation as homogeneous turbid layers, with a possible vertical heterogeneity in mSCOPE. Turbid medium is a statistical representation of vegetation using a leaf area volumetric density u_l $(m^2.m^{-3})$ and a Leaf Angular Distribution (LAD) $\frac{g(\theta_l)}{2\pi}$. It is equivalent to an infinite number of infinitely small plane elements distributed according to $\frac{g(\theta_l)}{2\pi}$ and having a total area per volume unit equal to u_l. To approximate this representation, the equivalent DART mock-up is constructed as a "quasi-turbid" medium: a cloud of very small facets distributed according to the same LAD $\frac{g(\theta_l)}{2\pi}$ and having a total area per volume unit equal to u_l. The comparison of DART-FT simulation for quasi-turbid medium with SCOPE and mSCOPE showed a good agreement between the models, as presented in the article of Malenovský et al., (2021). (cf. Section 2.1.3)

2.1.3 Article:

Remote Sensing of Environment 263 (2021) 112564

Contents lists available at ScienceDirect

Remote Sensing of Environment

journal homepage: www.elsevier.com/locate/rse

Discrete anisotropic radiative transfer modelling of solar-induced chlorophyll fluorescence: Structural impacts in geometrically explicit vegetation canopies

Zbyněk Malenovský [a,b,*], Omar Regaieg [c], Tiangang Yin [b,d], Nicolas Lauret [c], Jordan Guilleux [c], Eric Chavanon [c], Nuria Duran [c], Růžena Janoutová [e], Antony Delavois [c], Jean Meynier [c], Ghania Medjdoub [c], Peiqi Yang [f], Christiaan van der Tol [f], Douglas Morton [b], Bruce Douglas Cook [b], Jean-Philippe Gastellu-Etchegorry [c]

[a] School of Geography, Planning, and Spatial Sciences, College of Sciences Engineering and Technology, University of Tasmania, Private Bag 76, Hobart, TAS 7001, Australia
[b] NASA Goddard Space Flight Center, Biospheric Sciences Laboratory, 8800 Greenbelt Rd, Greenbelt, MD 20771, USA
[c] Centre d'Etudes Spatiales de la Biosphère - UT3, CNES, CNRS, IRD, Université de Toulouse, 31401 Toulouse Cedex 9, France
[d] Earth System Science Interdisciplinary Center, University of Maryland, College Park, MD 20740-3823, USA
[e] Global Change Research Institute of the Czech Academy of Sciences, Bělidla 986/4a, 60300 Brno, Czech Republic
[f] Faculty of Geo-Information Science and Earth Observation (ITC), University of Twente, PO Box 217, AE Enschede 7500, the Netherlands

ARTICLE INFO

Editor name: Jing M. Chen

Keywords:
DART
Fluspect
SCOPE
SIF
Sun-/shade-adapted leaves
LAI
Clumping
Wood

ABSTRACT

Solar-induced fluorescence (SIF) is a subtle but informative optical signal of vegetation photosynthesis. Remotely sensed SIF integrates environmental, physiological and structural changes that alter photosynthesis at leaf, plant and canopy scales. Radiative transfer models are ideally suited to investigate the complex sources of variability in the SIF signal to guide the interpretation of SIF retrievals from airborne and space-borne platforms. Here, we coupled the Fluspect-Cx model of leaf optical properties and chlorophyll-a fluorescence with the Discrete Anisotropic Radiative Transfer (DART) model to upscale SIF from individual leaves to three-dimensional (3D) structurally explicit canopies. For one-dimensional homogeneous (turbid-like) canopies, DART-SIF was nearly identical to SIF simulated in two existing models, SCOPE and mSCOPE (RMSE <0.221 $W.m^{-2}.\mu m^{-1}.sr^{-1}$). DART simulations in geometrically explicit 3D canopies offered four important insights regarding the influence of vegetation structure on the multi-angular top-of-canopy SIF signal. First, changes in the 3D canopy architecture of maize crops, represented by leaf density (leaf area index), and plant clumping (canopy closure) had a larger impact on SIF than the modelled photosynthetic efficiency distinction between sun-adapted and shade-adapted foliage. Second, clumping of leaves at the crop and stand levels was identified as one of the key driving factors of multi-angular anisotropy of red and far-red SIF (686 and 740 nm) for both maize and eucalyptus canopies. Third, non-photosynthetic woody material had a significant impact on top-of-canopy SIF in modelled 3D forest stands. Wood shadowing decreased the photosynthetically active radiation absorbed by green leaves, and consequently the SIF emissions, by 10% in sparse and 17% in dense eucalyptus stands. The wood obstruction (blocking) effect, quantified as a relative difference of SIF escape probabilities from canopies with and without wood in the nadir viewing direction, decreased far-red SIF by 4–6% but it had a smaller and sometimes positive influence (by less than 2%) on red SIF. Fourth, DART 3D radiative budget profiles revealed that the majority of the SIF signal from a dense eucalyptus stand originated from the top 25% of the simulated canopy. Interestingly, the introduction of bark-covered woody elements did not alter the simulated balance and omnidirectional escape factor of red SIF in this upper canopy part but did raise significantly both of them in case of far-red SIF. These results demonstrate the importance of 3D radiative transfer and radiative budget simulations for investigating SIF interactions in structurally complex plant canopies and for a better understanding of spatiotemporal and multi-angular remote sensing SIF observations.

* Corresponding author at: School of Geography, Planning, and Spatial Sciences, College of Sciences Engineering and Technology, University of Tasmania, Private Bag 76, Hobart, TAS 7001, Australia.
E-mail address: zbynek.malenovsky@gmail.com (Z. Malenovský).

https://doi.org/10.1016/j.rse.2021.112564
Received 18 September 2020; Received in revised form 10 May 2021; Accepted 14 June 2021
Available online 25 June 2021

1. Introduction

The potential for airborne and spaceborne monitoring of plant productivity has motivated optical remote sensing (RS) scientists since the launch of first Earth observing satellites (Ashley and Rea 1975; Blair and Baumgardner 1977). The faint signal of chlorophyll *a* fluorescence has been the target of vegetation RS for several decades (Rosema et al. 1991). Although recent technological advances in narrow-band imaging spectroscopy provide the first estimates of solar-induced chlorophyll fluorescence (SIF) from space (Frankenberg et al. 2011; Guanter et al. 2007; Joiner et al. 2011), the retrieval and use of the subtle SIF signal emitted in the red and near-infrared spectral regions to assess plant productivity is fraught with natural complexity of vegetated landscapes. Hence, RS applications of SIF, including physiological principles, instruments, measurement techniques and computer models (Mohammed et al. 2019), need a further development to improve our understanding and correct interpretation of the diurnal, seasonal, and interannual variabilities in the SIF signal observed with RS instruments at local, regional and global spatial scales. In particular, SIF variability originating from multiple scattering and reabsorption within structurally complex vegetation canopies is poorly understood, as are optical interactions in topographically rough and spatially heterogeneous natural and man-made landscapes (Zhang et al. 2020).

Radiative transfer modelling is a well-established and inseparable part of modern optical RS methods (Myneni and Ross 2012). Computer simulated radiative transfer in vegetation (Widlowski et al. 2015) has been used for local and global sensitivity analyses of various RS phenomena (e.g., Malenovský et al. 2008; Verrelst and Rivera 2017; Verrelst et al. 2010), and also for retrieval and interpretation of quantitative vegetation descriptors from remotely sensed spectral observations obtained through various inversion procedures (e.g., Croft et al. 2020; Malenovský et al. 2013; Verrelst et al. 2019). One of the most frequently used and well-established leaf-scale RTMs is PROSPECT (Féret et al. 2020; Féret et al. 2017; Jacquemoud and Baret 1990; Malenovský et al. 2006). Its first clone designed to simulate the chlorophyll-*a* fluorescence emission in plant leaves was FluorMODleaf (Pedrós et al. 2010), followed by computationally simpler Fluspect-B (Vilfan et al. 2016) and Fluspect-Cx (Vilfan et al. 2018). The Fluspect models reproduce leaf optical properties between 400 and 2500 nm together with 3D matrices of forward- and backward-emitted SIF per wavelength of photosynthetically active radiation (PAR) incident on the adaxial side of a dark-adapted leaf. Besides these semi-empirical models, physical 3D leaf fluorescence RTMs have been developed, e.g., the Monte

Carlo (MC) Photon Transport (Sušila and Nauš 2007) or the Fluorescence Leaf Canopy Vector Radiative Transfer model (Kallel 2020). The MC models are, however, computationally demanding and, therefore, less suitable for an operational use in routine applications.

Models of SIF radiative transfer are developed hand-in-hand with the RS experimental work conducted at leaf as well as canopy scales (Aasen et al. 2019). Leaf RTMs are usually embedded in canopy-scale RTMs that can be classified according to the canopy representation as one-dimensional (1D) or three-dimensional (3D). Strengths and weaknesses of available canopy RTM types are reviewed in Malenovský et al. (2019). 1D models, such as SAIL (Verhoef 1984), were designed for a horizontally homogeneous canopy with structural, optical and biochemical variability only in the vertical dimension (e.g., mono-species crops). The most frequently used SIF model for 1D canopies is a SAIL's successor called SCOPE (van der Tol et al. 2009; van der Tol et al. 2019; Yang et al. 2020a), recently extended for multi-layered canopies as mSCOPE (Yang et al. 2017). Both SCOPE models are not modelling just radiance and SIF transfer but also soil-vegetation-atmosphere temperature and energy balances, including photosynthetic processes. SCOPE is frequently used for its simplicity and robustness, but its 1D architecture is unsuitable for complex multi-species ecosystems with structurally heterogeneous canopy layers and rough topography (e.g., boreal forests or savannas; Liu et al. 2019a). Therefore, several 3D RTMs have been equipped with the ability to scale SIF from leaves to canopies to better capture the influence of structural heterogeneity of vegetation canopies. FluorWPS is a 3D MC ray-tracing SIF model (Zhao et al. 2016) that was developed and tested on 3D agricultural crops (Tong et al. 2021). Flux tracking of SIF simulated in the Discrete Anisotropic Radiative Transfer (DART) model (Gastellu-Etchegorry et al. 1996) was used to assess its multi-angular anisotropy in 3D maize canopies (Gastellu-Etchegorry et al. 2017). The FluorFLIGHT 3D model, developed from FLIGHT (North 1996), supported assessment of Mediterranean oak forest water stress and *Phytophthora* infections from airborne SIF data (Hernández-Clemente et al. 2017). Finally, the FLiES MC model (Sakai et al. 2020) was used to interpret space-borne SIF of Amazonian forests (Köhler et al. 2018).

Despite the fact that all RTMs rely on simplifications and assumptions, they are powerful tools to investigate the optical interactions of SIF, which is needed for scaling and interpretation of the SIF signals acquired by proximal, airborne and spaceborne instruments (Bendig et al. 2020; Gamon et al. 2019; Wyber et al. 2017). The main goal of this paper is to demonstrate the ability of the DART model coupled with Fluspect-Cx to assess the influence of canopy 3D

architecture on the top-of-canopy SIF (SIF_{TOC}) for cropland and forested environments that are difficult or even infeasible to investigate directly. DART simulations in this study address three primary research questions. First, in absence of a suitable 3D validation measurements and to verify their modelling consistency, do the DART, SCOPE and mSCOPE models provide comparable estimates of SIF_{TOC} for structurally homogenous vegetation in form of a turbid medium? Second, what is the SIF_{TOC} impact originating from biochemical leaf fluorescence efficiencies (*fqe*), varying for sun- and shade-adapted leaves, in comparison to increasing leaf density and clumping of maize (*Zea mays L.*) canopies? And third, what are the effects of woody trunks and branches on simulated SIF_{TOC}, SIF fluxes and escape factors from 3D forest abstractions of dense and sparse Australian white peppermint (*Eucalyptus pulchella*) stands?

2. Material and Methods

2.1 Implementation of leaf chlorophyll fluorescence in DART

We used the 3D DART model as the pilot RTM of this study. DART, being developed by researchers from the CESBIO Laboratory in Toulouse for more than 20 years (Gastellu-Etchegorry et al. 1996), was successfully cross compared with other state-of-the-art RTMs within the RAMI exercise (Widlowski et al. 2015). It produces at-sensor top-of-atmosphere (TOA) and bottom-of-atmosphere (BOA) multi-angular RS images by tracking optical and thermal photon fluxes through any type of 3D landscape with atmosphere (Gastellu-Etchegorry et al. 2015). Additionally, it calculates the quantitative 3D radiative budget, i.e., fluxes of intercepted, absorbed, reflected and emitted radiation, in the optical spectral domain (400-2500 nm) (Gastellu-Etchegorry et al. 2004). The presence of woody material was implemented in DART in 2008 (Malenovský et al. 2008), and radiative transfer of Fluspect-Cx modelled SIF emissions in 2017 (Gastellu-Etchegorry et al. 2017). The Fluspect-Cx implementation followed the approach that was previously applied to couple DART with the PROSPECT-D model (Féret et al. 2017), taking advantage of both models' computational similarities and commonalities in input/output handling. The DART version 5.7.3, used in this work, simulates SIF radiative transfer and budget for 3D vegetation canopies constructed from geometrically explicit triangular objects (facets). Based on user-defined input parameters (i.e., leaf chlorophyll *a*+*b*, total carotenoid and brown pigment contents, equivalent water thickness, dry leaf mass per area, leaf mesophyll structural parameter and specific fluorescence efficiencies), Fluspect generates four SIF matrices (M_{xyij}), where *x* is the photosystem PSI or PSII, y is the backward or forward

direction relative to radiation incident direction, *i* is the 1 nm excitation band in the photosynthetically active spectral region from 400 to 750 nm ($i \in$ [1 I]), and *j* is the 1 nm emitted SIF band ($j \in$ [1 J]) in the spectral region from 640 to 850 nm. Consequently, the Fluspect SIF leaf exitance (F_{xyj}) at band *j* (1 nm bandwidth) due to irradiance (E_i) in band *i* is:

$$F_{xyj} = M_{xyij}.E_i. \quad (1)$$

In contrast to Fluspect, DART works with any number of spectral bands that can have any bandwidth, for example with U excitation bands λ_u and V fluorescence bands λ_v. Hence, in DART, a leaf irradiance (E_u) leads to the leaf exitance:

$$F_{xyv} = M_{xyuv}.E_u, \quad (2)$$

where M_{xyuv} is derived from the Fluspect matrices (M_{xyij}) using an interpolation on spectral bands ($\Delta\lambda_u = \Sigma\alpha_{ui}.\Delta\lambda_i$, $\Delta\lambda_v = \Sigma\beta_{uj}.\Delta\lambda_j$) and the two-step weighted arithmetic averaging:

$$M_{xyuv} = \frac{\sum_j \beta_{uj}.\Delta\lambda_j.M_{xyuj}}{\sum_j \beta_{uj}.\Delta\lambda_j}, \text{ where} \quad (3)$$

$$M_{xyuj} = \frac{\sum_i \alpha_{ui}.\Delta\lambda_i.M_{xyij}}{\sum_i \alpha_{ui}.\Delta\lambda_i}. \quad (4)$$

DART spectral leaf SIF exitance is accurate only if the *u* bands cover the entire SIF excitation spectral interval and if they do not overlap. Similarly, it simulates the whole SIF domain only if the *v* bands cover the whole SIF emission spectral interval.

The Fluspect calibration optical parameters (i.e., specific absorption coefficients, refractive index of mesophyll cell walls and water, etc.) are stored in an external table called Optipar. We used the Optipar table released in 2015. Additionally to the standard PROSPECT leaf biochemical and structural inputs, Fluspect requires leaf fluorescence quantum efficiencies (*fqe*), in DART referred to as fluorescence yields, for PSI and PSII. The specification of *fqe* values in DART is flexible. They can be entered per individual foliage facet or specified as general parameters that represent all leaves or a group of leaves in a given canopy. Biologically meaningful foliage groups are, for instance, sunlit (i.e., leaves exposed to direct sun radiation) and shaded leaves (i.e., leaves in the shadow of other phytoelements), or sun-adapted (i.e., leaves exposed most of the time to a direct sun radiation and subsequently adapting their pigment pools for a high photoprotective capacity) and shade-adapted leaves (i.e., leaves growing most of their lifespan under a low-intensity diffuse light and consequently having no need for a high photoprotective capacity). It is important to keep in mind that a momentarily

shaded leaf can actually be sun-adapted and vice versa, depending on its instantaneous and total diurnal illumination.

The implementation of DART chlorophyll fluorescence emission F_{xyv} (Eq. 2) does not account for the microclimatic conditions influencing the actual leaf photosynthetic activity. However, F_{xyv} can be in a vertical canopy profile additionally weighted by an *eta* parameter, which adjusts the leaf SIF exitance according to actual local temperature, humidity, wind aerodynamics and other microclimatic environmental conditions. Similar to *fqe*, the *eta* profile can be inserted either for a whole canopy, per a foliage group, or per pre-defined leaf groups. Since DART modelling does not contain soil-vegetation-atmosphere transfer (SVAT) of energy, the *eta* parameter must be precomputed out of DART with a SVAT model (e.g., SCOPE; van der Tol et al. 2009) that considers dynamic meteorological factors as active parts in computation of the energy balance. DART simulates the total and the per-photosystem SIF_{TOC} radiance and TOC reflectance using the N-flux tracking transfer. Technical details about the SIF flux tracking in DART are available in the DART User's Manual (Chapter III.2.2.d; DART 2020), while DART physical principles and mathematical descriptions are detailed in the DART Handbook (DART 2019).

2.2 Comparison of DART and SCOPE/mSCOPE SIF radiative transfers

In absence of a suitable empirical verification data, we compared the DART SIF_{TOC} signal with comparable outcomes produced by the SCOPE model and its multi-layer extension, mSCOPE (both in version 1.62). SCOPE is a broadly accepted model that has been previously confronted and validated with SIF_{TOC} measurements of agricultural crops (van der Tol et al. 2016). It simulates vegetation canopy as a turbid medium of infinitely small leaves distributed in 60 horizontally homogeneous vertical layers (Yang et al. 2017), all of them with the same predefined leaf biochemical and canopy structural parameters. mSCOPE allows users to divide canopy into multiple horizontal layers and to assign to each one specific leaf optical properties and LAI. The methodology and graphical outputs of the DART and SCOPE/mSCOPE SIF radiative transfer comparison are, due to a large extent, provided in Appendix A.

2.3 DART modelled influence of geometrically explicit plant canopy structures on SIF

DART works with detailed and spatially explicit 3D representations of plant foliage and other canopy elements (e.g., trunks and branches), and can be, therefore, used to investigate how the structural components modulate the simulated SIF_{TOC} signal through optical photon

interactions as well as via foliage shading and physiological adaptations to prevailing photosynthetic light intensity. For this purpose, we built two realistic but structurally different mono-species canopies: i) an agricultural field of 1 m tall maize plants with eight leaves, created with the open source graphical software Blender (Blender 2007) according to a template produced by the plant architecture modelling L-system OpenAlea (Pradal et al. 2008), and ii) a 16 m tall forest stand of white peppermint trees, created from terrestrial laser scans of real trees (Janoutová et al. 2019) growing in southern Tasmania (Australia). 3D landscapes were built as juxtaposed scenes located at the same Latitude of 39.03°N and Longitude of 76.85°W (Maryland, USA) as previous simulations, with the solar angles for 10th July 2014 for the test of foliage sun and shade adaptation and for 26th August 2014 at 14.00 of local time (without the daylight saving) for tests of maize canopy clumping and eucalypt wood influence. All canopies were illuminated by the same DART-simulated BOA direct and diffuse solar irradiance, as described in the previous section 2.2. Ground of the 3D scenes was optically defined as the Lambertian loamy gravel brown dark soil with a linearly increasing reflectance ($\rho \approx 6\%$ at 550 nm, $\rho \approx 12\%$ at 686 nm and $\rho \approx 15\%$ at 740 nm).

2.3.1 Distinction and influence of sun- and shade-adapted foliage in maize crops

As explained by Nobel (1976) or Givnish (1988), leaves growing in a shaded environment are biochemically and anatomically different from those exposed for most of the day to direct solar irradiation. DART users can consider these differences and their influence on SIF_{TOC} by classifying the facets of 3D vegetation leaves in several classes, for which leaf optical or biochemical properties (including *fqe* and *eta* parameters) can be defined separately. The final number of classes depends on the structural complexity of canopies and the availability of measurements to support the detailed foliar parameterization. A simple two-class classification would split leaf facets into just sun- and shade-adapted cohorts (DART 2020), considering a long-term cumulative leave irradiance as the main driving force.

DART calculates intercepted, absorbed, reflected and emitted radiation, i.e. radiative budget, per 3D cell of the simulated scene and also for each surface facet in the scene (Gastellu-Etchegorry 2008), which can be used to distinguish between the sun- and shade-adapted leaf cohorts. The intercepted radiation flux $E(\lambda)$ [W.m^{-2}] can be converted into photosynthetic photon flux density Q (PPFD) [µmol.photons.m^{-2}.s^{-1}] by integrating the intercepted PAR (iPAR) per leaf facet as follows:

$$Q = \int_{\Delta\lambda_i} E(\lambda)\cdot d\lambda \cdot \frac{\int_{0.4\mu m}^{0.75\mu m} L_B(T,\lambda)\cdot\frac{\lambda}{h\cdot c}\cdot\frac{10^6}{Na}\cdot d\lambda}{\int_{0.4\mu m}^{0.75\mu m} L_B(T,\lambda)\cdot d\lambda}, \quad (5)$$

where $L_B(T,\lambda)$ is Planck's law at temperature T (T = 5800 K) and wavelength λ [μm], h is Planck's constant [J.s], c is speed of light [m.s^{-1}], Na is Avogadro's constant [mole^{-1}], and $\int_{\Delta\lambda_i}$ is the PAR spectral range from 400 to 750 nm. The Q value depends on the ratio of direct and diffuse irradiance spectrum, leaf optical properties and PAR multiple scattering. Influenced by literature findings about the potential of Q for differentiating sun- and shade-adapted leaves (Leuning et al. 1995; Niinemets et al. 2015), the following two classification algorithms were designed: i) a frequency double-threshold and ii) a probability distribution approach. Both methods are based on simulated leaf PAR irradiance values for T time steps during i days, with T being small enough to ensure an adequate angular sampling of leaf irradiance variation during the simulated days.

The first double-threshold approach asks user to specify high Q_H and low Q_L classification thresholds. The facets are then categorized at each time step T into the three groups: i) H for $Q > Q_H$, ii) L for $Q < Q_L$, and iii) M for $Q_H > Q > Q_L$. The number of occasions when a leaf facet appeared in each of these groups during the simulated day i is counted, resulting in [$N_{H,i}$, $N_{M,i}$, $N_{L,i}$] with $N_{H,i} + N_{M,i} + N_{L,i} = T$. Subsequently, a leaf facet is labelled as sun-adapted (i.e., $C_{f,i}$ = 1, with $f \in [1, F]$ where F is the total number of leaf facets) if: i) $N_{H,i} > \frac{T}{2}$ (i.e., leaf facet is categorized as sunlit for the majority of the T time steps), or ii) $N_{M,i} > \frac{T}{2}$ and $N_{H,i} > N_{L,i}$ (i.e., leaf irradiance is, for the majority of T time steps, between the two thresholds and a leaf facet is categorized as sunlit more frequently than shaded). Finally, a leaf facet is labelled as shade-adapted (i.e., $C_{f,i}$ = 0) in all other cases, which cover the following three conditions: i) $N_{L,i} > \frac{T}{2}$, ii) $N_{M,i} > \frac{T}{2}$ and $N_{H,i} < N_{L,i}$, and iii) none of the [$N_{H,i}$, $N_{M,i}$, $N_{L,i}$] values dominates during the simulated times. This way, a day series (an array of i values) of sun-adapted ($C_{f,i}$ = 1) and shade-adapted ($C_{f,i}$ = 0) states is generated per leaf facet f. The final class assignment is decided based on the median value of C_f across the entire examined time period.

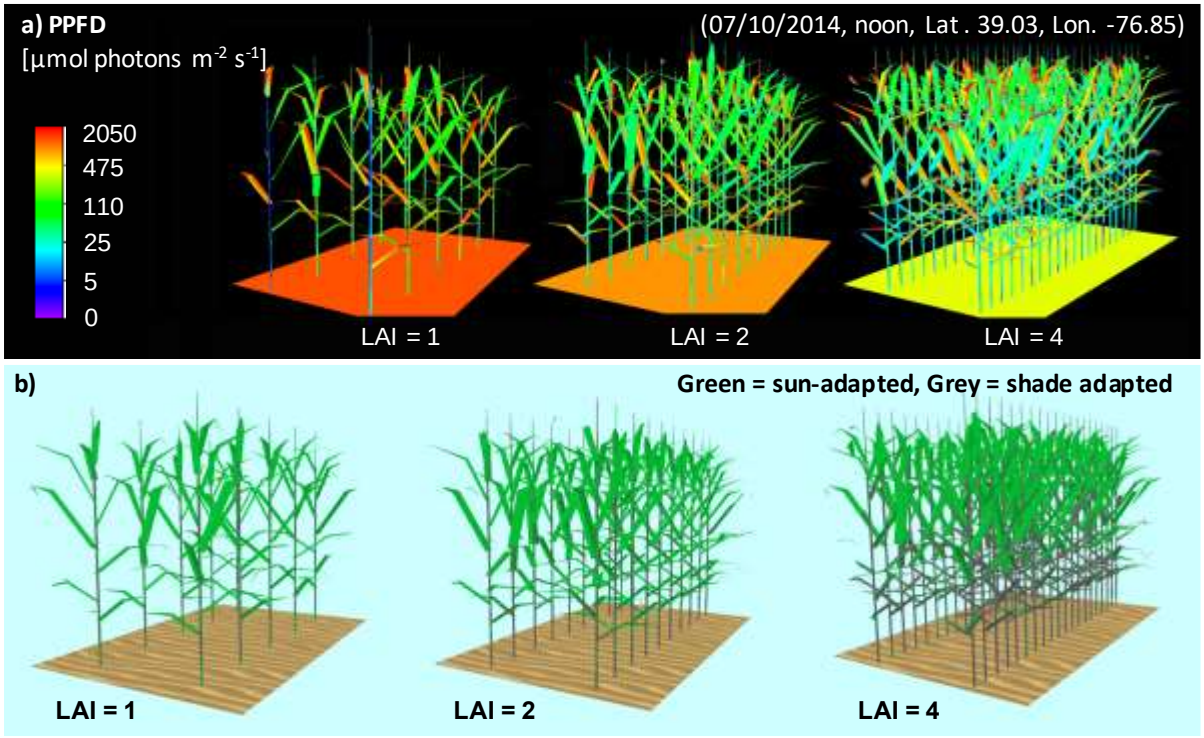

Figure 1. Incident photosynthetically active radiation expressed in photosynthetic photon flux density (PPFD) for three realistic 3D maize (*Zea mays L.*) canopies with LAI equal to 1, 2 and 4 (a). Distinction of sun- (green) and shade- (grey) adapted foliage based on double PPFD thresholds of 50 and 100 µmol.photons.m^{-2}.s^{-1} (b). To mimic realistic maize canopies, all three maize fields (1x1.5 m in size) were created with 1 m tall semi-randomly oriented plants, having eight fully developed bifacial leaves.

The second method uses the probability distribution of the simulated diurnal Q time series. The range of Q values is divided into equally or unequally distributed X intervals, and the Q values of leaf facets simulated at each time step T are categorized in a group x ($x \in [1, X]$). The probability distribution functions of $i \cdot T$ sampling points are then computed over x groups, resulting in the maximum occurrence (i.e., the highest probability density) in group $x_{\max}$ and the median occurrence in group x_{median}. A leaf facet is assigned as sun-adapted if $x_{\max} > \frac{x}{3}$ and $x_{\max} \leq x_{\text{median}}$, and shade-adapted in all other cases. Both methods are available in the DART toolbox directory as Python scripts, the decision which to use is solely of user discretion.

To demonstrate changes in SIF_{TOC} due to the distinction of sun- and shade-adapted leaves, we applied two double-threshold classifications on three maize fields (Figure 1). The first 'relaxed' classification used relatively high and far-apart thresholds of 50 and 100 µmol.photons.m^{-2}.s^{-1}, allowing for a larger portion of shade-adapted parts, whereas the second 'strict' classification used low and close thresholds of 15 and 25 µmol.photons.m^{-2}.s^{-1}, resulting in a smaller amount of strictly shade-adapted leaves and stems. The regularly spaced 1 m tall

plants with fully developed bifacial leaves were placed in fields (1x1.5 m in size) with a random geographical orientation and distances resulting in LAI = 1, 2 and 4. Specific leaf biochemical, structural and fluorescence properties were assigned to each leaf adaptation class as listed in Table 1 (note that foliage of scenarios without distinct light adaptations was assumed to have the properties of sun-adapted leaves and stems). Contrary to previous SIF simulations, PSII *fqe* values of medium magnitude were assigned to each leaf class, while PSI *fqe* values were kept constant under the assumption that PSI contributes to SIF signal of both leaf types equally (Liu et al. 2019a). In order to prevent its confounding effect, the energy balance (leaf photosynthesis) modelling was disregarded, i.e., the fluorescence efficiency weight *eta* was forced to one. The remaining inputs were arbitrarily defined within plausible dynamic ranges of published laboratory measurements (Hosgood et al. 1994; Jacquemoud and Baret 1990).

Table 1. Input parameters of the Fluspect-Cx model to simulate optical properties of sun- and shade-adapted leaves, as well as foliage without light adaptations and stems: content of chlorophyll *a+b* (Cab), total content of carotenoids (Car), equivalent water thickness (EWT), leaf mass per area (LMA), mesophyll optical thickness number (N) and fluorescence quantum efficiencies (*fqe*) for PSI and PSII.

Fluspect inputs	Cab [μg.cm^{-2}]	Car [μg.cm^{-2}]	EWT [cm]	LMA [g.cm^{-2}]	N	PSI *fqe*	PSII *fqe*
Sun-adapted and without adaptation leaves and stems	50	15	0.009	0.0021	1.5	0.002	0.016
Shade-adapted leaves and stems	75	20	0.012	0.0028	2.0	0.002	0.022

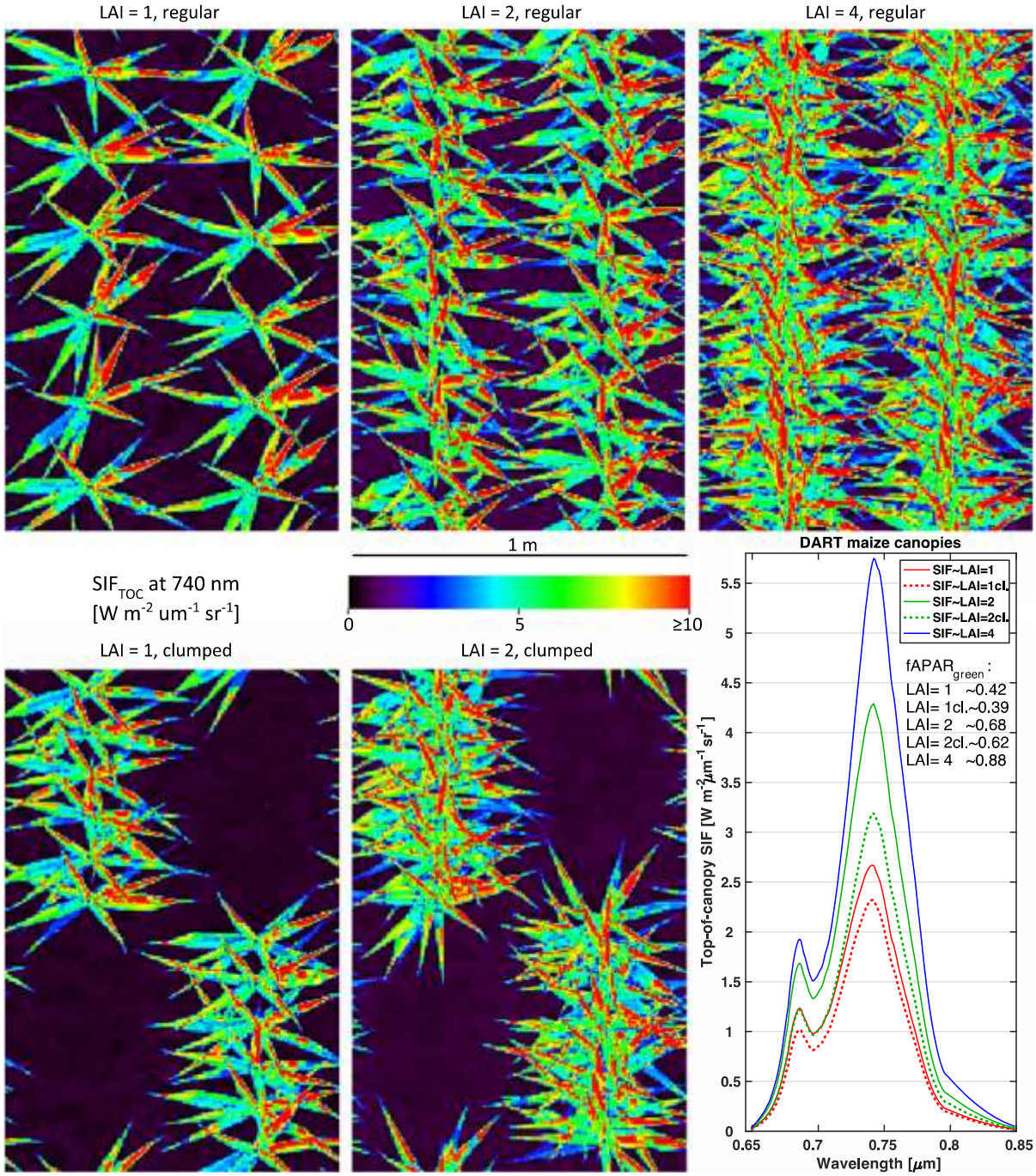

Figure 2. DART simulated images of top-of-canopy SIF at 740 nm for maize fields of three leaf area indices (LAI) and two canopy closures, 100% regular (top) and 50% clumped (bottom), given by the number of plants (LAI = 1 ~ 12 plants, LAI = 1 ~ 24 plants and LAI = 4 ~ 50 plants) associated with different plant distances. The graph (bottom-right) displays the corresponding modelled canopy SIF spectra between 650 and 850 nm and provides the $fAPAR_{green}$ values per scenario.

2.3.2 Canopy SIF changes due to leaf density and clumping of maize plants

Potential variability in SIF_{TOC} due to leaf density and plant clumping (i.e., canopy closure – CC) changes were simulated for virtual maize canopies of three plant densities (LAI = 1, 2

and 4) in a regular spatial distribution (CC ≈ 100%) and in two clumped formations (LAI = 1 and 2, CC ≈ 50%) (Figure 2). Compared to the previous exercise (Figure 1), distances between 6 (LAI = 1) or 12 (LAI = 2) of neighbouring regularly spaced plants in a row were shortened by half to create regular foliage clumps and canopy gaps of the same size. To keep consistency, the leaf and stem optical properties were those used for the turbid-like canopies (Table A1) and the sun- and shade-adaptations were not distinguished, i.e., all leaves were considered as equal.

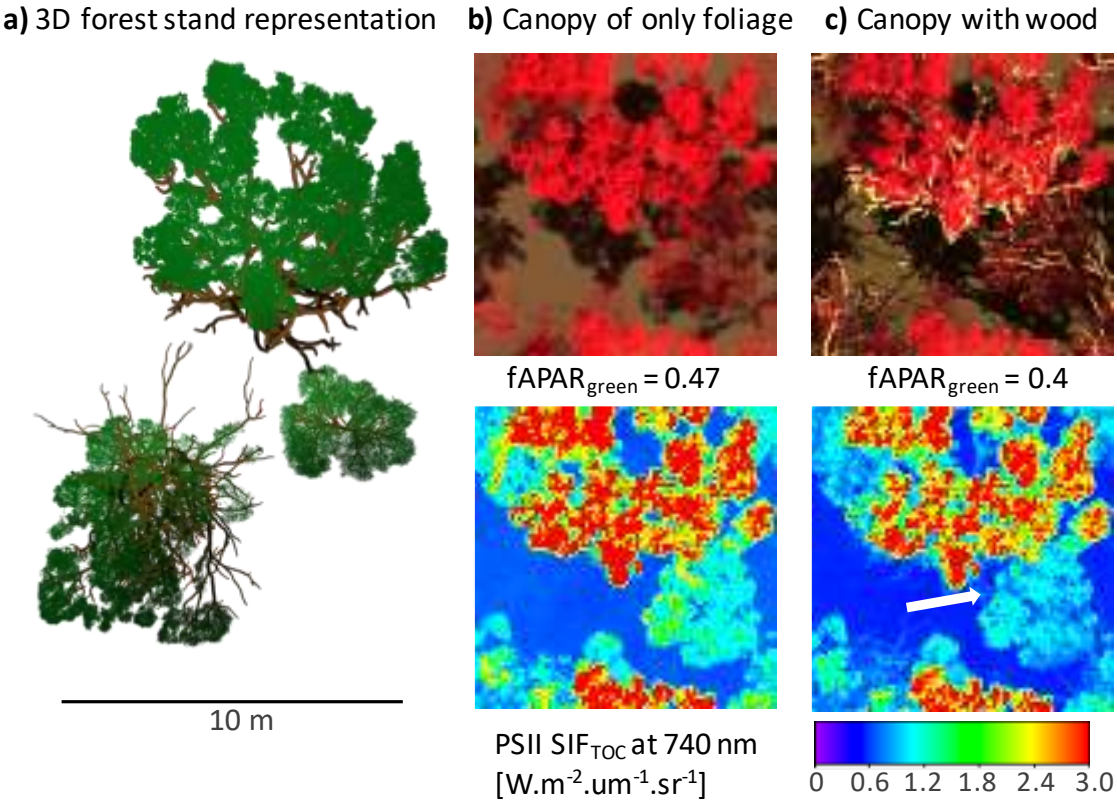

Figure 3. Nadir view of 3D representation of the dense white peppermint (*Eucalyptus pulchella*) test canopy derived from terrestrial laser scans of trees growing east of Hobart (Tasmania, Australia) (a). The virtual scene (LAI = 2) was used to simulate a near-infrared, red and green RGB false colour composite images in DART of top-of-canopy reflectance (top) as well as PSII SIF at 740 nm (bottom) of the canopy formed by: b) only foliage and c) foliage and woody material covered with bark. The white arrow points at the example of SIF reflection from an exposed tree branch surface.

2.3.3 Influence of leaf clumping, trunks and branches on SIF of white peppermint canopies

DART simulations of eucalyptus forest canopies were used to investigate potential impacts of leaf clumping and woody material, i.e., trunks and branches covered by bark, on SIF_{TOC} modelled at 686 and 740 nm. 3D representations of the eucalyptus trees were constructed based on 3D point clouds acquired with the terrestrial laser scanner (TLS) Trimble TX8 (Trimble Inc., USA). Three native white peppermint eucalypts of different age, height and general habitus

were scanned from several geolocations in dry sclerophyll forest located southeast of Hobart (Tasmania, Australia) to acquire their TLS point clouds with a point spacing of 11.3 mm at distance of 30 m. The TLS points of each tree were, after a mandatory pre-processing, semi-automatically separated in two groups: i) points of trunks and branches and ii) points representing foliage. Points classified as wood were used as attractors in an automatic procedure (Sloup 2013) to extract the external surfaces of trunks and main branches, as described in Verroust and Lazarus (1999). The foliage points were subsequently spatially collocated with the reconstructed wooden skeleton. 3D representation of leaves was created in Blender (Blender 2007) based on an average shape and size of actual leaves and then distributed automatically at the locations of foliage points according to the Erectophile LAD (Danson 1998), targeting two crown LAI values of 2 and 5. A complete description of this TLS-based 3D construction of trees, developed specifically for RTM purposes, is available in Janoutová et al. (2019). Two DART canopies (scenes), were constructed with the 3D tree representations: i) a dense canopy was created by placing three trees with the individual crown LAI = 2 within a scene of 81 m^2, while keeping CC ≈ 80% (Figure 3a), and ii) a sparse canopy was built by redistributing the same trees but with the crown LAI = 5 within a scene of 196 m^2 to achieve CC ≈ 40%. Combinations of the tree crown LAI and scene sizes ensured that both scenes had, for the purpose of comparability, the same canopy LAI = 2.5. Additionally, an identical bark directional-hemispherical reflectance ($\rho \approx 20\%$ at 550 nm, $\rho \approx 40\%$ at 686 nm and $\rho \approx 50\%$ at 740 nm), measured on actual bark samples collected in field, was applied in both canopies.

Besides standard forest canopies (e.g., Figure 3c), the virtual environment of the DART model also allows for simulating canopies composed of only foliage without woody components (Figure 3b). By comparing results from simulations with and without woody material, we quantified the magnitudes of shading and direct obstructing effects of woody material. Removing woody components increases the within-canopy iPAR (Q) due to the reduction in wood shadowing, which in turn increases SIF emitted by all previously shaded leaves. The obstruction impact of woody material is caused by its optical interactions with SIF photons. First, it diminishes (blocks) the within-canopy SIF at both 686 and 740 nm via bark scattering and absorption. Second, it affects, to some extent, SIF emission through reflection of SIF at 686 nm that can be reabsorbed and later reemitted by chlorophyll pigments.

2.4 Computation of canopy $fAPAR_{green}$, SIF balance, escape factors and differences

The main driver of green foliage SIF emissions (including stems of the maize plants) in DART simulations that do not contain a modulation of PSI and PSII *fqe* values by *eta* coefficients is the fraction of absorbed photosynthetically active radiation ($fAPAR_{green}$). Therefore, a change of $fAPAR_{green}$ in these simulations indicates a change in the ratio of sunlit and shaded photosynthetically active plant parts, which results in an equal relative change in SIF leaf emission of both photosystems. To be able to investigate the impact of different 3D canopy architectures on their $fAPAR_{green}$, we calculated $fAPAR_{green}$ for all SIF_{TOC} simulating scenarios from the DART radiative budget of a single broad PAR band (λ = [400 750] nm) as:

$$fAPAR(\lambda)_{green} = \frac{APAR(\lambda)_{green}}{PAR(\lambda)_{TOC}}, \quad (6)$$

where $APAR(\lambda)_{green}$ is PAR absorbed by all green plant constituents of a given DART scene and $PAR(\lambda)_{TOC}$ is the solar incoming PAR simulated at the top of canopy. The relative difference [%] in $fAPAR_{green}$ of clumped (C) compared to regularly spaced (R) maize canopies was calculated as:

$$\varepsilon_{fAPAR(\lambda)} = 100.\frac{fAPAR(\lambda)_{green\_C} - fAPAR(\lambda)_{green\_R}}{fAPAR(\lambda)_{green\_R}}. \quad (7)$$

Similarly, the shading effect of woody components on eucalyptus SIF emissions was assessed through the relative difference [%] of canopy $fAPAR_{green}$ obtained for simulations containing just foliage (F) and foliage with wood (FW) as follows:

$$\varepsilon_{fAPAR(\lambda)} = 100.\frac{fAPAR(\lambda)_{green\_F} - fAPAR(\lambda)_{green\_FW}}{fAPAR(\lambda)_{green\_FW}}. \quad (8)$$

DART-simulated 3D radiative budget of SIF allows for locating origins of remotely sensed SIF using the SIF balance ($SIF(\lambda)_{bal}$) [$W.m^{-2}.\mu m^{-1}$], computed by subtracting the absorbed SIF flux from the total emitted SIF flux (i.e., $SIF(\lambda)_{PSI}$ plus $SIF(\lambda)_{PSII}$) of a given wavelength (λ) per a vertical canopy layer. A positive $SIF(\lambda)_{bal}$ means that the canopy layer acts as a SIF source, while a negative $SIF(\lambda)_{bal}$ indicates canopy parts acting as SIF sinks. Subsequently, relative difference [%] of $SIF(\lambda)_{bal}$ between clumped (C) and regularly spaced (R) maize canopies, computed as:

$$\varepsilon_{SIF(\lambda)bal} = 100.\frac{SIF(\lambda)_{bal\_C} - SIF(\lambda)_{bal\_R}}{SIF(\lambda)_{bal\_R}}, \quad (9)$$

reveals if the maize foliage clumping causes a further reduction ($\varepsilon_{SIF(\lambda)bal} < 0$) or an enhancement ($\varepsilon_{SIF(\lambda)bal} > 0$) or no change ($\varepsilon_{SIF(\lambda)bal} = 0$) of SIF balance per a canopy layer.

The proportion of SIF photons that exit the top of canopy is described by the SIF_{TOC} escape probability factor (SIF_{esc}). In practice, this is the ratio of SIF photons escaping from the top of canopy in any direction to all SIF photons emitted from all canopy leaves in forward or backward directions (Guanter et al. 2014). SIF_{esc} is required for scaling of SIF_{TOC} measurements down at the spatial level of individual leaves (van der Tol et al. 2019), and subsequently essential for correct estimation of vegetation gross primary production (GPP) from airborne and spaceborne SIF observations (e.g., He et al. 2017; Zhang et al. 2020). Since most of RS observations capture SIF_{TOC} from nadir, we computed the relative canopy SIF escape probability factor of a given wavelength (λ) in the nadir direction ($SIF\mathit{nadir}(\lambda)_{esc}$) from SIF radiative budgets of the eucalyptus scenarios. First, we converted SIF emissions of PSI and PSII per m^2 of abaxial and adaxial leaf facets into SIF emissions per m^2 of the scene ($F(\lambda)_{PSI}$ and $F(\lambda)_{PSII}$) [$W.m^{-2}.\mu m^{-1}$] and then calculated $SIF\mathit{nadir}(\lambda)_{esc}$ as:

$$SIF\mathit{nadir}(\lambda)_{esc} = \frac{\pi \cdot (L\mathit{nadir}(\lambda)_{PSI} + L\mathit{nadir}(\lambda)_{PSII})}{F(\lambda)_{PSI} + F(\lambda)_{PSII}}, \quad (10)$$

where $L\mathit{nadir}(\lambda)_{PSI}$ and $L\mathit{nadir}(\lambda)_{PSII}$ [$W.m^{-2}.\mu m^{-1}.sr^{-1}$] are DART modelled PSI and PSII SIF radiances at the wavelength (λ), respectively, escaping from the simulated scene in the nadir viewing direction. The π multiplication in Eq. 10 is removing the angular dependency [sr^{-1}], resulting in relative values of $SIF\mathit{nadir}(\lambda)_{esc}$ between 0 and 1. Since the escape probability factor is predominantly dependent on direct optical interactions with canopy elements that attenuate an emitted SIF signal, we quantified the obstruction (blocking) effect of eucalyptus woody components on canopy SIF in the nadir viewing direction through the relative difference [%] of $SIF\mathit{nadir}(\lambda)_{esc}$, computed from the foliage only (F) and the foliage with wood (FW) simulations as follows:

$$\varepsilon_{SIF(\lambda)esc} = 100. \frac{SIF\mathit{nadir}(\lambda)_{esc\_F} - SIF\mathit{nadir}(\lambda)_{esc\_FW}}{SIF\mathit{nadir}(\lambda)_{esc\_FW}}. \quad (11)$$

Finally, to analyse differences in SIF fluxes escaping from individual simulated canopy layers in all directions (i.e., towards layers of the upper and lower hemispheres), we computed from DART 3D radiative budget their relative omnidirectional escape factor ($SIF\mathit{omni}(\lambda)_{esc}$) as:

$$SIF\mathit{omni}(\lambda)_{esc} = \frac{(F(\lambda)_{PSI} + F(\lambda)_{PSII}) - (A(\lambda)_{PSI} + A(\lambda)_{PSII})}{F(\lambda)_{PSI} + F(\lambda)_{PSII}}, \quad (12)$$

where $A(\lambda)_{PSI}$ and $A(\lambda)_{PSII}$ [$W.m^{-2}.\mu m^{-1}$] are DART modelled absorptances of PSI and PSII SIF, respectively, expressed for the wavelength (λ) per m^2 of the scene. If $SIF\mathit{omni}(\lambda)_{esc} \leq 0$, then

the canopy layer does not contribute to the SIF_{TOC} signal, i.e., its $SIF(\lambda)_{bal}$ is either neutral or negative.

2.5 DART settings common to all SIF canopy simulations

DART simulations were carried out with the flux-tracking algorithm using the following settings: no elimination of low energy rays, relative accuracy on scene albedo equal to 10^{-6}, 25 duplications of the initially simulated scene, the scene illumination mesh size equal to 5.10^{-4} m (with a semi-random spatial distribution of illumination rays), and cell sub-sampling with 8^3 sub-cells per cell and 1 sub face per cell face. An optimal number of 20 flux-tracking iterations, which were required to obtain a 10^{-2} relative accuracy of the scene reflectance, was determined through a simplified accuracy sensitivity study. Intermediate results of the last few iterations were used to extrapolate the final values of simulated radiative budget, bidirectional reflectance function and SIF products. TOC reflectance and SIF were simulated in 212 viewing directions (Yin et al. 2013), distributed systematically throughout the upward hemisphere, with an oversampling of the upward hot-spot region (25 directions in a solid angle of 0.01 sr around the hotspot direction) and 34 virtual viewing directions in the solar principle plane. Leaf facets were simulated as double-faces without the solar penumbra effect, all optical properties were assumed to be Lambertian, and the scene ground surface was horizontal.

2.6 Comparative statistical indicators

Comparative statistical indicators, specifically a root mean square error (RMSE) and an index of agreement (d), were computed to assess these similarities as well as anticipated statistical dissimilarities between different DART scenarios (i.e., turbid-like vs. maize and eucalypt canopies). As explained in Willmott (1981), the dimensionless index of agreement complements the RMSE by indicating the degree of correspondence between two tested datasets in magnitude and direction, where d = 1 means full agreement and d = 0 means total disagreement. Also, the similarity of DART and SCOPE multi-angular SIF_{TOC} was assessed through fitting a linear regression model, where the regression coefficient of determination (R^2) indicated how much of the variability in a reference RT model (i.e., SCOPE) results can be explained by corresponding regressed values simulated in DART.

3. Results

3.1 Comparison of nadir DART and SCOPE/mSCOPE canopy SIF simulations

The SCOPE and DART nadir SIF_{TOC} signatures of turbid medium vegetation canopies were nearly identical (Figure A2). Results between 641 and 850 nm were comparable for all simulated input combinations (i.e., three LAI, three LAD and three soil types). High SIF_{TOC}, observed for canopies of Planophile LAD, is caused by their high PAR interception efficiency. The highest RMSE = 0.162 $W.m^{-2}.\mu m^{-1}.sr^{-1}$ and the lowest d = 0.9965 were found for the Erectophile canopy of LAI = 1, covering soil with $\rho = 50\%$. Despite being the worst case, the values indicate only minor differences between DART and SCOPE results. Statistical analyses revealed that the total SIF_{TOC} RMSE originates mainly from RMSE for PSII, which was twice the RMSE for PSI simulations for all three LADs (results not shown). Despite a significantly higher variability in RMSE than other two LADs, the Planophile LAD showed the highest index of agreement and R^2 computed between the two models.

mSCOPE allowed us to introduce a biochemical/optical heterogeneity in the vertical dimension of simulated canopies. Additionally, we tested DART SIF simulation performance when using the energy balance *eta* coefficients produced by mSCOPE. Comparison of total nadir SIF_{TOC} radiances produced by both models revealed almost the same results (Figure A3). The indices of agreement were in all cases larger than 0.99, regardless exclusion or inclusion of the mSCOPE *eta* coefficients in conducted simulations. The highest RMSE of just 0.221 $W.m^{-2}.\mu m^{-1}.sr^{-1}$ and the lowest d = 0.9985 was found for simulation of 2-layered canopy with LAI = 2 and with the leaf energy balance included (Figure A3b).

3.2 Multi-angular comparison of DART and SCOPE canopy SIF simulations

The similarity of DART and SCOPE SIF_{TOC} simulations at 686 and 740 nm was also investigated for viewing directions other than the nadir view. We compared values simulated in the solar principal plane, with particular attention to the hotspot region, and computed absolute differences between 27 DART and SCOPE turbid medium scenarios in all 212 viewing directions. The smallest differences and the best agreement were found for SIF_{TOC} at 686 nm, Erectophile LAD and LAI = 1 (Figure A4), while the worse agreement and largest differences were obtained for SIF_{TOC} at 740 nm, Spherical LAD and LAI = 4 (Figure A5). Here, SCOPE simulated slightly smaller SIF_{TOC} values, except for VZA > 75°, where SIF_{TOC} dropped unexpectedly steeply down. Also, SCOPE values around the hotspot angles were about 1 $W.m^{-}$

^{2}.µm^{-1}.sr^{-1} lower than the corresponding DART values. This is caused by differences in the vegetation hotspot algorithms. SCOPE uses a Kuusk's analytical approximation, which does not account for a bi-directional gap-fraction correlation with the canopy depth and consequently underestimates the hotspot effect (Kallel and Nilson 2013), whereas hotspot in DART simulations is physically modelled.

Analysis of multi-angular SIF differences among the three LADs stressed smaller dissimilarities at 686 nm, having the best fit for the Spherical LAD, followed by the Erectophile LAD, and then by the Planophile LAD. At 740 nm, the closest match occurred for the Planophile LAD, while the Spherical and the Erectophile LADs showed equal discrepancies (Figure A6). Nonetheless, the maximal absolute SIF_{TOC} difference between DART and SCOPE oblique viewing directions of all scenarios was found to be < 0.8 W.m^{-2}.µm^{-1}.sr^{-1}.

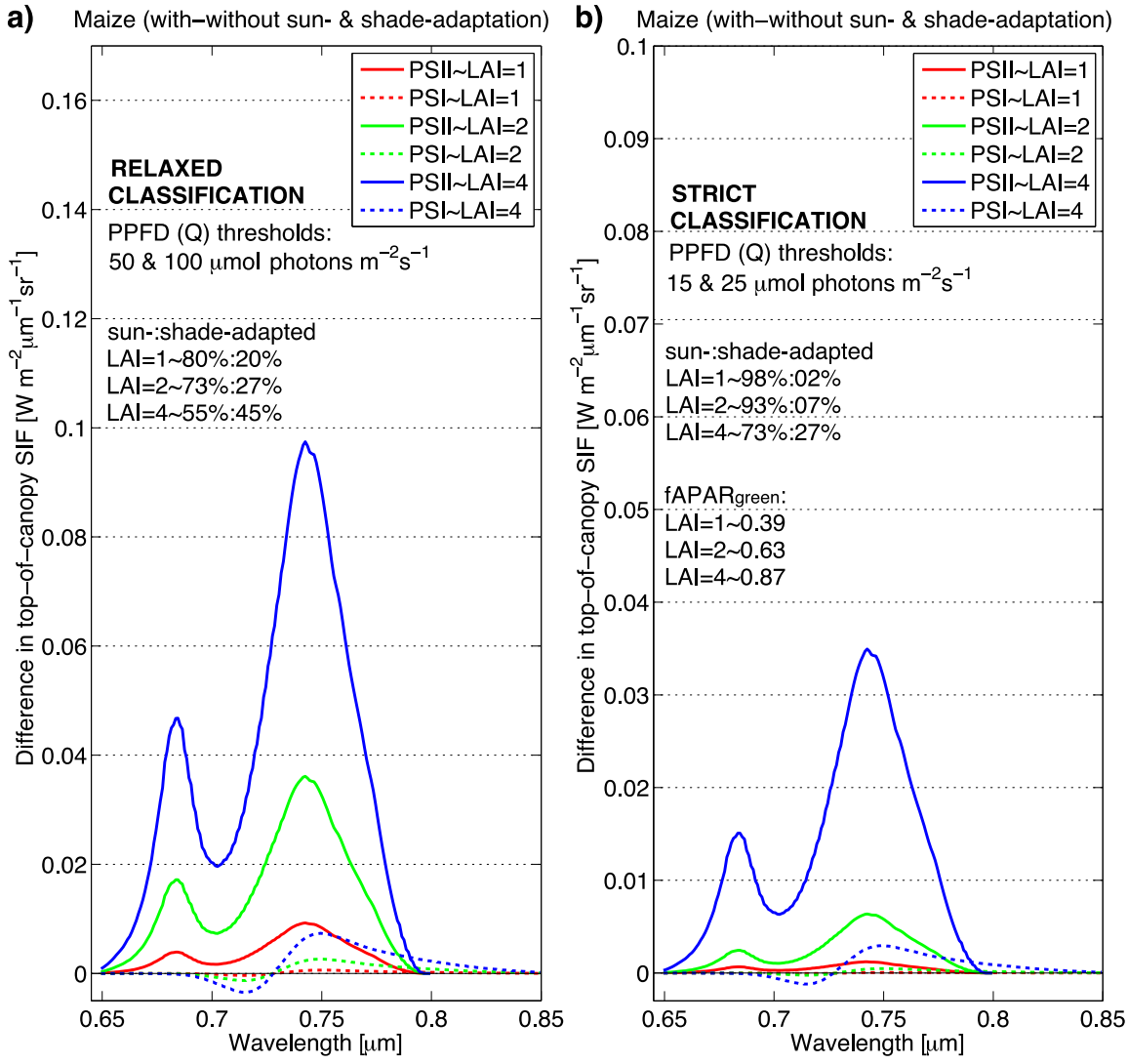

Figure 4. Differences in DART top-of-canopy SIF radiance due to distinction of sun- and shade-adapted leaves of regular maize canopies with LAI = 1, 2 and 4. Graphs illustrate two simulated scenarios of photosynthetic photon flux density (PPFD or Q) classification thresholds: a) a 'relaxed' scenario with high PPFD thresholds of 50 and 100 μmol.photons.m^{-2}.s^{-1}, and b) a 'strict' scenario with low PPFD thresholds of 10 and 25 μmol.photons.m^{-2}.s^{-1}. For details about the double-threshold leaf light adaptation classification see section 2.3.1.

3.3 Effect of sun- and shade-adapted maize foliage classification

Two double-threshold classifications were used to assess the impact of sun- and shade-adapted foliage differentiation on nadir PSI and PSII SIF_{TOC} between 650-850 nm. The first one, called 'relaxed', used the far-apart high Q thresholds (50 and 100 μmol.photons.m^{-2}.s^{-1}), resulting in the sun-to-shade adapted foliage ratio ranging from 80:20% (LAI = 1) to 55:45% (LAI = 4). Figure 4a shows that differences between SIF_{TOC} signatures for simulations with and without the differentiation of sun-/shade-adapted leaves were all positive for PSII, with the highest value ≈ 0.1 W.m^{-2}.μm^{-1}.sr^{-1} around 740 nm for LAI = 4 ($fAPAR_{green}$ = 0.87). Surprisingly, the same differences for PSI between 700 and 725 nm were negative, demonstrating a greater PSI SIF absorption by shade-adapted leaves having a higher chlorophyll *a+b* content of 75 μg.cm^{-2}. Contrary to PSII SIF_{TOC}, where *fqe* was increased from 0.016 to 0.022 for shade-adapted leaves (Table 2), the constant PSI *fqe* of 0.002 could not compensate this increased chlorophyll absorption. The second classification, called 'strict', used the closer and lower Q thresholds (15 and 25 μmol.photons.m^{-2}.s^{-1}), resulting in canopies with a dominant portion of sun-adapted leaves. The sun-to-shade adapted foliage ratio ranged from 98:2% (LAI = 1) to 73:27% (LAI = 4). Consequently, the SIF_{TOC} differences were proportionally smaller (Figure 4b), with the largest value of 0.035 W.m^{-2}.μm^{-1}.sr^{-1} for PSII SIF_{TOC} at 740 nm (LAI = 4). PSI SIF_{TOC} differences were also reduced and remained negative between 700 and 725 nm.

3.4 Influence of foliage density and clumping in maize canopies

Figure 2 illustrates the impact of a leaf density increase (i.e., doubled LAI) and the clumping of maize plants for LAI of 1 and 2. Nadir images of maize canopy SIF_{TOC} at 740 nm show the spatial dependence of SIF_{TOC} radiance on the absorption of iPAR and on the distribution of plant shadows. A linear increase of LAI triggered a non-linear and wavelength-specific increase of SIF_{TOC}. A bit more than 2-fold increase in far-red wavelengths from LAI = 1 to LAI = 4 corresponds to a similar increase in canopy $fAPAR_{green}$, which is not the case for the red SIF_{TOC} nadir signal (Figure 2). The canopy clumping causes a decrease of SIF_{TOC} at all

wavelengths. The 50% decrease in CC caused SIF_{TOC} reduction at 740 nm of about 0.4 for LAI = 1 and 1.0 $W.m^{-2}.\mu m^{-1}.sr^{-1}$ for LAI = 2, whereas reduction of LAI from 2 to 1 resulted in larger SIF_{TOC} declines of about 0.75 for CC = 50% and 1.6 $W.m^{-2}.\mu m^{-1}.sr^{-1}$ for CC = 100%.

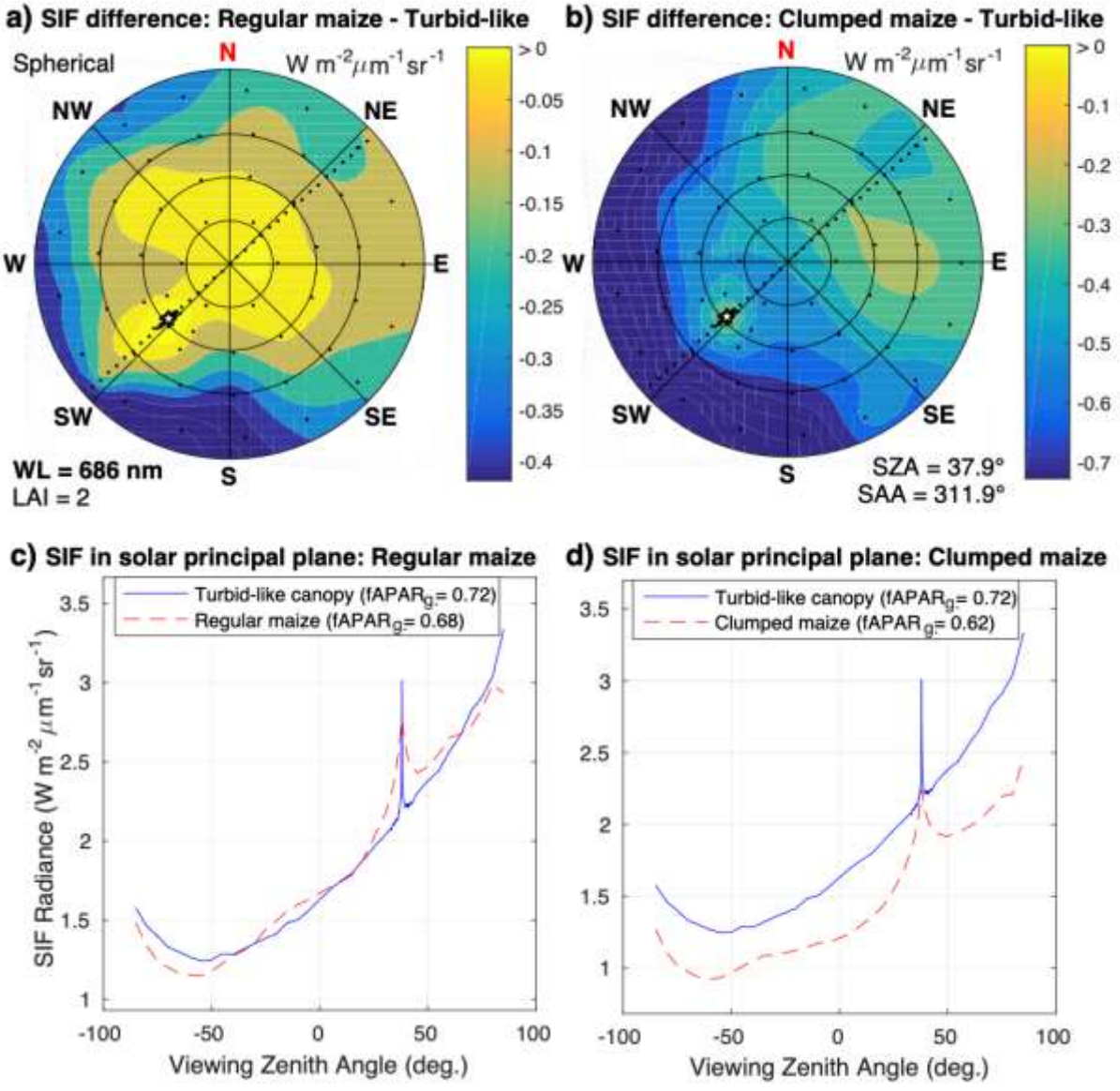

Figure 5. Multi-angular differences in SIF radiance at 686 nm between a) regular, b) clumped DART 3D maize canopies and a DART simulated turbid-like canopy with LAI = 2, Spherical LAD and loamy soil as ground. SIF radiances in the solar principal plane for the turbid-like canopy together with the regular (RMSE = 0.27 and d = 0.9) and the clumped (RMSE = 0.36 and d = 0.81) maize canopies are illustrated in c) and d), respectively. Notations: the white star shows the solar position and black dots indicate the simulated viewing directions; LAD ~ leaf angle distribution; LAI ~ leaf area index; WL ~ wavelength; SZA ~ solar zenith angle; SAA ~ solar azimuth angle; R^2 ~ coefficient of determination; RMSE ~ root mean square error [$W.m^{-2}.\mu m^{-1}.sr^{-1}$]; d ~ index of agreement: 0 = no agreement, 1 = full agreement.

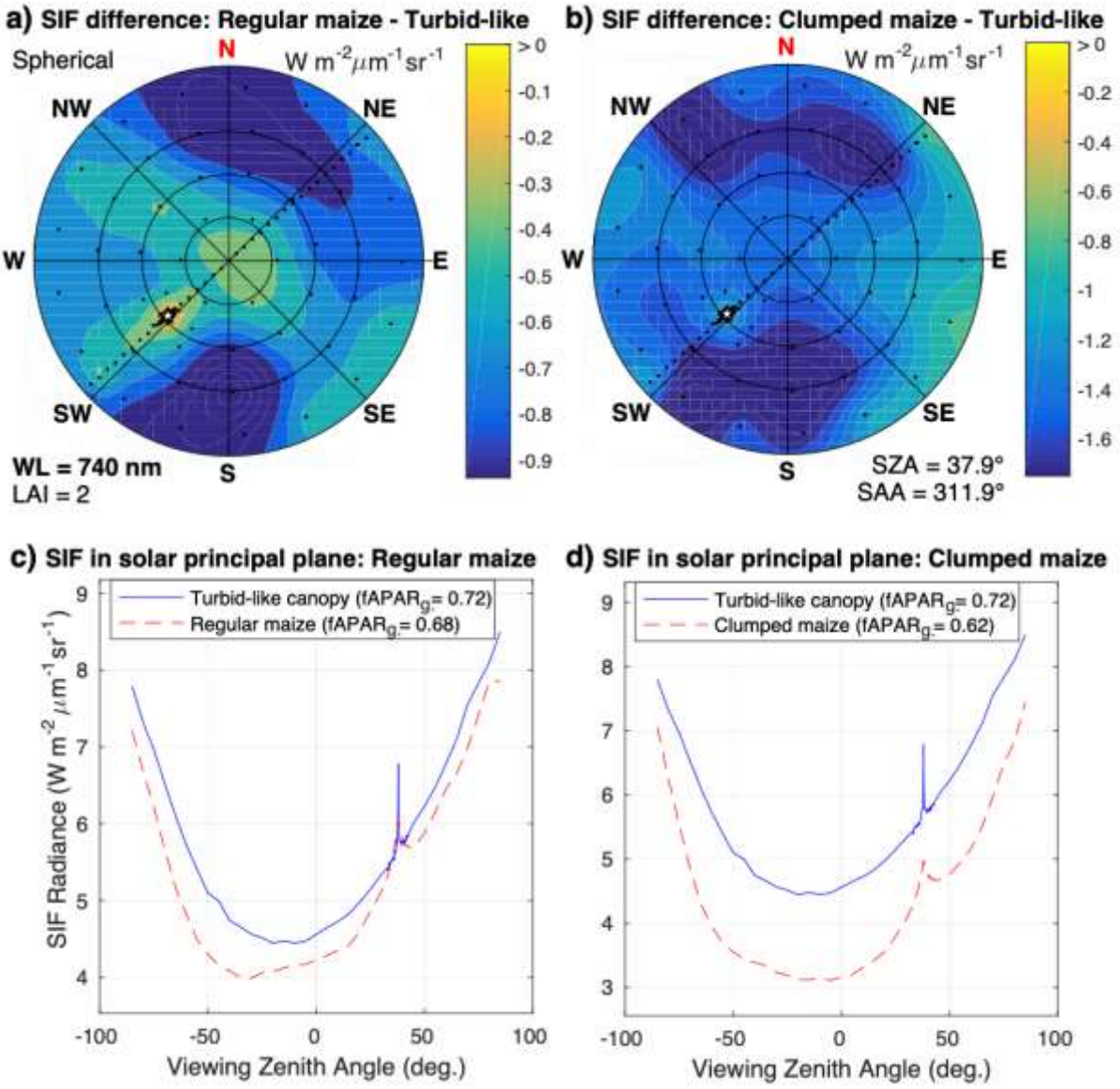

Figure 6. Multi-angular differences in SIF radiance at 740 nm between a) regular, b) clumped DART 3D maize canopies and a DART simulated turbid-like canopy with LAI = 2, Spherical LAD and loamy soil as ground. SIF radiances in the solar principal plane for the turbid-like canopy together with the regular (RMSE = 0.42 and d = 0.92) and the clumped (RMSE = 1.22 and d = 0.62) maize canopies are illustrated in c) and d), respectively (for abbreviations and symbols see Figure 5).

The interpretation of canopy architectural effects can be taken further by investigating the multi-angular differences for SIF_{TOC} at 686 (Figure 5) and 740 nm (Figure 6), computed between the turbid-like vegetation canopy, i.e., a random distribution of many small leaf facets with the Spherical LAD, and the maize regular and clumped canopies of much larger leaves, both with LAI = 2. DART simulated multi-angular SIF_{TOC} values of the turbid-like and regular maize canopies at 686 nm are very close (RMSE = 0.27 $W.m^{-2}.\mu m^{-1}.sr^{-1}$, d = 0.9) (see Figure

5ac), indicating rather similar SIF absorptions within canopies and by soil. The maximum difference of just about -0.4 $W.m^{-2}.\mu m^{-1}.sr^{-1}$ appeared in very oblique viewing directions, in which maize plants scattered less SIF. Despite its slightly lower $fAPAR_{green}$ (0.68 vs. 0.72), the maize canopy scattered a bit more SIF in viewing directions around nadir and hotspot, producing a positive difference. This is caused by the maize geometrically explicit non-random LAD and large-sized leaf facets, redirecting the scattered SIF prevailingly in these directions. Larger size of maize leaves is decreasing scattering of photons, and consequently the diffuse fluxes, and causing a broader base of the SIF_{TOC} hotspot peak, observed when comparing the hotspots regions of maize and the turbid-like medium simulations. Although the multi-angular pattern for the clumped maize canopy looks also very similar (RMSE = 0.36 $W.m^{-2}.\mu m^{-1}.sr^{-1}$, d = 0.81), the differences are all negative and significantly larger, with the maximum of about -0.75 $W.m^{-2}.\mu m^{-1}.sr^{-1}$ (Figure 5bd). It means that the 50% foliage clumping increased scattering and the subsequent within-canopy absorption of SIF at 686 nm, because SIF absorption by the loamy soil beneath the clumped canopy was 7% lower than in the regular canopy, i.e., unable to cause the SIF_{TOC} reduction. The angular distributions of the same differences at 740 nm look different (Figure 6), as they are ruled mainly by scattering related to the canopy architecture. The decrease in intensity of maize far-red SIF_{TOC} is driven by the species-specific foliage distribution and geometry, significantly larger maize leaf size combined with a high leaf single scattering albedo at 740 nm and the soil absorption. SIF_{TOC} differences in Figure 6 are negative for both regular (RMSE = 0.42 $W.m^{-2}.\mu m^{-1}.sr^{-1}$, d = 0.92) and clumped canopy of LAI = 2, but larger for the latter one (RMSE = 1.22 $W.m^{-2}.\mu m^{-1}.sr^{-1}$, d = 0.62). Results of DART radiative budget revealed that the introduction of clumping did not increase but lowered (by 12%) the amount of soil intercepted and absorbed SIF. Hence, it is not soil but clumping-induced within canopy SIF optical interactions that are responsible for this extra reduction of SIF_{TOC}.

The relative contribution from different canopy parts (horizontal layers) to SIF_{TOC} and its modulation by $fAPAR_{green}$ or by SIF scattering and absorption can be investigated by plotting vertical canopy height profiles of $fAPAR_{green}$ together with corresponding SIF balances of both fluorescence wavelengths. Figure 7a shows that SIF balances are positive at all heights, i.e., every layer act as a SIF source, and they follow, in general, changes in $fAPAR_{green}$. The foliage clumping decreased significantly $fAPAR_{green}$, $SIF(\lambda)_{bal}$ and also $SIFomni(\lambda)_{esc}$ (not shown) in the upper half of the canopy with LAI = 2, causing the overall reduction of SIF_{TOC}, but it

increased all of them in canopy parts below. It means that the lower leaves of the clumped canopy contributed to the simulated SIF_{TOC} more than the same leaves of the regular canopy.

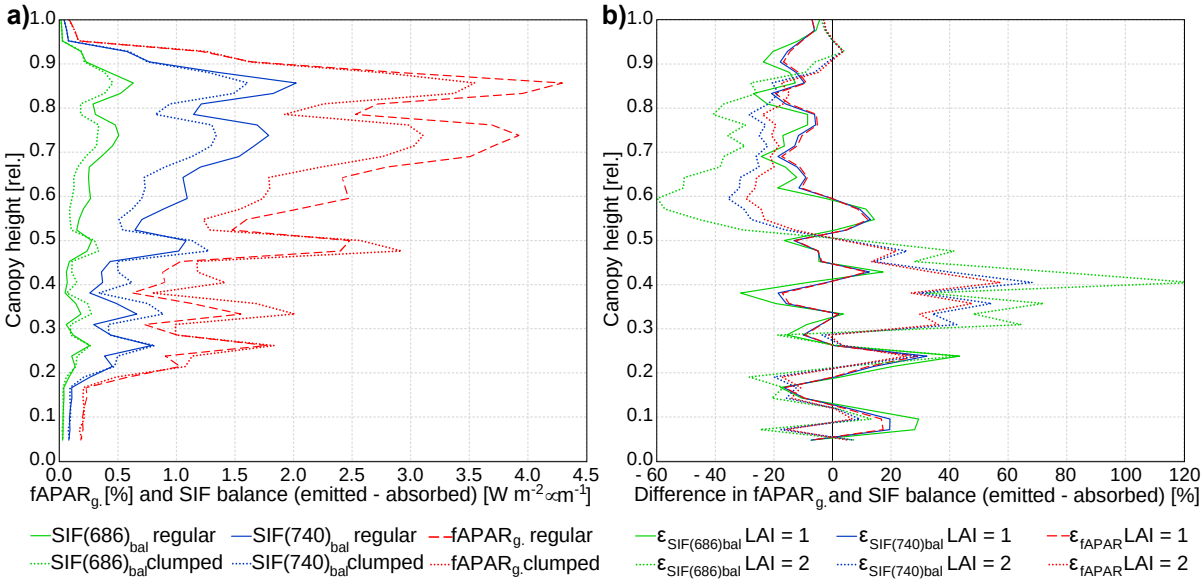

Figure 7. Vertical profiles of a) $fAPAR_{green}$, SIF balances (for maize canopies of LAI = 2) and b) their relative differences at 686 and 740 nm computed between regularly spaced and clumped canopies of the same LAI (for LAI = 1 and 2). Each 2.5 cm thick canopy layer is presented as a point of the relative canopy height [0-1]. For details about computations of $fAPAR_{green}$, SIF balance ($SIF(\lambda)_{bal}$) and their relative differences ($\varepsilon_{fAPAR(\lambda)}$ and $\varepsilon_{SIF(\lambda)bal}$) see section 2.4.

Figure 7b, depicting the $fAPAR_{green}$ and $SIF(\lambda)_{bal}$ relative differences between the regular and clumped canopies, provides a further insight in this behaviour and dependencies between SIF and $fAPAR_{green}$ radiative budgets. It illustrates a clumping-induced steady reduction of $fAPAR_{green}$ and SIF balance differences in upper 40% of the canopy with LAI = 1, whereas the differences in lower 60% fluctuate between positive and negative values. $\varepsilon_{SIF(740)bal}$ for LAI = 1 follows quite closely $\varepsilon_{fAPAR(\lambda)}$, suggesting that variability of SIF fluxes at 740 nm is ruled mainly by clumping-induced changes in distribution of shadows and sun flecks, while $\varepsilon_{SIF(686)bal}$ shows a bit more negative or positive deviations from $\varepsilon_{fAPAR(\lambda)}$, caused by a local increase or decrease in chlorophyll absorption of SIF at 686 nm. SIF_{TOC} for LAI = 2 is formed by steady but greater negative differences in the canopy top half that are partially balanced out by nearly 2-fold larger positive differences between 30 and 50% of the canopy relative height. Comparable differences for both LAI cases between the bottom and 30% of the canopy height indicate very similar $fAPAR_{green}$ and SIF radiative budgets, driven by mostly diffused low-intensity PAR. The negative $\varepsilon_{fAPAR(\lambda)}$ and $\varepsilon_{SIF(\lambda)bal}$ values in the upper half of the canopy are

caused by combination of higher (doubled) LAI with foliage clumping that increased internal shadowing and consequently reduced $fAPAR_{green}$. It also enhanced a number of SIF photons interacting with leaf facets, resulting in a higher fluorescence absorption, especially at 686 nm. Scientifically interesting is the opposite behaviour between 30 and 50% of the canopy height, where it boosted $fAPAR_{green}$ and consequently SIF emissions, but simultaneously diminished SIF absorption, which is evidenced by $\varepsilon_{SIF(686)bal}$ and $\varepsilon_{SIF(740)bal} > \varepsilon_{fAPAR(\lambda)}$. The total energy released from these positive $SIF(\lambda)_{bal}$ differences was, nevertheless, unable to fully compensate the negative $SIF(\lambda)_{bal}$ differences induced by clumping in the upper canopy parts (Figure 7a).

3.5 Impacts of foliage clumping and wood of white peppermint trees

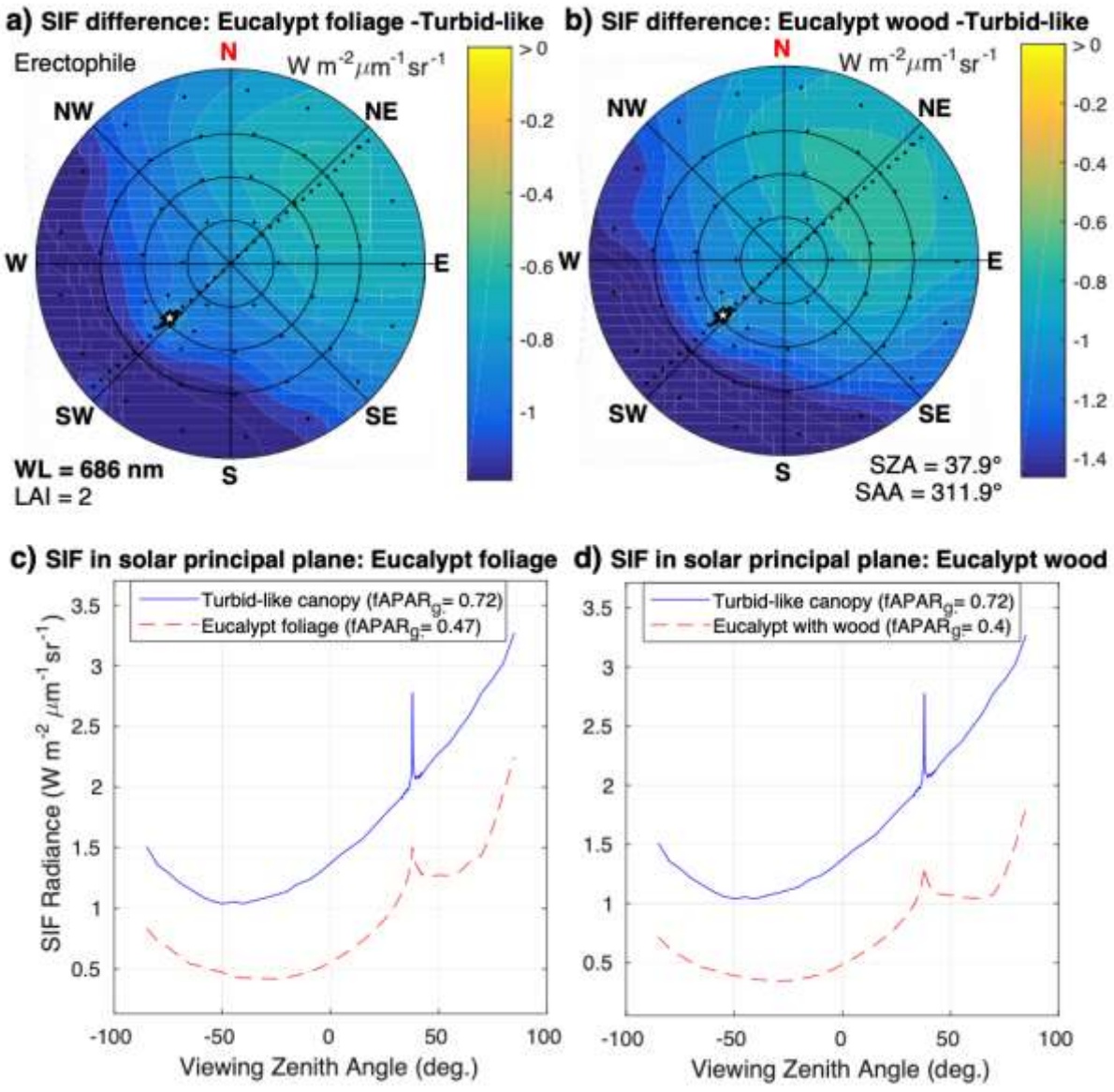

Figure 8. Multi-angular differences in SIF radiance at 686 nm between a) a dense eucalyptus canopy created only by foliage, b) the same canopy containing also woody components and a DART simulated turbid-like canopy, all with LAI = 2, Erectophile LAD and loamy soil as ground. SIF radiances in the solar principal plane for the turbid-like canopy together with the foliage-only (RMSE = 0.82 and d = 0.55) and the foliage with wood (RMSE = 1.0 and d = 0.47) eucalypt canopies are illustrated in c) and d), respectively (for abbreviations and symbols see Figure 5).

DART 3D modelling allowed us to investigate previously unquantified impacts of foliage structure and woody material on $fAPAR_{green}$ and on optical interactions of SIF photons inside white peppermint canopies. Figure 3 shows nadir PSII SIF_{TOC} images at 740 nm for dense eucalyptus forest canopies without and with presence of the woody parts. A simple visual comparison of the two images reveals a lower SIF_{TOC} in the lower right corner of the image caused by a deeper shadowing after inclusion of trunks and branches. One can also detect several large non-fluorescing branches in the SIF_{TOC} image, visible due to a strong reflection of far-red SIF photons by peppermint bark ($\rho_{740\ nm} \approx 50\%$).

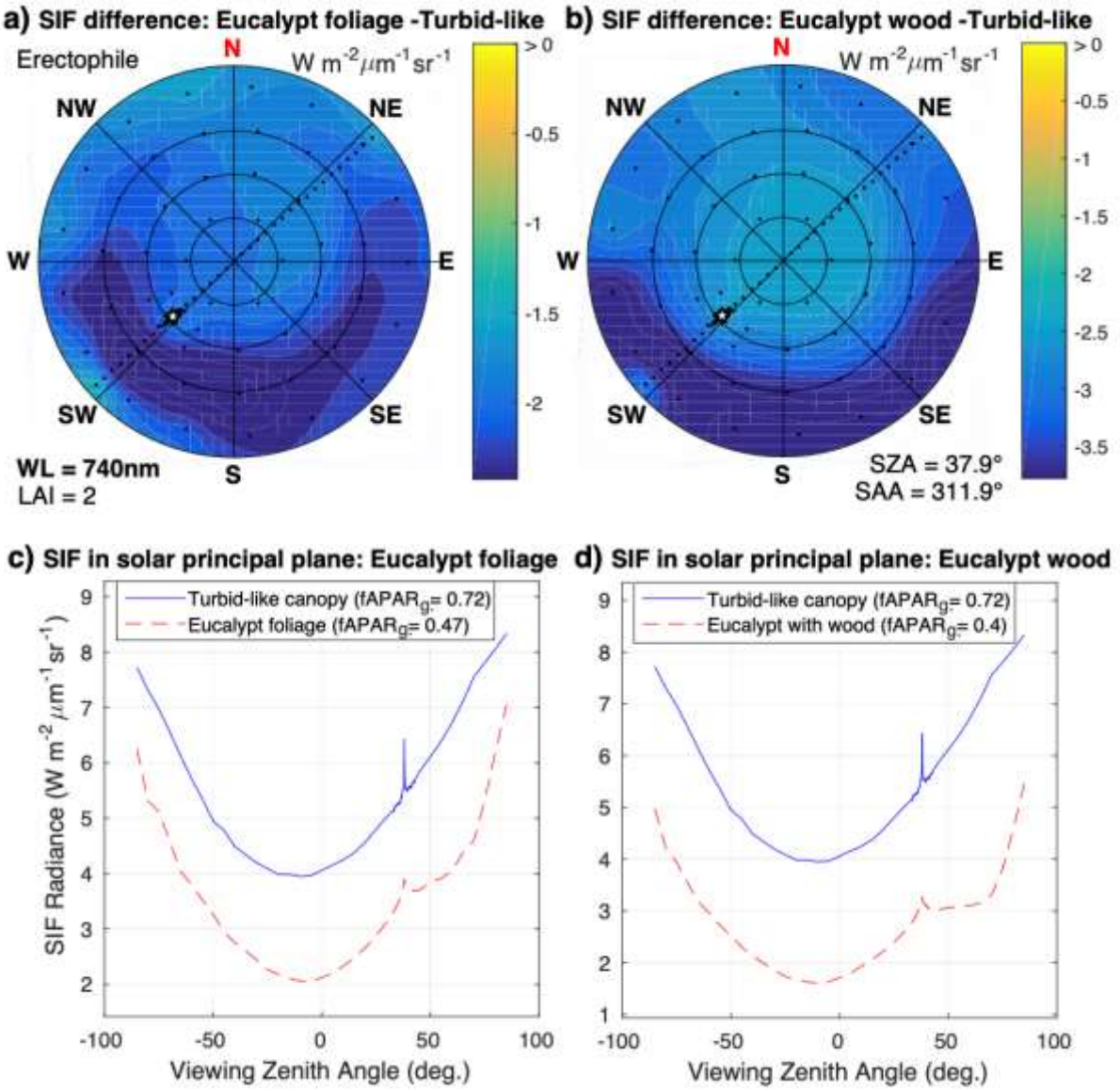

Figure 9. Multi-angular differences in SIF radiance at 740 nm between a) a dense eucalyptus canopy created only by foliage, b) the same canopy containing also woody components and a DART simulated turbid-like canopy, all with LAI = 2, Erectophile LAD and loamy soil as ground. SIF radiances in the solar principal plane for the turbid-like canopy together with the foliage-only (RMSE = 1.93 and d = 0.47) and the foliage with wood (RMSE = 2.68 and d = 0.35) eucalypt canopies are illustrated in c) and d), respectively (for abbreviations and symbols see Figure 5).

In comparison with the multi-directional SIF radiance of the turbid-like canopy, the dense eucalyptus stand without wood showed statistically significant decreases in SIF_{TOC} at 686 nm (RMSE = 0.82 $W.m^{-2}.\mu m^{-1}.sr^{-1}$, d = 0.55) (Figure 8ac) and even greater at 740 nm (RMSE = 1.93 $W.m^{-2}.\mu m^{-1}.sr^{-1}$, d = 0.47) (Figure 9ac). This drop, reaching up to -1.2 $W.m^{-2}.\mu m^{-1}.sr^{-1}$ and almost -2.5 $W.m^{-2}.\mu m^{-1}.sr^{-1}$, respectively, can be explained by the Erectophile LAD of the small-sized narrow white peppermint leaves, and by their strong and spatially irregular

clumping at the branch level. Presence of woody structures did not change considerably the angular patterns of the SIF_{TOC} differences, but caused its further suppression at 686 nm (RMSE = 1.0 $W.m^{-2}.\mu m^{-1}.sr^{-1}$, d = 0.47) (Figure 8bd) and even larger differences at 740 nm (RMSE = 2.68 $W.m^{-2}.\mu m^{-1}.sr^{-1}$, d = 0.35) (Figure 9bd). Interestingly, it deepened the shape the solar principal plane SIF_{TOC} curve in back-scattering oblique viewing directions behind the hotspot region, producing the maximum difference of almost -1.4 $W.m^{-2}.\mu m^{-1}.sr^{-1}$ at 686 nm and around -3.7 $W.m^{-2}.\mu m^{-1}.sr^{-1}$ at 740 nm.

The DART ability to simulate forest stands with and without woody elements opened an opportunity for quantification of their potential impacts on SIF emitted, observed and escaped in the nadir direction from white peppermint dense and sparse canopies (Table 2). We quantified the wood shading effect, causing changes in canopy $fAPAR_{green}$ due to the scattering and absorption of iPAR, and the obstruction (blocking) effect of eucalyptus wood, caused by scattering and absorption of SIF photons by bark. As expected, wood shadowing lowered SIF emitted at both investigated wavelengths by the percentage equal to the $fAPAR_{green}$ reduction, i.e., by 17.0% for the dense and 9.7% for the sparse canopy. Comparison of the foliage only SIF_{TOC} with the foliage and wood SIF_{TOC} revealed lesser impacts at 686 nm than at 740 nm. SIF escape probability factors of the simulated eucalyptus canopies were generally low: $SIF\mathit{nadir}(686)_{esc} \leq 0.15$ and $SIF\mathit{nadir}(740)_{esc} \leq 0.27$. Overall, the wood obstruction effect was greater on far-red than red SIF escape factors, causing a consistent decrease of 4-6% in $SIF\mathit{nadir}(740)_{esc}$, but almost no change in $SIF\mathit{nadir}(686)_{esc}$ for the sparse and less than 2% increase for the dense canopy (Table 2).

Table 2. DART simulated impacts of woody material and bark on $fAPAR_{green}$ of leaves, SIF leaf emissions, nadir top-of-canopy SIF_{TOC} and nadir SIF escape probability factor at 686 and 740 nm of two white peppermint (*Eucalyptus pulchella*) stands with dense and sparse canopy covers (CC) and LAI = 2.5. The relative impact on canopy SIF emitted by leaves (Bold fonts), is caused either by shadows casted on photosynthetically active foliage (*shading effect*; Eq. 8) or by absorption and scattering of SIF photons by bark-covered wood in combination with green foliage (*obstruction effect*; Eq. 11); (↓) indicates a decreasing and (↑) an increasing effect.

DART scenario	Dense canopy (CC ≈ 80%)			Sparse canopy (CC ≈ 40%)		
DART outcome	Foliage only	Foliage & Wood	**Relative impact** [%]	Foliage only	Foliage & Wood	**Relative impact** [%]
$fAPAR_{green}$ of leaves	0.466	0.399		0.306	0.279	

Shading effect ($\varepsilon_{\mathrm{fAPAR}(400-750)}$)			**17.0 (↓)**			**9.7 (↓)**
Red SIF (686 nm)						
Emitted by leaves [W.m^{-2}.µm^{-1}]	11.626	9.939		7.618	6.945	
Nadir SIF$_{\mathrm{TOC}}$ [W.m^{-2}.µm^{-1}.sr^{-1}]	0.554	0.481		0.303	0.275	
SIF*nadir*(686)$_{\mathrm{esc}}$ [rel.]	0.150	0.152		0.125	0.124	
Obstruction effect ($\varepsilon_{\mathrm{SIF}(686)\mathrm{esc}}$)			**-1.5** (↑)			**0.6** (↓)
Far-red SIF (740 nm)						
Emitted by leaves [W.m^{-2}.µm^{-1}]	24.461	20.914		16.029	14.613	
Nadir SIF$_{\mathrm{TOC}}$ [W.m^{-2}.µm^{-1}.sr^{-1}]	2.093	1.693		1.260	1.108	
SIF*nadir*(740)$_{\mathrm{esc}}$ [rel.]	0.269	0.254		0.247	0.238	
Obstruction effect ($\varepsilon_{\mathrm{SIF}(740)\mathrm{esc}}$)			**5.7** (↓)			**3.6** (↓)

611

612 More detailed understanding of the wood-induced effects inside the dense white
613 peppermint canopy can be obtained from analysing its DART-simulated vertical profiles of SIF
614 balances and omnidirectional SIF escape factors. Plots of SIF(λ)$_{\mathrm{bal}}$ in Figure 10a and
615 SIF*omni*(λ)$_{\mathrm{esc}}$ in Figure 10b, shown across the relative stand height, revealed two significant
616 findings. First, every leaf-containing part of the canopy comprised of only foliage is acting as
617 a SIF source (SIF*omni*(λ)$_{\mathrm{esc}}$ > 0), but the presence of woody components turned the parts
618 emitting only a little fluorescence into SIF sinks (SIF*omni*(λ)$_{\mathrm{esc}}$ = 0). Second, a majority of the
619 SIF$_{\mathrm{TOC}}$ signal originates from leaves occupying top 25% percent of the eucalyptus canopy
620 height. Although the close-up of the 0-30% canopy height section in Figure 10a shows a strong
621 SIF absorption by trunks and lower branches that results in SIF(λ)$_{\mathrm{bal}}$ < 0 (especially at 740 nm),
622 different SIF energy budget results were obtained for top 25% (i.e., 75-100%) of the canopy.
623 The wood presence in this highly emitting canopy part increased the SIF(686)$_{\mathrm{bal}}$ values only
624 negligibly, as the bark and photosynthesizing leaves were capable of absorbing nearly all extra
625 SIF photons reflected at 686 nm by woody structures. This result is in line with a very slight
626 increase of SIF*nadir*(686)$_{\mathrm{esc}}$ listed in Table 2. Wood presence, however, decreased absorptance
627 and increased more than 2-fold reflectance of SIF at 740 nm, which significantly enhanced
628 (almost doubled) the SIF(740)$_{\mathrm{bal}}$ values in this upper canopy part. Despite this limited local
629 boost, wood obstructions suppressed values of both SIF(740)$_{\mathrm{bal}}$ and SIF*omni*(740)$_{\mathrm{esc}}$ in the rest

of the canopy profile, leading to an overall 5.7% reduction in canopy SIF*nadir*$(740)_{esc}$ (Table 2) and, consequently, in a decrease of multi-angular SIF_{TOC} (Figure 9ab).

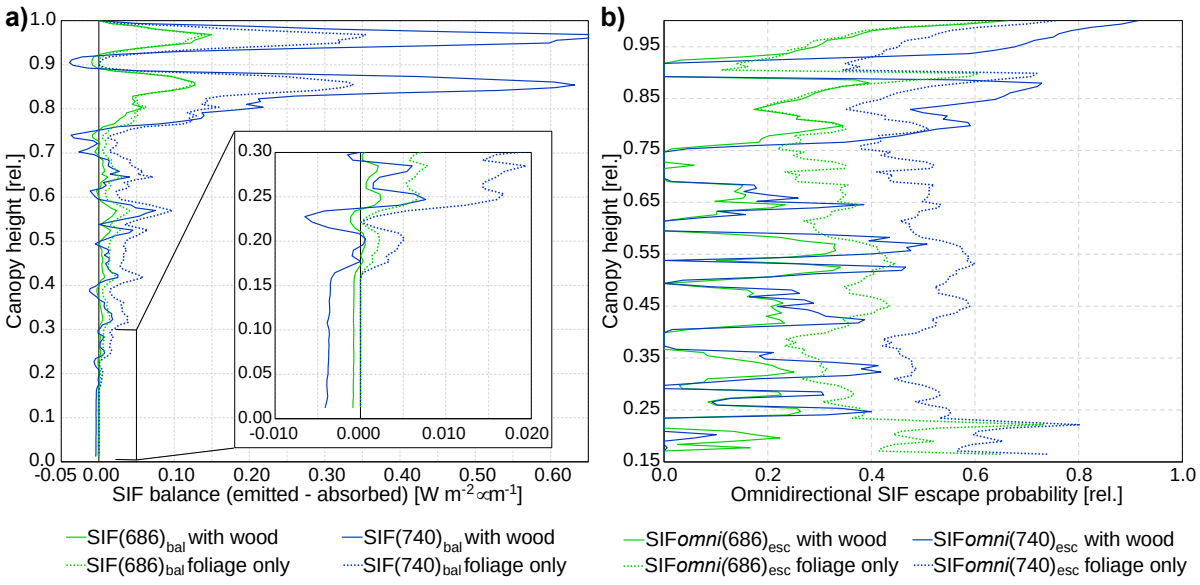

Figure 10. Vertical profiles of a) SIF balances (SIF$(\lambda)_{bal}$) and b) relative omnidirectional SIF escape factors (SIF*omni*$(\lambda)_{esc}$) at 686 and 740 nm for a dense white peppermint (*Eucalyptus pulchella*) canopy (CC ≈ 80% and LAI = 2) created only by foliage (dashed lines) and the same canopy containing also woody components (solid lines). Each 10 cm thick canopy layer is presented as a point of the relative canopy height [0-1]. For details about computations of SIF$(\lambda)_{bal}$ and SIF*omni*$(\lambda)_{esc}$ see section 2.4.

4. Discussion

4.1 Comparison of DART and SCOPE/mSCOPE models

DART outputs were nearly in a perfect agreement with the corresponding results obtained for simple, turbid medium vegetation scenes with SCOPE and mSCOPE. Better agreements were obtained for the SIF_{TOC} local maximum at 686 nm, where the signal is attenuated by the SIF chlorophyll absorption. Since the SIF_{TOC} values at 740 nm are controlled dominantly by canopy structural traits, the smallest discrepancies were obtained for the geometrically more uniform Planophile LAD. Here, the SIF_{TOC} signal is dominated by the first order scattering of prevailingly horizontally oriented leaves, lowering the occurrence of fluorescence absorption. The largest multi-angular SIF_{TOC} differences in all tested LAD and LAI scenarios occurred in very oblique viewing angles, in which the modelled radiance is impacted by uncertainties in angular discretization of the upper hemisphere.

Despite of a generally high agreement with SCOPE/mSCOPE simulations, this model cross comparison is not a fully sufficient replacement of an independent validation of the DART model, which is expected to be performed with real canopy SIF_{TOC} measurements in a near future. Nonetheless, this comparison provides the evidence that current integration of the Fluspect model and implementation of the 3D flux-tracking radiative transfer of SIF emitted from geometrically explicit leaves are as plausible as already validated 1D radiative transfer modelling approaches of SCOPE and mSCOPE models (Migliavacca et al. 2017; Pacheco-Labrador et al. 2019; van der Tol et al. 2016; Vilfan et al. 2019). This conclusion provides us with a high level of confidence that the radiative transfer modelling of SIF in DART can be used to investigate the major canopy structural controls of SIF_{TOC} in geometrically explicit 3D canopies, which structural complexity cannot be represented and tested in SCOPE or mSCOPE.

4.2 SIF changes due to classification of sun-/shade-adapted leaves and canopy structure

Distinct parametrization of sun- and shade-adapted leaves did not result in major differences in SIF_{TOC}, but other canopy structural parameters were found to be more important. The specific distinction of leaf *fqe* for sun- and shade-adapted foliage appeared to have a smaller impact on DART simulated nadir SIF_{TOC} than increasing LAI and foliage clumping reducing CC from 100% to 50% (c.f., Figure 1 and Figure 3). Yet, the impact of the leaf-light adaptation effect might increase, if a DART user applies Q double-threshold values that favour strongly the shade- over the sun-adapted class and simultaneously increases the PSI and PSII *fqe* inputs. Secondly, the influence of the shade-adapted class would be more significant when tested for naturally more clumped and taller (e.g., forest) canopies. Therefore, identification of correct Q thresholds and sun/shade *fqe* values are, together with measurements of canopy gaps and foliage clumping, essential for further investigation of the photosynthetic light adaptations and their impacts on SIF_{TOC}.

When evaluating impacts of maize canopy structural traits, our nadir SIF_{TOC} results indicated a general superior role of LAI over the foliage clumping. However, doubling the foliage clumping of maize crop with LAI = 2 caused such a strong increase in absorption of red SIF photons by chlorophylls that diminished and fully equalled the previous increase in SIF_{TOC} between 650 and 725 nm caused by doubling the number of regularly spaced plants, i.e., twice higher LAI (Figure 2). Interpretation of DART 3D radiative budget computed for the two SIF local maximums informed us that this strong red SIF reduction took place in the upper half of

683 the canopy (specifically between 50 and 90% of the canopy height; Figure 7), because the
684 clumping caused a slight enhancement of SIF energy fluxes in most of the lower half canopy
685 parts and the absorption of SIF by soil background was after the clumping introduction lowered.
686 The fact that relative differences of red SIF balances in upper halves of the clumped and
687 unclumped canopies are 2-fold more negative than the same differences of $fAPAR_{green}$ (Figure
688 7b) indicates that the increase in foliage shadowing is responsible only for a half of this
689 clumping-induced SIF reduction. The second half is caused by a more frequent recollision and
690 consequent greater absorption of red SIF photons by leaf photosynthetic pigments. Clumping
691 driven results for LAI = 1 showed less consistent and milder effects, which means that canopy
692 must have a certain minimal leaf density to produce these interactions.

693 Clumping impacts caused by decreasing CC can be also demonstrated on the example of
694 white peppermint stands without woody material. According to results listed in Table 2,
695 decrease of CC from 80% to 40% triggered a reduction in $fAPAR_{green}$ and, consequently, in
696 emitted SIF by 34%, and simultaneously lowered the SIF_{TOC} by 45% at 686 nm and by 40% at
697 740 nm. Thereby, if one accepts an assumption that scattering rates of red and far-red SIF
698 photons by the canopy structures (including structures of a leaf interior without foliar pigments)
699 are equal, then doubling the leaf density while keeping a constant canopy LAI = 2 induced an
700 additional 5% decrease in red SIF_{TOC} attributed to a higher red SIF absorption by chlorophylls.
701 It is important to mention that different quantitative impacts of LAI and foliage clumping on
702 SIF_{TOC} might be revealed if the classification of sun-/shade-adapted leaves is included and
703 different (i.e., light adaptation specific) PSI and PSII *fqe* values are specified by a DART user.
704 Since the natural variability in *fqe* and leaf biochemistry was not accounted for in this study, a
705 direct comparison (validation) of these results with SIF observations of real croplands or forests
706 (e.g., Guan et al. 2015; He et al. 2020; Peng et al. 2020; Wang et al. 2020) would be misleading.

707 Multi-angular DART simulations of SIF_{TOC} demonstrate that the influence of leaf size,
708 foliage angularity and its clumping (CC) is equally or even more crucial for modulating SIF_{TOC}
709 in oblique viewing directions. The polar plots of SIF_{TOC} at 686 nm for maize (Figure 5b) and
710 eucalyptus (Figure 8a) canopies with LAI = 2 revealed the largest influence in very oblique
711 backward directions behind the hotspot and the smallest impact in forward directions opposite
712 to the hotspot. The patterns of angular anisotropy for SIF_{TOC} at 740 nm are rather different. A
713 significant impact of maize canopy structure was found around the Northern and the Southern

viewing angles (Figure 6b), whereas only the Southern viewing directions were impacted by the eucalyptus canopy architecture (Figure 9a). Thus, far-red SIF_{TOC} of each architecturally distinct plant formation (i.e., plant functional type) must be approached individually and the canopy specific structural confounding effects must be removed or at least reduced before any application of remotely sensed SIF_{TOC}. This recommendation is in line with a number of recent works developing far-red SIF_{TOC} normalization approaches to mitigate the canopy structural effects (Liu et al. 2019b; Yang and van der Tol 2018; Yang et al. 2020b; Zeng et al. 2019).

4.3 Impacts of wood structures on eucalyptus SIF_{TOC} signal and SIF escape factors

Accounting for presence of bark-covered wood structures in our eucalyptus simulations decreased nadir 740 nm SIF_{TOC} by about 23% for the dense canopy and by 13% for the sparse canopy (Table 2). Results suggest that approximately one quarter of the total SIF reduction is caused by direct optical interactions (obstruction) of far-red SIF photons with bark surfaces in combination with green leaves under the natural geometrical distributions, whereas three quarters of the reduction resulted from the reduction in $APAR_{green}$ due to wood shadowing. Having the bark reflectance and absorptance at 740 nm both equal to 50%, the wood structures of white peppermint trees acted, on one hand, as strong reflectors and boosted the far-red SIF emission produced in top 25% of the dense canopy (Figure 10a). On the other hand, they acted as a far-red SIF sink in the rest of the canopy, i.e., in lower 75% of the canopy relative height. Although it is expected that tree species with a lower bark near infrared reflectance will demonstrate radiative budgets with a higher far-red SIF obstruction (absorptance), the consistently decreasing nadir obstruction effects of both modelled eucalyptus stand indicate that the wood obstruction is a regular confounding factor that must be treated as a systematic error source. Therefore, it should be accounted for, or if feasible even corrected, when interpreting far-red SIF_{TOC} data sensed remotely over forests.

The effect of woody material on nadir SIF_{TOC} at 686 nm was smaller, because the total pool of canopy red SIF photons originating just from PSII is naturally small and additionally reduced by absorption of photosynthetic pigments. Interestingly, the bark absorptance of 60% and reflectance of 40% at 686 nm, in combination with the specific geometry of eucalypt tree crowns (i.e., a strong branch foliage clumping with Erectophile LAD), decreased the red SIF nadir escape factor of the sparse canopy by 0.6%, whereas the same SIF escape factor in the dense canopy was increased by 1.5%. If we accept these simulations as generally applicable,

we may conclude that the presence of wood affects the red SIF forest canopy balance in both negative and positive ways. However, the impact is generally small, predominantly influencing the less emitting lower 75% of the canopy height rather than larger emissions originating from top 25% of the canopy. Since we modelled and analysed only two mono-species eucalyptus stands, additional simulations for other tree species, including natural variability in species-specific optical, biochemical and structural properties, will be essential to draw more comprehensive and generic conclusions regarding the wood obstruction effects.

DART estimates of the relative eucalyptus canopy SIF escape factor in the nadir direction, which can be used to compute the apparent SIF efficiency (a gross primary production proxy less impacted by canopy structures; Wang et al. 2020), were quite low, smaller than 0.15 for red and 0.27 for far-red SIF. Nonetheless, the omnidirectional escape factors of individual canopy layers were higher, reaching up to 0.65 for red and 0.9 for far-red SIF in the highly emissive top 25% of the canopy height (Figure 10b). These numbers and results in Figures 9 and 10 suggest that oblique multi-directional observations of forest canopies (e.g., with tower-based instruments) should capture more SIF photons than a single nadir measurement, and, thus, provide a stronger SIF_{TOC} signal. Once again, more simulations covering different forest types and their natural variability are required to conclude if these interpretations have a general applicability or if the white peppermint canopies represent a unique and possibly extreme case.. Despite a limited size of this study, we demonstrate that the entire 3D structural complexity, including woody material, must be taken into account when assessing quantity of SIF photons scattered and absorbed by canopy components and those escaping from a forest canopy.

4.4 Development of DART SIF modelling for large canopies and landscapes

DART SIF simulations for geometrically explicit representations of terrestrial vegetation have computational limitations regarding a simulated scene size and a number of objects (i.e., triangular facets) creating 3D mock-ups of plant canopies. Theoretically, one can create an extensive landscape occupied with an unlimited population of plants and other 3D objects (e.g., open-water bodies, roads, buildings, etc.), but the SIF simulation, and mainly radiative budget, of such a scene might be practically unfeasible as the computer memory and processor capabilities are not unlimited. Therefore, another two approaches, allowing more efficient simulations of large canopies and extensive landscapes, are being implemented and tested in DART: i) SIF modelling for vegetation canopies represented by 3D turbid voxels (i.e., voxels

filled with a vegetation turbid medium), and ii) a direct and reverse MC modelling called DART-Lux (Gastellu-Etchegorry et al. 2020). The latter one is especially highly promising for simulating extensive SIF_{TOC} images. It uses only the landscape elements contributing to the formation of a simulated image, which decreases the computer time and memory by a factor as large as 100. Once fully tested and solidified, both approaches will provide DART users with potential satellite SIF observations adapted to common ground sampling distances of hundreds of meters. Such simulations could test multiple SIF confounding optical effects, for instance, those originating from photosynthetically inactive Earth surfaces of rough terrain configurations resulting in dynamic spatiotemporal irradiation changes and shadow patterns.

5. Conclusions

Physical and technical implementation of discrete anisotropic radiative transfer modelling for solar-induced chlorophyll fluorescence in geometrically explicit 3D plant canopies was described and compared with complementary cases simulated in 1D models SCOPE and mSCOPE. The cross-comparison revealed that DART simulations of SIF_{TOC} for geometrically simple and spatially homogenous canopies produced nearly the same results as both 1D models. The largest SIF_{TOC} differences occurred in very oblique viewing angles that are impacted by higher modelling uncertainties than the directions closer to nadir.

Further exploitation of DART ability to simulate SIF images and radiative budgets of virtual 3D maize crops showed that the distinction and adjustment of fluorescence efficiencies for sun- and shade-adapted leaves had a smaller impact on DART simulated SIF_{TOC} than an increase in leaf density (LAI) and local foliage clumping. When analysing nadir SIF_{TOC} impacts by foliar density traits, we found a superior role of LAI over the foliage clumping. Nonetheless, the foliage clumping was shown to be an important controlling factor of maize and eucalyptus SIF_{TOC} simulated at 686 and 740 nm in oblique viewing directions, and also a crucial driver of the red SIF balance, i.e., SIF emission and absorption, in vertical profile of irregularly spaced maize crop with LAI = 2. These study outcomes must be, however, reproduced for other plant functional types to confirm and investigate further the influences of leaf light intensity adaptations and density traits on SIF variability inside and at the top of different canopies.

DART simulations of two white peppermint eucalyptus stands suggested that woody material has a significant impact on SIF_{TOC}. Trunks and branches cast shadows on photosynthesizing leaves, decreasing their SIF emissions by about 15% in dense and 8% in

807 sparse canopy simulations. Although the absorbance and reflectance of eucalyptus bark (both
808 about 50% at 740 nm), in combination with a multiple scattering and absorption by leaves,
809 nearly doubled the pool of far-red SIF photons in the top 25% part of dense canopy, they
810 reduced the overall canopy escape of far-red SIF in the nadir viewing direction by 6% and 4%
811 in the sparse stand. Interestingly, the nadir escape factors of red SIF from dense and sparse
812 canopies were almost unimpacted by presence of woody material, despite a relatively high 40%
813 reflectance of bark at 686 nm. These unique results demonstrate that further development of
814 SIF 3D radiative transfer modelling has a potential to reveal new insights in SIF observations
815 of spectrally, spatially and topographically heterogeneous vegetated landscapes, acquired at
816 different spatial scales by proximal, airborne and space-borne optical sensors.

817 **Acknowledgments**

818 Authors are grateful to Luke Wallace and Samuel Hillman from the RMIT University in
819 Melbourne for acquisition and pre-processing of TLS point clouds of the white peppermint
820 eucalypt trees, permitting their 3D virtual constructions. We also acknowledge constructive
821 reviews of the anonymous peers that helped us to improve scientific quality and readability of
822 this manuscript. Contribution of Z. Malenovský was funded by the NASA Earth Science
823 Division (ESD) in support of the 'FLuorescence Airborne Research Experiment (FLARE)' and
824 by the Australian Research Council Future Fellowship 'Bridging Scales in Remote Sensing of
825 Vegetation Stress' (FT160100477). Contribution of the CESBIO Laboratory authors was
826 supported by the TOSCA project 'Fluo3D' and by the PhD program of the French Space Center
827 (CNES) and the Centre National de Recherche Scientifique (CNRS). Work of R. Janoutová was
828 supported by the Ministry of Education, Youth and Sports of CR within the CzeCOS program
829 (grant LM2018123). Involvement of P. Yang was supported by the Netherlands Organization
830 for Scientific Research (grant ALWGO.2017.018).

831

Appendix A: Comparison of DART and SCOPE/mSCOPE SIF radiative transfers

Since SCOPE and mSCOPE are turbid medium models, we prepared DART 3D scenes mimicking their 1D canopies as closely as possible. SCOPE, mSCOPE and DART were adjusted to use the same bottom-of-atmosphere (BOA) solar direct and diffuse irradiance, simulated with DART atmosphere radiative transfer module using the United States standard atmosphere gas model (NOAA et al. 1976) and the rural area aerosol model with a visibility of 23 km. The scene was a 1 m height vegetation canopy above a bare soil with three Lambertian reflectance (ρ) properties: i) black soil ($\rho = 0$), ii) half-reflective soil ($\rho = 0.5$), and iii) loamy gravel brown dark soil with ρ linearly increasing with wavelength ($\rho \approx 6\%$ at 550 nm, $\rho \approx 12\%$ at 686 nm and $\rho \approx 15\%$ at 740 nm). Every leaf facet had the same specific Lambertian reflectance and transmittance, i.e., there was no division of leaf optical properties on sunlit or sun-adapted and shaded or shade-adapted leaves. For the DART-SCOPE comparison, the *eta* fluorescence weight parameters were forced to one. For the DART-mSCOPE comparison, we split turbid scenes into two and three almost equally high layers (see Figure A1ab). Leaves of 2- and 3-layer simulations were divided into sunlit and shaded (see % of sunlit leaves in each layer in Figure A1cd) and the *eta* parameters simulated per layer for both leaf cohorts in mSCOPE were entered in the corresponding DART simulations. Leaf optical properties were simulated with the same Fluspect version, using the input parameters listed in Table A1. In attempt to simulate strong SIF_{TOC} signals, the *fqe* values for PSI and PSII were selected close to their potential maximums. Simulations considered three leaf densities, specified by the leaf area index (LAI) equal to 1, 2 and 4. In SCOPE simulations, we tested three leaf angle distributions (LAD): Spherical, Erectophile and Planophile (Danson 1998), whereas we applied only the Spherical function, the most frequent naturally occurring LAD, in mSCOPE simulations. All leaves were homogenously distributed throughout the canopies, i.e. the foliage clumping index (Chen and Black 1992) was equal to 1. The DART leaf facets were equilateral triangles with the surface area of 0.08 cm^2. Such small leaf area ensured independency of DART simulated TOC reflectance and SIF from the solar azimuth angle. The leaf width required for SCOPE/mSCOPE computations in the hot-spot direction was set to the height of DART facets, i.e., 0.37 cm. The solar azimuth angle (SAA) was fixed to 311.89° (anticlockwise from South) and the solar zenith angle (SZA) to 37.94° (i.e., solar elevation angle of 52.06°) as for Washington D.C. (USA) area (the Beltsville Agricultural Research Center; Lat. 39.03°N, Long. 76.85°W) on 26th August 2014 at 14.00 local time (i.e., at 13.50 solar time). Nadir SIF_{TOC}

radiance [$W.m^{-2}.\mu m^{-1}.sr^{-1}$] between 640 and 850 nm (1 nm bandwidth) was simulated for all combinations of the input parameters with the three RTMs. The obtained PSI, PSII and total SIF_{TOC} values were compared statistically (as described in Section 2.6).

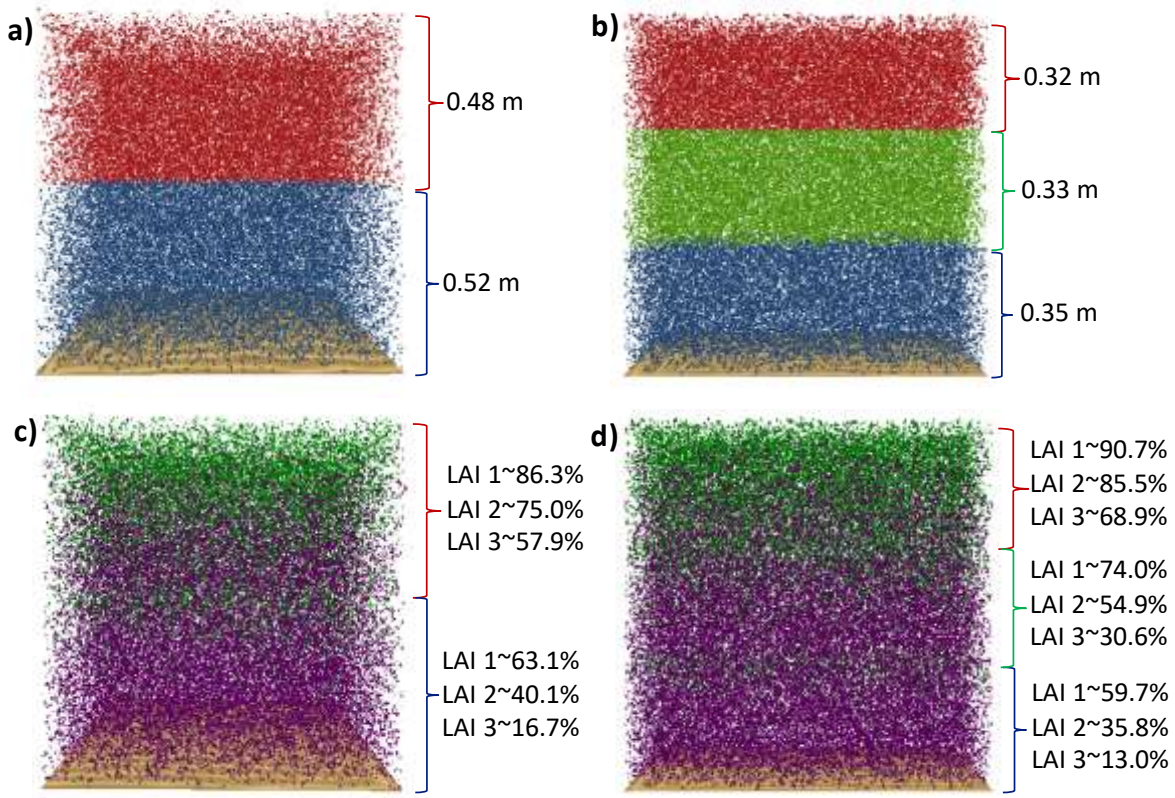

Figure A1. DART representations of a) 2- and b) 3-layered turbid-like canopies designed for comparison with the mSCOPE model (numbers indicate the height of each layer). Illustration of sunlit (under direct illumination; green) and shaded (under diffuse illumination, violet) triangular leaves for both c) 2- and d) 3-layered canopies (numbers indicate % of sunlit leaves per layer for each simulated LAI).

Table A1: Input parameters of the Fluspect model used to simulate optical properties of SCOPE/mSCOPE turbid medium leaves and corresponding DART leaves (for explanations of input abbreviations see caption of Table 1).

Fluspect inputs (m)SCOPE layers	Cab [$\mu g.cm^{-2}$]	Car [$\mu g.cm^{-2}$]	EWT [cm]	LMA [$g.cm^{-2}$]	N	PSI *fqe*	PSII *fqe*
mSCOPE first layer (from top)	40	10	0.006	0.0014	1.0	0.006	0.03
SCOPE & mSCOPE second layer	60	15	0.009	0.0021	1.5	0.006	0.03
mSCOPE third layer (from top)	80	20	0.012	0.0028	2	0.006	0.03

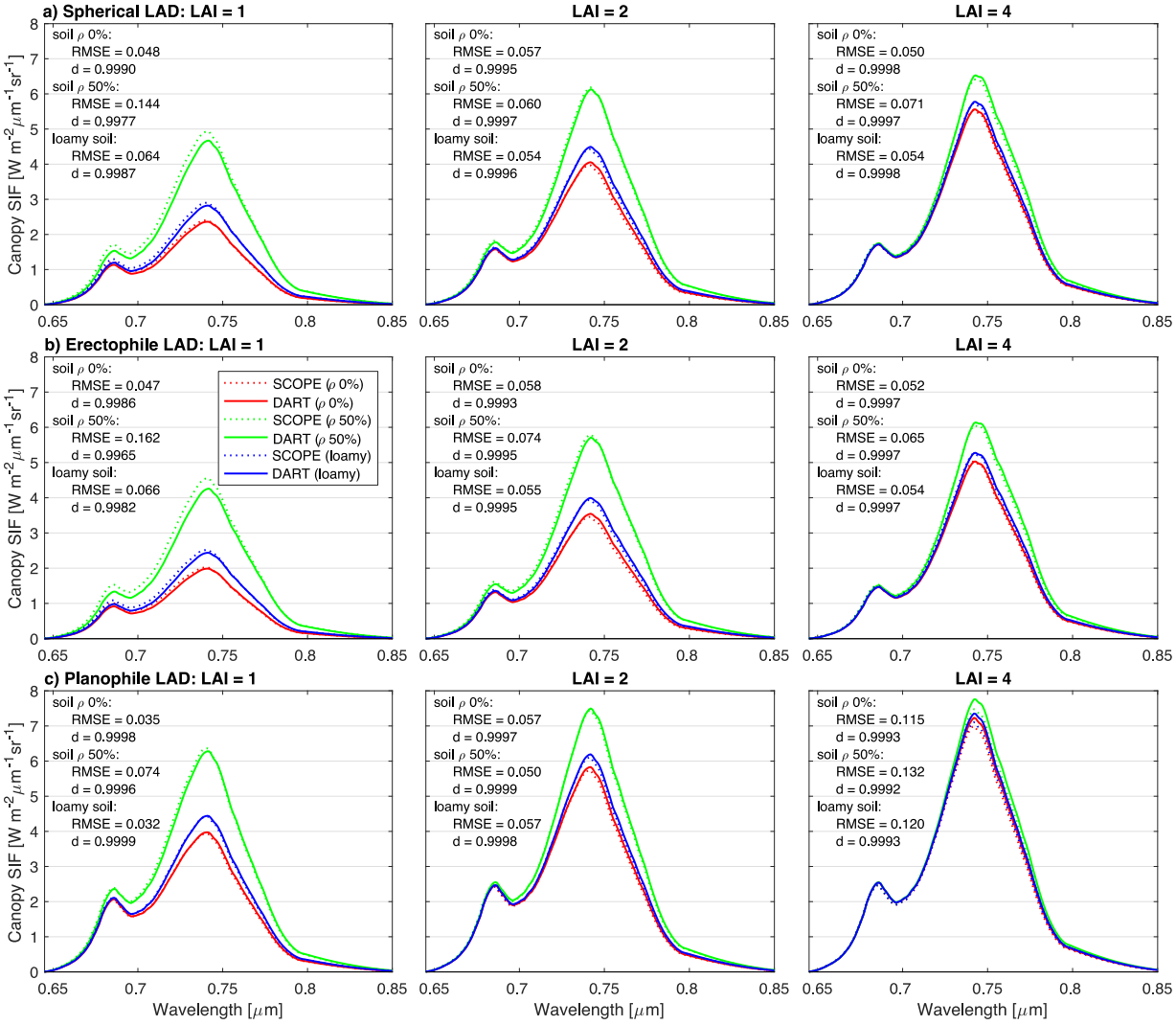

Figure A2. DART and SCOPE total nadir SIF of vegetation canopies with LAI=1, 2 and 4, three soils (ρ = 0%, ρ = 50%, ρ = loamy dark gravel soil), and with a) Spherical, b) Erectophile, and c) Planophile LAD (RMSE ~ root mean square error; d ~ index of agreement: 0 = no agreement, 1 = full agreement).

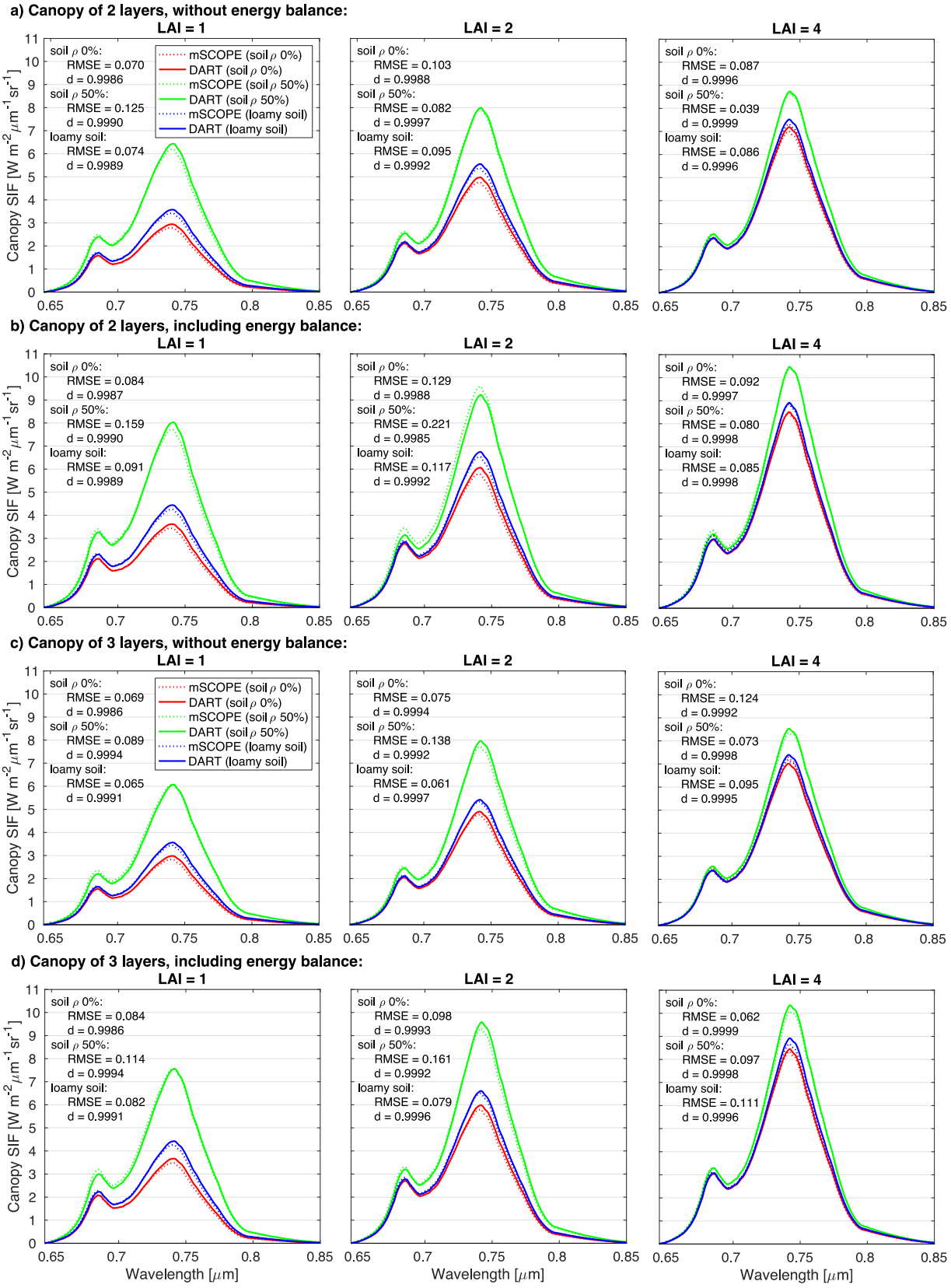
a) Canopy of 2 layers, without energy balance:
b) Canopy of 2 layers, including energy balance:
c) Canopy of 3 layers, without energy balance:
d) Canopy of 3 layers, including energy balance:
LAI = 1
LAI = 2
LAI = 4
Canopy SIF [W m-2 μm-1 sr-1]
Wavelength [μm]
mSCOPE (soil ρ 0%)
DART (soil ρ 0%)
mSCOPE (soil ρ 50%)
DART (soil ρ 50%)
mSCOPE (loamy soil)
DART (loamy soil)
soil ρ 0%:
soil ρ 50%:
loamy soil:
RMSE
d

881

Figure A3. DART and mSCOPE nadir SIF of vegetation canopies simulated with the Spherical LAD, three soils (ρ = 0%, ρ = 50%, ρ = loamy dark gravel soil) in two layers a) without and b) with energy balance, and in three layers c) without and d) with energy balance (for abbreviations see Figure A2).

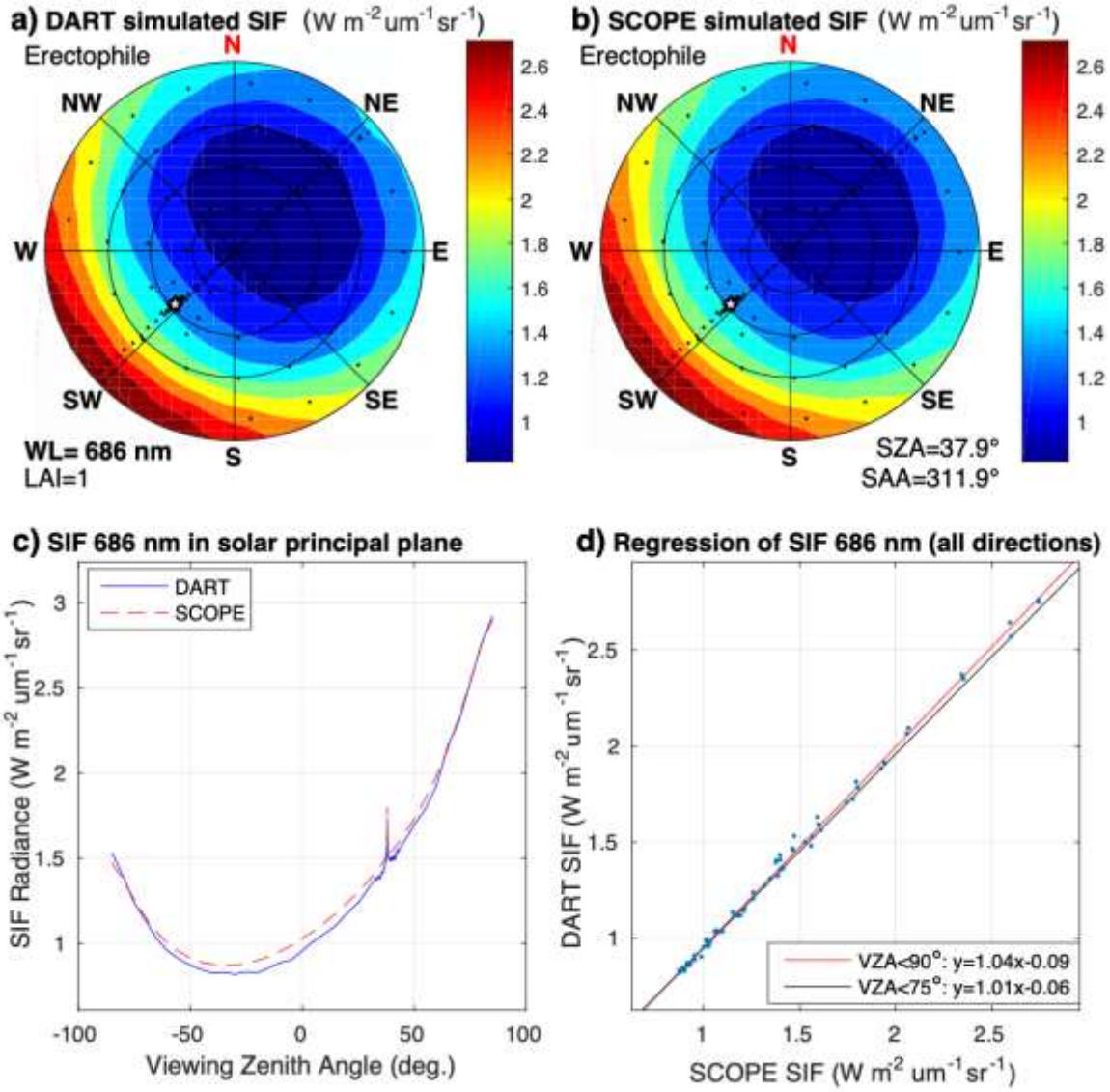

Figure A4. Best agreement when comparing a) DART and b) SCOPE multi-angular SIF of a turbid medium canopy was found for the Erectophile LAD and a null soil reflectance. SIF radiance in the solar principal plane and linear regression of turbid-like DART and turbid SCOPE simulations (R^2 = 0.99, RMSE = 0.03, d = 1.0 for all simulated viewing directions, i.e., VZA<90°, and RMSE = 0.02 for VZA<75°) are shown in c) and d) graphs, respectively (for abbreviations and symbols see Figure 5).

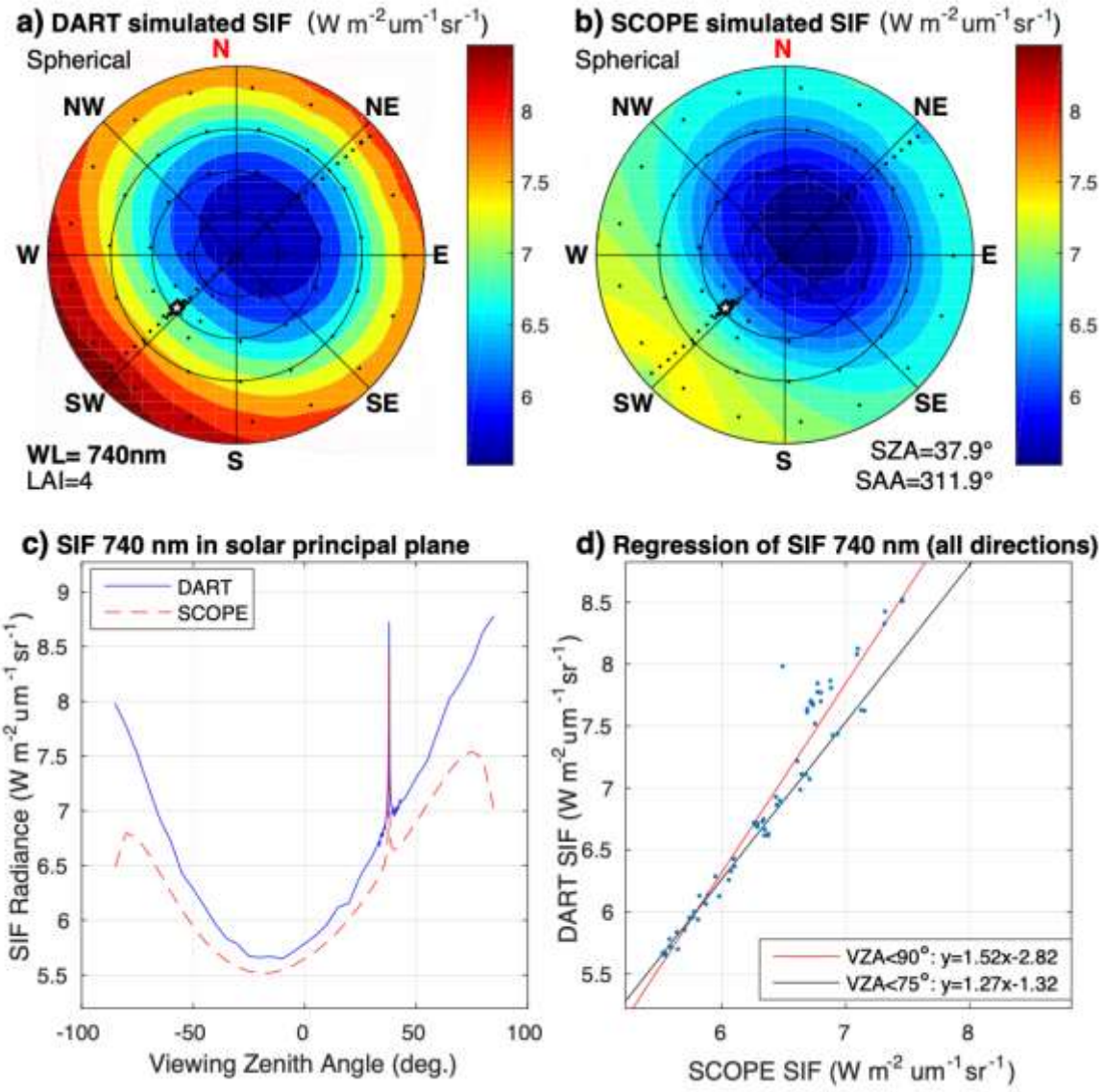

Figure A5. Worst agreement when comparing a) DART and b) SCOPE multi-angular SIF of turbid medium canopy with the Spherical LAD and a 50% reflective soil. SIF radiance in the solar principal plane and linear regression of turbid-like DART and turbid SCOPE simulations (R^2 = 0.94, RMSE = 0.21, d = 1.0 for VZA < 90° and R^2 = 0.99, RMSE = 0.07 for VZA < 75°) are shown in c) and d) graphs, respectively (for abbreviations and symbols see Figure 5).

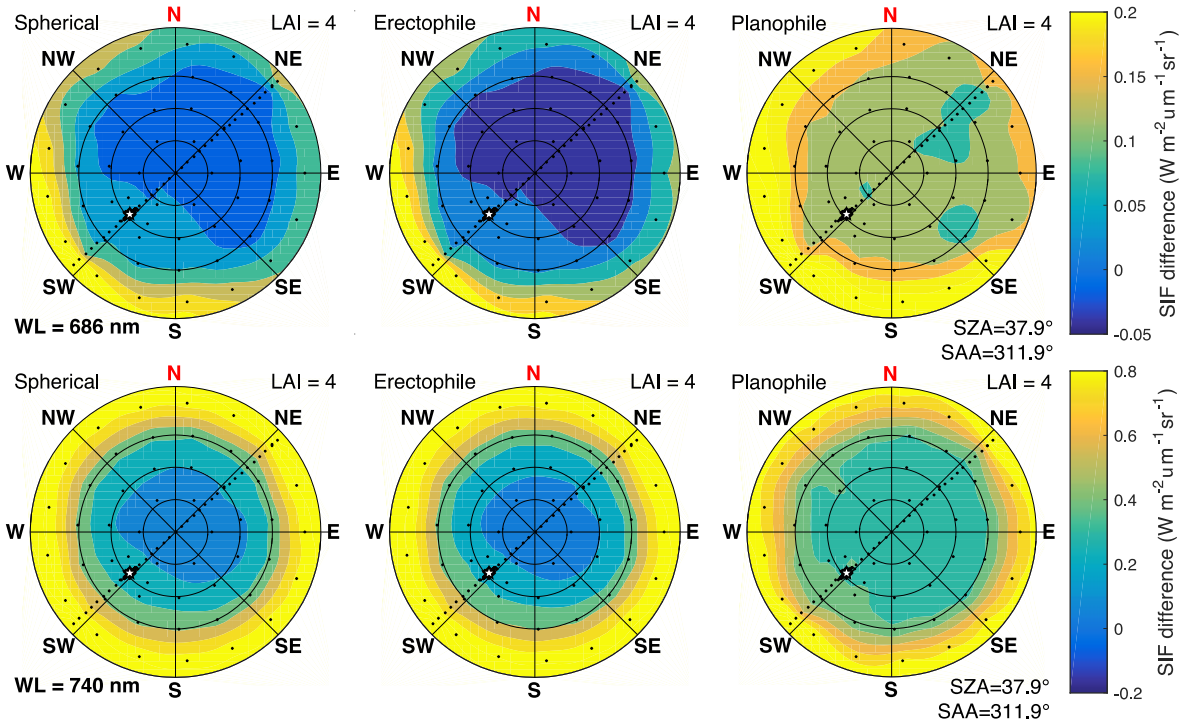

Figure A6. DART–SCOPE differences in multi-angular SIF radiance at 686 and 740 nm for a canopy with LAI = 4, having Spherical, Erectophile and Planophile LADs (the white star shows the solar position and black dots indicate the simulated viewing directions; for abbreviations see Figure 5).

References

Aasen, H., Van Wittenberghe, S., Sabater Medina, N., Damm, A., Goulas, Y., Wieneke, S., Hueni, A., Malenovský, Z., Alonso, L., Pacheco-Labrador, J., Cendrero-Mateo, P.M., Tomelleri, E., Burkart, A., Cogliati, S., Rascher, U., & Mac Arthur, A. (2019). Sun-Induced Chlorophyll Fluorescence II: Review of Passive Measurement Setups, Protocols, and Their Application at the Leaf to Canopy Level. *Remote Sensing, 11*, 927

Ashley, M.D., & Rea, J. (1975). Seasonal vegetation differences from ERTS imagery. *Journal of American Society of Photogrammetry, 41*, 713-719

Bendig, J., Malenovský, Z., Gautam, D., & Lucieer, A. (2020). Solar-Induced Chlorophyll Fluorescence Measured From an Unmanned Aircraft System: Sensor Etaloning and Platform Motion Correction. *IEEE Transactions on Geoscience and Remote Sensing, 58*, 3437-3444

914 Blair, B.O., & Baumgardner, M.F. (1977). Detection of the Green and Brown Wave in
915 Hardwood Canopy Covers Using Multidate, Multispectral Data from LANDSAT-11.
916 *Agronomy Journal, 69*, 808-811
917 Blender (2007). https://www.blender.org/ (12 February 2020)
918 Chen, J.M., & Black, T.A. (1992). Defining leaf area index for non-flat leaves. *Plant, Cell &*
919 *Environment, 15*, 421-429
920 Croft, H., Chen, J.M., Wang, R., Mo, G., Luo, S., Luo, X., He, L., Gonsamo, A., Arabian, J.,
921 Zhang, Y., Simic-Milas, A., Noland, T.L., He, Y., Homolová, L., Malenovský, Z., Yi, Q.,
922 Beringer, J., Amiri, R., Hutley, L., Arellano, P., Stahl, C., & Bonal, D. (2020). The global
923 distribution of leaf chlorophyll content. *Remote Sensing of Environment, 236*, 111479
924 Danson, F.M. (1998). Teaching the physical principles of vegetation canopy reflectance using
925 the SAIL model. *Photogrammetric Engineering & Remote Sensing, 64*, 809-812
926 DART (2019).
927 https://dart.omp.eu/Public/documentation/contenu/documentation/DART_handbook.pdf
928 (6 February 2020)
929 DART (2020).
930 https://dart.omp.eu/Public/documentation/contenu/documentation/DART_User_Manual.p
931 df (6 February 2020)
932 Féret, J.B., Berger, K., de Boissieu, F., & Malenovský, Z. (2020). PROSPECT-PRO for
933 estimating content of nitrogen-containing leaf proteins and other carbon-based
934 constituents. *Remote Sensing of Environment*, in review
935 Féret, J.B., Gitelson, A.A., Noble, S.D., & Jacquemoud, S. (2017). PROSPECT-D: Towards
936 modeling leaf optical properties through a complete lifecycle. *Remote Sensing of*
937 *Environment, 193*, 204-215
938 Frankenberg, C., Butz, A., & Toon, G.C. (2011). Disentangling chlorophyll fluorescence from
939 atmospheric scattering effects in O2 A-band spectra of reflected sun-light. *Geophysical*
940 *Research Letters, 38*
941 Gamon, J.A., Somers, B., Malenovský, Z., Middleton, E.M., Rascher, U., & Schaepman, M.E.
942 (2019). Assessing Vegetation Function with Imaging Spectroscopy. *Surveys in*
943 *Geophysics, 40*, 489-513
944 Gastellu-Etchegorry, J.-P., Wang, Y., Regaieg, O., Yin, T., Malenovský, Z., Zhen, Z., Yang,
945 X., Tao, Z., Landier, L., Al Bitar, A., Deschamps, A., Lauret, N., Guilleux, J., Chavanon,

E., Cao, B., Qi, J., Kallel, A., Mitraka, Z., Chrysoulakis, N., Cook, B., & Morton, D. (2020). Recent improvements in the DART model for atmosphere, topography, large landscape, chlorophyll fluorescence, satellite image inversion. In, *IEEE International Geoscience and Remote Sensing Symposium* (p. 5). Virtual Symposium: IEEE

Gastellu-Etchegorry, J.-P., Yin, T., Lauret, N., Cajgfinger, T., Gregoire, T., Grau, E., Feret, J.-B., Lopes, M., Guilleux, J., Dedieu, G., Malenovský, Z., Cook, B., Morton, D., Rubio, J., Durrieu, S., Cazanave, G., Martin, E., & Ristorcelli, T. (2015). Discrete Anisotropic Radiative Transfer (DART 5) for Modeling Airborne and Satellite Spectroradiometer and LIDAR Acquisitions of Natural and Urban Landscapes. *Remote Sensing, 7*, 1667-1701

Gastellu-Etchegorry, J.P. (2008). 3D modeling of satellite spectral images, radiation budget and energy budget of urban landscapes. *Meteorology and Atmospheric Physics*, *102*, 187

Gastellu-Etchegorry, J.P., Demarez, V., Pinel, V., & Zagolski, F. (1996). Modeling radiative transfer in heterogeneous 3-D vegetation canopies. *Remote Sensing of Environment, 58*, 131-156

Gastellu-Etchegorry, J.P., Lauret, N., Yin, T., Landier, L., Kallel, A., Malenovský, Z., Bitar, A.A., Aval, J., Benhmida, S., Qi, J., Medjdoub, G., Guilleux, J., Chavanon, E., Cook, B., Morton, D., Chrysoulakis, N., & Mitraka, Z. (2017). DART: Recent Advances in Remote Sensing Data Modeling With Atmosphere, Polarization, and Chlorophyll Fluorescence. *IEEE Journal of Selected Topics in Applied Earth Observations and Remote Sensing, 10*, 2640-2649

Gastellu-Etchegorry, J.P., Martin, E., & Gascon, F. (2004). DART: a 3D model for simulating satellite images and studying surface radiation budget. *International Journal of Remote Sensing, 25*, 73-96

Givnish, T.J. (1988). Adaptation to Sun and Shade: a Whole-Plant Perspective. *Functional Plant Biology, 15*, 63-92

Guan, K., Pan, M., Li, H., Wolf, A., Wu, J., Medvigy, D., Caylor, K.K., Sheffield, J., Wood, E.F., Malhi, Y., Liang, M., Kimball, J.S., Saleska, Scott R., Berry, J., Joiner, J., & Lyapustin, A.I. (2015). Photosynthetic seasonality of global tropical forests constrained by hydroclimate. *Nature Geoscience, 8*, 284-289

Guanter, L., Alonso, L., Gómez-Chova, L., Amorós-López, J., Vila, J., & Moreno, J. (2007). Estimation of solar-induced vegetation fluorescence from space measurements. *Geophysical Research Letters, 34*

Guanter, L., Zhang, Y., Jung, M., Joiner, J., Voigt, M., Berry, J.A., Frankenberg, C., Huete, A.R., Zarco-Tejada, P., Lee, J.-E., Moran, M.S., Ponce-Campos, G., Beer, C., Camps-Valls, G., Buchmann, N., Gianelle, D., Klumpp, K., Cescatti, A., Baker, J.M., & Griffis, T.J. (2014). Global and time-resolved monitoring of crop photosynthesis with chlorophyll fluorescence. *Proceedings of the National Academy of Sciences, 111*, E1327-E1333

He, L., Chen, J.M., Liu, J., Mo, G., & Joiner, J. (2017). Angular normalization of GOME-2 Sun-induced chlorophyll fluorescence observation as a better proxy of vegetation productivity. *Geophysical Research Letters, 44*, 5691-5699

He, L., Magney, T., Dutta, D., Yin, Y., Köhler, P., Grossmann, K., Stutz, J., Dold, C., Hatfield, J., Guan, K., Peng, B., & Frankenberg, C. (2020). From the Ground to Space: Using Solar-Induced Chlorophyll Fluorescence to Estimate Crop Productivity. *Geophysical Research Letters, 47*, e2020GL087474

Hernández-Clemente, R., North, P.R.J., Hornero, A., & Zarco-Tejada, P.J. (2017). Assessing the effects of forest health on sun-induced chlorophyll fluorescence using the FluorFLIGHT 3-D radiative transfer model to account for forest structure. *Remote Sensing of Environment, 193*, 165-179

Hosgood, B., Jacquemoud, S., Andreoli, G., Verdebout, J., Pedrini, A., & Schmuck, G. (1994). Leaf Optical Properties Experiment 93 (LOPEX93). In, *European Commission No. EUR 16095 EN*. Joint Research Centre, Institute for Remote Sensing Applications

Jacquemoud, S., & Baret, F. (1990). PROSPECT: A model of leaf optical properties spectra. *Remote Sensing of Environment, 34*, 75-91

Janoutová, R., Homolová, L., Malenovský, Z., Hanuš, J., Lauret, N., & Gastellu-Etchegorry, J.-P. (2019). Influence of 3D Spruce Tree Representation on Accuracy of Airborne and Satellite Forest Reflectance Simulated in DART. *Forests, 10*, 292

Joiner, J., Yoshida, Y., Vasilkov, A.P., Yoshida, Y., Corp, L.A., & Middleton, E.M. (2011). First observations of global and seasonal terrestrial chlorophyll fluorescence from space. *Biogeosciences, 8*, 637-651

Kallel, A. (2020). FluLCVRT: Reflectance and fluorescence of leaf and canopy modeling based on Monte Carlo vector radiative transfer simulation. *Journal of Quantitative Spectroscopy and Radiative Transfer, 253*, 107183

Kallel, A., & Nilson, T. (2013). Revisiting the vegetation hot spot modeling: Case of Poisson/Binomial leaf distributions. *Remote Sensing of Environment, 130*, 188-204

Köhler, P., Guanter, L., Kobayashi, H., Walther, S., & Yang, W. (2018). Assessing the potential of sun-induced fluorescence and the canopy scattering coefficient to track large-scale vegetation dynamics in Amazon forests. *Remote Sensing of Environment, 204*, 769-785

Leuning, R., Kelliher, F.M., De Pury, D.G.G., & Schulze, E.D. (1995). Leaf nitrogen, photosynthesis, conductance and transpiration: scaling from leaves to canopies. *Plant, Cell & Environment, 18*, 1183-1200

Liu, W., Atherton, J., Mõttus, M., Gastellu-Etchegorry, J.-P., Malenovský, Z., Raumonen, P., Åkerblom, M., Mäkipää, R., & Porcar-Castell, A. (2019a). Simulating solar-induced chlorophyll fluorescence in a boreal forest stand reconstructed from terrestrial laser scanning measurements. *Remote Sensing of Environment, 232*, 111274

Liu, X., Guanter, L., Liu, L., Damm, A., Malenovský, Z., Rascher, U., Peng, D., Du, S., & Gastellu-Etchegorry, J.-P. (2019b). Downscaling of solar-induced chlorophyll fluorescence from canopy level to photosystem level using a random forest model. *Remote Sensing of Environment, 231*, 110772

Malenovský, Z., Homolová, L., Lukeš, P., Buddenbaum, H., Verrelst, J., Alonso, L., Schaepman, M.E., Lauret, N., & Gastellu-Etchegorry, J.-P. (2019). Variability and Uncertainty Challenges in Scaling Imaging Spectroscopy Retrievals and Validations from Leaves Up to Vegetation Canopies. *Surveys in Geophysics, 40*, 631-656

Malenovský, Z., Homolová, L., Zurita-Milla, R., Lukeš, P., Kaplan, V., Hanuš, J., Gastellu-Etchegorry, J.-P., & Schaepman, M.E. (2013). Retrieval of spruce leaf chlorophyll content from airborne image data using continuum removal and radiative transfer. *Remote Sensing of Environment, 131*, 85-102

Malenovský, Z., Martin, E., Homolová, L., Gastellu-Etchegory, J.-P., Zurita-Milla, R., Schaepman, M.E., Pokorný, R., Clevers, J.G.P.W., & Cudlín, P. (2008). Influence of woody elements of a Norway spruce canopy on nadir reflectance simulated by the DART model at very high spatial resolution. *Remote Sensing of Environment, 112*, 1-18

Malenovský, Z., Ufer, C., Lhotáková, Z., Clevers, J.G.P.W., Schaepman, M.E., Albrechtová, J., & Cudlín, P. (2006). A new hyperspectral index for chlorophyll estimation of a forest canopy: Area under curve normalised to maximal band depth between 650-725 nm *EARSeL eProceedings, 5*, 161-172

Migliavacca, M., Perez-Priego, O., Rossini, M., El-Madany, T.S., Moreno, G., van der Tol, C., Rascher, U., Berninger, A., Bessenbacher, V., Burkart, A., Carrara, A., Fava, F., Guan,

J.H., Hammer, T.W., Henkel, K., Juarez-Alcalde, E., Julitta, T., Kolle, O., Martín, M.P., Musavi, T., Pacheco-Labrador, J., Pérez-Burgueño, A., Wutzler, T., Zaehle, S., & Reichstein, M. (2017). Plant functional traits and canopy structure control the relationship between photosynthetic CO2 uptake and far-red sun-induced fluorescence in a Mediterranean grassland under different nutrient availability. *New Phytologist, 214*, 1078-1091

Mohammed, G.H., Colombo, R., Middleton, E.M., Rascher, U., van der Tol, C., Nedbal, L., Goulas, Y., Pérez-Priego, O., Damm, A., Meroni, M., Joiner, J., Cogliati, S., Verhoef, W., Malenovský, Z., Gastellu-Etchegorry, J.-P., Miller, J.R., Guanter, L., Moreno, J., Moya, I., Berry, J.A., Frankenberg, C., & Zarco-Tejada, P.J. (2019). Remote sensing of solar-induced chlorophyll fluorescence (SIF) in vegetation: 50 years of progress. *Remote Sensing of Environment, 231*, 111177

Myneni, R.B., & Ross, J. (2012). *Photon-Vegetation Interactions: Applications in Optical Remote Sensing and Plant Ecology*. Springer Berlin Heidelberg

Niinemets, Ü., Keenan, T.F., & Hallik, L. (2015). A worldwide analysis of within-canopy variations in leaf structural, chemical and physiological traits across plant functional types. *New Phytologist, 205*, 973-993

NOAA, NASA, & Air-Force, U.S. (1976). *U.S. Standard Atmosphere, 1976*. Washington D.C.: NOAA, U.S. Government Printing Office

Nobel, P.S. (1976). Photosynthetic Rates of Sun versus Shade Leaves of Hyptis emoryi Torr. *Plant Physiology, 58*, 218-223

North, P.R.J. (1996). Three-dimensional forest light interaction model using a monte carlo method. *IEEE Transactions on Geoscience and Remote Sensing, 34*, 946-956

Pacheco-Labrador, J., Perez-Priego, O., El-Madany, T.S., Julitta, T., Rossini, M., Guan, J., Moreno, G., Carvalhais, N., Martín, M.P., Gonzalez-Cascon, R., Kolle, O., Reischtein, M., van der Tol, C., Carrara, A., Martini, D., Hammer, T.W., Moossen, H., & Migliavacca, M. (2019). Multiple-constraint inversion of SCOPE. Evaluating the potential of GPP and SIF for the retrieval of plant functional traits. *Remote Sensing of Environment, 234*, 111362

Pedrós, R., Goulas, Y., Jacquemoud, S., Louis, J., & Moya, I. (2010). FluorMODleaf: A new leaf fluorescence emission model based on the PROSPECT model. *Remote Sensing of Environment, 114*, 155-167

Peng, B., Guan, K., Zhou, W., Jiang, C., Frankenberg, C., Sun, Y., He, L., & Köhler, P. (2020). Assessing the benefit of satellite-based Solar-Induced Chlorophyll Fluorescence in crop yield prediction. *International Journal of Applied Earth Observation and Geoinformation, 90*, 102126

Pradal, C., Dufour-Kowalski, S., Boudon, F., Fournier, C., & Godin, C. (2008). OpenAlea: a visual programming and component-based software platform for plant modelling. *Functional Plant Biology, 35*, 751-760

Rosema, A., Verhoef, W., Schroote, J., & Snel, J.F.H. (1991). Simulating fluorescence light-canopy interaction in support of laser-induced fluorescence measurements. *Remote Sensing of Environment, 37*, 117-130

Sakai, Y., Kobayashi, H., & Kato, T. (2020). FLiES-SIF ver. 1.0: Three-dimensional radiative transfer model for estimating solar induced fluorescence. *Geosci. Model Dev. Discuss., 2020*, 1-36

Sloup, P. (2013). https://is.muni.cz/th/325196/fi_m/?lang=en (18 February 2020)

Sušila, P., & Nauš, J. (2007). A Monte Carlo study of the chlorophyll fluorescence emission and its effect on the leaf spectral reflectance and transmittance under various conditions. *Photochemical & Photobiological Sciences, 6*, 894-902

Tong, C., Bao, Y., Zhao, F., Fan, C., Li, Z., & Huang, Q. (2021). Evaluation of the FluorWPS Model and Study of the Parameter Sensitivity for Simulating Solar-Induced Chlorophyll Fluorescence. *Remote Sensing, 13*

van der Tol, C., Rossini, M., Cogliati, S., Verhoef, W., Colombo, R., Rascher, U., & Mohammed, G. (2016). A model and measurement comparison of diurnal cycles of sun-induced chlorophyll fluorescence of crops. *Remote Sensing of Environment, 186*, 663-677

van der Tol, C., Verhoef, W., Timmermans, J., Verhoef, A., & Su, Z. (2009). An integrated model of soil-canopy spectral radiances, photosynthesis, fluorescence, temperature and energy balance. *Biogeosciences, 6*, 3109-3129

van der Tol, C., Vilfan, N., Dauwe, D., Cendrero-Mateo, M.P., & Yang, P. (2019). The scattering and re-absorption of red and near-infrared chlorophyll fluorescence in the models Fluspect and SCOPE. *Remote Sensing of Environment, 232*, 111292

Verhoef, W. (1984). Light scattering by leaf layers with application to canopy reflectance modeling: The SAIL model. *Remote Sensing of Environment, 16*, 125-141

Verrelst, J., Malenovský, Z., Van der Tol, C., Camps-Valls, G., Gastellu-Etchegorry, J.-P., Lewis, P., North, P., & Moreno, J. (2019). Quantifying Vegetation Biophysical Variables from Imaging Spectroscopy Data: A Review on Retrieval Methods. *Surveys in Geophysics, 40*, 589-629

Verrelst, J., & Rivera, J.P. (2017). Chapter 16 - A Global Sensitivity Analysis Toolbox to Quantify Drivers of Vegetation Radiative Transfer Models. In G.P. Petropoulos, & P.K. Srivastava (Eds.), *Sensitivity Analysis in Earth Observation Modelling* (pp. 319-339): Elsevier

Verrelst, J., Schaepman, M.E., Malenovský, Z., & Clevers, J.G.P.W. (2010). Effects of woody elements on simulated canopy reflectance: Implications for forest chlorophyll content retrieval. *Remote Sensing of Environment, 114*, 647-656

Verroust, A., & Lazarus, F. (1999). Extracting skeletal curves from 3D scattered data. In, *Proceedings Shape Modeling International '99. International Conference on Shape Modeling and Applications* (pp. 194-201)

Vilfan, N., van der Tol, C., Muller, O., Rascher, U., & Verhoef, W. (2016). Fluspect-B: A model for leaf fluorescence, reflectance and transmittance spectra. *Remote Sensing of Environment, 186*, 596-615

Vilfan, N., van der Tol, C., & Verhoef, W. (2019). Estimating photosynthetic capacity from leaf reflectance and Chl fluorescence by coupling radiative transfer to a model for photosynthesis. *New Phytologist, 223*, 487-500

Vilfan, N., Van der Tol, C., Yang, P., Wyber, R., Malenovský, Z., Robinson, S.A., & Verhoef, W. (2018). Extending Fluspect to simulate xanthophyll driven leaf reflectance dynamics. *Remote Sensing of Environment, 211*, 345-356

Wang, C., Guan, K., Peng, B., Chen, M., Jiang, C., Zeng, Y., Wu, G., Wang, S., Wu, J., Yang, X., Frankenberg, C., Köhler, P., Berry, J., Bernacchi, C., Zhu, K., Alden, C., & Miao, G. (2020). Satellite footprint data from OCO-2 and TROPOMI reveal significant spatio-temporal and inter-vegetation type variabilities of solar-induced fluorescence yield in the U.S. Midwest. *Remote Sensing of Environment, 241*, 111728

Widlowski, J.-L., Mio, C., Disney, M., Adams, J., Andredakis, I., Atzberger, C., Brennan, J., Busetto, L., Chelle, M., Ceccherini, G., Colombo, R., Côté, J.-F., Eenmäe, A., Essery, R., Gastellu-Etchegorry, J.-P., Gobron, N., Grau, E., Haverd, V., Homolová, L., Huang, H., Hunt, L., Kobayashi, H., Koetz, B., Kuusk, A., Kuusk, J., Lang, M., Lewis, P.E., Lovell,

J.L., Malenovský, Z., Meroni, M., Morsdorf, F., Mõttus, M., Ni-Meister, W., Pinty, B., Rautiainen, M., Schlerf, M., Somers, B., Stuckens, J., Verstraete, M.M., Yang, W., Zhao, F., & Zenone, T. (2015). The fourth phase of the radiative transfer model intercomparison (RAMI) exercise: Actual canopy scenarios and conformity testing. *Remote Sensing of Environment, 169*, 418-437

Willmott, C.J. (1981). On the validation of models. *Physical Geography, 2*, 184-194

Wyber, R., Malenovský, Z., Ashcroft, M., Osmond, B., & Robinson, S. (2017). Do Daily and Seasonal Trends in Leaf Solar Induced Fluorescence Reflect Changes in Photosynthesis, Growth or Light Exposure? *Remote Sensing, 9*, 604

Yang, P., Prikaziuk, E., Verhoef, W., & van der Tol, C. (2020a). SCOPE 2.0: A model to simulate vegetated land surface fluxes and satellite signals. *Geosci. Model Dev. Discuss., 2020*, 1-26

Yang, P., & van der Tol, C. (2018). Linking canopy scattering of far-red sun-induced chlorophyll fluorescence with reflectance. *Remote Sensing of Environment, 209*, 456-467

Yang, P., van der Tol, C., Campbell, P.K.E., & Middleton, E.M. (2020b). Fluorescence Correction Vegetation Index (FCVI): A physically based reflectance index to separate physiological and non-physiological information in far-red sun-induced chlorophyll fluorescence. *Remote Sensing of Environment, 240*, 111676

Yang, P., Verhoef, W., & van der Tol, C. (2017). The mSCOPE model: A simple adaptation to the SCOPE model to describe reflectance, fluorescence and photosynthesis of vertically heterogeneous canopies. *Remote Sensing of Environment, 201*, 1-11

Yin, T., Gastellu-Etchegorry, J.-P., Lauret, N., Grau, E., & Rubio, J. (2013). A new approach of direction discretization and oversampling for 3D anisotropic radiative transfer modeling. *Remote Sensing of Environment, 135*, 213-223

Zeng, Y., Badgley, G., Dechant, B., Ryu, Y., Chen, M., & Berry, J.A. (2019). A practical approach for estimating the escape ratio of near-infrared solar-induced chlorophyll fluorescence. *Remote Sensing of Environment, 232*, 111209

Zhang, Z., Zhang, Y., Porcar-Castell, A., Joiner, J., Guanter, L., Yang, X., Migliavacca, M., Ju, W., Sun, Z., Chen, S., Martini, D., Zhang, Q., Li, Z., Cleverly, J., Wang, H., & Goulas, Y. (2020). Reduction of structural impacts and distinction of photosynthetic pathways in a global estimation of GPP from space-borne solar-induced chlorophyll fluorescence. *Remote Sensing of Environment, 240*, 111722

Zhao, F., Dai, X., Verhoef, W., Guo, Y., van der Tol, C., Li, Y., & Huang, Y. (2016). FluorWPS: A Monte Carlo ray-tracing model to compute sun-induced chlorophyll fluorescence of three-dimensional canopy. *Remote Sensing of Environment, 187*, 385-399

2.2 Vegetation simulated as turbid medium

A DART turbid cell contains one or more types of turbid vegetation, and eventually, other scene elements made of facets. Leaves simulated as turbid medium are treated statistically using analytical equations that treat leaves as a whole and not as individual leaves. A type of turbid vegetation is characterized by a Leaf Angular Distribution (LAD) $\frac{g(\theta_l)}{2\pi}$, a leaf area volume density u_l (m^2/m^3), and hemispherical spectral leaf optical properties (top side reflectance ρ_{top} and transmittance τ_{top}, bottom side reflectance ρ_{bot} and transmittance τ_{bot}).

2.2.1 Modeling approach

First order scattering and SIF emission

A source radiation vector $W_{in}(\lambda, \Omega_s)$ incident in a direction Ω_s that crosses a turbid cell (*i.e.*, voxel) (Figure 2-1) is partly intercepted and partly transmitted. Its intercepted part is:

$$W_{int}(\lambda, \Omega_s) = W_{in}(\lambda, \Omega_s).[1 - e^{-G(\Omega_s).u_l.\Delta l(\Omega_s)}] \quad (2.1)$$

with $G(\Omega_s) = \int_0^{\frac{\pi}{2}} \frac{g(\theta_l)}{2\pi} \int_0^{2\pi} |\Omega_l.\Omega_s|.d\varphi_l.sin\theta_l.d\theta_l$ and $\Delta l(\Omega_s)$ the path length of $W_{in}(\lambda, \Omega_s)$ inside the cell.

Radiation intercepted by a turbid cell is either absorbed or scattered. The first order energy scattered in the discrete direction $(\Omega_v, \Delta\Omega_v)$ due to the interception of $W_{int}(\lambda, \Omega_s)$ is:

$$W_{1,scat}(\lambda, \Omega_s, \Omega_v, \Delta\Omega_v) = W_{in}(\lambda, \Omega_s).T_{scat}(\lambda, \Omega_s, \Omega_v, \Delta\Omega_v) \quad (2.2)$$

with $T_{scat}(\lambda, \Omega_s, \Omega_v, \Delta\Omega_v)$ the scattering transfer function:

$$T_{scat}(\lambda, \Omega_s, \Omega_v, \Delta\Omega_v) = \sum_{\theta_{l,i}} \frac{g(\theta_{l,i})}{2\pi} \sum_{\varphi_{l,i}} \frac{\alpha_\lambda}{\pi} |\Omega_{l,ij}.\Omega_s|.|\Omega_{l,ij}.\Omega_v| \Delta\varphi_{l,j} \sin\theta_{l,i} \Delta\theta_{l,i} \frac{\Delta\Omega_v}{G(\Omega_s)} \quad (2.3)$$

$$\alpha_\lambda = \begin{cases} \rho_{top} \text{ if } \Omega_{l,ij}.\Omega_s < 0 \text{ and } \Omega_{l,ij}.\Omega_v > 0 \\ \tau_{top} \text{ if } \Omega_{l,ij}.\Omega_s < 0 \text{ and } \Omega_{l,ij}.\Omega_v < 0 \\ \rho_{bot} \text{ if } \Omega_{l,ij}.\Omega_s > 0 \text{ and } \Omega_{l,ij}.\Omega_v < 0 \\ \tau_{bot} \text{ if } \Omega_{l,ij}.\Omega_s > 0 \text{ and } \Omega_{l,ij}.\Omega_v > 0 \end{cases}$$

In presence of SIF emission, any radiation vector has 3 components: total, PSI and PSII radiation. SIF emission and radiation scattering are computed in each discrete direction. SIF excitation-emission matrices play a role for SIF emission similar to that of leaf reflectance and transmittance for scattering. SIF emission at spectral band (λ_w,$\Delta\lambda_w$) in the discrete direction ($\Omega_v, \Delta\Omega_v$), by the photosystem x (*i.e.*, 1 or 2), due to the intercepted radiation $W_{int}(\lambda_u, \Omega_s)$ at spectral band ($\lambda_u, \Delta\lambda_u$) is:

$$W_{PSx}(\lambda_u \rightarrow \lambda_w, \Omega_s, \Omega_v, \Delta\Omega_v) = W_{in}(\lambda_u, \Omega_s).T_{PSx}(\lambda_u, \lambda_w, \Omega_s, \Omega_v, \Delta\Omega_v) \quad (2.4)$$

with $T_{PSx}(\lambda_u, \lambda_w, \Omega_s, \Omega_v, \Delta\Omega_v)$ the fluorescence transfer function:

$$T_{PSx}(\lambda_u, \lambda_w, \Omega_s, \Omega_v, \Delta\Omega_v) = \sum_{\theta_{l,i}} \frac{g(\theta_{l,i})}{2\pi} \sum_{\varphi_{l,i}} \frac{M_{xyuv}}{\pi} \left|\Omega_{l,ij}.\Omega_s\right|.\left|\Omega_{l,ij}.\Omega_v\right| \Delta\varphi_{l,j} \sin\theta_{l,i}\, \Delta\theta_{l,i} \frac{\Delta\Omega_v}{G(\Omega_s)} \quad (2.5)$$

$$M_{xyuw} = \begin{cases} M^{top}_{x,backward,u,w} \text{ if } \Omega_{l,ij}.\Omega_s < 0 \text{ and } \Omega_{l,ij}.\Omega_v > 0 \\ M^{top}_{x,forward,u,w} \text{ if } \Omega_{l,ij}.\Omega_s < 0 \text{ and } \Omega_{l,ij}.\Omega_v < 0 \\ M^{bot}_{x,backward,u,w} \text{ if } \Omega_{l,ij}.\Omega_s > 0 \text{ and } \Omega_{l,ij}.\Omega_v < 0 \\ M^{bot}_{x,forward,u,w} \text{ if } \Omega_{l,ij}.\Omega_s > 0 \text{ and } \Omega_{l,ij}.\Omega_v > 0 \end{cases}$$

The first order SIF emission at the spectral band (λ_w,$\Delta\lambda_w$) is the sum of the contribution of all the excitation spectral bands to the emission in this band.

$$W_{1,PSx}(\lambda_w, \Omega_s, \Omega_v, \Delta\Omega_v) = \sum_u W_{PSx}(\lambda_u \rightarrow \lambda_w, \Omega_s, \Omega_v, \Delta\Omega_v) \quad (2.6)$$

Transmission and interception of first order rays

$W_{1,scat}(\lambda, \Omega_s, \Omega_v, \Delta\Omega_v)$ and $W_{1,PSx}(\lambda_w, \Omega_s, \Omega_v, \Delta\Omega_v)$ are partly transmitted through the cell along the path $\Delta l(M, \Omega_v)$ between the emission point M and the cell border and give:

- The first order scattered flux and SIF flux that exit the cells in the direction ($\Omega_v, \Delta\Omega_v$):

$$W_{1,scat,\alpha}(\lambda, \Omega_s, \Omega_v, \Delta\Omega_v) = W_{1,scat}(\lambda, \Omega_s, \Omega_v, \Delta\Omega_v).e^{-G(\Omega_s).u_l.\Delta l(M,\Omega_v)} \quad (2.7)$$

$$W_{1,PSx,\alpha}(\lambda_w, \Omega_s, \Omega_v, \Delta\Omega_v) = W_{1,PSx}(\lambda_w, \Omega_s, \Omega_v, \Delta\Omega_v).e^{-G(\Omega_s).u_l.\Delta l(M,\Omega_v)} \quad (2.8)$$

- The associated total and SIF intercepted fluxes in the cell in all directions are:

$$W_{1,int,1}(\lambda,\Omega_s)=\sum_v W_{1,scat}(\lambda,\Omega_s,\Omega_v,\Delta\Omega_v).\left(1-e^{-G(\Omega_s).u_l.\Delta l(M,\Omega_v)}\right) \quad (2.9)$$

$$W_{1,PSx,int,1}(\lambda_w,\Omega_s)=\sum_v W_{1,PSx}(\lambda_w,\Omega_s,\Omega_v,\Delta\Omega_v).\left(1-e^{-G(\Omega_s).u_l.\Delta l(M,\Omega_v)}\right) \quad (2.10)$$

Within cell multiple scattering and SIF emission

The intercepted flux $W_{1,int,1}(\lambda,\Omega_s)$ is scattered and partly transmitted, then partly intercepted, and so on. Assuming the isotropy of the within cell scattered rays, the multiple scattered flux that escapes the cell is:

$$\begin{aligned} W_{1,int,\beta}(\lambda,\Omega_s) &= W_{1,int,1}(\lambda,\Omega_s).[\omega\bar{T}+\omega\bar{T}(\omega-\omega\bar{T})+\omega\bar{T}(\omega-\omega\bar{T})^2+\cdots] \\ &= W_{1,int,1}(\lambda,\Omega_s).\frac{\omega\bar{T}}{[1-\omega(1-\bar{T})]} \end{aligned} \quad (2.11)$$

with ω the leaf single scattering albedo and $\bar{T}$ the mean cell transmittance along the paths $\Delta l(M,\Omega_v)$ from the cell center to the cell faces:

$$\bar{T}=\frac{1}{4\pi}\int_{4\pi} e^{-G(\Omega_v).u_l.\Delta l(M,\Omega_v)}.d\Omega_v \quad (2.12)$$

Similarly, for the SIF energy:

$$W_{1,PSx,int,\beta}(\lambda_w,\Omega_s)=W_{1,PSx,int,1}(\lambda_w,\Omega_s).\frac{\omega_w\bar{T}}{[1-\omega_w(1-\bar{T})]} \quad (2.13)$$

The propagation of $W_{1,int,1}(\lambda,\Omega_s)$ in the cell after multiple scattering gives rise to absorption:

$$\begin{aligned} W_{1,abs}(\lambda,\Omega_s) &= W_{1,int,1}(\lambda,\Omega_s)-W_{1,int,\beta}(\lambda,\Omega_s) \\ &= W_{1,int,1}(\lambda,\Omega_s).\frac{1-\omega\bar{T}}{[1-\omega(1-\bar{T})]} \end{aligned} \quad (2.14)$$

Similarly, for the SIF energy:

$$W_{1,PSx,abs}(\lambda,\Omega_s)=W_{1,PSx,int,1}(\lambda_w,\Omega_s).\frac{1-\omega_w\bar{T}}{[1-\omega_w(1-\bar{T})]} \quad (2.15)$$

Therefore, the propagation of $W_{1,int,1}(\lambda,\Omega_s)$ gives also rise to new SIF emission:

$$W_{1,int,PSx}(\lambda_w,\Omega_s)=\sum_u 2.\frac{W_{1,abs}(\lambda_u,\Omega_s)}{1-\omega_u}.M_{xuv} \quad (2.16)$$

where $M_{xuv}=\frac{M^{top}_{x,forward,uv}+M^{top}_{x,backward,uv}+M^{bot}_{x,forward,uv}+M^{bot}_{x,backward,uv}}{4}$

Part of this emitted SIF exits the cell directly, or after simple or multiple scattering:

$$W_{1,int,PSx,\gamma}(\lambda_w,\Omega_s) = W_{1,int,PSx}(\lambda_w,\Omega_s).[\bar{T}+\omega\bar{T}(1-\bar{T})+\omega^2.\bar{T}(1-\bar{T})^2+\cdots] = W_{1,int,PSx}(\lambda_w,\Omega_s).\frac{\bar{T}}{[1-\omega(1-\bar{T})]} \quad (2.17)$$

The SIF emitted in each direction is then:

$$W_{1,int,PSx,\gamma}(\lambda_w,\Omega_s\rightarrow\Omega_v) = W_{1,int,PSx,\gamma}(\lambda_w,\Omega_s).\xi(M,\Omega_v) \quad (2.18)$$

with

$$\xi(M,\Omega_v) = \frac{e^{-G(\Omega_v)u_l\Delta l(M,\Omega_v)}.\int_{4\pi}\int_{2\pi}|\Omega_s.\Omega_l|\frac{g(\theta_l)}{2\pi}f(\Omega_l,\Omega_s\rightarrow\Omega_v)d\Omega_l d\Omega_s\Delta\Omega_v}{\int_{4\pi}e^{-G(\Omega_v)u_l\Delta l(M,\Omega_v)}.\int_{4\pi}\int_{2\pi}|\Omega_s.\Omega_l|\frac{g(\theta_l)}{2\pi}f(\Omega_l,\Omega_s\rightarrow\Omega_v)d\Omega_l d\Omega_s d\Omega_v} \quad (2.19)$$

The propagation of $W_{1,int,PSx}$ in the cell can further give rise to absorption and SIF emission, which in turn can give rise to higher order SIF emissions. However, these SIF emissions are small enough to be neglected.

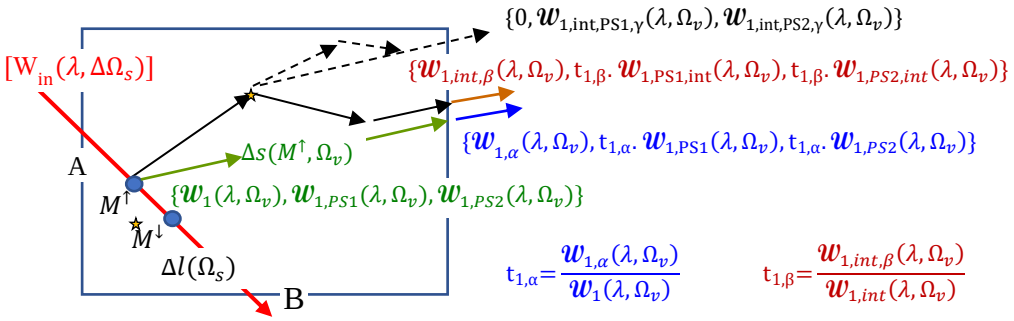

Figure 2-1: Incident source vector $[W_{in}(\lambda,\Delta\Omega_s)]$ onto a turbid cell, with source points $M^{\uparrow}$ and $M^{\downarrow}$, and energy $\{W_1(\lambda,\Omega_v), W_{1,PS1}(\lambda,\Omega_v), W_{1,PS2}(\lambda,\Omega_v)\}$ from $M^{\uparrow}$. $\Delta l(\Omega_s)$ is the distance between the entry A and exit B of the incident ray. $\Delta s(M^{\uparrow},\Omega_v)$ is the distance between $M^{\uparrow}$ and the cell exit along direction Ω_v. $W_{1,\alpha}(\lambda,\Omega_v)$ is equal to the direct transmission of $W_1(\lambda,\Omega_v)$ outside the cell without any scattering, whereas $W_{1,int,\beta}(\lambda,\Omega_v)$ is the transmission of $W_1(\lambda,\Omega_v)$ outside the cell with scattering events.

η factors

As for vegetation simulated as facets, the η factors simulated by SCOPE can be imported to scale the leaf-level SIF emission in order to consider the effects of local environment.

SCOPE computes two types of η factors:

- $\eta_{sunlit}(n, \theta_l, \varphi_l)$ for sunlit leaves at layer n, and leaves with a leaf zenith and azimuth angles θ_l and φ_l, respectively. In this case, an average profile is computed for each layer:

$$\bar{\eta}_{sunlit}(n) = \int_0^{2\pi} \int_0^{\frac{\pi}{2}} \eta_{sunlit}(n, \theta_l, \varphi_l).\frac{g(\theta_l)}{2\pi}.sin\,\theta_l\,.d\theta_l.d\varphi_l \approx \sum_{\varphi_l}\sum_{\theta_l} \eta_{sunlit}(n, \theta_l, \varphi_l).\frac{g(\theta_l)}{2\pi}.sin\,\theta_l\,.\Delta\theta_l.\Delta\varphi_l \quad (2.20)$$

- $\eta_{shaded}(n)$ for shaded cells at layer n. It is used as is.

The number of layers in the DART simulation and in the SCOPE imported η files usually differ. If the number of DART layers is lower, the corresponding layers of the η profile are averaged, if it is higher, the values of the η profiles are interpolated to provide a value for each layer.

2.2.2 Results

The accuracy of DART-FT modeling in turbid vegetation was tested by comparing it with DART-FT modeling in quasi-turbid vegetation, because the latter one has already been successfully tested with the SCOPE model. Figure 2-2 shows DART-FT SIF emission and nadir radiance for a homogeneous canopy simulated as turbid medium and quasi turbid medium. The agreement is very good for the two types of vegetation representation, with relative differences less than 0.1% for emitted SIF and less than 0.8% for radiance. The relative difference is lower for SIF emission than for SIF radiance because SIF radiance has an additional step from the emission to the top of canopy. The large absorption of SIF by the vegetation explains that the red peak of PSII is relatively smaller for SIF radiance than for SIF emission.

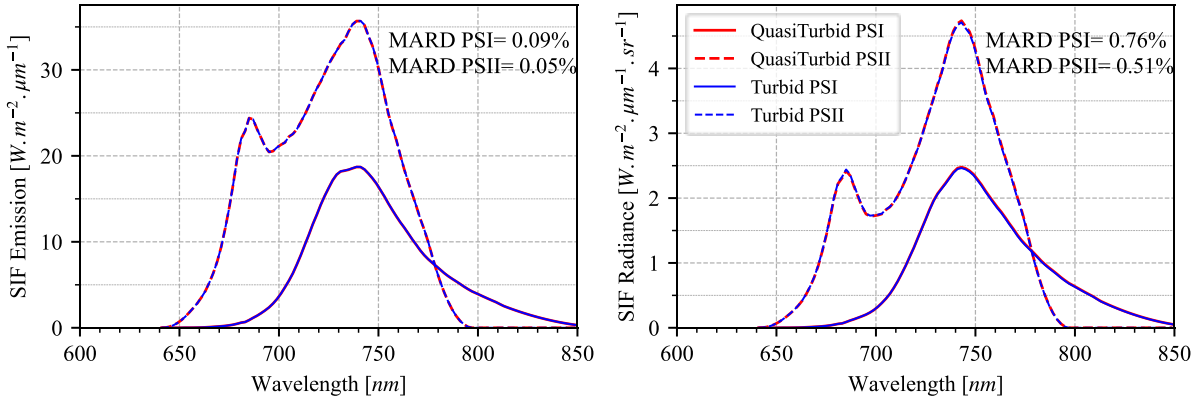

Figure 2-2: DART-FT SIF emission and nadir radiance for a homogeneous canopy simulated as turbid medium and quasi turbid medium.

2.3 Conclusion

In this chapter, the SIF modeling approaches in DART-FT were presented for facets-based and turbid-based vegetation. Up to now, the impact for the local climatology on the SIF emission can be considered only via the coupling with SCOPE 1D energy module. The results were in good agreement with the SCOPE/mSCOPE models. However, DART-FT requires very huge computation time and memory to simulate SIF for large scale scenes, which would be very important notably to simulate images of spaceborne sensors. For example, the spatial resolution of the FLEX satellite will be 300 m. Therefore, a more efficient modeling strategy is needed to meet these needs. This highlights the interest of the new Monte Carlo modeling strategy in DART-Lux because of its much better computational efficiency in terms of simulation time and memory. However, for this objective, the SIF modeling must be introduced in DART-Lux. This introduction is presented in the next chapter.

Appendix 2-1: Nomenclature

Symbol	Description	Unit
$\frac{g(\theta)}{2\pi}$	Leaf angular distribution function	sr^{-1}
$G(\Omega_s)$	Mean projection of leaf normal on the direction Ω_s	-
$\bar{T}$	Mean cell transmittance	-
$T_{PSx}(\lambda_u, \lambda_w, \Omega_s, \Omega_v, \Delta\Omega_v)$	Fluorescence transfer function: excitation band u, emission band w, incident direction Ω_s, outgoing direction $(\Omega_v, \Delta\Omega_v)$	-
$T_{scat}(\lambda, \Omega_s, \Omega_v, \Delta\Omega_v)$	Scattering transfer function: incident direction Ω_s, outgoing direction $(\Omega_v, \Delta\Omega_v)$	-
$W_{in}(\lambda, \Omega_s)$	Source vector of incident radiation in direction Ω_s	$W.\mu m^{-1}$
$W_{int}(\lambda, \Omega_s)$	Intercepted radiation from $W_{int}(\lambda, \Omega_s)$	$W.\mu m^{-1}$
$W_{PSx}(\lambda_u \rightarrow \lambda_w, \Omega_s, \Omega_v, \Delta\Omega_v)$	First order SIF at photosystem x and band w due to excitation in band u	$W.\mu m^{-1}$
$W_{1,scat}(\lambda, \Omega_s, \Omega_v, \Delta\Omega_v)$	First order scattering due to $W_{int}(\lambda, \Omega_s)$	$W.\mu m^{-1}$
$W_{1,scat,\alpha}(\lambda, \Omega_s, \Omega_v, \Delta\Omega_v)$	Part of $W_{1,scat}$ that exits the cell	$W.\mu m^{-1}$
$W_{1,int,\beta}(\lambda, \Omega_s)$	Part of $W_{1,int,1}$ that exits the cell after multiple scattering	$W.\mu m^{-1}$
$W_{1,int,PSx}(\lambda_w, \Omega_s)$	SIF emission at photosystem x due to the propagation of $W_{1,int,1}$	$W.\mu m^{-1}$
$W_{1,int,1}(\lambda, \Omega_s)$	Intercepted part from first order scattered radiation	$W.\mu m^{-1}$
$W_{1,abs}(\lambda, \Omega_s)$	Absorbed part from first order scattered radiation	$W.\mu m^{-1}$
$W_{1,PSx}(\lambda_w, \Omega_s, \Omega_v, \Delta\Omega_v)$	First order SIF due to $W_{int}(\lambda, \Omega_s)$	$W.\mu m^{-1}$
$W_{1,PSx,\alpha}(\lambda_w, \Omega_s, \Omega_v, \Delta\Omega_v)$	Part of $W_{1,PSx,\alpha}$ that exits the cell	$W.\mu m^{-1}$

$W_{1,PSx,int,\beta}(\lambda_w, \Omega_s)$	Part of $W_{1,PSx,int,1}$ that exits the cell after multiple scattering	$W.\mu m^{-1}$
$W_{1,PSx,int,1}(\lambda_w, \Omega_s)$	Interception due to first order SIF radiation	$W.\mu m^{-1}$
$W_{1,PSx,abs}(\lambda, \Omega_s)$	Absorbed part from first order SIF radiation	$W.\mu m^{-1}$
$W_{1,int,PSx,\gamma}(\lambda_w, \Omega_s)$	Part of $W_{1,int,PSx}$ that exits the cell after simple or multiple scattering	$W.\mu m^{-1}$
$W_{1,int,PSx,\gamma}(\lambda_w, \Omega_s \rightarrow \Omega_v)$	Part of $W_{1,int,PSx,\gamma}$ that exits from direction Ω_v	$W.\mu m^{-1}$
u_l	Leaf volume density	$m^2.m^{-3}$
$\rho_{top}\ \tau_{top}\ \rho_{bot}\ \tau_{bot}$	Leaf top reflectance, top transmittance, bottom reflectance, bottom transmittance respectively	-
η	Fluorescence eta factor	-
$\xi(M, \Omega_v)$	Fraction of radiation scattered in direction Ω_v	-
$\Delta l(\Omega_s)$	Path along Ω_s	m

Chapter 3

SIF modeling in DART-Lux

DART-Lux is based on an adaptation of the LuxCoreRender opensource rendering software. A fundamental adaptation was to replace the RGB triple color channel hardly coded in this software, to multiband modeling to allow multispectral and hyperspectral simulations. This step was needed to simulate SIF because SIF modeling usually needs a large number of spectral bands at a fine spectral resolution over the whole SIF excitation and emission spectral domains. However, to simulate SIF emission, it is essential to have an interdependency between spectral bands as the excitation at a certain wavelength can induce fluorescence emission at other wavelengths, which is not possible using the original LuxCoreRender nor the first versions of DART-Lux. Moreover, the turbid medium is a representation of vegetation that is specific for remote sensing models and is not included in rendering software originally designed for other purposes. This chapter presents the new modeling that I designed and implemented into DART-Lux in order to solve these issues. The first section presents the SIF modeling for facets-based vegetation and all the consequent modeling adaptations that were made to allow DART-Lux to simulate SIF. An article describing the methodology and evaluating the accuracy of the SIF modeling in DART-Lux of which I am the first author has been submitted to the International Journal of Applied Earth Observation and Geoinformation. The second section presents first the turbid volume vegetation modeling in DART-Lux which was introduced by analogy to the fluids modeling. Then, the SIF modeling for turbid vegetation is introduced.

3.1 Vegetation simulated as facets

3.1.1 Modeling approach

The implementation of SIF emission in DART-Lux for vegetation simulated as facets also uses the fluorescence excitation-emission matrices computed by Fluspect and resampled to the user-defined DART bands. The same rule of covering all the excitation spectral interval (*i.e.*, [400 – 750 nm]) with non-overlapping bands applies. To include the SIF radiation, physical quantities in DART-Lux should have 3 components for total, PSI and PSII radiation. However, to evaluate the SIF radiance for light paths traced from the sensor (*i.e.*, in the backward direction), this is not sufficient. A higher dimensional representation needed to be introduced to account for the three components and all the possible interactions. The detailed description of this methodology and its implementation is available in a submitted paper (cf. Section 3.1.3).

3.1.2 Results

Model-to-model comparisons were used to evaluate the implementation of SIF in DART-Lux. Canopy SIF emission and radiance simulated by DART-Lux were compared to those simulated by DART-FT and SCOPE for different types of canopies. DART-Lux closely matched DART-FT in all configurations, with less than 2% of relative difference. It also matched SCOPE for homogeneous canopies, but not with 3D canopy (maize crop field) especially for oblique viewing directions. Computation time and memory requirements were usually lower than DART-FT. The gain in computational efficiency relative to DART-FT was systematically very large for large and complex scenes. However, this large gain decreased when the number of spectral bands increases. The theory of the new SIF modeling and results are detailed in a submitted paper (cf. Section 3.1.3).

3.1.3 Submitted article

Bi-directional Monte-Carlo modelling of solar-induced chlorophyll fluorescence images for 3D vegetation canopies in the DART model

Omar Regaieg, Nicolas Lauret, Yingjie Wang, Jordan Guilleux, Eric Chavanon, Jean-Philippe Gastellu-Etchegorry

CESBIO - UPS, CNES, CNRS, IRD, Université de Toulouse, 31401 Toulouse cedex 9, France.

Abstract

Remote sensing (RS) of solar-induced chlorophyll fluorescence (SIF) has a great potential for monitoring plant photosynthetic activity. Radiative transfer models (RTM) are essential to better interpret and extract information from SIF signals. DART is one of the most comprehensive and accurate 3D RTMs. Its standard mode DART-FT simulates SIF using a discrete ordinate method but is not adapted to large landscapes due to computational constraints. DART-Lux, the new mode based on a bi-directional path tracing algorithm, greatly improves DART computational efficiency for simulating images. This paper presents the theory of a novel SIF modelling algorithm in DART-Lux. We verified its accuracy with DART-FT and the SCOPE model for three types of canopies: turbid medium, maize field and forest. DART-Lux closely matches DART-FT (relative difference < 2%) with much better computational efficiency depending on the scene complexity, number of spectral bands and needed accuracy. For example, simulation time is reduced by a factor of ≈48, and memory usage by ≈50 for a maize field at 1 cm resolution. It allowed to simulate SIF images of large scenes as the $3 \times 3\ km^2$ Ripperdan agricultural site that DART-FT could not simulate. The new SIF modelling algorithm opens new horizons for RS studies of large and complex landscapes. It is available as part of released DART versions (v1152 onwards) (https://dart.omp.eu/).

Keywords

SIF, Remote sensing, Bi-directional path tracing, 3D vegetation structure, DART

I. Introduction

Solar-induced fluorescence (SIF) of vegetation is a spontaneous radiation re-emission from 640 to 850 nm due to absorbed sunlight from 400 to 750 nm. In competition with the photochemical and heat dissipation processes, it allows an electron from a chlorophyll molecule excited by absorbing a quantum of light, to dispose of its excess energy. It provides

valuable information on real-time plants photosynthetic activity (Mohammed et al., 2019) which enables early stress detection (Song et al., 2018) and gross primary production (GPP) estimation (Zhang et al., 2020).

The fluorescence quantum efficiency (*fqe*) of chlorophyll in vivo does not exceed 10%, with typical values under steady-state illumination of 0.5–3% (Porcar-Castell et al., 2014). Hence, the SIF remote sensing (RS) signal is a small fraction of sunlight scattered by a vegetation canopy. The resulting difficulty in interpreting SIF RS signal in terms of vegetation functioning traits is largely amplified by the dependence of the SIF signal on the vegetation 3D structure, combined with illumination and observation conditions (Hornero et al., 2021; Regaieg et al., 2021). This stresses the importance of physical models to link the within canopy SIF emission with RS signals. An ideal radiative model of SIF includes two major sub-models: (1) Leaf SIF emission model considering the incident spectral irradiance, leaf structure and biochemistry, and the probability of a photon absorbed by photosystems I (PSI) and II (PSII) to be re-emitted as SIF (*i.e.*, *fqe*) derived from leaf physiological modelling. (2) Radiative transfer (RT) model of the radiation propagation in the canopy to simulate the SIF radiance at the bottom and/or top of the atmosphere (*i.e.*, RS signal).

Here, we consider top of canopy SIF modelling including vegetation 3D architecture. Canopy SIF models are generally canopy reflectance models with an imbedded leaf-level fluorescence model. For example, FLSAIL (Rosema et al., 1991), FluorSAIL (Miller, 2005) and SCOPE (van der Tol et al., 2009) models combine leaf SIF modelling with the SAIL canopy reflectance model (Verhoef, 1984). SAIL is one-dimensional (1D), as it represents vegetation as superimposed homogeneous layers filled by a turbid medium: infinite number of infinitely small plane elements characterized by a statistical leaf angular distribution (LAD), a leaf area index (LAI), and optical properties. It simulates the radiative transfer with four streams: a source term for direct solar radiation, one stream for upward and one stream for downward fluxes, and scattered radiance is integrated along the observation direction. SCOPE is a reference model for 1D SIF modelling (Damm et al., 2015; Verrelst et al., 2019). The 1D models' major limitation is neglecting the vegetation horizontal heterogeneity. Accounting for vertical heterogeneity as in mSCOPE (Yang et al., 2017) only partly improves the situation. Indeed, the canopy horizontal heterogeneity has usually a much greater influence on RS signals than vertical heterogeneity (Regaieg et al., 2021). Some approaches aiming to simulate SIF at the global scale account for the influence of the canopy horizontal heterogeneity using clumping

indices (Braghiere et al., 2021). However, they cannot fully capture the actual canopies 3D architecture including local topography, and the presence of woody elements, that impact remotely sensed SIF signals (Malenovský et al., 2021; Regaieg et al., 2021).

3D SIF RTMs adapted to realistic vegetation canopies descriptions represented as facets or 3D turbid medium are of great interest because of the 1D models limitation. For example, FLiES-SIF (Sakai et al., 2020) simulates SIF tree canopies having geometrically simple crowns (*e.g.*, cone, cylinder, spheroid) whereas FluorFLIGHT (Hernández-Clemente et al., 2017), FluorWPS (Zhao et al., 2016), DART (Malenovský et al., 2021) and FluCVRT (Kallel, 2020) simulate SIF for any canopy type. FluCVRT includes 3D leaf-level SIF modelling. These models use Monte Carlo ray tracing techniques, apart from DART that uses an adapted forward discrete ordinates method, called DART-FT (Flux Tracking). DART-FT simulates the canopy SIF radiance and reflectance images, the canopy 3D SIF radiative budget (RB) per photosystem, and therefore the canopy fluorescence escape factor (Guanter et al., 2014). DART-FT SIF modelling has been validated with model comparison (Malenovský et al., 2021), and successfully used in various SIF studies such as sensitivity analysis of the SIF signal in architecturally complex forest canopies (W. Liu et al., 2019; Malenovský et al., 2021), scaling canopy-level SIF down to photosystems level (X. Liu et al., 2019), and studying the far-red SIF escape probability from forest canopies (W. Liu et al., 2020).

Compared to 1D models, 3D models use more parameters, are more computationally demanding and therefore are not well adapted to regional or global scales. Indeed, forward models like DART-FT spend much time and memory tracking fluxes that contribute little to the simulated images. Based on the Bidirectional Path Tracing (BDPT) algorithm (Veach, 1998), based on Monte Carlo modelling, the new DART mode called DART-Lux (Wang et al., 2022) highly reduces computer time and memory requirements to simulate images of large and complex landscapes. Therefore, we designed a novel SIF modelling method adapted to the BDPT algorithm for accurate and computationally efficient simulations of SIF RS images of 3D vegetation canopies. To our knowledge, no similar SIF modelling method has ever been developed for BDPT algorithms.

II. DART-Lux

DART is an accurate and comprehensive 3D RT model developed at CESBIO since 1992 and patented in 2003. It simulates RS images of VIS / NIR / TIR spectro-radiometers, LiDAR

observations, and 3D RB of natural and urban landscapes (Wang et al., 2020). Its standard mode, DART-FT, represents landscapes by 3D arrays of voxels filled with facets (*e.g.*, vegetation, buildings), turbid medium and fluids. It iteratively tracks radiation in a user-defined number of discrete directions. DART-Lux, DART's latest mode (Wang et al., 2022), uses the BDPT algorithm with Monte Carlo integration techniques. It can largely decrease time and memory requirements for DART images simulation of large and complex landscapes. It uses the geometry instance, "depth-first" approaches (Cormen et al., 2009) and the BDPT algorithm (Pharr et al., 2016) that preferentially tracks fluxes that contribute most to observations by constructing paths that start both from the sensor and light sources. It is adapted to any configuration with any light sources and landscape elements with any Bidirectional Scattering Distribution Function (BSDF). The radiance measurement $L^{(j)}$ of pixel j of the simulated image is:

$$L^{(j)} = \int_{\mathcal{D}} C^{(j)}(\bar{p}) dA(\bar{p}) \qquad (1)$$

where $\bar{p}$ is a light transport path,

$\mathcal{D}$ is the set of all light transport paths. $\mathcal{D} = \bigcup_{k=1}^{\infty} \mathcal{D}_k$, with $\mathcal{D}_k$ the set of all paths $\bar{p}_k = (p_0, ..., p_k)$ of length k (*i.e.*, k segments, $k+1$ vertices p_i; $i \in [0, k]$, p_0 on the sensor, p_k on the light source),

$dA(\bar{p})$ is the area product for path $\bar{p}$; *e.g.*, $dA(\bar{p}_k) = dA(p_0) \dots dA(p_k)$ with area $dA(p_i)$ at vertex i

and $C^{(j)}(\bar{p})$ is the contribution function of path $\bar{p}$ to the measurement $L^{(j)}$ of pixel j.

$L^{(j)}$ is computed as:

$$L^{(j)} = \int_{A_0} \int_{\Omega_0} W_e^{(j)}(p_0, \Omega) \cdot L(p_1 \rightarrow p_0) \cdot \left| cos\, \theta_i^{p_0} \right| \cdot d\Omega dA(p_0) \qquad (2)$$

where A_0 is lens area,

Ω_0 is the solid angle that encloses all incident directions from the optical system to the sensor plane,

$W_e^{(j)}(p_0, \Omega)$ is the importance function (Nicodemus, 1978),

$\theta_i^{p_0}$ is the angle between the incident direction and the sensor principal optical axis

and $L(p_1 \rightarrow p_0) = \sum_{k=1}^{\infty} L(\bar{p}_k)$ is the radiance at sensor's vertex p_0 from a surface's vertex p_1 with $L(\bar{p}_k)$ the radiance incident on p_0 due to all paths $\bar{p}_k$ of length k; *e.g.*, $\bar{p}_k = (p_k, \dots, p_1, p_0)$.

The radiance incident at vertex p_i of a path $\bar{p}_k$ is the radiance from the vertex p_{i+1} that illuminates the vertex p_i. A path results of the connection of a vertex of the sensor sub-path created with t vertices from the sensor and a vertex of the source sub-path created with s vertices from the light source. Figure 1 shows a case with four vertices (p_0, p_1, p_2, p_3), with p_0 on the sensor and p_3 on the source. In DART-Lux, the maximum scattering order (*i.e.*, number of ray bounces on the scene surfaces) is a user-defined parameter. It defines the maximum length of the light transport paths. In this figure, this maximum length is three ($k = 3$: 4 vertices and 3 segments) and the scattering order is 2.

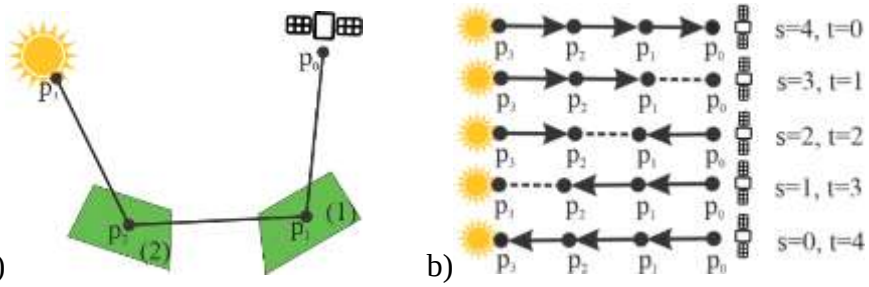

a) b)

Figure 1. (a) Path $\bar{p}_3$ with four vertices p_i (i ∈ {0..k} with k = 3). (b) The five ways to construct $\bar{p}_3$, with s and t vertices (s+t = k+1 = 4) for the sources and sensor sub-paths, respectively.

In DART-Lux, the BDPT algorithm estimates $L^{(j)}$ at sensor p_0 from the contributions of sampled paths constructed by incremental path tracing from both the light source and the sensor. For example, if a path $\bar{p}_k$ starts from the sensor, a point p_0 is randomly sampled on the senor and a ray is traced from p_0 and in the direction defined by sensor properties, until intersecting a surface at a point p_1. Then, the path is iteratively constructed using the two steps:

1) At each vertex p_i, starting from i=1, sample a new direction according to the BSDF, knowing the incident direction. Stop if i=k.

2) Find the next vertex p_{i+1} by tracing a ray from p_i along the sampled direction.

A Monte Carlo integration technique estimates the pixel radiance measurement with an importance sampling technique (Kalos & Whitlock, 1986). Paths that most impact the radiance

reaching the sensor have a higher probability to be sampled. Multiple Importance Sampling (MIS) (Veach & Guibas, 1995) is used to combine the different ways to sample the same path (*e.g.*, Figure 1.b shows the five ways to sample the path in Figure 1.a) using weighting functions that give the weight $w_i(x)$ per sample x drawn from the sampling way i. The Russian Roulette (Veach & Guibas, 1995) is used to randomly stop the calculation at a certain path length to save computer time. A probability q is set to stop a ray and not to evaluate the integrand for the particular sample, and a probability $(1\text{-}q)$ to evaluate the integrand and to weight it by $\frac{1}{1-q}$, to account for all the samples that are not evaluated. The theory of DART-Lux was presented in more details by Wang et al. (2022).

The DART-Lux image (5 m resolution, 100 bands in [0.4-0.85 µm]) of the 3×3 km^2 Ripperdan farm site with vines and more than 600.000 trees (Figure 12.b) shows its potential. It needed 16.9 GB of memory and 13 min 4 s of simulation time with an Intel Xeon W-2295 CPU @ 3.00GHz (18 cores, 36 threads). DART-FT was not run because it needed about 50 TB of memory and 1600 h of simulation time.

III. DART-Lux canopy SIF modelling

Despite its interest in accurate and fast radiance simulations of large landscapes, to our knowledge, the BDPT algorithm has never been applied to canopy SIF modelling. Its adaptation to SIF modelling in DART-Lux is presented here. It relies on the surface form of the Light Transport Equation (LTE) to compute as an integral over all scene surfaces A the radiance reaching a vertex p from a vertex p' (Figure 2):

$$L(p' \rightarrow p) = L_e(p' \rightarrow p) + \int_A f(p'' \rightarrow p' \rightarrow p) \cdot L(p'' \rightarrow p') \cdot G(p'' \leftrightarrow p') \cdot dA(p'') \quad (3)$$

where $L_e(p' \rightarrow p)$ is the radiance emitted from p' to p, if p' belongs to a light source, $L_e(p' \rightarrow p) = 0$ otherwise,

$G(p'' \leftrightarrow p') = V(p'' \leftrightarrow p') \cdot \frac{|cos\theta_o''| \cdot |cos\theta_i'|}{||p'-p''||^2}$, with index o for outgoing and index i for incident,

$f(p'' \rightarrow p' \rightarrow p)$ is the BSDF of surface Σ,

$L(p'' \rightarrow p')$ is the radiance reaching p' from p",

V is the binary visibility function: $V(p''\leftrightarrow p')=1$ if p' and p'' are mutually visible, and 0 otherwise,

$cos\theta_0'' = \overrightarrow{n''} \cdot \frac{\overrightarrow{p''p'}}{||p'-p''||}$, and $cos\theta_i' = \frac{\overrightarrow{p'p''}}{||p'-p''||} \cdot \overrightarrow{n'}$,

$\overrightarrow{n'}$ and $\overrightarrow{n''}$ are the normal vectors to the surface Σ at p' and to the surface A at p'', respectively.

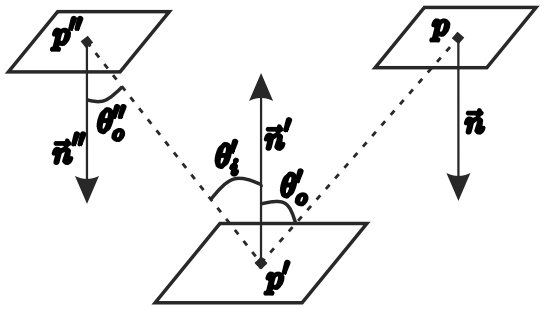

Figure 2. LTE geometry: the vertex p' scatters the ray coming from the vertex p'' towards the vertex p

Expanding Eq (3) by iteratively replacing $L(p''\rightarrow p')$ by its right-hand term gives $L(\bar{p}_k)$ for $k \geq 2$:

$$L(\bar{p}_k) = \int_A \int_A \dots \int_A L_e(p_k \rightarrow p_{k\text{-}1}) \cdot \left(\prod_{i=1}^{k-1} f(p_{i+1} \rightarrow p_i \rightarrow p_{i\text{-}1}) \cdot G(p_{i+1} \leftrightarrow p_i) \right) \cdot dA(p_2) \dots dA(p_k) \quad (4)$$

We denote $P(\bar{p}_k)$ the integrand in Eq (4), and $T(\bar{p}_k)$, the "light path throughput", the term between brackets in $P(\bar{p}_k)$:

$$T(\bar{p}_k) = \prod_{i=1}^{k-1} f(p_{i+1} \rightarrow p_i \rightarrow p_{i-1}) \cdot G(p_{i+1} \leftrightarrow p_i) \quad (5)$$

$$P(\bar{p}_k) = L_e(p_k \rightarrow p_{k-1}) \cdot T(\bar{p}_k) \quad (6)$$

If p_i belongs to a bi-Lambertian surface, with normal $\vec{n}_i$, reflectance ρ_i and transmittance τ_i:

$$f(p_{i+1} \rightarrow p_i \rightarrow p_{i-1}) = \begin{cases} \frac{\rho_i}{\pi}, if\ (\overrightarrow{p_i p_{i+1}} . \overrightarrow{n_i}) \cdot (\overrightarrow{p_i p_{i-1}} . \overrightarrow{n_i}) \geq 0 \\ \frac{\tau_i}{\pi}, \text{otherwise} \end{cases} \quad (7)$$

As for DART-FT (Malenovský et al., 2021), the Fluspect model (Vilfan et al., 2018) is used to simulate leaf-level SIF. It uses the leaf biochemical properties and *fqe*s input parameters to compute four leaf EEFMs (Excitation-Emission Fluorescence Matrices) $M_{x,y,ij}$ for the N user

defined spectral bands ($i \in \{1..N\}$ for excitation and $j \in \{1..N\}$ for emission), for the photosystem x (PSI or PSII) and direction y (forward or backward). The reflectance ρ and EEFM backward matrices ($M_{x,backward,ij}$) play equivalent roles for scattering and SIF emission respectively, and so do the surface transmittance τ and EEFM forward matrices ($M_{x,forward,ij}$). In the Fluspect model, the leaves are bi-Lambertian and SIF emitted radiance is isotropic. Therefore, the direction sampling method for SIF is the same as for scattering by bi-Lambertian surfaces with the PDF $p(\Omega) = \frac{\cos\theta}{\pi}$ where θ is the angle between the surface normal and the sampled direction Ω, for any incident direction.

To estimate the pixel radiance measurement, the contribution of each sampled path is evaluated by multiplying the integrand $P(\bar{p}_k)$ of Eq (4) by the importance function and the cosine term in Eq (2).

For N simulated spectral bands, the light source spectral radiance L_e, the bi-Lambertian surface spectral reflectance and transmittance, and also the sub- and full-path throughputs are vectors of N elements. A path throughput is computed by successive element wise vector multiplications of the multi-spectral reflectance or transmittance value at each vertex by a geometric term G, divided by π (Eq (5), (7)). This product is associative and can be computed starting from the light source or starting from the sensor. A full path being the connection of a light sub-path and a sensor sub-path, its throughput is the element wise product of the light and sensor sub-path throughputs. Its multiplication by the light radiance $L_e(p_k \rightarrow p_{k-1})$ gives the integrand $P(\bar{p}_k)$.

For the simplicity of the equations below, we avoid writing the scalar multiplicative terms G and $\frac{1}{\pi}$. They are still considered in the computations. If the SIF emission is considered, three components of the radiance need to be computed: 1) the total radiance including the scattered radiation plus SIF emission, 2) the PSI SIF radiance component, 3) the PSII SIF radiance component. For N simulated spectral bands, a fluorescent surface S_l is characterized by four $N \times N$ EEFMs, in addition to its non-fluorescent BSDF. For photosystem x and for direction y, the EEFM is:

$$M_{xy}^{l} = \begin{pmatrix} f_{xy1,1}^{l} & \cdots & f_{xy1,N}^{l} \\ \vdots & \ddots & \vdots \\ f_{xyN,1}^{l} & \cdots & f_{xyN,N}^{l} \end{pmatrix}$$

where $f^l_{xyi,j}$ is the EEFM element for an excitation spectral band (central wavelength: λ_i, bandwidth: $\Delta\lambda_i$) and an emission band $(\lambda_j, \Delta\lambda_j)$,

For a path with two segments, the integrand of SIF radiance component of photosystem x and direction y is the matrix product of the light source spectral radiance L_e and the EEFM M_{xy}:

$$P_x(\bar{p}_2) = L_e \times M^l_{xy} = (e_1, e_2, \ldots, e_N) \times \begin{pmatrix} f^l_{xy1,1} & \cdots & f^l_{xy1,N} \\ \vdots & \ddots & \vdots \\ f^l_{xyN,1} & \cdots & f^l_{xyN,N} \end{pmatrix} = \left(\sum_{i=1}^{N} e_i . f^l_{xyi,1}, \ldots, \sum_{i=1}^{N} e_i . f^l_{xyi,N}\right)$$

Therefore, for a path $\bar{p}_k$ with $k+1$ vertices p_l, $l \in \{0..k\}$, the integrand for the total radiance (*i.e.*, sum of scattered radiance, PSI and PSII SIF emissions radiance) is:

$$P_{total}(\bar{p}_k) = L_e \times T_{tot}(\bar{p}_k) \quad (8)$$

where $T_{tot}(\bar{p}_k) = T^1_{\text{tot}} \times \ldots \times T^{k-1}_{\text{tot}}$ is the total throughput,

$$T^l_{\text{tot}} = R_l + M^l_{PSIy} + M^l_{PSIy} = \begin{pmatrix} r^l_1 + f^l_{\text{PSIy1,1}} + f^l_{\text{PSIIy1,1}} & \cdots & f^l_{\text{PSIy1,N}} + f^l_{\text{PSIIy1,N}} \\ \vdots & \vdots & \vdots \\ f^l_{\text{PSIyN,1}} + f^l_{\text{PSIIyN,1}} & \cdots & r^l_N + f^l_{\text{PSIyN,N}} + f^l_{\text{PSIIyN,N}} \end{pmatrix},$$

r^l_i is the reflectance or transmittance of the surface S_l at the band $(\lambda_i, \Delta\lambda_i)$, $R_l = \begin{pmatrix} r^l_1 & \cdots & 0 \\ \vdots & \ddots & \vdots \\ 0 & \cdots & r^l_N \end{pmatrix}$,

and $f^l_{PSIyi,j}$ and $f^l_{PSIIyi,j}$ the EEFM elements for an excitation band $(\lambda_i, \Delta\lambda_i)$ and an emission band $(\lambda_j, \Delta\lambda_j)$ for PSI and PSII respectively, for direction y.

As the matrix product is associative, the product in Eq (8) can be cut into a light sub-path sub-product (*i.e.*, N-element vector resulting from successive vector-matrix products), and a sensor sub-path sub-product (*i.e.*, $N \times N$ matrix resulting from successive matrix-matrix products). However, Eq (8) provides only the total radiance (N-element vector). To have the PSI and PSII radiance separately as well, two additional N-element vectors need to be computed. For the path $\bar{p}_k$, in addition to $P_{total}(\bar{p}_k)$, the $P_{PSI}(\bar{p}_k)$ and $P_{PSII}(\bar{p}_k)$ need to be computed. For a light path $\bar{p}_3$ with 3 segments (two fluorescent surfaces) (Figure 1), $P_{PSI}(\bar{p}_3)$ and $P_{PSII}(\bar{p}_3)$ are:

$$P_{PSI}(\bar{p}_3) = L_e \times [T^1_{\text{tot}} \times M^2_{PSIy} + M^1_{PSIy} \times R_2] \quad (9)$$

$$P_{PSII}(\bar{p}_3) = L_e \times [T^1_{\text{tot}} \times M^2_{PSIIy} + M^1_{PSIIy} \times R_2] \quad (10)$$

The bracketed terms in Eq (9) and (10) represent the interactions between the two surfaces that generate the two SIF radiance components. Eq (9) and (10) cannot be written as an associative product of terms each of which depends on the properties of a single vertex. Thus, they cannot be computed starting both from the light source and from the sensor. Therefore, the block matrix M_B^l is introduced:

$$M_B^l = \begin{pmatrix} T_{\text{tot}}^l & M_{PSIy}^l & M_{PSIIy}^l \\ 0 & R_l & 0 \\ 0 & 0 & R_l \end{pmatrix} \tag{11}$$

The light radiance vector is also written as a block matrix: $L_{e,B} = (L_{e,total}; L_{e,PSI}; L_{e,PSII})$, where $L_{e,total}$, $L_{e,PSI}$ and $L_{e,PSII}$ are N-element vectors. Since light sources do not emit SIF, $L_{e,PSI}$ and $L_{e,PSII}$ are null vectors. If M_B^{k-1} is the block matrix of the first surface hit by the light source, the incident radiance vector $L_{B,k\text{-}2}=L_{e,B}\times M_B^{k-1}$ at vertex k-2 is:

$$L_{B,k\text{-}2} = \left(L_{e,total}; 0; 0\right) \times \begin{pmatrix} R_{k-1} + M_{PSIy}^{k-1} + M_{PSIIy}^{k-1} & M_{PSIy}^{k-1} & M_{PSIIy}^{k-1} \\ 0 & R_{k-1} & 0 \\ 0 & 0 & R_{k-1} \end{pmatrix} \tag{12}$$

$$= \left(L_{e,total} \times \left(R_{k\text{-}1} + M_{PSIy}^{k-1} + M_{PSIIy}^{k-1}\right); L_{e,total} \times M_{PSIy}^{k-1}; L_{e,total} \times M_{PSIIy}^{k-1}\right)$$

$$= (L_{total,k\text{-}2}; L_{PSI,k\text{-}2}; L_{PSII,k\text{-}2})$$

Similarly, at vertex k-3, the incident radiance vector $L_{B,k\text{-}3}=L_{B,k\text{-}2}\times M_B^{k-2}$ is:

$$L_{B,k\text{-}3} = \left(L_{total,k\text{-}2}; L_{PSI,k\text{-}2}; L_{PSII,k\text{-}2}\right) \times \begin{pmatrix} R_{k\text{-}2}+M_{PSIy}^{k-2}+M_{PSIIy}^{k-2} & M_{PSIy}^{k-2} & M_{PSIIy}^{k-2} \\ 0 & R_{k\text{-}2} & 0 \\ 0 & 0 & R_{k\text{-}2} \end{pmatrix}$$

$$= \left(L_{total,k\text{-}2} \times (R_{k\text{-}2}+M_{PSIy}^{k-2}+M_{PSIIy}^{k-2});\ L_{total,k\text{-}2} \times M_{PSIy}^{k-2} + L_{PSI,k\text{-}2} \times R_{k\text{-}2};\right.$$

$$\left. L_{total,k\text{-}2} \times M_{PSIIy}^{k-2} + L_{PSII,k\text{-}2} \times R_{k\text{-}2}\right)$$

$$= (L_{Total,k\text{-}3}; L_{PSI,k\text{-}3}; L_{PSII,k\text{-}3})$$

And so on, for each vertex p_l of the light sub path until reaching the sensor, the exiting radiance block matrix is:

$$L_{B,l}\times M_{B,l}=\left(L_{total,l}; L_{PSI,l}; L_{PSII,l}\right) \times \begin{pmatrix} R_l+M_{PSIy}^l+M_{PSIIy}^l & M_{PSIy}^l & M_{PSIIy}^l \\ 0 & R_l & 0 \\ 0 & 0 & R_l \end{pmatrix}$$

$$=\left(L_{total,l}\times\left(R_l+M_{PSIy}^{l}+M_{PSIIy}^{l}\right);\ L_{total,l}\times M_{PSIy}^{l}+L_{PSI,l}\times R_l;\ L_{total,l}\times M_{PSII}^{l}+L_{PSII}\times R_l\right)$$

All components of the total, PSI and PSII spectral radiance terms of p_l are considered:

-Total radiance $L_{total,l}\times\left(R_l+M_{PSIy}^{l}+M_{PSIIy}^{l}\right)$ of surface p_l hit by a ray of incident radiance $L_{total,l}$

-PSI radiance: sum of the emitted PSI radiance $L_{total,l}\times M_{PSIy}^{l}$ at p_l due to $L_{total,l}$, and PSI radiance $L_{PSI,l}\times R_l$ coming from the previous vertex and scattered at p_l.

-PSII radiance: sum of the emitted PSII radiance $L_{total,l}\times M_{PSII}^{l}$ at p_l due to $L_{total,l}$, and PSII radiance $L_{PSII,l}\times R_l$ coming from the previous vertex and scattered at p_l.

These equations can be used starting from the light source and starting from the sensor because they include associative products of matrices and each matrix depends on the properties of a single vertex. For a light path with $L+2$ vertices (*i.e.*, L hit surfaces of matrices M_B^l with $l\in\{1..L\}$), the integrand $P_B(\bar{p}_{L+2})$ including the total, PSI and PSII signals from this path is:

$$P_B(\bar{p}_{L+2})=L_{e,B}\times M_{B,1}\times M_{B,2}\times ...\times M_{B,L}$$

If the light path $\bar{p}_{L+2}$ has S vertices in the light sub-path and T vertices in the sensor sub-path, excluding the light source and sensor vertices ($L+2=S+T$), the throughput of the light sub-path is $M_B^{light}=M_{B,1}\times M_{B,2}\times ...\times M_{B,S}$ and of the sensor sub path $M_B^{sensor}=M_{B,S+1}\times M_{B,S+2}\times ...\times M_{B,S+T}$. After connecting the two sub-paths, the integrand is:

$$P_B(\bar{p}_{L+2})=L_{e,B}\times M_B^{light}\times M_B^{sensor}\qquad(13)$$

The light sub-path starts from the light source, then hits the surfaces from 1 to S. It gives the block matrix $E_B\times M_B^{light}$ of three N-element vectors. The sensor sub-path hits the surfaces $S+T$ to $S+1$. The matrix product being not commutative, $E_B\times M_B^{light}$ and M_B^{sensor} are computed in opposite directions.

Eq (13) is computationally expensive. For N spectral bands, a sensor sub-path throughput is a $3N\times 3N$ matrix. For optimization, diagonal matrices are considered whenever possible when multiplying matrices, and only $R_l+M_{PSIy}^{l}+M_{PSII}^{l}$, M_{PSI}^{l}, M_{PSII}^{l} and R_l only are stored instead of

$M_B^l = \begin{pmatrix} R_l + M_{PSIy}^l + M_{PSII}^l & M_{PSI}^l & M_{PSII}^l \\ 0 & R & 0 \\ 0 & 0 & R \end{pmatrix}$ because the product of matrices of this form has the same form (*cf.* Appendix 1).

As DART-FT (Malenovský et al., 2021), DART-Lux can import SCOPE η factors vertical profiles for sunlit and shaded leaves to account for the influence of local bioclimatology on leaf-level SIF emission. With the hypothesis that only PSII emission is affected, we have:

$$M_{B,\eta} = \begin{pmatrix} R + M_{PSI} + \eta . M_{PSII} & M_{PSI} & \eta . M_{PSII} \\ 0 & R & 0 \\ 0 & 0 & R \end{pmatrix}$$

Increasing the number of Monte Carlo samples/pixel $N_{samples}$ in the simulated images improves accuracy and increases simulation time. The optimal average $N_{samples}$ depends on the scene properties, pixel size, and expected precision and simulation time.

PSI and PSII radiance images (Figure 12) of the $3 \times 3\ km^2$ Ripperdan zone illustrate the potential of DART-Lux SIF modelling for large landscapes. It needed 42.9 GB of memory and 2h 44 min in simulation time with an Intel Xeon W-2295 CPU @ 3.00GHz (18 cores, 36 threads). DART-FT was not run due to huge computational demands: more than 100 TB of memory and 15000 h of simulation time.

IV. Assessment of DART-Lux SIF modelling

Malenovský et al. (2021) validated DART-FT SIF modelling against the SCOPE/mSCOPE model for homogeneous canopies. Here, the accuracy and computer efficiency of DART-Lux SIF modelling are assessed for three canopies, using DART-FT SIF as a reference. DART-Lux is also compared to SCOPE for homogeneous scenes. These model cross-comparisons between models M_1 and M_2 for N spectral bands and a given physical quantity q, are done with the Mean Absolute Relative Difference (MARD):

$$\mathrm{MARD}_{\mathrm{M_1/M_2}} = \frac{1}{\sum_{i=1}^{N} \Delta\lambda_i} \sum_{i=1}^{N} \frac{|q_{M1,i} - q_{M2,i}|}{q_{M2,i}} . \Delta\lambda_i \qquad (14)$$

IV.1 Study cases

Three vegetation canopies (Figure 3) are studied. 1) Homogeneous turbid scene: 1 m high, LAI=1, spherical LAD, nadir observation and solar direction (θ_s=30°, ϕ_s=225°). 2) Maize crop

field: 7.5 m × 5 m scene, 600 maize plants, 40 cm spaced rows, 15 cm within row plant distance, LAI=1.9, three viewing directions (nadir; θ_v=30°, ϕ_v=0°; θ_v=60°, ϕ_v=0°), and three solar directions (θ_s=42.78°, ϕ_s=82.98°; θ_s=31.46°, ϕ_s=69.88°; θ_s=21.41°, ϕ_s=48.32°). 3) Tree plot: 10m x 10m scene, 10 randomly distributed trees "*populus_tremuloides"* with branch and trunk reflectance from the DART spectral database, LAI=1.9, nadir viewing direction and (θ_s=30°, ϕ_s=225°). Simulations are over [400-850 nm] with 451 bands ($\Delta\lambda = 1$ nm) for the homogeneous site and maize field, and 45 bands ($\Delta\lambda =$ 10 nm) for the tree plot. Atmosphere (gas model: USSTD76, aerosol model: RURALV23), leaf biochemistry and structure (Table 1), and ground reflectance "*loam_gravelly_brown_dark*" in DART database. Spatial resolution is 0.1 m for the tree plot and the homogenous site. It is 0.5 m and 0.01 m for the maize field, with 0.01 m selected to mimick the simulation of images of large scenes. It implied using fewer spectral bands in order to maintain reasonable computational needs for DART-FT: 35 excitation bands over [400-750 nm] and one emission band ($\lambda_c = 765\ nm, \Delta\lambda = 1\ nm$).

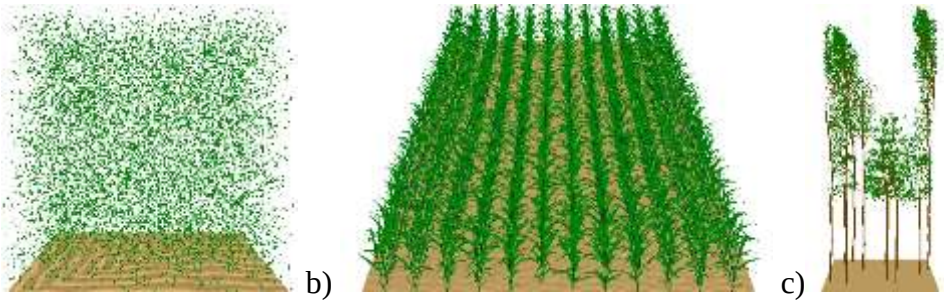

Figure 3. The simulated 3D mock-ups. a) Homogeneous medium b) Maize field. c) Tree plot.

Table 1. Leaf biochemistry and structure for the three study sites.

Parameter	Symbol	Unit	Homogeneous canopy	Maize field	Tree plot
Leaf structure parameter	N	-	1.8	1.5	1.8
Chlorophyll a+b content	C_{ab}	$\mu g.cm^{-2}$	45	50	30
Carotenoid content	C_{ca}	$\mu g.cm^{-2}$	15	15	10
Water content	C_w	cm	0.009	0.009	0.012
Dry matter content	C_{dm}	$g.cm^{-2}$	0.002	0.0021	0.01
fqe for photosystem I	ϕ_{PSI}	-	0.002	0.002	0.002
fqe for photosystem II	ϕ_{PSII}	-	0.01	0.01	0.01

IV.2 Homogeneous turbid canopy

SCOPE is a reference model for simulating the SIF radiance of homogeneous vegetation. Here, DART-FT and DART-Lux SIF simulate the homogeneous turbid scene of SCOPE as a homogeneous quasi turbid medium for two cases depending if SCOPE simulates or not the energy balance (EB):

- No EB: the η factors are set to one in DART-FT and DART-Lux.
- EB: DART-FT and DART-Lux use the SCOPE η factors for the default meteorological parameters.

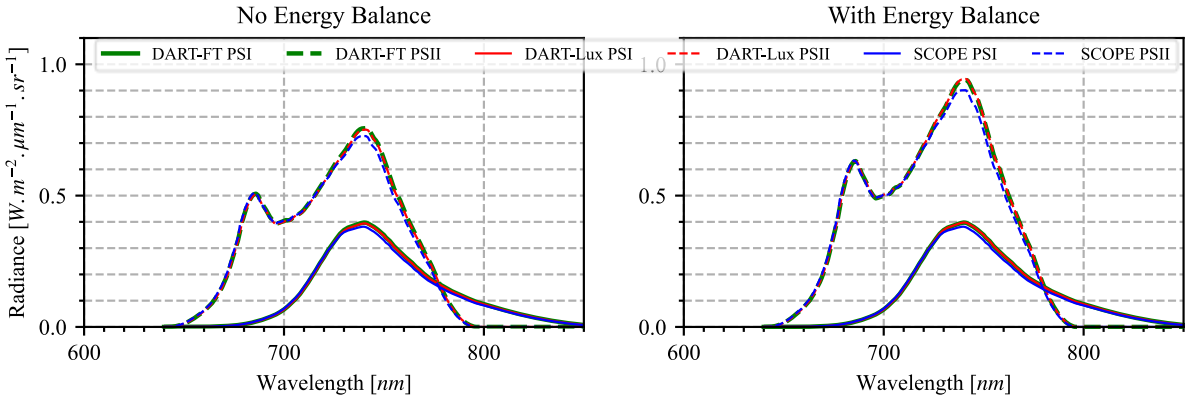

Figure 4. Homogeneous site: DART-FT, DART-Lux and SCOPE PSI and PSII nadir radiance, without (left) and with (right) computation of the canopy energy balance.

Figure 4 shows DART-Lux, DART-FT and SCOPE PSI and PSII nadir radiance. DART-Lux closely matches DART-FT and, to a lesser extent, SCOPE. Without EB, $MARD_{DART\text{-}Lux/DART\text{-}FT}$ is 0.7% for PSI and 0.53% for PSII, and $MARD_{DART\text{-}Lux/SCOPE}$ is 5.24% for PSI and 4.93% for PSII. Without neglect of EB, $MARD_{DART\text{-}Lux/DART\text{-}FT}$is 0.08% for PSI and 0.19% for PSII, and $MARD_{DART\text{-}Lux/SCOPE}$ is 5.57% for PSI and 5.15% for PSII.

IV.3 Maize field

The canopy nadir reflectance (Figure 5) and SIF PSI and PSII radiance (Figure 6, Table 2) simulated by DART-FT, DART-Lux and SCOPE for the three viewing directions and three sun directions show that:

- DART-Lux and DART-FT match: $MARD_{reflectance} < 1.3\%$ and $MARD_{SIF\ radiance} < 1\%$.
- DART-Lux and DART-FT poorly match SCOPE: $MARD_{reflectance}$ up to 16% and $MARD_{SIF\ radiance}$ from 3% to 19%, depending on the solar and viewing angles, with larger MARD for large angles.

Table 3 shows the computer time and RAM needs of DART-Lux and DART-FT at 0.5 m and 0.01 m resolutions, and also the main input parameters that influence their computational needs. Compared to DART-FT (200 discrete directions and illumination step $=10^{-3}$ m), DART-Lux (7^2 scene repetitions, maximal scattering order = 15, Russian Roulette starts at order 12 with cut-off probability =0.5) decreases the memory by a factor of ≈34 and computer time by ≈1.4 at 0.5 m resolution. It decreases the memory by ≈48 and computer time by ≈50 at 0.01 m resolution. Figure 7 shows nadir radiance images at 0.01 m resolution: DART-Lux RGB color composite, and also DART-Lux and DART-FT PSI and PSII nadir radiance images.

353 Table 2. Maize field: MARD of DART-Lux canopy SIF PSI and PSII radiance compared to
354 DART-FT and SCOPE for 3 viewing directions and 3 sun directions.

		Nadir	$\theta_v = 30° \ \phi_v = 0°$	$\theta_v = 60° \ \phi_v = 0°$
$\theta_s = 42.78°$	$\phi_s = 82.98°$	$\mathrm{MARD}_{\mathrm{DART-Lux/DART-FT}}$:		
		PSI: 0.46%, PSII: 0.44%	PSI: 0.56%, PSII: 0.42%	PSI: 0.67%, PSII: 0.58%
		$\mathrm{MARD}_{\mathrm{DART-Lux/SCOPE}}$:		
		PSI: 3.19%, PSII: 4.24%	PSI: 9.61%, PSII: 7.81%	PSI: 18.84%, PSII: 14.51%
$\theta_s = 31.46°$	$\phi_s = 69.88°$	$\mathrm{MARD}_{\mathrm{DART-Lux/DART-FT}}$:		
		PSI: 0.53%, PSII: 0.43%	PSI: 0.76%, PSII: 0.61%	PSI: 0.71%, PSII: 0.40%
		$\mathrm{MARD}_{\mathrm{DART-Lux/SCOPE}}$:		
		PSI: 4.04%, PSII: 4.30%	PSI: 10.04%, PSII: 8.03%	PSI: 16.78%, PSII: 12.87%
$\theta_s = 21.41°$	$\phi_s = 48.32°$	$\mathrm{MARD}_{\mathrm{DART-Lux/DART-FT}}$:		
		PSI: 0.88%, PSII: 0.63%	PSI: 0.92%, PSII: 0.67%	PSI: 0.29%, PSII: 0.27%
		$\mathrm{MARD}_{\mathrm{DART-Lux/DART-FT}}$:		
		PSI: 3.20%, PSII: 4.06%	PSI: 9.05%, PSII: 7.77%	PSI: 15.54%, PSII: 11.67%

355

Table 3. Maize field: input parameters and computational needs of DART-FT and DART-Lux.

		DART-FT	DART-Lux		
5 m spatial resolution, 451 spectral bands	Viewing direction	All	Nadir	θ_v=30°, ϕ_v=0°	θ_v=60°, ϕ_v=0°
	Computer time	1 h 31 min	1 h 7 min	1 h 9 min	1 h 2 min
	Samples per pixel	-	100	120	180
	Memory	51 GB	1.5 GB		
0.01 m spatial resolution, 36 spectral bands	Viewing direction	All	Nadir		
	Computer time	8 h 13 min	10 min 10 s		
	Samples per pixel	-	20		
	Memory	105.8 GB	8.2 GB		

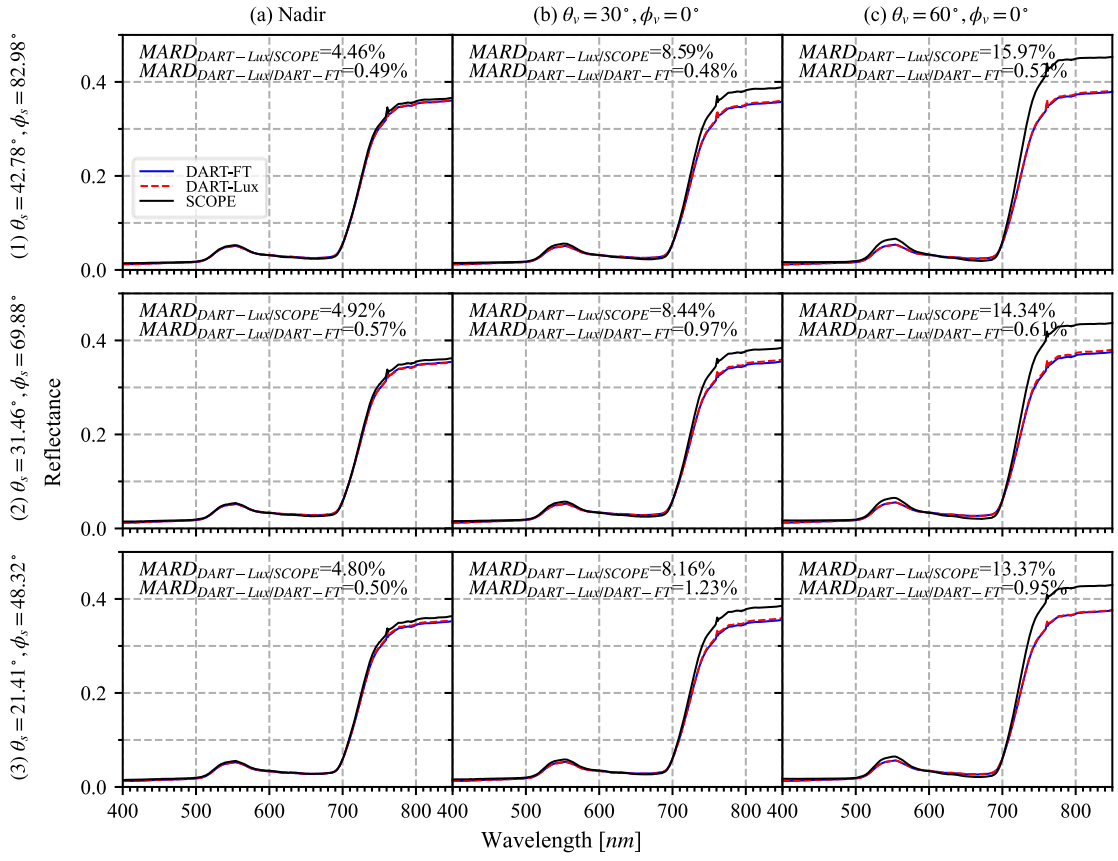

Figure 5. Maize field: DART-FT, DART-Lux and SCOPE reflectance for 3 solar directions and 3 viewing directions with no account of bioclimatology on SIF emission.

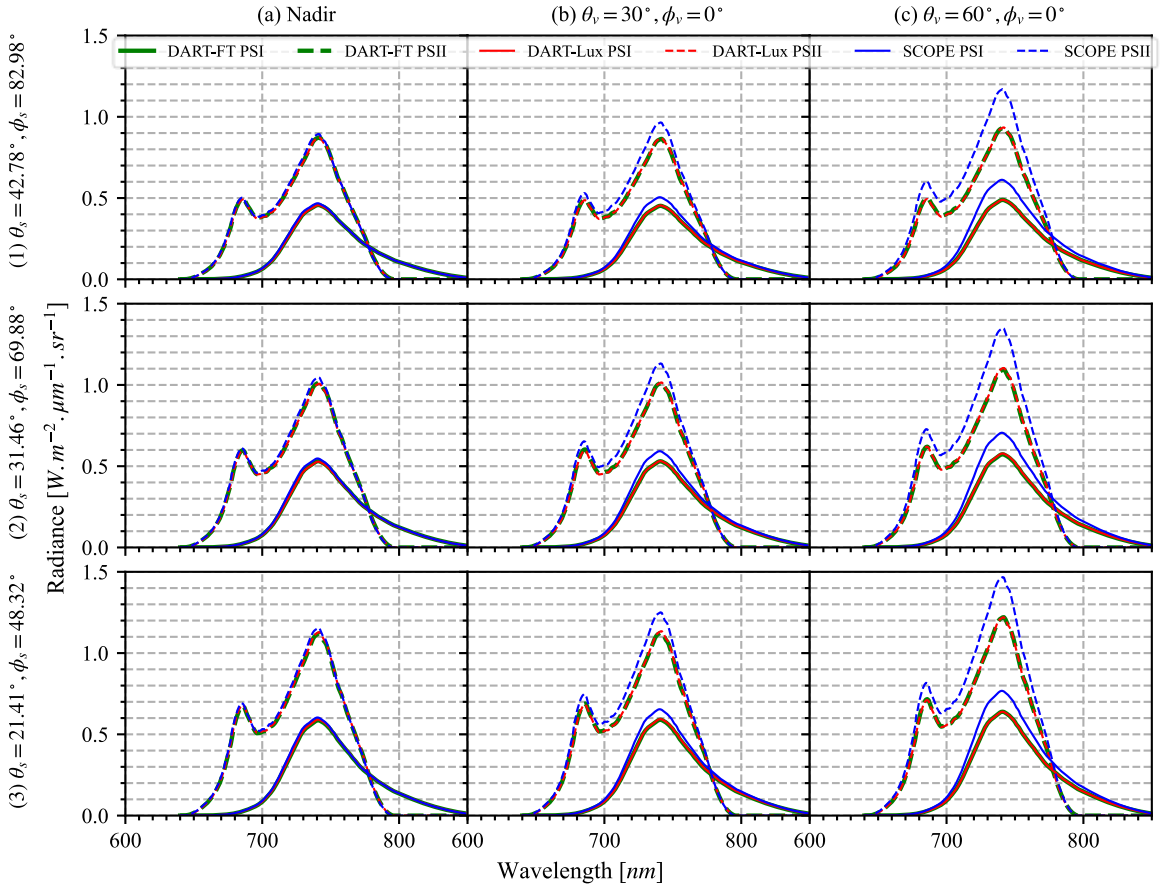

Figure 6: Maize field: DART-FT, DART-Lux and SCOPE SIF PSII and PSII radiance, for 3 solar directions and 3 viewing directions with no account of bioclimatology on SIF emission.

DART-FT and DART-Lux were also run using the η factors calculated by SCOPE with its default meteorological input parameters. Although these η factors should depend on the canopy 3D architecture, we made this approximation (*i.e.*, application of 1D information in a 3D model) because of the unavailability of 3D energy balance model. DART-Lux and DART-FT match as for the case "No energy balance": the MARD for canopy SIF radiance and for canopy reflectance (not shown here) keep the same order of magnitude. The differences with SCOPE are also similar.

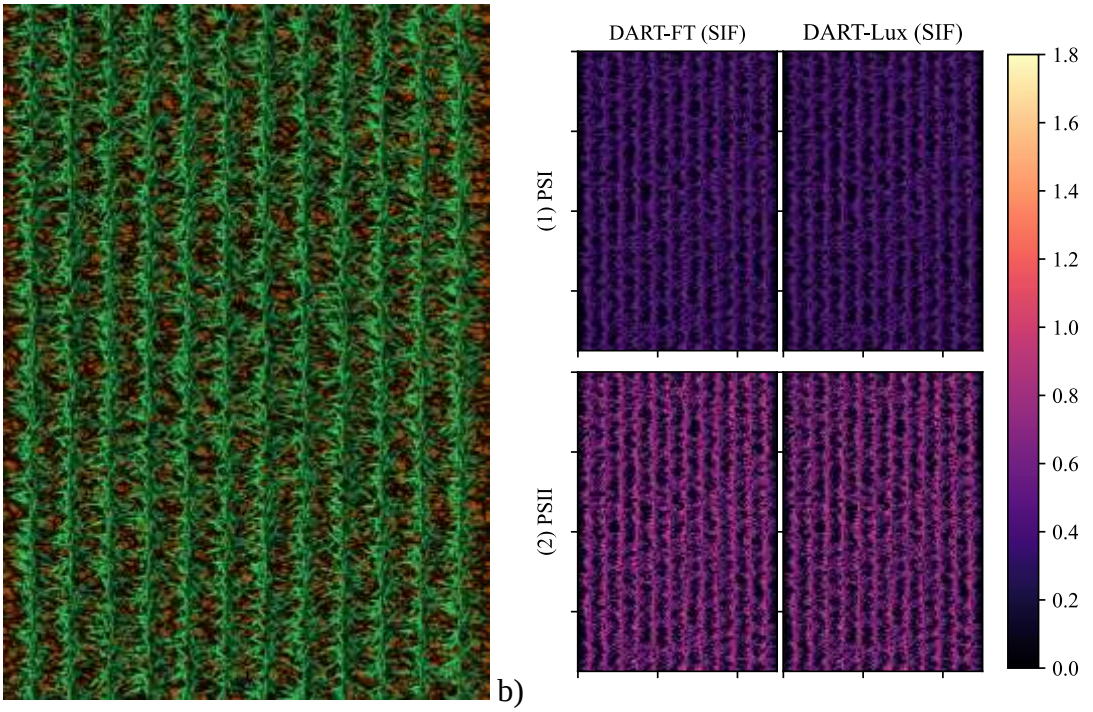

Figure 7. Maize field: nadir radiance images at 1 cm resolution ($W.m^{-2}.\mu m^{-1}.sr^{-1}$). a) DART-Lux RGB color composite. b) DART-FT and DART-Lux SIF (PSI and PSII). λ_c=765 nm, $\Delta\lambda$=1 nm.

IV.4 Trees plot simulation

The reflectance and SIF radiance of DART-Lux match DART-FT DART-FT (100 discrete directions, illumination step = 10^{-3} m), DART-Lux (17^2 scene repetitions, maximal scattering order = 15, Russian Roulette starts at order 12 with cut-off probability =0.5, 200 samples per pixel) (Figure 8): MARD is 0.27% for reflectance and less than 0.15% for SIF radiance, with memory need reduced by ~13 and computer time by more than 5 times (Table 4). Figure 9 shows the root mean square deviation (RMSD) of DART-Lux and DART-FT PSI and PSII radiance with the number of samples/pixel (*i.e.*, simulation time).

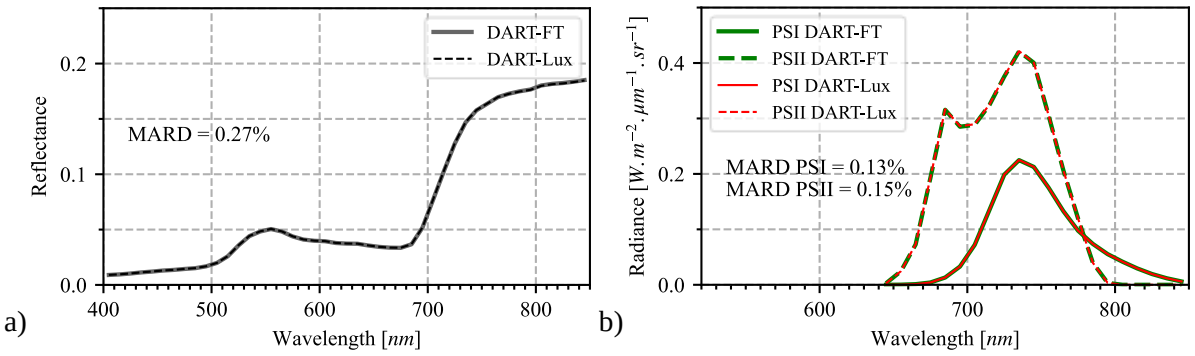

Figure 8. Tree plot: DART-Lux and DART-FT total (a) and PSI and PSII (b) nadir spectral radiance.

Table 4. Computational needs of DART-FT and DART-Lux for the tree plot simulation (spatial resolution: 0.1 m, 45 spectral bands)

	DART-FT	DART-Lux
Computer time	22 min	4 min
Memory	9.2 GB	0.715 GB

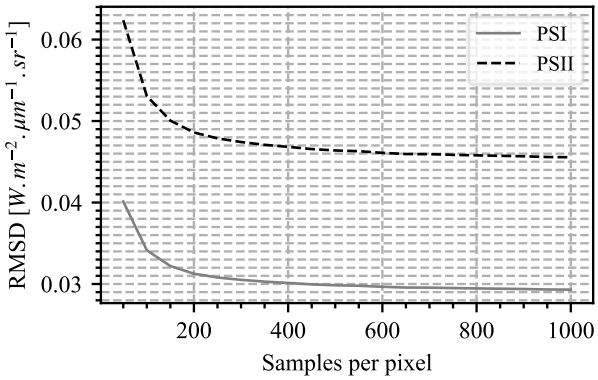

Figure 9. RMSD of the DART-Lux and DART-FT PSI and PSII radiance images at 765 nm as a function of the number of samples/pixel in DART-Lux.

Figure 10 shows the pixel-wise comparison of DART-FT and DART-Lux PSII images at 765 nm, for 200 samples/pixel and for 1000 samples/pixel. The pixel-wise MARD is computed by replacing the average on spectral bands by the average on the image pixels. The pixel-wise MARD for 200 samples/pixel (16.89%) is larger than for 1000 samples/pixel (13.88%). Inversely, the R^2 slightly increases from 200 samples/pixel to 1000 samples/pixel. The MARDs are much higher than the spectrally averaged MARD for the total scene (0.15%, Figure 8) in

particular because the images have many pixels. The MARDs and R^2 for PSI (not shown here) are nearly the same as for PSII.

Figure 11 shows DART-Lux images of the tree plot with 1000 samples/pixel. The SIF signal from the bare ground comes from the SIF radiation emitted by the vegetation that is scattered by the ground.

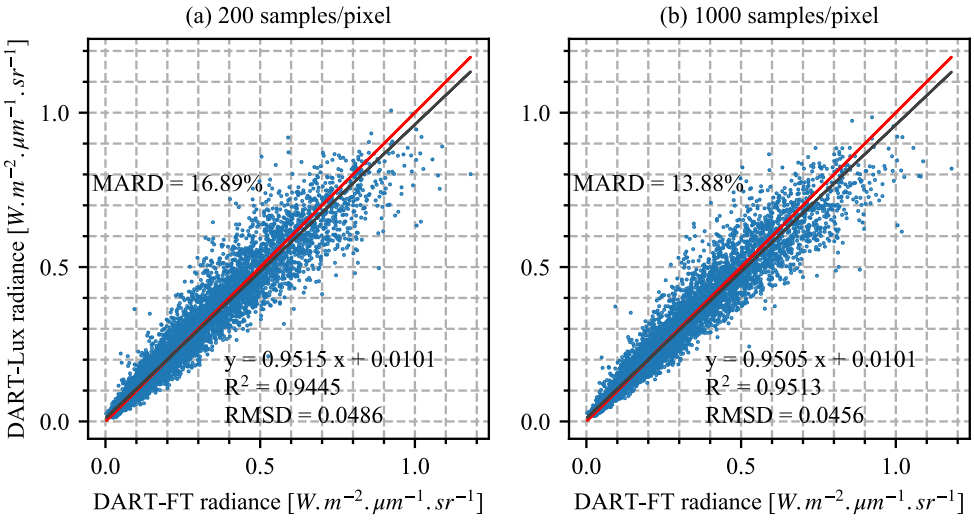

Figure 10. Pixel-wise comparison of DART-FT and DART-Lux PSII radiance images with samples/pixel = 200 (a) and 1000 (b). θ_s=30°, ϕ_s=225 °. $\lambda_c = 765\ nm, \Delta\lambda = 10\ nm$.

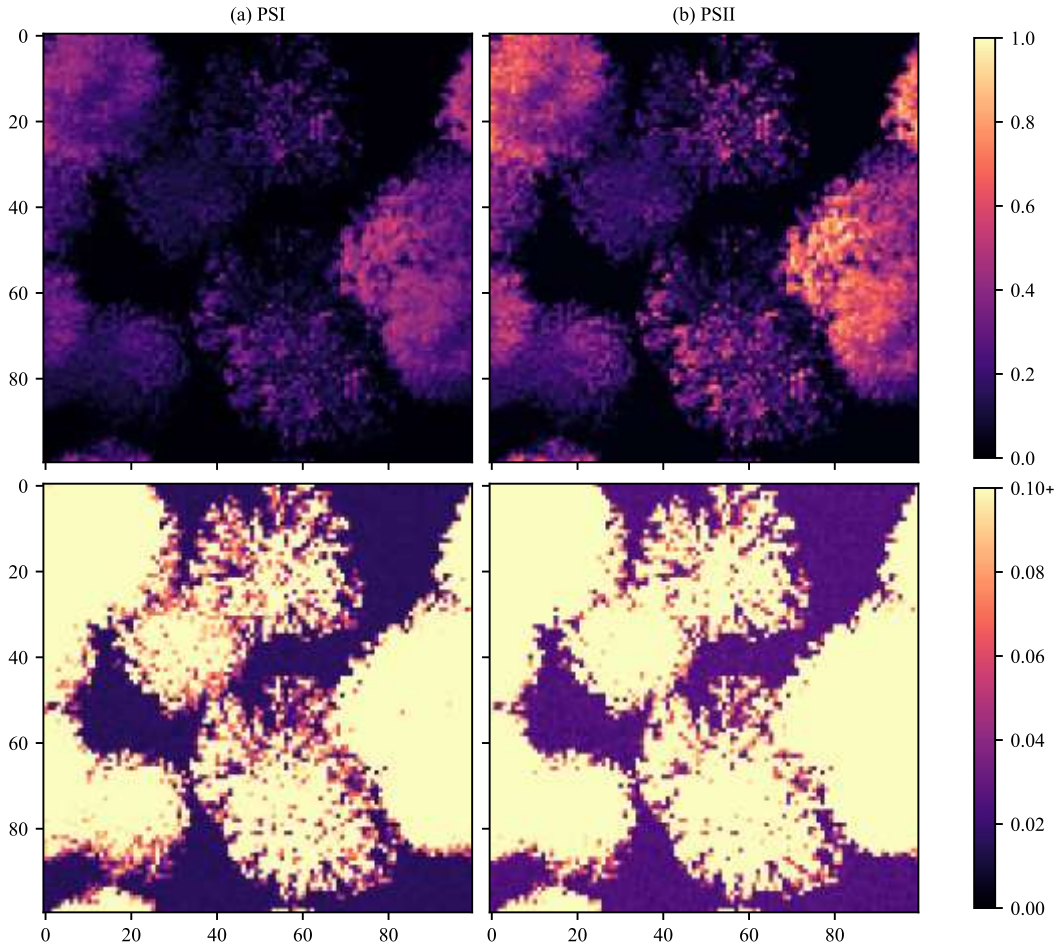

Figure 11. Tree plot: DART-Lux PSI and PSII SIF nadir radiance images ($W.m^{-2}.\mu m^{-1}.sr^{-1}$), with normal (top) and stretched (bottom) color scales. $\lambda_c = 765\ nm, \Delta\lambda = 10\ nm$.

V. Discussion

DART-FT and DART-Lux have different radiative transfer modelling strategies. DART-FT is determinist. It tracks radiation fluxes in N discrete directions that sub-divide the 4π space with an iterative approach that scatters at iteration $i+1$ radiation intercepted in iteration i (Gastellu-Etchegorry et al., 1996). DART-Lux is probabilistic. Indeed, it uses Monte-Carlo integration techniques to solve the LTE by sampling the possible light paths, evaluating their contributions, and giving higher importance weights to most likely paths (Wang et al., 2022).

For small scenes, DART-Lux and DART-FT SIF closely match, with relative difference always smaller than 2%. This difference is small enough to be explained by the parameters that drive the precision of DART-Lux (*e.g.*, number of samples/pixel) and DART-FT (*e.g.*, dimension of voxels, numbers of discrete directions, etc.). For these scenes, compared to

DART-FT, DART-Lux efficiency is not as pronounced as for larger sites as Ripperdan (Figure 12).

Homogeneous vegetation: DART-Lux closely matches DART-FT and also SCOPE to a lesser extent. Its relative differences are less than 1% with DART-FT, and ≈5% for SCOPE. Four major factors can explain that differences are higher for SCOPE. 1) SCOPE simulates radiative transfer with four fluxes and assumes the isotropy of downward and upward scattered radiation, which is not exact (except for the special case of exactly horizontal leaves). On the other hand, DART-FT uses many (here: 200) discrete directions, which allows an accurate representation of the anisotropy of the downward and upward scattered radiation. DART-Lux simulates this anisotropy even more accurately than DART-FT because it can track photons in any direction. 2) SCOPE discretizes the LAD with 13 leaf zenith angles, whereas DART-FT and DART-Lux randomly sample the LAD with a number of samples equal to the number of facets used to simulate the quasi-turbid medium. DART and SCOPE more closely match (results not shown here) by introducing into the code of SCOPE a more accurate LAD with 90 leaf zenith angles. 3) The quasi-turbid medium is not exactly the turbid medium of SCOPE because its facets cannot be infinitely small and infinitely numerous. 4) The application of the SCOPE η factors in SCOPE, on the one hand, and in DART-FT and DART-Lux, on the other hand, differs. Indeed, SCOPE applies vertical profiles of η factors to homogeneous layers and DART to facets with interpolations on the η. For this simulation, the η factors (*i.e.*, impact of local climatology) do not impact PSI SIF radiance and increase PSII radiance by ≈25%.

Maize field: the DART-FT and DART-Lux total and SIF radiance closely match and tend to be smaller than for SCOPE, especially for oblique viewing directions, with relative difference possibly larger than 25% for PSII in the NIR. This difference is explained by the canopy 3D architecture (3D maize plants, rows) with the clumping of the maize plants in DART, whereas for SCOPE, the vegetation is homogeneous which is more effective for intercepting radiation and therefore for SIF emission, and also for allowing the emitted SIF radiation to escape the canopy. The $\mathrm{MARD}_{\mathrm{DART-SCOPE}}$ exceeds 10% in most configurations and increases to reaches 18% for the oblique viewing angle $\theta_v = 60°$. Indees, in SCOPE simulations, radiation interception and therefore SIF emission occur mostly at the top layers of the canopy. When θ_v increases, the SIF seen by the sensor increases because the contribution of the top layers to the signal increases. Similarly, for the 3D maize scene, the SIF seen by the sensor from the plants

tends to increase when θ_v increases. However, in these simulations, this increase is less important than for 1D because the viewing direction is parallel to the maize rows and therefore the soil, that does not emit SIF, keeps to be seen by the sensor when θ_v increases. As with the homogeneous canopy, local bioclimatology (*i.e.*, η factors) greatly influences SIF emission, and therefore the canopy SIF radiance. Also, at 0.01m resolution, DART-Lux deduces by ≈50 the memory usage and simulation time of DART-FT.

Tree plot: the pixel-wise RMSE (Figure 9) of the DART-Lux and DART-FT SIF radiance images decreases with the number of samples/pixel in DART-Lux. This is explained by the decrease of the Monte Carlo noise in DART-Lux. For example, the pixel-wise MARD decreases from 16.89% for 200 samples/pixel down to 13.88% with 1000 samples/pixel. Here, convergence occurs for ≈ 1000 samples/pixel. The optimal number of samples/pixel depends on several factors including the expected accuracy on scene radiance, and the spatial extent and complexity of the studied landscape. The accuracy of the representation of the 3D landscape should also be considered.

Because Monte Carlo-based radiative transfer models are expected to be more accurate than discrete ordinate models, and because the BDPT algorithm is unbiased (Wang et al., 2022), the convergence of $RMSE_{DART\text{-}FT\text{-}DART\text{-}Lux}$ is probably an indication of the accuracy of DART-FT, with DART-Lux giving the exact value.

Results stress that the reduction of simulation time $CT_{FT/Lux}=\frac{\text{DART-FT computer time}}{\text{DART-Lux computer time}}$ of DART-Lux relative to DART-FT can be very important, especially for large and complex scenes. $CT_{FT/Lux}$≈5800 for the Ripperdan site. Indeed, the simulation time of DART-FT greatly increases with the number of facets, conversely to DART-Lux if the number of samples/pixel remains constant. Also, $CT_{FT/Lux}$ decreases with the number of simulated spectral bands. Indeed, the DART-FT forward flux tracking simulates SIF with vector-to-matrix products which gives a number of multiplication operations proportional to N^2, with N the number of spectral bands. On the other hand, because DART-Lux path tracing is bi-directional, for rays traced in the backward direction, the SIF emission is modelled by a matrix-to-matrix product which gives a number of multiplication operations proportional to N^3. In the absence of SIF simulation, $CT_{FT/Lux}$ is relatively independent of the number of spectral bands.

Because it usually needs much less RAM than DART-FT for complex scenes especially if it uses the cloning approach (Wang et al., 2022), DART-Lux is well adapted to large and complex landscapes for which DART-FT can be inoperative due to hardware constraints. Cloning can be used for elements of the simulated landscape are identical except for a geometric transformation: only a single 3D object and a specific geometric transformation (*i.e.*, spatial shift and scaling-rotation matrix) for each clone are stored in memory. Then, the memory needed in DART-Lux increases very little with the number of scene elements, conversely to DART-FT because a geometric transformation matrix usually needs much less memory than a 3D object. Moreover, for DART-Lux, the computation time does not increase a lot when the scene complexity (*i.e.*, total number of scene facets) increases since the algorithmic complexity of Monte Carlo methods depend only on the number of samples, conversely to DART-FT where the total number of tracked rays highly increases with scene complexity. This makes DART-Lux more computational efficiency for large landscapes, which may be impossible for DART-FT due to hardware limitations. This is illustrated by the $3 \times 3\ km^2$ SIF radiance image of Ripperdan (Figure 12). Indeed, its simulation only needed 42.9 GB of computer memory and 2 h 44 min of computation time for DART-Lux and was impossible for DART-FT.

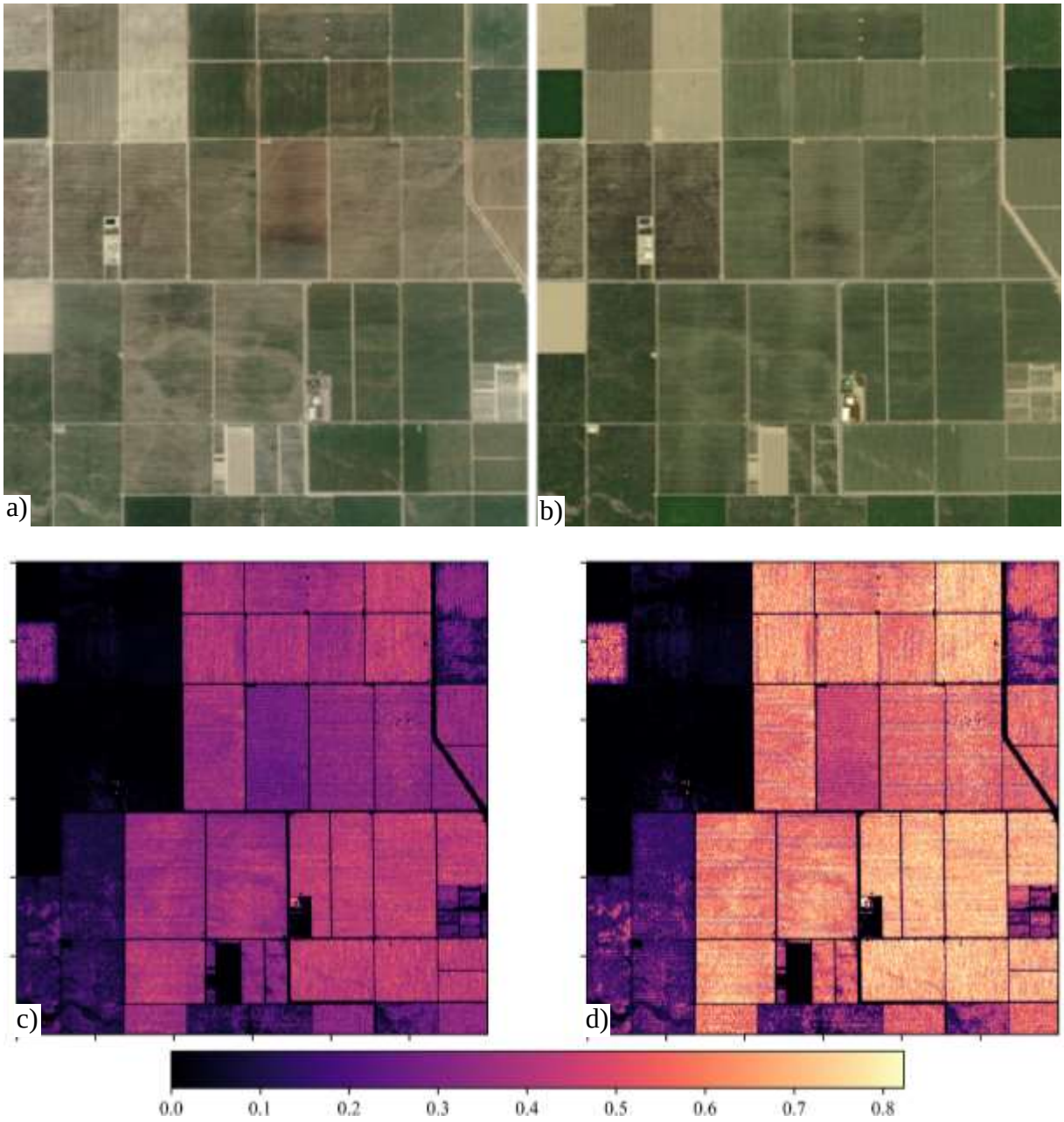

Figure 12. Ripperdan $3km \times 3km$ agricultural site (vineyards and trees), USA (36° 55' N, 119° 58' W). a) Google image used to create the DART-Lux's 3D scene. b) DART-Lux RGB color composite. DART-Lux PSI (c) and PSII (d) radiance images ($W/m^2/\mu m/sr$) at $760\ nm$ simulated with 100 bands in [0.4µm - 0.75µm]). SIF radiance is null for the road (top right), bare earth fields (top left) and built areas (bottom center). DART-Lux images are at 5m spatial resolution.

VI. Conclusion

We designed a new SIF radiative transfer modelling that adapts the equations governing the SIF emission to the Bidirectional Path Tracing (BDPT) algorithm (Veach, 1998) that constructs light paths from the light source and from the sensor. This is a novel SIF modelling approach. Indeed, apart from DART-Lux, to our knowledge, all Monte Carlo RT models that simulate SIF (*e.g.*, FLiES-SIF, FluorFLIGHT, FluorWPS, FluCVRT) use forward tracing, although the BDPT algorithm is more powerful for simulating SIF images. Adapting the BDPT algorithm to SIF modelling greatly improves the efficiency of DART for SIF images simulation, due to the efficiency of backward tracing, especially for sensors with narrow fields of view (Disney et al., 2000).

For that, we adapted the equations that allow to compute the SIF emission for the BDPT algorithms. The new equations allow to compute the radiance starting both from the light source and from the sensor, and to obtain the total signal (scattered + emitted SIF radiance) in addition to the SIF radiance components per photosystem separately. Simulations conducted with simple 3D canopies illustrated that DART-Lux and DART-FT SIF images have a good agreement. In addition, DART-Lux and 1D SCOPE gave similar total and SIF radiance values when using a very similar scene representation (*i.e.*, homogeneous turbid medium and quasi-turbid medium). They tend to greatly differ if the 3D architecture of the studied landscape is considered. To account for the effect of local climatological conditions (*e.g.*, leaf temperature) on leaf-level SIF emission, DART-Lux can be coupled with the 1D energy balance module of SCOPE by importing vertical profiles of η factors, similarly to DART-FT (Malenovský et al., 2021).

Compared to DART-FT, DART-Lux SIF modelling greatly decreases computational needs (*i.e.*, RAM and computer time). This decrease was ≈50 for the maize field with a spatial resolution equal to 0.01m, and was larger than 10^3 for the $3 \times 3\ km^2$ Ripperdan agricultural site zone. This makes DART a powerful model to simulate SIF images of large and complex landscapes, with many spectral bands. It opens new horizons for RS studies of vegetation. The novel SIF simulation in DART-Lux is already in the released DART versions (v1152 onwards) (https://dart.omp.eu).

Acknowledgements

This work was funded as the “Fluo3D” project by the TOSCA program of the French National Space Agency (Centre National d’Etudes Spatiales), and by the CNRS (Centre National de la Recherche Scientifique) through the 80|Prime program.

Appendix 1. Block matrices product

The product of the block matrices $M_1 = \begin{pmatrix} A_1 & B_1 & C_1 \\ 0 & D_1 & 0 \\ 0 & 0 & D_1 \end{pmatrix}$ and $M_2 = \begin{pmatrix} A_2 & B_2 & C_2 \\ 0 & D_2 & 0 \\ 0 & 0 & D_2 \end{pmatrix}$, with D_1 and D_2 diagonal matrices, is a block matrix with same form as M_1 and M_2:

$$M_1 \times M_2 = \begin{pmatrix} A_1 & B_1 & C_1 \\ 0 & D_1 & 0 \\ 0 & 0 & D_1 \end{pmatrix} \times \begin{pmatrix} A_2 & B_2 & C_2 \\ 0 & D_2 & 0 \\ 0 & 0 & D_2 \end{pmatrix} = \begin{pmatrix} A_1.A_2 & A_1B_2 + B_1D_2 & A_1C_2 + C_1D_2 \\ 0 & D_1D_2 & 0 \\ 0 & 0 & D_1D_2 \end{pmatrix}$$

with D_1D_2 a diagonal matrix.

References

Braghiere, R. K., Wang, Y., Doughty, R., Sousa, D., Magney, T., Widlowski, J.-L., Longo, M., Bloom, A. A., Worden, J., Gentine, P., & Frankenberg, C. (2021). Accounting for canopy structure improves hyperspectral radiative transfer and sun-induced chlorophyll fluorescence representations in a new generation Earth System model. *Remote Sensing of Environment*, *261*, 112497. https://doi.org/10.1016/j.rse.2021.112497

Cormen, T. H., Leiserson, C. E., Rivest, R. L., & Stein, C. (2009). *Introduction to Algorithms* (3rd ed.). MIT Press.

Damm, A., Guanter, L., Paul-Limages, E., Tol, C. van der, Hueni, A., Buchmann, N., Eugster, W., Ammann, C., & Schaepman, M. E. (2015). Far-red sun-induced chlorophyll fluorescence shows ecosystem - specific relationships to gross primary production: An assessment based on observational and modeling approaches. *Remote Sensing of Environment*, *166*, 91–105. https://doi.org/10.1016/j.rse.2015.06.004

Disney, M. I., Lewis, P., & North, P. R. J. (2000). Monte Carlo ray tracing in optical canopy reflectance modelling. *Remote Sensing Reviews*, *18*(2–4), 163–196. https://doi.org/10.1080/02757250009532389

Gastellu-Etchegorry, J.-P., Demarez, V., Pinel, V., & Zagolski, F. (1996). Modeling radiative transfer in heterogeneous 3-D vegetation canopies. *Remote Sensing of Environment*, *58*(2), 131–156. https://doi.org/10.1016/0034-4257(95)00253-7

Guanter, L., Zhang, Y., Jung, M., Joiner, J., Voigt, M., Berry, J. A., Frankenberg, C., Huete, A. R., Zarco-Tejada, P., Lee, J.-E., Moran, M. S., Ponce-Campos, G., Beer, C., Camps-Valls, G., Buchmann, N., Gianelle, D., Klumpp, K., Cescatti, A., Baker, J. M., & Griffis, T. J. (2014). Global and time-resolved monitoring of crop photosynthesis with chlorophyll fluorescence. *Proceedings of the National Academy of Sciences*, *111*(14), E1327–E1333. https://doi.org/10.1073/pnas.1320008111

Hernández-Clemente, R., North, P. R. J., Hornero, A., & Zarco-Tejada, P. J. (2017). Assessing the effects of forest health on sun-induced chlorophyll fluorescence using the FluorFLIGHT 3-D radiative transfer model to account for forest structure. *Remote Sensing of Environment*, *193*, 165–179. https://doi.org/10.1016/j.rse.2017.02.012

Hornero, A., North, P. R. J., Zarco-Tejada, P. J., Rascher, U., Martín, M. P., Migliavacca, M., & Hernandez-Clemente, R. (2021). Assessing the contribution of understory sun-induced chlorophyll fluorescence through 3-D radiative transfer modelling and field data. *Remote Sensing of Environment*, *253*, 112195. https://doi.org/10.1016/j.rse.2020.112195

Kallel, A. (2020). FluLCVRT: Reflectance and fluorescence of leaf and canopy modeling based on Monte Carlo vector radiative transfer simulation. *Journal of Quantitative Spectroscopy and Radiative Transfer*, *253*, 107183. https://doi.org/10.1016/j.jqsrt.2020.107183

Kalos, M. H., & Whitlock, P. A. (1986). *Monte Carlo methods. Vol. 1: Basics*. Wiley-Interscience.

Liu, W., Atherton, J., Mõttus, M., Gastellu-Etchegorry, J.-P., Malenovský, Z., Raumonen, P., Åkerblom, M., Mäkipää, R., & Porcar-Castell, A. (2019). Simulating solar-induced chlorophyll fluorescence in a boreal forest stand reconstructed from terrestrial laser scanning measurements. *Remote Sensing of Environment*, *232*, 111274. https://doi.org/10.1016/j.rse.2019.111274

Liu, W., Luo, S., Lu, X., Atherton, J., & Gastellu-Etchegorry, J.-P. (2020). Simulation-Based Evaluation of the Estimation Methods of Far-Red Solar-Induced Chlorophyll Fluorescence Escape Probability in Discontinuous Forest Canopies. *Remote Sensing*, *12*(23), Article 23. https://doi.org/10.3390/rs12233962

Liu, X., Guanter, L., Liu, L., Damm, A., Malenovský, Z., Rascher, U., Peng, D., Du, S., & Gastellu-Etchegorry, J.-P. (2019). Downscaling of solar-induced chlorophyll fluorescence from canopy level to photosystem level using a random forest model. *Remote Sensing of Environment*, *231*, 110772. https://doi.org/10.1016/j.rse.2018.05.035

Malenovský, Z., Regaieg, O., Yin, T., Lauret, N., Guilleux, J., Chavanon, E., Duran, N., Janoutová, R., Delavois, A., Meynier, J., Medjdoub, G., Yang, P., van der Tol, C., Morton, D., Cook, B. D., & Gastellu-Etchegorry, J.-P. (2021). Discrete anisotropic radiative transfer modelling of solar-induced chlorophyll fluorescence: Structural impacts in geometrically explicit vegetation canopies. *Remote Sensing of Environment*, *263*, 112564. https://doi.org/10.1016/j.rse.2021.112564

Miller, J. (2005). *Development of a Vegetation Fluorescence Canopy Model*.

Mohammed, G. H., Colombo, R., Middleton, E. M., Rascher, U., van der Tol, C., Nedbal, L., Goulas, Y., Pérez-Priego, O., Damm, A., Meroni, M., Joiner, J., Cogliati, S., Verhoef, W., Malenovský, Z., Gastellu-Etchegorry, J.-P., Miller, J. R., Guanter, L., Moreno, J., Moya, I., … Zarco-Tejada, P. J. (2019). Remote sensing of solar-induced chlorophyll fluorescence (SIF) in vegetation: 50 years of progress. *Remote Sensing of Environment*, *231*, 111177. https://doi.org/10.1016/j.rse.2019.04.030

Nicodemus, F. E. (Fred E. (1978). *Self-study manual on optical radiation measurements: Part I--Concepts, Chapters 4 and 5*. National Bureau of Standards (U.S.). http://archive.org/details/selfstudymanualo9102nico

Pharr, M., Jakob, W., & Humphreys, G. (2016). *Physically Based Rendering: From Theory to Implementation* (3rd ed.). Morgan Kaufmann Publishers Inc.

Porcar-Castell, A., Tyystjärvi, E., Atherton, J., van der Tol, C., Flexas, J., Pfündel, E. E., Moreno, J., Frankenberg, C., & Berry, J. A. (2014). Linking chlorophyll a fluorescence to photosynthesis for remote sensing applications: Mechanisms and challenges. *Journal of Experimental Botany*, *65*(15), 4065–4095. https://doi.org/10.1093/jxb/eru191

Regaieg, O., Yin, T., Malenovský, Z., Cook, B. D., Morton, D. C., & Gastellu-Etchegorry, J.-P. (2021). Assessing impacts of canopy 3D structure on chlorophyll fluorescence radiance and radiative budget of deciduous forest stands using DART. *Remote Sensing of Environment*, *265*, 112673. https://doi.org/10.1016/j.rse.2021.112673

Rosema, A., Verhoef, W., Schroote, J., & Snel, J. F. H. (1991). Simulating fluorescence light-canopy interaction in support of laser-induced fluorescence measurements. *Remote Sensing of Environment*, *37*(2), 117–130. https://doi.org/10.1016/0034-4257(91)90023-Y

Sakai, Y., Kobayashi, H., & Kato, T. (2020). FLiES-SIF version 1.0: Three-dimensional radiative transfer model for estimating solar induced fluorescence. *Geoscientific Model Development*, *13*(9), 4041–4066. https://doi.org/10.5194/gmd-13-4041-2020

Song, L., Guanter, L., Guan, K., You, L., Huete, A., Ju, W., & Zhang, Y. (2018). Satellite sun-induced chlorophyll fluorescence detects early response of winter wheat to heat

642 stress in the Indian Indo-Gangetic Plains. *Global Change Biology*, *24*(9), 4023–4037.
643 https://doi.org/10.1111/gcb.14302

644 van der Tol, C., Verhoef, W., Timmermans, J., Verhoef, A., & Su, Z. (2009). An integrated
645 model of soil-canopy spectral radiances, photosynthesis, fluorescence, temperature
646 and energy balance. *Biogeosciences*, *6*(12), 3109–3129. https://doi.org/10.5194/bg-6-
647 3109-2009

648 Veach, E. (1998). *Robust monte carlo methods for light transport simulation* [Phd]. Stanford
649 University.

650 Veach, E., & Guibas, L. J. (1995). Optimally combining sampling techniques for Monte Carlo
651 rendering. *Proceedings of the 22nd Annual Conference on Computer Graphics and*
652 *Interactive Techniques*, 419–428. https://doi.org/10.1145/218380.218498

653 Verhoef, W. (1984). Light scattering by leaf layers with application to canopy reflectance
654 modeling: The SAIL model. *Remote Sensing of Environment*, *16*(2), 125–141.
655 https://doi.org/10.1016/0034-4257(84)90057-9

656 Verrelst, J., Malenovsky, Z., Tol, C. van der, Camps-Valls, G., Gastellu-Etchegorry, J.-P.,
657 Lewis, P., North, P., & Moreno, J. (2019). Quantifying Vegetation Biophysical
658 Variables from Imaging Spectroscopy Data: A Review on Retrieval Methods. *Surveys*
659 *in Geophysics*, *40*(3), 589–629. https://doi.org/10.1007/s10712-018-9478-y

660 Vilfan, N., van der Tol, C., Muller, O., Rascher, U., & Verhoef, W. (2016). Fluspect-B: A
661 model for leaf fluorescence, reflectance and transmittance spectra. *Remote Sensing of*
662 *Environment*, *186*, 596–615. https://doi.org/10.1016/j.rse.2016.09.017

663 Vilfan, N., Van der Tol, C., Yang, P., Wyber, R., Malenovský, Z., Robinson, S. A., &
664 Verhoef, W. (2018). Extending Fluspect to simulate xanthophyll driven leaf
665 reflectance dynamics. *Remote Sensing of Environment*, *211*, 345–356.
666 https://doi.org/10.1016/j.rse.2018.04.012

667 Wang, Y., Kallel, A., Yang, X., Regaieg, O., Lauret, N., Guilleux, J., Chavanon, E., &
668 Gastellu-Etchegorry, J.-P. (2022). DART-Lux: An unbiased and rapid Monte Carlo
669 radiative transfer method for simulating remote sensing images. *Remote Sensing of*
670 *Environment*, *274*, 112973. https://doi.org/10.1016/j.rse.2022.112973

Wang, Y., Lauret, N., & Gastellu-Etchegorry, J.-P. (2020). DART radiative transfer modelling for sloping landscapes. *Remote Sensing of Environment*, *247*, 111902. https://doi.org/10.1016/j.rse.2020.111902

Yang, P., Verhoef, W., & van der Tol, C. (2017). The mSCOPE model: A simple adaptation to the SCOPE model to describe reflectance, fluorescence and photosynthesis of vertically heterogeneous canopies. *Remote Sensing of Environment*, *201*, 1–11. https://doi.org/10.1016/j.rse.2017.08.029

Zhang, Z., Zhang, Y., Porcar-Castell, A., Joiner, J., Guanter, L., Yang, X., Migliavacca, M., Ju, W., Sun, Z., Chen, S., Martini, D., Zhang, Q., Li, Z., Cleverly, J., Wang, H., & Goulas, Y. (2020). Reduction of structural impacts and distinction of photosynthetic pathways in a global estimation of GPP from space-borne solar-induced chlorophyll fluorescence. *Remote Sensing of Environment*, *240*, 111722. https://doi.org/10.1016/j.rse.2020.111722

Zhao, F., Dai, X., Verhoef, W., Guo, Y., van der Tol, C., Li, Y., & Huang, Y. (2016). FluorWPS: A Monte Carlo ray-tracing model to compute sun-induced chlorophyll fluorescence of three-dimensional canopy. *Remote Sensing of Environment*, *187*, 385–399. https://doi.org/10.1016/j.rse.2016.10.036

3.2 Vegetation simulated as turbid medium

The LuxCoreRender software can simulate the propagation of radiation in volumes filled with fluids. It uses the Schlick phase function in order to approximate the Henyey-Greenstein phase function commonly used in DART for simulating scattering by aerosols in the atmosphere. The Schlick phase function is more convenient for computer graphics because it is faster to compute, although it is less accurate. Based on this implementation, I introduced into DART-Lux (1) the double Henyey-Greenstein and the Rayleigh scattering phase functions in order to simulate radiation propagation in fluids, as in DART-FT, then (2) turbid vegetation modeling, including SIF modeling. The modeling approach is presented below, after the introduction of the Light Transport Equation generalized for scenes containing surfaces and scattering media volumes.

3.2.1 Modeling approach

Generalized Light Transport Equation

The surface form of the Light Transport Equation gives the radiance reaching a vertex p from a surface A, after being scattered at a vertex p' on a surface Σ (here, emission is omitted):

$$L(p' \to p) = \int_A f(p'' \to p' \to p).L(p'' \to p').G(p'' \leftrightarrow p').dA(p'') \quad (3.1)$$

with $G(p'' \leftrightarrow p') = V(p'' \leftrightarrow p').\frac{|cos\theta_0''|.|cos\theta_i'|}{||p'-p''||^2}$,

$f(p'' \to p' \to p)$: BSDF of surface Σ,

$L(p'' \to p')$: radiance reaching p'' from p',

V: binary visibility function,

$cos\theta_0'' = \overrightarrow{n''}.\frac{\overrightarrow{p''p'}}{||p'-p''||}$, $cos\theta_i' = \frac{\overrightarrow{p''p'}}{||p'-p''||}\overrightarrow{n'}$,

$\overrightarrow{n'}$ and $\overrightarrow{n''}$: normal vectors to the surface Σ at p' and to the surface A at p'' respectively.

To allow the simulation of volumes, the Light Transport Equation is generalized for scenes including scattering surfaces and volume scattering media:

$$L(p' \to p) = \int_A \hat{f}(p'' \to p' \to p).L(p'' \to p').\hat{G}(p'' \leftrightarrow p').dA(p'') \quad (3.2)$$

with $\hat{f}(p'' \to p' \to p) = \begin{cases} \frac{\sigma_s}{\sigma_s+\sigma_a}.p_s(p'' \to p' \to p), & \text{if } p' \text{is a volume vertex} \\ f(p'' \to p' \to p), & \text{if } p' is \text{ a surface vertex} \end{cases}$

σ_s, and σ_a: scattering and absorption extinction coefficients of the volume,

$p_s(p'' \to p' \to p)$: normalized scattering phase function of the volume,

$\hat{G}(p'' \leftrightarrow p') = V(p'' \leftrightarrow p').Tr(p' \to p'').\frac{C(p',p'').C(p'',p')}{||p'-p''||^2}$,

$Tr(p' \to p'')$: path transmittance between p' and p'',

$C(p,p') = \begin{cases} \left|\overrightarrow{n_p}.\frac{\overrightarrow{pp'}}{||p-p'||}\right|, \text{if } p \text{ is a surface vertex} \\ 1, \text{if } p \text{ is a volume vertex} \end{cases}$.

Monte-Carlo path tracing (Fluids analogy)

In radiative transfer theory, fluids are usually assumed to have a sufficiently high particle density to be treated statistically using the Beer law. Also, the density of particles is assumed not to be too large in order to ensure that the absorbance of the fluid is proportional to the fluid density. Because the turbid medium model is similar to the fluid model, and because the fluids are simpler to treat using their analytical phase functions in the frame of Monte-Carlo path tracing, fluids modeling is presented first, then, turbid modeling is derived from it.

Monte-Carlo path tracing aims to randomly sample light paths by ensuring that the most probable paths have higher chances to be sampled. For fluid volumes, this is done in two steps:

a) Sampling a traveling distance

A ray entering a fluid volume is partly transmitted. The Beer law gives the direct transmittance:

$$T_t(\Delta L) = e^{-\sigma_t.\Delta L} \quad (3.3)$$

with ΔL the travel distance and $\sigma_t = \sigma_s + \sigma_a$ the total extinction coefficient (m^2 of interceptor / m^3). σ_t is the sum of scattering and absorption extinction coefficients. Here, it is assumed to be isotropic.

Complementarily, the probability that a ray is intercepted after a travel distance less or equal than ΔL is $1 - T_t(\Delta L)$. It is the Cumulative Distribution Function (CDF) $P_{\sigma_t}(\Delta L)$ that an

interception occurs at a distance $l \leq \Delta L$, which is the integral of the Probability Density Function (PDF) $p_{\sigma_t}(l)$ that an interception occurs at a distance l per distance unit:

$$P_{\sigma_t}(\Delta L) = \int_0^{\Delta L} p_{\sigma_t}(l).dl = 1 - e^{-\sigma_t.\Delta L} \tag{3.4}$$

$$p_{\sigma_t}(l) = \frac{dP_{\sigma_t}(l)}{dl} = \sigma_t.e^{-\sigma_t.l} \tag{3.5}$$

Sampling $p_{\sigma_t}(l)$ gives a sampled travel distance Δl in the medium. The inversion method (cf. Appendix 3-1) is used to draw a random sample u from a given PDF $p(x)$: the inverse function of its CDF is applied to a random number ξ uniformly sampled between 0 and 1. Hence, the travel distance Δl through the medium is sampled using a random number $\xi \sim \mathcal{U}([0,1])$:

$$\Delta l = P_{\sigma_t}^{-1}(\xi) = -\frac{\ln(1-\xi)}{\sigma_t} \tag{3.6}$$

If $\Delta l < \Delta L$, with ΔL the pathlength needed by the ray to exit the medium, the ray is scattered after the pathlength Δl. If $\Delta l > \Delta L$, the ray is transmitted through the medium.

In fluids, the extinction coefficients usually vary with the wavelength. For a multiband ray, Δl is sampled using the spectral average $\bar{\sigma}_t$ over all bands. Then, if a ray is intercepted (i.e., $\Delta l < \Delta L$), its transmittance $Tr_{ray,int}$ is null for all spectral bands, and if a ray is transmitted ($\Delta l \geq \Delta L$), its transmittance $Tr_{ray,trans}$ is 1 for all spectral bands. The expected value of the transmittance for all spectral bands can be written:

$$E[Tr(\bar{\sigma}_t, \Delta L)] = \int_0^{\Delta L} 0.p_{\bar{\sigma}_t}(l)dl + \int_{\Delta L}^{+\infty} 1.p_{\bar{\sigma}_t}(l)dl = e^{-\bar{\sigma}_t.\Delta L} \tag{3.7}$$

The obtained expected transmittance is a transmittance corresponding to the averaged $\bar{\sigma}_t$ for all spectral bands. A transmittance correction factor $f = \frac{e^{-\sigma_t.\Delta L}}{e^{-\bar{\sigma}_t.\Delta L}}$ is applied per spectral band in order to get the correct expected transmittance for each spectral band:

$$E[Tr(\bar{\sigma}_t, \sigma_t, \Delta L)] = \int_{\Delta L}^{+\infty} \frac{e^{-\sigma_t.\Delta L}}{e^{-\bar{\sigma}_t.\Delta L}}.p_{\bar{\sigma}_t}(l)dl = \frac{e^{-\sigma_t.\Delta L}}{e^{-\bar{\sigma}_t.\Delta L}}.e^{-\bar{\sigma}_t.\Delta L} = e^{-\sigma_t.\Delta L} \tag{3.8}$$

If an interception occurs, the intercepted ray is scattered with a radiance multiplied by the albedo $\frac{\sigma_s}{\bar{\sigma}_t}$ because part of the intercepted ray is absorbed.

For turbid medium, the extinction coefficient $\sigma_t(\Omega_s)$ depends on the incident direction. It is isotropic only if the Leaf Angular Distribution is spherical:

$$\sigma_t(\Omega_s) = G(\Omega_s).u_l \tag{3.9}$$

with $G(\Omega_s) = \int_0^{\frac{\pi}{2}} \frac{g(\theta_l)}{2\pi} \int_0^{2\pi} |\Omega_l.\Omega_s|.d\phi_l.sin\theta_l.d\theta_l$,

u_l the leaf volume density and

$\frac{g(\theta_l)}{2\pi}$ the Leaf Angular Distribution function.

The PDF of interception and scattering of a ray after a travel path l through the medium is:

$$p(l, \Omega_s) = G(\Omega_s).u_l.e^{-G(\Omega_s).u_l.l} \tag{3.10}$$

The extinction coefficient σ_t=G$(\Omega_s).u_l$ does not depend on wavelength. Hence, the transmittance correction factor f applied for fluids is not needed.

Being a function of the direction Ω_s, the term G must be computed per traced direction. Because its computation on the fly is computationally expensive, G is precomputed for N discrete directions. Then, since any direction can be sampled, G is interpolated using the values for the directions that neighbor the sampled direction. If a volume contains several types of turbid/fluid medium, the sampling of distance is done using an equivalent extinction coefficient that is the sum of the extinction coefficients of all the elements in the volume.

Radiation reflected by vegetation covers has usually a sharp maximum in the retro-illumination direction. Indeed, shadows cast by the leaves in the incident direction cannot be seen in this direction because they are hidden by the leaves themselves. For directions close to the retro-illumination direction, shadows can be observed, which usually translates in a decrease of reflectance. This is known as the hot spot effect. The approach of Kuusk, (1985) is widely used to model the hot spot effect. In the standard DART model (*i.e.*, DART-FT), Gastellu-Etchegorry et al. (1996) adapted the approach of Kuusk (1985) to finite dimensions turbid cells. Although some hot spot models are more accurate (Gobron et al., 1997; Kallel & Nilson, 2013), the Kuusk model is selected for DART-Lux because of its simplicity and adaptability to the Monte Carlo method. For example, Antyufeev & Marshak (1990) used it in their Monte Carlo model. DART-FT also uses it, which eases comparison with DART-Lux.

For a viewing direction Ω_v such that $\Omega_s.\Omega_v$<0 and a path length Δl, the transmittance is no longer $Tr(\Delta l, \Omega_v) = e^{-u_l.G(\Omega_v).\Delta l}$. It is (cf. Appendix 3-2):

$$Tr(\Delta l, \Omega_s \rightarrow \Omega_v) \quad = e^{-u_l.G(\Omega_v).(\Delta l+\frac{\beta}{\alpha}(e^{-\alpha.\Delta l}-1))} = e^{-\zeta.\varphi(\Delta l)} \tag{3.11}$$

with: $\alpha=\frac{\Delta(\Omega_s,\Omega_v).|\mu_v|}{S_l}$, $\beta=\sqrt{\frac{G(\Omega_s).|\mu_v|}{G(\Omega_v).|\mu_s|}}$, $\Delta(\Omega_s,\Omega_v)=\sqrt{\frac{1}{\mu_v^2}+\frac{1}{\mu_s^2}+\frac{2.\Omega_s.\Omega_v}{|\mu_s.\mu_v|}}$, $\mu_s=\cos\theta_s$, $\mu_v=\cos\theta_v$,

$s_l=\frac{\pi.d_l.G(\Omega_v)}{4.\mu_v.\int_{2\pi}\int_{\frac{\pi}{2}}\frac{g(\Omega_l)}{2\pi}.\frac{\sin\theta_l.d\theta_l.d\phi_l}{\sqrt{1+\tan^2\theta_l.\sin^2\theta_l}}}$, d_l the leaf dimension, u_l the leaf volume density.

$\zeta= u.G(\Omega_v)$, and $\phi(\Delta l)=\Delta l+\frac{\beta}{\alpha}(e^{-\alpha.\Delta l}\text{-}1)$, which is positive because $Tr(\Delta l, \Omega_s \rightarrow \Omega_v) \leqslant 1$.

With the notation $x = \phi(\Delta l)$, the transmittance is written:

$$Tr(x, \Omega_s \rightarrow \Omega_v) = e^{-\zeta.x} \tag{3.12}$$

The PDF of the random variable X for sampling x in $Tr(x, \Omega_s \rightarrow \Omega_v)$ is:

$$p_X(x) = \zeta.e^{-\zeta.x} \tag{3.13}$$

The CDF of the random variable X is:

$$P_X(x) = 1 - e^{-\zeta.x} \tag{3.14}$$

The CDF of the random variable L, for sampling a travel distance l in the hot spot configuration, knowing that the function ϕ is strictly increasing in the range of interest (cf. Appendix 3-3), is:

$$P_L(l) = p(L \leq l) = P\big(X \leq \phi(l)\big) = P_X\big(\phi(l)\big) = \zeta.e^{-\zeta.\phi(l)} \tag{3.15}$$

The PDF of the random variable L is then:

$$p_L(l) = \frac{dP_L(l)}{dl} = -\frac{d\phi(l)}{dl}.\zeta^2.e^{-\zeta.\phi(l)} \tag{3.16}$$

To sample l, with $\xi \sim \mathcal{U}([0,1])$

$$x = \phi(l) = -\frac{\ln(1-\xi)}{\zeta} \leftrightarrow l = \phi^{-1}\left(-\frac{\ln(1-\xi)}{\zeta}\right) \tag{3.17}$$

The expression of ϕ^{-1} is computed in Appendix 3-3.

b) Sampling a scattering direction

The scattering direction is sampled according to the scattering phase function $p(\mu)$, which is the angular distribution of scattered radiation, with $\mu=\cos\theta$ and θ the angle between the incident and outgoing directions. The sampled direction is defined by 2 angles: the angle θ between the incident and outgoing rays, and an azimuthal angle φ in the plane perpendicular to

the scattered direction. If the scattering phase function is azimuthally symmetric (*i.e.*, depends only on θ), the scattering direction is sampled as:

$$\begin{cases} \cos\theta = P^{-1}(\xi_1) \\ \varphi = 2.\pi.\xi_2 \end{cases} \tag{3.18}$$

with $P(x) = \int_{-1}^{x} p(\mu)d\mu$ the CDF, $\xi_1 \sim \mathcal{U}([0,1])$ and $\xi_2 \sim \mathcal{U}([0,1])$.

- **Henyey-Greenstein phase function**

$$\frac{p(\theta)}{2\pi} = \frac{1}{4\pi}.\frac{1-g^2}{[1+g^2-2.g.\cos(\theta)]^{\frac{3}{2}}} \tag{3.19}$$

This phase function is normalized:

$$\int_0^{2\pi}\int_0^{\pi} \frac{p(\theta)}{2\pi}.\sin(\theta)\,d\theta\,d\varphi = 1 \tag{3.20}$$

with the asymmetry parameter $g \in]-1,1[$. It is negative for backward scattering, positive for forward scattering, and null for isotropic scattering.

It can be written as a function of $\mu = \cos(\theta)$:

$$p(\mu) = \frac{1}{2}.\frac{1-g^2}{[1+g^2-2.g.\mu]^{\frac{3}{2}}} \tag{3.21}$$

Then, we have:

$$\int_{-1}^{1} p(\mu)d\mu = 1 \tag{3.22}$$

To sample $\mu = \cos(\theta)$ from $p(\mu)$, we compute the cumulated density function:

$$P(x) = \int_{-1}^{x} p(\mu)d\mu = \begin{cases} \frac{1-g^2}{2g}\left[(1+g^2-2gx)^{-\frac{1}{2}} - \frac{1}{1+g}\right], & \text{if } g \neq 0 \\ \frac{x+1}{2}, & if\ g = 0 \end{cases} \tag{3.23}$$

The value of μ that is sampled is:

$$\mu = P^{-1}(\xi), \qquad \xi \sim \mathcal{U}([0,1])$$

$$\mu = \begin{cases} \frac{1}{2g}.\left[1+g^2-\left(\frac{1-g^2}{1-g+2.g.\xi}\right)^2\right], & \text{if } g \neq 0 \\ 2.\xi - 1, & \text{if } g = 0 \end{cases} \tag{3.24}$$

- **Double Henyey-Greenstein phase function**

It is a weighted sum of two Henyey-Greenstein phase functions.

$$\frac{p(\theta)}{2\pi} = a.\frac{1}{4\pi}.\frac{1-g_1^2}{[1+g_1^2-2.g_1.cos(\theta)]^{\frac{3}{2}}} + (1-a).\frac{1}{4\pi}.\frac{1-g_2^2}{[1+g_2^2-2.g_2.cos(\theta)]^{\frac{3}{2}}} \quad (3.25)$$

with $a \in [0,1]$. Usually, forward scattering is larger than backward scattering, which corresponds to a > 0.5. It can be sampled using random numbers $\xi_1 \sim \mathcal{U}([0,1])$ and $\xi_2 \sim \mathcal{U}([0,1])$:

If $\xi_1 < a$,

$$\mu = \begin{cases} \frac{1}{2g_1}.\left[1+g_1^2-\left(\frac{1-g_1^2}{1-g_1+2.g_1.\xi_2}\right)^2\right], & \text{if } g_1 \neq 0 \\ 2.\xi_2 - 1, & \text{if } g_1 = 0 \end{cases} \quad (3.26)$$

Else

$$\mu = \begin{cases} \frac{1}{2g_2}.\left[1+g_2^2-\left(\frac{1-g_2^2}{1-g_2+2.g_2.\xi_2}\right)^2\right], & \text{if } g_2 \neq 0 \\ 2.\xi_2 - 1, & \text{if } g_2 = 0 \end{cases} \quad (3.27)$$

Figure 3-1 shows a test of this sampling method for the case a = 0.75, g_1 = 0.3, g_2 = -0.3.

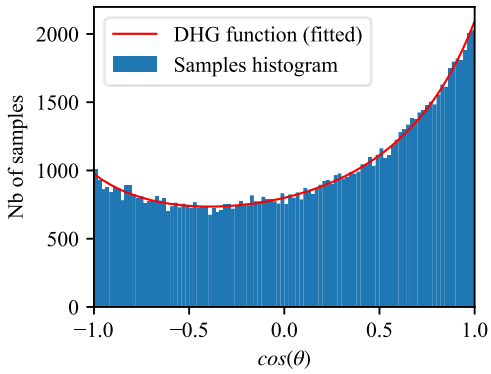

Figure 3-1: Double Henyey-Greenstein phase function sampling test: histogram of 10^5 samples and its fitted function (a = 0.75, g_1 = 0.3, g_2 = -0.3)

- **Rayleigh phase function**

The general form of the Rayleigh scattering phase function is:

$$\frac{p(\theta)}{2\pi} = \frac{1}{4\pi}.[A.(1+\cos^2(\theta)) + C] \quad (3.28)$$

The sampling method for the Rayleigh phase function is (cf. Appendix 3-4):

$$\mu = \left(\beta + \sqrt{\alpha^3 + \beta^2}\right)^{\frac{1}{3}} - \frac{\alpha}{\left(\beta + \sqrt{\alpha^3 + \beta^2}\right)^{\frac{1}{3}}} \tag{3.29}$$

with $\alpha = 1 + \frac{C}{A}$, $\beta = (\frac{3}{A}.\xi - \frac{3C}{2A} - 2)$, $\xi \sim \mathcal{U}([0,1])$

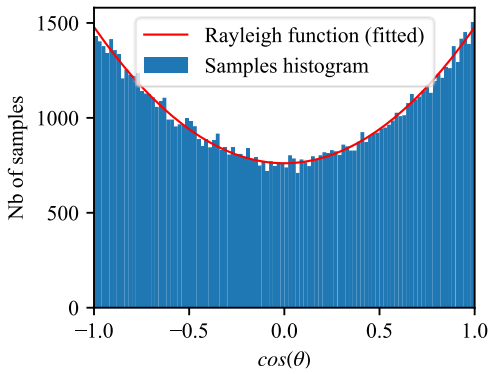

Figure 3-2: Rayleigh phase function sampling test: histogram of 10^5 samples and its fitted function (A = 0.7175, C = 0.0435)

The Henyey-Greenstein and Rayleigh scattering phase functions depend only on the cosine of the angle θ between the incident and the outgoing directions. Therefore, the incident and outgoing directions play symmetric roles. It explains that these phase functions are adapted to bi-directional modeling with the same PDF used to sample scattering directions for the light and sensor sub-paths.

- **Turbid vegetation phase function**

For a vegetation turbid medium, the scattering transfer function is:

$$T_{scat}(\Omega_s \rightarrow (\Omega_v, \Delta\Omega_v)) = \frac{1}{G(\Omega_s)}.\int_{\Delta\Omega_v}\int_{2\pi} |\Omega_s.\Omega_l|.\frac{g(\Omega_l)}{2\pi}.f(\Omega_l, \Omega_s \rightarrow \Omega_v).d\Omega_l.d\Omega_v \tag{3.30}$$

where $f(\Omega_l, \Omega_s \rightarrow \Omega_v)$: leaf scattering phase function.

$T_{scat}(\Omega_s \rightarrow (\Omega_v, \Delta\Omega_v))$ scattered power $W_{scat}(\Omega_s \rightarrow \Omega_v)$ in direction $(\Omega_v, \Delta\Omega_v)$, per power $W_{int}(\Delta l_i, \Omega_s)$ intercepted in pathlength Δl_i in direction Ω_s.

To define a probability density function (PDF) equivalent to the scattering phase functions for fluids, the PDF of a given direction is assumed to be proportional to the power scattered in this direction. Then, we have:

$$p(\Omega_v|\Omega_s) = \frac{\frac{1}{G(\Omega_s)}.\int_{2\pi}|\Omega_s.\Omega_l|.\frac{g(\Omega_l)}{2\pi}.f(\Omega_f,\Omega_s\rightarrow\Omega_v).d\Omega_l}{\int_{4\pi}\frac{1}{G(\Omega_s)}.\int_{2\pi}|\Omega_s.\Omega_l|.\frac{g(\Omega_l)}{2\pi}.f(\Omega_l,\Omega_s\rightarrow\Omega_v).d\Omega_l.d\Omega_v} \quad (3.31)$$

$p(\Omega_v|\Omega_s)$ is normalized: $\int_{4\pi} p(\Omega_v|\Omega_s).d\Omega_v = 1$.

Assuming that the leaves are bi-Lambertian surfaces:

$$p(\Omega_v|\Omega_s) = \frac{\frac{1}{G(\Omega_s)}.\int_{2\pi}|\Omega_s.\Omega_l|.\frac{g(\Omega_l)}{2\pi}.\alpha(\Omega_l,\Omega_s\rightarrow\Omega_v).|\Omega_v.\Omega_l|d\Omega_l}{\int_{4\pi}\frac{1}{G(\Omega_s)}.\int_{2\pi}|\Omega_s.\Omega_l|.\frac{g(\Omega_l)}{2\pi}.\alpha(\Omega_l,\Omega_s\rightarrow\Omega_v).|\Omega_v.\Omega_l|d\Omega_l.d\Omega_v} \quad (3.32)$$

where: $\alpha(\Omega_l,\Omega_s\rightarrow\Omega_v) = \begin{cases} \frac{\rho_{top}}{\pi} \text{ if } \Omega_l.\Omega_s < 0 \text{ and } \Omega_l.\Omega_v > 0 \\ \frac{\tau_{top}}{\pi} \text{ if } \Omega_l.\Omega_s < 0 \text{ and } \Omega_l.\Omega_v < 0 \\ \frac{\rho_{bot}}{\pi} \text{ if } \Omega_l.\Omega_s > 0 \text{ and } \Omega_l.\Omega_v < 0 \\ \frac{\tau_{bot}}{\pi} \text{ if } \Omega_l.\Omega_s > 0 \text{ and } \Omega_l.\Omega_v > 0 \end{cases}$

When sampling a scattering direction for a bi-Lambertian surface, the incident and outgoing directions play symmetric roles. For a turbid medium made only of bi-Lambertian surfaces, this symmetry is conserved. Hence, this PDF can be used to sample scattering directions in both direct and reverse directions (*i.e.*, for both light and source sub-paths).

The denominator of Eq (3.32) can be simplified:

$$D = \int_{4\pi}\frac{1}{G(\Omega_s)}.\int_{2\pi}|\Omega_s.\Omega_l|.\frac{g(\Omega_l)}{2\pi}.f(\Omega_l,\Omega_s\rightarrow\Omega_v).d\Omega_l.d\Omega_v \quad (3.33)$$

$$= \frac{1}{G(\Omega_s)}.\int_{4\pi} f(\Omega_l,\Omega_s\rightarrow\Omega_v).d\Omega_v.\int_{2\pi}|\Omega_s.\Omega_l|.\frac{g(\Omega_l)}{2\pi}.d\Omega_l.$$

The leaf scattering phase function $f(\Omega_l,\Omega_s\rightarrow\Omega_v)$ verifies:

$$\int_{4\pi} f(\Omega_l,\Omega_s\rightarrow\Omega_v).d\Omega_v = \omega \quad (3.34)$$

with ω is the leaf single scattering albedo.

$\omega = \rho + \tau$, if the optical properties of the two faces are identical,

$\omega = \frac{1}{2}(\rho_{top}+\rho_{bot}) + \frac{1}{2}(\tau_{top}+\tau_{bot})$, if the optical properties of the two faces of the leaf differ.

Then: $D = \frac{\omega.G(\Omega_s)}{G(\Omega_s)} = \omega$

Finally,

$$p(\Omega_v|\Omega_s) = \frac{1}{\omega.G(\Omega_s)}.\int_{2\pi}|\Omega_s.\Omega_l|.\frac{g(\Omega_l)}{2\pi}.f(\Omega_l,\Omega_s \to \Omega_v).d\Omega_l \quad (3.35)$$

Computing this PDF is very expensive. It cannot be solved and sampled analytically using the inversion method directly. Antyufeev & Marshak 1990 used an indirect approach by sampling first a random leaf orientation from the LAD function $\frac{g(\Omega_f)}{2\pi}$, then sampling a scattering direction according the leaf BSDF $f(\Omega_f,\Omega_s \to \Omega_v)$. This approach uses a sampling method per LAD function, and implies treating the turbid medium as individual leaves, and not as a whole which increases variance (cf. Section 4.1). Thus, another approach was designed by precomputing the discrete probability distribution for N discrete direction $(\Omega_n,\Delta\Omega_n), n \in \{1,..,N\}$:

$$p\big((\Omega_n,\Delta\Omega_n)\big|\Omega_s\big) = \int_{\Delta\Omega_n} p(\Omega_v|\Omega_s).d\Omega_v \quad (3.36)$$

With the assumption that $\Delta\Omega_n$is small enough to consider that the PDF is constant over $\Delta\Omega_n$:

$$p\big((\Omega_n,\Delta\Omega_n)\big|\Omega_s\big) = \frac{\Delta\Omega_n}{\omega.G(\Omega_s)}.\int_{2\pi}|\Omega_s.\Omega_l|.\frac{g(\Omega_l)}{2\pi}.f(\Omega_l,\Omega_s \to \Omega_v).d\Omega_l \quad (3.37)$$

In DART-FT, the Phase module precomputes the transfer function for the discrete directions:

$$\bar{\bar{T}}(\lambda,\Omega_s,\Omega_v,\Delta\Omega_v) = \frac{\Delta\Omega_v}{G(\Omega_s)}.\int_{2\pi}|\Omega_s.\Omega_l|.\frac{g(\Omega_l)}{2\pi}.f(\Omega_l,\Omega_s \to \Omega_v).d\Omega_l \quad (3.38)$$

This precomputation is used to compute the discrete probability distribution for all outgoing directions, for each incident direction:

$$p\big((\Omega_n,\Delta\Omega_n)\big|\Omega_s\big) = \frac{\bar{\bar{T}}(\lambda,\Omega_s,\Omega_v,\Delta\Omega_v)}{\omega} \quad (3.39)$$

Then, the PDF for the direction Ω_n is given by:

$$p(\Omega_n|\Omega_s) = \frac{\bar{\bar{T}}(\lambda,\Omega_s,\Omega_n,\Delta\Omega_n)}{\omega.\Delta\Omega_n} \quad (3.40)$$

$p(\Omega_n|\Omega_s)$ is computed for N ingoing and N outgoing discrete directions. However, in DART-Lux, rays can propagate in any direction. Therefore, the PDF for any direction is computed with a two-step interpolation. 1) For each neighbor direction of the incident direction, the PDF is

interpolated using the values in neighboring directions of the outgoing direction. 2) Then, results of the first interpolation are interpolated for neighbor directions of the incident direction.

If the volume contains several types of turbid/fluid medium, the scattering direction is determined in two steps. 1) A scattering medium is randomly selected: the probability of selecting a medium is proportional to its scattering extinction coefficient for fluids, and to its extinction coefficient in the incident direction for the turbid medium. 2) Then, a scattering direction is sampled according to the scattering phase function of the selected medium.

SIF modeling

Once the turbid medium is introduced in DART-Lux, modeling the SIF emission in this medium is straightforward using the Monte Carlo path sampling method presented above. Similarly to the scattering phase functions, SIF transfer functions precomputed by the phase module of DART-FT for discrete directions (c.f. Eq (2.5)) are used to evaluate the SIF radiance for the sampled light paths along with the block matrix representation introduced in Section 3.1.

3.2.2 Results

Fluids

The accuracy of fluid modeling in DART-Lux is assessed by comparing DART-Lux and DART-FT nadir images of a parallelepiped fluid volume ($0.8 \times 0.8 \times 1\ m^3$) over a lambertian surface ($1 \times 1\ m^2$) of reflectrance "loam_gravelly_brown_dark". Figure 3-3 shows RGB color composites at 2 cm resolution, for two fluid phase functions: a) Double Henyey-Greenstein ($a = 0.75$, $g_1 = 0.3$, g_2 =-0.3, $\sigma_a = 0.4\ m^2.m^{-3}$, $\sigma_s = 0.1\ m^2.m^{-3}$), and b) Rayleigh (optical property: "rayleigh_air", particle density: $5.10^{29}\ m^{-3}$). DART-FT and DART-Lux images are similar with close average reflectance values in the blue, green and red spectral bands (relative differences < 1%). DART-Lux images have some Monte Carlo noise.

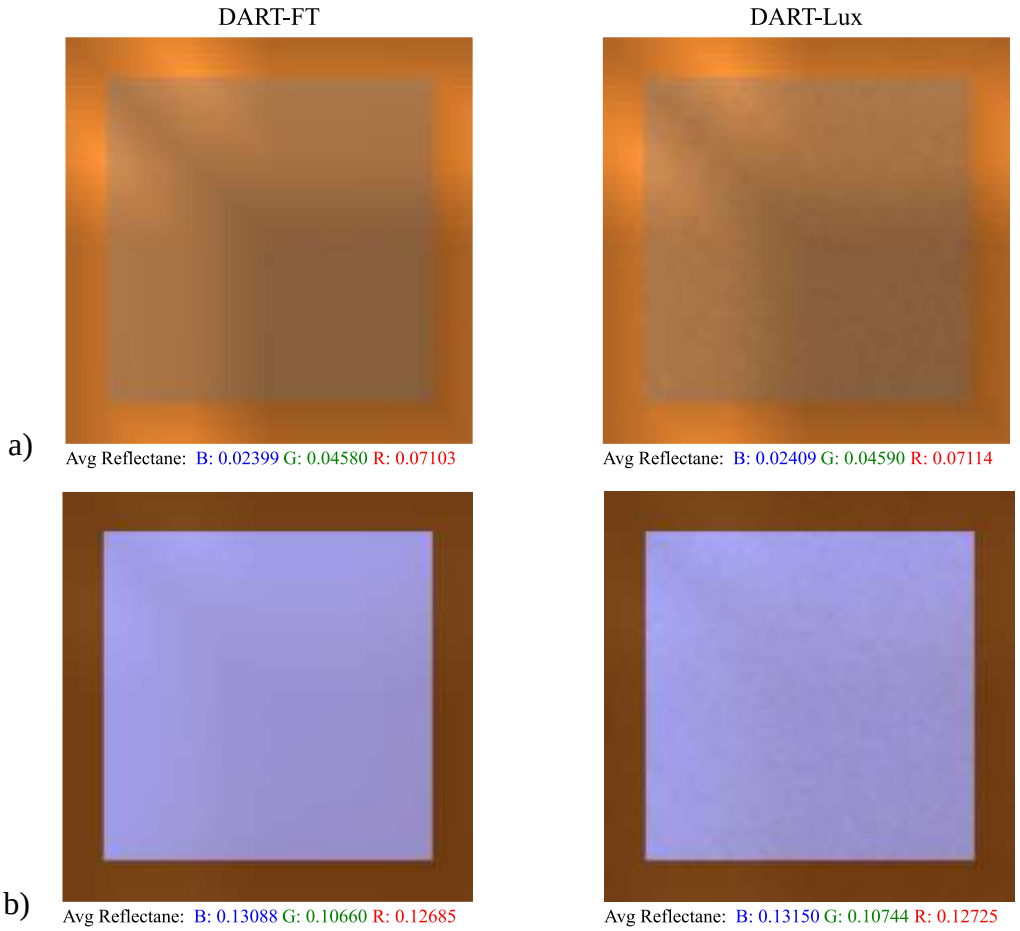

Figure 3-3: DART-FT and DART-Lux RGB nadir images of a fluid volume with fluid phase function double Henyey-Greenstein (a) and Rayleigh (b).

Turbid medium

The accuracy of DART-Lux SIF modeling in a turbid medium is assessed by comparison with DART-FT for the case of a turbid volume (LAI = 1, spherical LAD) over a non-reflective ground and an incident sun radiation with a zenith angle equal to 30°. Figure 3-4 shows the scene total nadir reflectance and scene SIF PSI and PSII nadir radiance simulated by DART-FT and DART-Lux. Figure 3-5 shows the DART-FT and DART-Lux directional reflectance in the solar plane for a near infrared spectral band. The hot spot appears clearly. In both cases, DART-Lux closely agrees with DART-FT: relative difference is 1.21% for reflectance, 0.60% for PSI radiance, and 63% for PSII radiance.

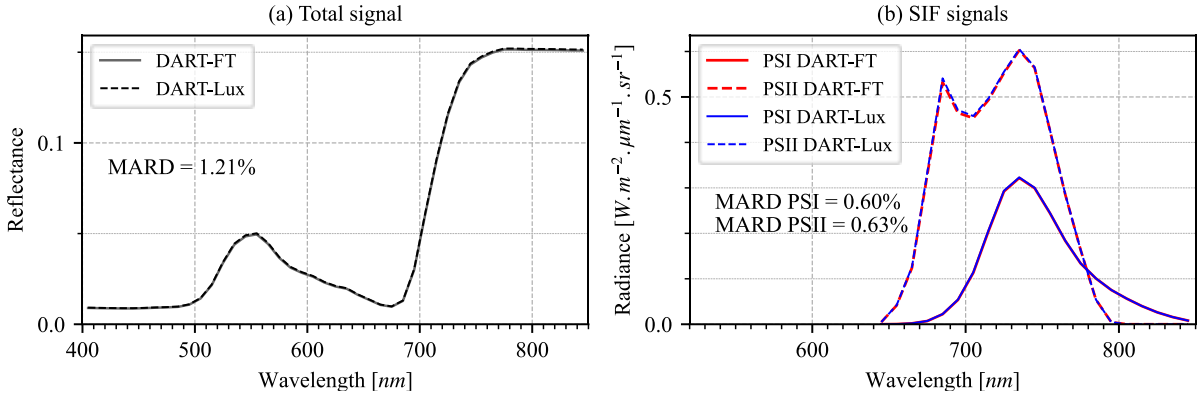

Figure 3-4: Nadir total reflectance and SIF PSI and PSII radiance comparison between DART-FT and DART-Lux for a simple turbid plot

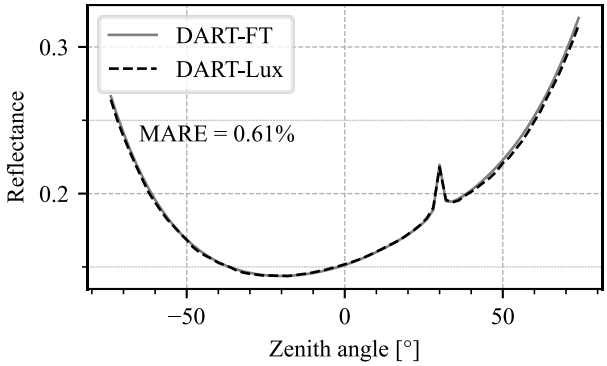

Figure 3-5: Comparison of the directional reflectance for a NIR band in the solar plane between DART-FT and DART-Lux for simple turbid plot

Figure 3-6 shows the mock-up of a realistic scene used to assess DART-Lux SIF modeling. It is a 25 m x 25 m subzone (1 m x 1 m x 1 m voxels) of the CI1 tree plot of the SERC forest that Yin et al. (2022) derived from airborne LiDAR measurements. Figure 3-7 compares the spectral nadir reflectance and also PSI and PSII radiance simulated by DART-FT and DART-Lux for 45 spectral bands from 400 to 850 nm. DART-Lux and DART-FT closely agree: relartive difference is 1.15% for reflectance, 0.51% for PSI radiance and 0.40% for PSII radiance.

This simulation took 2 h 16 min and 4.8 GB of memory for DART-FT, 2 min 38 s and 1.5 GB for DART-Lux. It stresses the computational efficiency of DART-Lux for large and complex scenes.

Figure 3-6: 25 m x 25 m turbid mockup derived from LiDAR point cloud of SERC forest (USA) with pure green voxels (leaves or wood) and mixed brown voxels (leaves and wood).

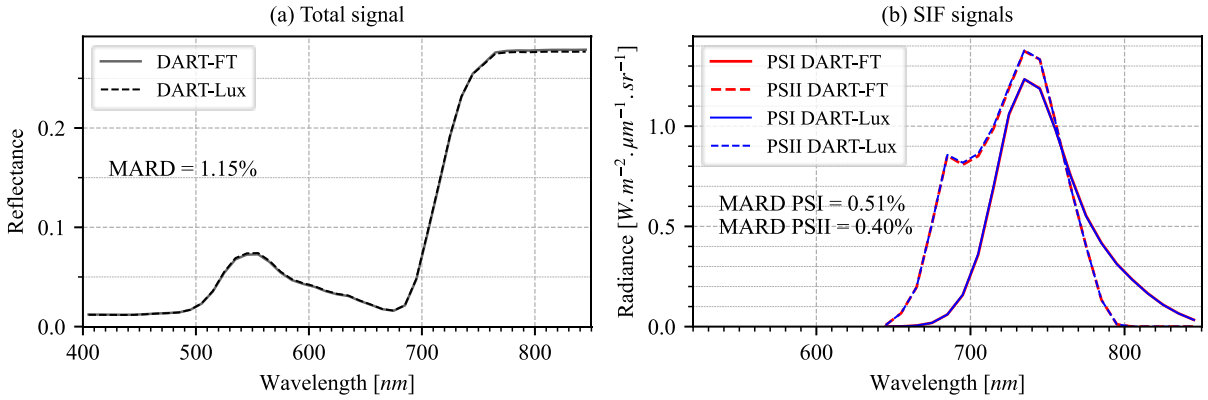

Figure 3-7: Nadir total reflectance and SIF radiance simulated using DART-FT (turbid) and DART-Lux (turbid) comparison

3.3 Conclusion

The theory of SIF emission modeling in DART-Lux has been introduced. It relies on major changes in DART-Lux. First, the SIF emission equations that include interdependence between spectral were adapted to the bi-directional path tracing algorithm and in particular to the sub-paths traced in the backward direction. Second, the turbid vegetation has been introduced, after having introduced fluid volumes using the double Henyey-Greenstein and the Rayleigh phase functions. DART-Lux now simulates SIF emission and observation for vegetation simulated as facets and/or as turbid volumes. It usually is much smaller simulation time and computer memory that DART-FT, with a gain in computational efficiency that depends on the scene complexity and on the number of simulated spectral bands. Therefore, it allows the study of much larger and more complex landscapes than DART-FT.

Appendix 3-1: Inversion method

The inversion method is used to draw random samples from a random variable of a given PDF, using the inverse function of its CDF and a random number uniformly sampled over [0,1].

Let a real random variable X with a PDF $p_X(x)$ that we want to sample. The CDF of X is:

$$P_X(x) = p(X \leq x) = \int_{-\infty}^{x} p_X(t).dt$$

Let Ξ a random variable uniformly distributed over [0,1] and the random variable $U{=}P_X^{-1}(\Xi)$.

The PDF of Ξ is: $p_\Xi(\xi) = \begin{cases} 1, \text{if } \xi \in [0,1] \\ 0, \text{otherwise} \end{cases}$

The CDF of Ξ is: $P_\Xi(\xi) = \int_{-\infty}^{\xi} p_\Xi(t).dt = \begin{cases} 0, \text{if } \xi < 0 \\ \xi, \text{if } \xi \in [0,1] \\ 1, \text{if } \xi > 1 \end{cases}$

Let us compute the CDF of the random variable U:

$$\begin{aligned} P_U(u) &= p(U \leq u) \\ &= p(P_X^{-1}(\Xi) \leq u) \\ &= p\big(\Xi \leq P_X(u)\big) \\ &= P_\Xi(P_X(u)) = P_X(u) \text{ (since } P_X(u) \in [0,1]) \end{aligned}$$

It implies that the random variable $U{=}P_X^{-1}(\Xi)$ has the PDF of X:

$$p_U(u) = \frac{dP_U(u)}{du} = \frac{dP_X(u)}{du} = p_X(u)$$

Therefore, the random variable U can be used to draw samples of X.

Appendix 3-2: Transmittance in hot spot configuration

For a turbid cell, transmittance in the hot spot configuration (Gastellu-Etchegorry et al., 1996) is:

$$Tr(\Omega_s, \Delta l) = \exp\left(-\int_{\Delta l} a(\Omega_s, \Omega_v, r).dr\right)$$

with $a(\Omega_s, \Omega_v, r) = u_l.G(\Omega_v).\left(1\text{-}\sqrt{\frac{G(\Omega_s).|\mu_v|}{G(\Omega_v).|\mu_s|}}.e^{-\frac{\Delta(\Omega_s,\Omega_v)}{s_f}.r.\mu_v}\right) = u_l.G(\Omega_v).(1\text{-}\beta.e^{-\alpha.r})$

Therefore: $Tr(\Omega_s, \Delta l) = e^{-u_l.G(\Omega_v).[\Delta l + \frac{\beta}{\alpha}(e^{-\alpha.\Delta l}-1)]}$

Appendix 3-3: Studying the function $\phi(l)$

$\phi(l) = l + \frac{\beta}{\alpha}(e^{-\alpha.l} - 1), l \in \mathbb{R}$

$\phi'(l) = 1 - \beta.e^{-\alpha l}$

$\phi'(l) = 0 \leftrightarrow \beta.e^{-\alpha l} = 1 \leftrightarrow l = l_0 = \dfrac{\ln(\beta)}{\alpha}$

$\phi''(l) = \alpha.\beta.\mathrm{e}^{-\alpha.l} > 0 \Rightarrow \phi'$ is strictly increasing on $\mathbb{R}$.

$\phi'(l_0)=0$ implies $\phi'(l)>0\ \forall l \in]l_0,+\infty[$ and $\phi'(l)<0$ (*i.e.*, ϕ strictly decreasing) $\forall l \in]-\infty, l_0[$

If $l_0 > 0$ (i.e., $\beta > 1$), the equality $\phi(0) = 0$ implies that ϕ can be negative for $l > 0$

$$\phi(l) = 0 \leftrightarrow l + \frac{\beta}{\alpha}(e^{-\alpha.l} - 1) = 0 \leftrightarrow l + \frac{\beta}{\alpha}.e^{-\alpha.l} - \frac{\beta}{\alpha} = 0$$

$$\leftrightarrow l.e^{\alpha.l} + \frac{\beta}{\alpha} - \frac{\beta}{\alpha}.e^{\alpha.l} = 0$$

$$\leftrightarrow l.e^{\alpha.l} - \frac{\beta}{\alpha}.e^{\alpha.l} = -\frac{\beta}{\alpha}$$

$$\leftrightarrow \alpha.l.e^{\alpha.l} - \beta.e^{\alpha.l} = -\beta$$

$$\leftrightarrow (\alpha.l - \beta).e^{\alpha.l-\beta} = -\beta e^{-\beta}$$

$$\leftrightarrow \alpha.l - \beta = W\left(-\beta e^{-\beta}\right)$$

$$\leftrightarrow \alpha.l = W\left(-\beta e^{-\beta}\right) + \beta$$

where W is "the Lambert W function" (Dence, 2013) defined as: $z = x.\exp(x) \leftrightarrow x = W(z)$. In the real domain, W has two branches: W_0 and W_{-1} ($W_0 \geq W_{-1}$). The branch W_0 is used to have $l \geq 0$

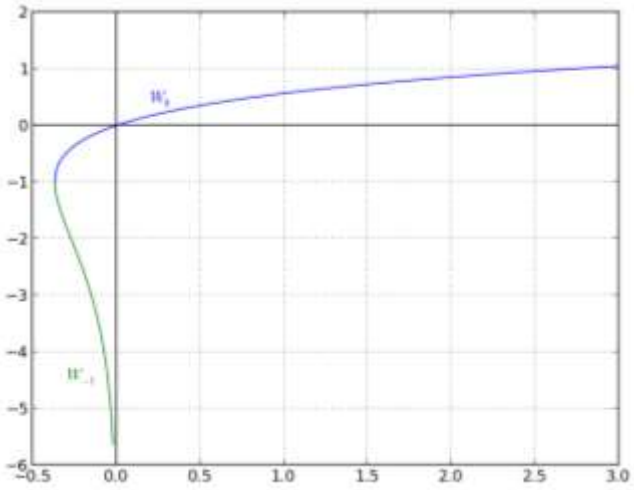

Figure 3-8: The W_0 (blue) and W_{-1} (green) branches curves of the Lambert W function

$$\leftrightarrow l = l_{w0} = \frac{W_0(-\beta e^{-\beta})+\beta}{\alpha} \text{ or } l = l_{w\text{-}1} = \frac{W_{-1}(-\beta e^{-\beta})+\beta}{\alpha}, (l_{w0} > l_{w\text{-}1})$$

If $\beta \leqslant 1$, then $l_0 \leqslant 0$ and φ strictly increasing on $[0,+\infty[\Rightarrow \phi$ bijective from $[0,+\infty[$ to $\phi([0,+\infty[)=[0,+\infty[$. Otherwise, we can prove that $l_{w0} \geq l_0$:

Then, $\phi'(l) > 0, \forall l \in]l_{w0}, +\infty[$. Hence, ϕ is strictly increasing on $]l_{w0}, +\infty[$.

Then, ϕ is bijective from $[l_{w0}, +\infty[$ to $\phi([l_{w0}, +\infty[) = [0, +\infty[$

Then for a sampled $x = \phi(l) > 0$, ϕ is bijective and we can find $\phi^{-1}(x)$.

Because $W_0(-\beta e^{-\beta}) \geq -1$, then: $W_0(-\beta e^{-\beta}) + \beta \geq -1 + \beta$

Since $-1 + \beta \geq \ln(\beta)$, then $W_0(-\beta e^{-\beta}) + \beta \geq \ln(\beta)$

Hence $l_{w0} \geq l_0 = \frac{\ln(\beta)}{\alpha}$

Computation of ϕ^{-1}

$$x = l + \frac{\beta}{\alpha}(e^{-\alpha.l} - 1) \leftrightarrow x = l + \frac{\beta}{\alpha}.e^{-\alpha.l} - \frac{\beta}{\alpha}$$

$$\leftrightarrow x.e^{\alpha.l} = l.e^{\alpha.l} + \frac{\beta}{\alpha} - \frac{\beta}{\alpha}.e^{\alpha.l}$$

$$\leftrightarrow -\frac{\beta}{\alpha} = l.e^{\alpha.l} - \frac{\beta}{\alpha}.e^{\alpha.l} - x.e^{\alpha.l}$$

$$\leftrightarrow -\frac{\beta}{\alpha} = \left(l - \frac{\beta}{\alpha} - x\right).e^{\alpha.l}$$

$$\leftrightarrow -\beta = (\alpha.l - \beta - \alpha.x).e^{\alpha.l}$$

$$\leftrightarrow -\beta.e^{-\alpha.x-\beta} = (\alpha.l - \beta - \alpha.x).e^{\alpha.l-\alpha.x-\beta}$$

$$\leftrightarrow \alpha.l - \alpha.x - \beta = W(-\beta.e^{-\alpha.x-\beta})$$

$$\leftrightarrow l = \frac{W(-\beta.e^{-\alpha.x-\beta}) + \alpha.x + \beta}{\alpha}$$

Appendix 3-4: Sampling the Rayleigh phase function

The general form of the Rayleigh scattering phase function is

$$\frac{p(\theta)}{2\pi} = \frac{1}{4\pi}.[A.(1+\cos^2(\theta)) + C]$$

It can be written as a function of $\mu = \cos(\theta)$

$$p(\mu) = \frac{1}{2}.[A.(1+\mu^2) + C] \quad \text{with } \int_{-1}^{1} p(\mu).d\mu = 1$$

The CDF of $p(\mu)$ is: $P(x) = \int_{-1}^{x} p(\mu).d\mu$

$$= \frac{1}{2}\int_{-1}^{x} [A.(1+\mu^2) + C].d\mu$$

$$= \frac{1}{2}\left[A.\left(x + \frac{x^3}{3} + \frac{4}{3}\right) + C.(x+1)\right]$$

$$= \frac{A}{6}.x^3 + x\left(\frac{A}{2} + \frac{C}{2}\right) + \frac{2}{3}A + \frac{C}{2}$$

To sample randomly a value μ using a random number $\xi \sim \mathcal{U}([0,1])$:

$$P(\mu) = \xi \leftrightarrow \frac{A}{6}.\mu^3 + \left(\frac{A}{2} + \frac{C}{2}\right)\mu + \frac{2}{3}A + \frac{C}{2} - \xi = 0$$

$$\leftrightarrow \mu^3 + 3\left(1 + \frac{C}{A}\right)\mu - 2\left(\frac{3\xi}{A} + \frac{3C}{2A} - 2\right) = 0$$

$$\leftrightarrow \mu^3 + 3\alpha\mu - 2\beta = 0 \text{ with } \alpha = 1 + \frac{C}{A}, \beta = (\frac{3}{A}.\xi - \frac{3C}{2A} - 2),$$

This equation has a unique real solution: $\mu = \left(\beta + \sqrt{\alpha^3 + \beta^2}\right)^{\frac{1}{3}} - \frac{\alpha}{\left(\beta + \sqrt{\alpha^3 + \beta^2}\right)^{\frac{1}{3}}}$

Appendix 3-5: Nomenclature

Symbol	Description	Unit
$L(p' \to p)$	Radiance reaching p from p'	$W.m^{-2}.\mu m^{-1}.sr^{-1}$
$p_{\sigma_t}(l)$	Probability density function of having an interception at distance l	m^{-1}
$P_{\sigma_t}(l)$	Cumulated density function of p_{σ_t}	-

$Tr(\Delta l, \Omega_v)$	Path transmittance for a distance Δl along the direction Ω_v	-
σ_a	Absorption extinction coefficient	$m^2.m^{-3}$
σ_s	Scattering extinction coefficient	$m^2.m^{-3}$
σ_t	Total extinction coefficient	$m^2.m^{-3}$
Δl	Travel distance	m
ΔL	Distance until the border of the volume	m

Chapter 4

Impact of vegetation 3D structure on SIF

1D SIF models are widely used for SIF studies. They might be appropriate to use for closed and homogeneous canopies with small leaves and no distinguishable rows, but they are much less appropriate for canopies with a strongly marked 3D structure. Section 2 of this chapter presents a study of the impact of vegetation 3D structure on SIF emission and observation over eight forest sites. This was done with a quasi-turbid representation of vegetation because DAT-Lux did not yet simulate turbid SIF modeling. This work was published in the Remote Sensing of Environment journal. Section 1 compares the quasi-turbid representation of vegetation to the turbid representation of vegetation.

4.1 Turbid versus quasi turbid modeling in DART-Lux

The study presented in section 4.2 was conducted before the introduction of turbid medium and SIF modeling with turbid medium in DART-Lux. Therefore, each turbid medium voxel was simulated as a voxel randomly filled by facets (*i.e.*, quasi-turbid medium) with the same leaf area as the turbid voxel. The quasi-turbid representation was created using the cloning capacity of DART-Lux in order to minimize the computer memory: each quasi-turbid voxel is a linear combination of a limited number of base 3D objects made as a random distribution of facets with a specific leaf area. Now that turbid modeling is available in DART-Lux, it is useful to

assess the validity of the quasi-turbid representation. The case study is the CI1 tree plot of the SERC forest (Regaieg et al., 2021) that Yin et al. (2022) derived by from airborne LiDAR point cloud. Its mean LAI value is 5.517 $m^2.m^{-2}$ and its mean Wood Area Index value is 0.792 $m^2.m^{-2}$. The comparison is done without and with SIF simulation, for 45 spectral bands over [400,850nm] and a scene repetition equal to1 (*i.e.*, the studied scene is surrounded by 8 identical scenes). The scattering phase function of the turbid medium is pre-computed for 200 discrete directions.

4.1.1 No SIF simulation

Figure 4-1 shows the DART-Lux nadir reflectance of the CI1 tree plot simulated with the turbid and quasi-turbid representations, without SIF simulation. The quasi-turbid approximation shows a good accuracy with around 2% of relative difference.

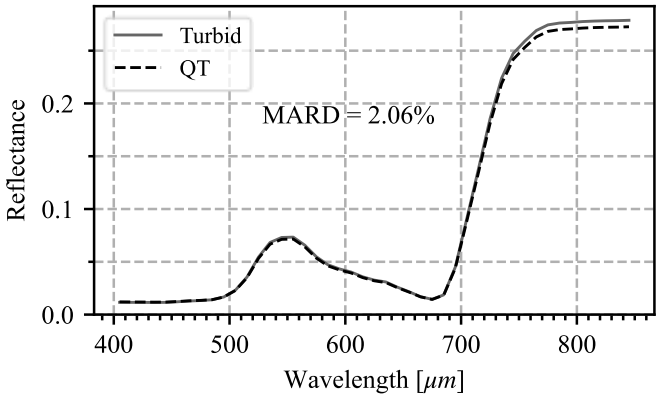

Figure 4-1: Nadir reflectance of the CI1 tree plot simulated as turbid and quasi-turbid (QT).

The Monte Carlo noise in DART-Lux images influences their pixel values. This is a constraint to be quantified. Here, it is done by running 10 times each simulation. Figure 4-2 shows the relative standard deviation images of the 10 runs averaged over all the spectral bands for the turbid and quasi-turbid representations. Each image is an average image of all spectral images of which each pixel value is the standard deviation of the 10 values from the 10 runs divided by the average of these 10 values. The relative standard deviation and therefore the Monte Carlo noise is lower for the turbid representation. This is mainly due to the fact that with, vegetation interaction is simulated using a single scattering phase function for a turbid representation, whereas for a quasi turbid medium, its simulation takes into account the discrete spatial and

angular distribution of individual leaves. For example, in order to mimick accurately the leaf angle distribution of the turbid medium, a very large number of leaves must be simulated.

Table 4-1 shows the comparison of the computation time and RAM requirements for the quasi-turbid and turbid simulations. The turbid simulation is slower than the quasi-turbid simulaltion, due to the use of computationally expensive operations such as the interpolation of phase function precomputed for a finite number of directions. On the other hand, it needs less RAM. Indeed, a turbid voxel is made of 12 facets (i.e., 2 triangles per voxel face) which is much less than the number of facets used to simulate a quasi turbid voxel.

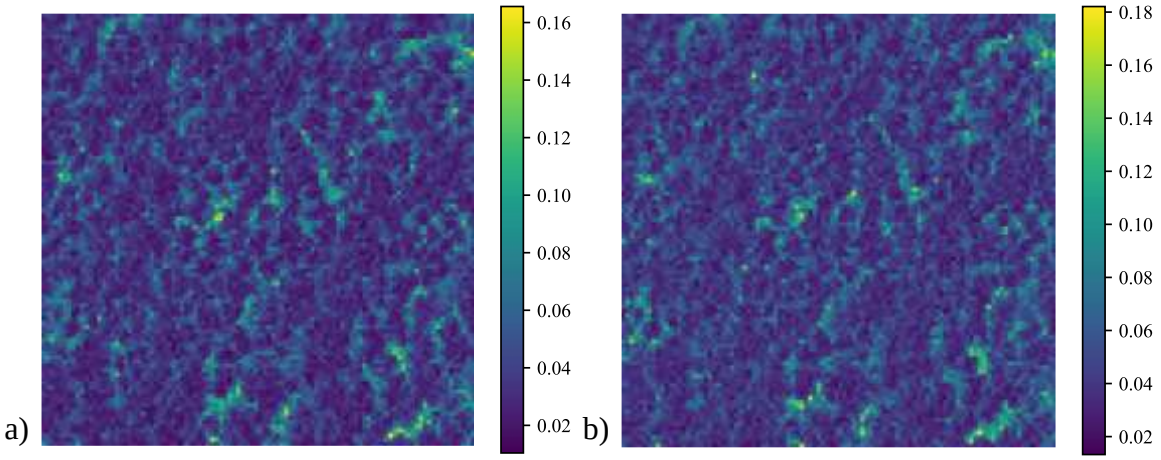

Figure 4-2: Relative standard deviation SD_r images averaged over all the spectral bands. a) Turbid mdium (mean SD_r = 0.0398). b) Quasi turbid medium (mean SD_r =0.0475).

Table 4-1: Computational needs for quasi-turbid and turbid DART-Lux simulations.

	Quasi-Turbid	Turbid
Computation Time	15 min	36 min
RAM	13.1 GB	5.2 GB

4.1.2 With SIF simulation

Figure 4-3 shows the canopy nadir PSI and PSII radiance for the turbid and quasi-turbid representations. The order of magnitude of the relative difference between the two representations is the same as if the SIF is not simulated (Figure 4-1).

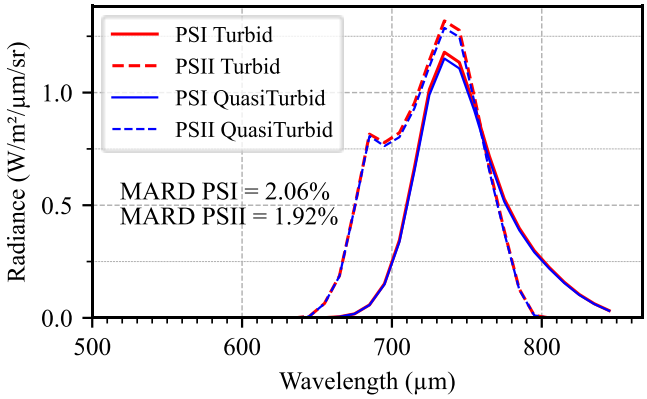

Figure 4-3: PSI and PSII radiance of CI1 tree plot for the turbid and quasi-turbid representations.

Figure 4-4 shows the relative standard deviation images of 10 runs averaged over all the spectral bands for tubrid-and quasi turbid simulations, for PSI and PSII SIF radiance. As for the total signal, the Monte Carlo noise for SIF is higher for the quasi-turbid represenation.

Table 4-2 shows the computation time and RAM requirements for quasi-turbid and turbid SIF simulations. The increase factor of computation time between quasi-turbid and turbid is higher if SIF is simulated. Indeed, the interpolation on the SIF transfer functions ($N \times N$ matrices for N spectral bands) is more computationally expensive than the interpolation of normal scattering phase functions (N-element vector for N spectral bands).

The RAM requirements is nearly the same for quasi-turbid no SIF and SIF simulations, while, it is larger for the turbid SIF compared to the turbid with no SIF because the SIF tranfer functions computed for all incident and outgoing directions, and also excitationand emission bands, for PSI and PSII, can be voluminous. However, in this case, the RAM requirement is still less than for the quasi-turbid simuation.

This work stresses that depending on configurations (*i.e.*, number of spectral bands, dimension of the study area, etc.), the quasi turbid or the turbid representation can be prefered.

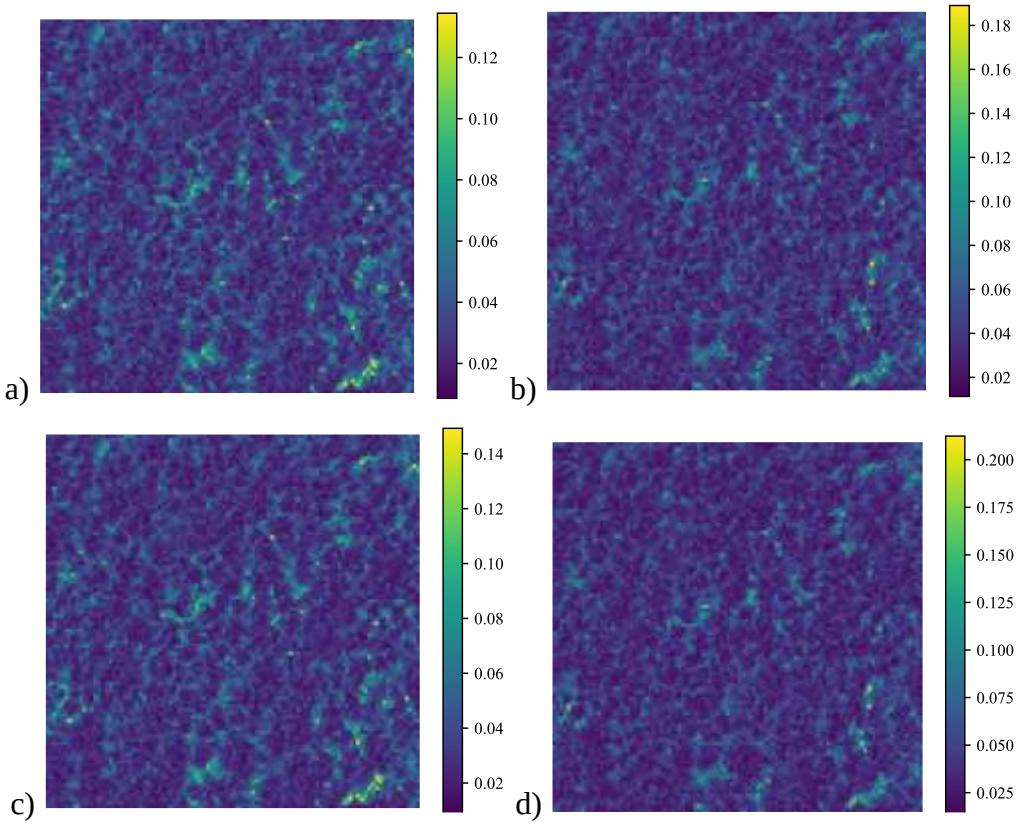

Figure 4-4: Relative standard deviation images for SIF averaged over the spectral bands where it is non null. a) PSI turbid (average = 0.0327) b) PSI quasi-turbid (average = 0.0412) c) PSII turbid (average = 0.0341) d) PSII quasi-turbid (average = 0.0430).

Table 4-2: Computational requirements for quasi-turbid and turbid SIF simulations

	Quasi-Turbid	Turbid
Computation Time	1 h 25 min	5 h 25 min
RAM	13.1 GB	8.1 GB

4.2 Article

The use of 1D SIF models like SCOPE implies to use a less accurate representation of vegetation as horizontally homogeneous layers and to neglect the 3D structure of canopies although it highly impacts the propagation of light and SIF radiation with the canopy. It neglects

other important elements of the canopy as well, that interact with radiation and influence the SIF emission and the measured signal such as the local topography and the woody elements of the trees. Hence, the use of 1D models can induce errors in SIF simulations and consequently errors in the interpretation of SIF measurements. Therefore, it is important to study the impact of 3D structure on the SIF and to quantify the simulation errors that are made when simulating the SIF with 1D models. Consequently, 3D radiative transfer models are more accurate. In addition, a 3D models like DART can simulate the SIF for any 1D and 3D representation of vegetation, which is very useful for many studies.

This study was conducted on eight realistic 3D mock-ups derived by inversion of airborne LiDAR measurements over the SERC forest (Yin et al., 2022). It allowed one to stress that compared to 3D representations, 1D representations can lead to very large errors on PAR absorption, SIF emission, and SIF radiance from morning to evening, depending on the landscape 3D architecture. In this work, the order of magnitude of errors was often larger than 30%. This work was published in Remote Sensing of Environment (Regaieg et al., 2021).

Remote Sensing of Environment 265 (2021) 112673

Contents lists available at ScienceDirect

Remote Sensing of Environment

journal homepage: www.elsevier.com/locate/rse

Assessing impacts of canopy 3D structure on chlorophyll fluorescence radiance and radiative budget of deciduous forest stands using DART

Omar Regaieg [a,*], Tiangang Yin [b,c,**], Zbyněk Malenovský [d], Bruce D. Cook [b], Douglas C. Morton [b], Jean-Philippe Gastellu-Etchegorry [a]

[a] Centre d'Etudes Spatiales de la Biosphere – UT3, CNES, CNRS, IRD, Université de Toulouse, 31401 Toulouse Cedex 9, France
[b] NASA Goddard Space Flight Center, Biospheric Sciences Laboratory, 8800 Greenbelt Rd, Greenbelt, MD 20771, USA
[c] Earth System Science Interdisciplinary Center, University of Maryland, College Park, MD 20740-3823, USA
[d] School of Geography, Planning, and Spatial Sciences, University of Tasmania, Private Bag 76, Hobart, TAS 7001, Australia

ARTICLE INFO

Editor: Jing M. Chen

Keywords:
SIF
Radiative transfer modeling
Radiative budget
Photosynthetic active radiation
Escape factor
3D forest architecture
Wood

ABSTRACT

Although remote sensing (RS) of solar-induced chlorophyll fluorescence (SIF) is increasingly used as a valuable source of information about vegetation photosynthetic activity, the RS SIF observations are significantly influenced by canopy-specific structural features (*i.e.*, canopy architecture including leaf area index and presence of woody components), atmospheric conditions during their acquisition (*e.g.*, proportion of direct and diffuse irradiance) and observational geometric configurations (*e.g.*, sun and viewing directions). Radiative transfer (RT) models have the potential to provide a better understanding of the canopy structural effects on the SIF emission and RS signals. Here, we used the DART model to assess the daily influence, from morning to evening, of forest 3D architecture on SIF nadir radiance, emission, escape factor and nadir yield of eight 100 m × 100 m forest study plots established in a temperate deciduous forest of the Smithsonian Environmental Research Center (Edgewater, MD, USA). The 3D architecture of each plot was derived from airborne LiDAR. DART simulations of these 3D forest plots and their 1D (*i.e.*, vertical profile of sun-adapted and shade-adapted leaves) and 0D (*i.e.*, homogeneous layer of sun-adapted leaves above an homogeneous layer of shade-adapted leaves) abstractions were compared to assess the relative errors (ε_{1D_3D} and ε_{0D_3D}) associated with horizontal and vertical structural heterogeneity, respectively. Forest 3D structure, especially horizontal heterogeneity, had a great influence on forest nadir SIF radiance, resulting in ε_{1D-3D} up to 55% at 8:00 and 18:00 (*i.e.*, for oblique sun directions). The key indicators of this impact, in the descending order of importance, were the SIF escape factor (ε_{1D-3D} up to 40%), the attenuation of incident photosynthetically active radiation (ε_{1D-3D} less than 5%), and the SIF emission yield (ε_{0D-3D} less than 2%). The influence of forest architecture on the nadir SIF escape factor and SIF yield (ε_{1D_3D} up to 40%) varied over time, with differences in forest stand structure, and per spectral domain, being always larger between 640 and 700 nm than between 700 and 850 nm. In addition, woody elements demonstrated a large influence on forest SIF radiance due to their "shading" effect (ε up to 17%) and their "blocking" effect (ε ≈ 10%), both of them higher for far-red than for red SIF. These results underline the importance of 3D forest canopy architecture, especially 2D heterogeneity, and inclusion of woody elements in RT modeling used for interpretation of the RS SIF signal, and subsequently for the estimation of gross primary production and detection of vegetation stress.

* Corresponding author.
** Corresponding author at: NASA Goddard Space Flight Center, Biospheric Sciences Laboratory, 8800 Greenbelt Rd, Greenbelt, MD 20771, USA.
E-mail addresses: omar.regaieg@gmail.com (O. Regaieg), tiangang.yin.85@gmail.com (T. Yin).

https://doi.org/10.1016/j.rse.2021.112673
Received 20 May 2021; Received in revised form 8 August 2021; Accepted 20 August 2021
Available online 28 August 2021

1. Introduction

Solar-induced chlorophyll fluorescence (SIF) is a photoprotective electromagnetic radiation emitted by chlorophyll molecules in response to absorption of photosynthetically active radiation (PAR) by green vegetation. Since the energy emitted as SIF is complementary to the energy entering the photochemical processes and the excessive energy dissipated as heat (Baker, 2008; Mohammed et al., 2019), it is considered as an indicator of the functional state of plant photosynthesis (Baker, 2008). SIF measurements are complicated by the fact that SIF represents only a small fraction of absorbed PAR and spectrally overlaps with radiation reflected by Earth surface elements and the atmosphere. However, the improvement of remote sensing (RS) optical sensors and techniques for retrieving the SIF signal (Meroni et al., 2009; Mohammed et al., 2019) has opened new avenues for monitoring the functional state of vegetation. SIF can be used to track actual photosynthetic efficiency (Rossini et al., 2015; Campbell et al., 2019; Yang et al., 2021), to improve assessment of plant gross primary production (Guanter et al., 2014; Z. Liu et al., 2019), and to detect vegetation stress (Ač et al., 2015). This diverse potential of SIF for vegetation monitoring spurred the development of methods for space-borne measurements and new satellite missions, such as the FLuorescence EXplorer (FLEX) selected by the European Space Agency (ESA) as its 8th Earth explorer scientific mission (Drusch et al., 2017).

Besides plant photosynthetic activity, SIF observations are impacted by other confounding factors, notably the structure of vegetation canopies (Fournier et al., 2012; Migliavacca et al., 2017) and PAR availability. They are of SIF also influenced by sun-canopy-sensor angular and directional effects (Zhang, Zhang, Porcar-Castell, et al., 2020; Zhang, Zhang, Zhang, et al., 2020), and are driven by wavelength-dependent phenomena of SIF emission, scattering, and re-absorption. For instance, Fournier et al. (2012) found that the red-to-far-red fluorescence ratio could decrease by a factor of two between the leaf level and the canopy level, due to a higher absorption of red SIF by the vegetation canopy. Therefore, accurate interpretation and use of SIF RS observations require understanding of three consecutive processes: i) interception of photosynthetically active radiation (PAR; 400 - 750 nm) and its absorption by foliar elements ($APAR_{green}$; $W.m^{-2}$), due to chlorophyll pigments in leaves, ii) leaf SIF emission from photosystems I and II (PSI and PSII) in thylakoid membranes, due to $APAR_{green}$, and iii) propagation of the SIF radiation through the canopy, including its scattering and absorption by different canopy elements, *i.e.*, leaves, woody elements, litter, bare soil, and others (van der Tol et al., 2019).

Radiative transfer models (RTMs) are powerful tools used for various vegetation RS applications, ranging from sensitivity analyses (Malenovský et al., 2008) to quantitative retrievals of models' biophysical inputs (Brede et al., 2020; Verrelst et al., 2019). The increasing need for understanding and interpreting the SIF signal at canopy level resulted in coupling canopy RTMs with a leaf-level SIF model, most frequently with Fluspect (Vilfan et al., 2016). The pioneer in one-dimensional (1D) SIF canopy modeling is SCOPE (van der Tol et al., 2009). Based on SAIL RTM (Verhoef, 1984) and coupled with leaf-level SIF and biochemistry models, SCOPE models photosynthesis and the full energy balance (Damm et al., 2015; Migliavacca et al., 2017; Verrelst et al., 2015, 2016). Despite its extension to vertically heterogeneous canopies (Yang et al., 2017), SCOPE's 1D formulation makes it less suitable for structurally complex and spatially heterogeneous canopies, such as forests. This explains the recent development of three-dimensional (3D) SIF RTMs, such as FluorFLIGHT (Hernández-Clemente et al., 2017), based on the 3D FLIGHT model (North, 1996), FLiES-SIF (Sakai et al., 2020) based on the FLiES model (Kobayashi & Iwabuchi, 2008) that simulate SIF for tree canopies, FluorWPS (Zhao et al., 2016) based on the WPS model (Zhao et al., 2015) designed to simulate SIF of structurally complex canopies and the FluLCVRT model (Kallel, 2020) that simulates SIF for 3D canopies including 3D leaf-level SIF modeling. The work presented in this paper was carried out with the 3D discrete anisotropic radiative transfer (DART) model (Gastellu-Etchegorry et al., 2017) coupled with Fluspect-Cx (Vilfan et al., 2018). DART simulates both the 3D SIF radiative budget (*i.e.,* interception, absorption, emission and scattering) and the SIF signal remotely sensed at the bottom of atmosphere (BOA) and top of atmosphere (TOA) for forest or crop canopies. It upscales leaf-level SIF to canopy SIF, while considering the user-defined leaf biochemistry and fluorescence quantum yield efficiencies of PSI and PSII, and accounting for the actual 3D vegetation architecture. DART has been cross compared with the SCOPE modeling of the same 1D vegetation scenarios (Malenovský et al., 2021), and used in various studies for sensitivity analyses of the SIF signal in architecturally complex forest canopies (W. Liu et al., 2019; Malenovský et al., 2021), scaling canopy-level SIF down to the level of photosystems (X. Liu et al., 2019), and studying the escape probability of far-red SIF from discontinuous forest canopies (W. Liu et al., 2020).

The main objective of this paper is to assess the impact of temperate deciduous forest architecture on the diurnal variability in the nadir SIF RS signal and within-canopy SIF emission by green leaves. SIF canopy signals were simulated with a new Monte Carlo mode of

DART, called DART-Lux, whereas the radiative budget of within canopy SIF emission was simulated using the standard flux tracking mode of DART, called DART-FT. (cf. section 2.1).

2. Material and methods

2.1. Discrete anisotropic radiative transfer (DART) modeling approaches

DART (https://dart.omp.eu) is a comprehensive physically based 3D RTM developed by the CESBIO Laboratory (Toulouse, France) since 1993 (Gastellu-Etchegorry et al., 1996, 2015). It is continuously improved both scientifically (*e.g.*, light polarization and radiative coupling between the atmosphere and Earth surfaces) and technically (*e.g.*, computational efficiency in terms of simulation time and computer memory). It simulates the radiative budget (RB) as well as TOA, BOA, and in-situ RS observations (*i.e.*, LiDAR and imaging spectroradiometer data, either pushbroom scanner, hemispherical or frame camera) of urban and natural landscapes from the visible to the thermal infrared spectral domains, for any experimental and instrumental configuration (solar illumination, viewing direction, atmosphere condition, spatial and spectral resolutions, etc.). DART is made of three radiative transfer modeling modules:

1. DART-FT (Flux Tracking) simulates passive optical RS signals and 3D RB, including SIF, using an adaptation of the N-flux discrete ordinates' method (Yin et al., 2013, 2015). Landscapes are simulated as the juxtaposition of planar triangular facets in 3D arrays of voxels that contain fluid and turbid medium (*i.e.*, vegetation volume statistically characterized by a leaf angular distribution (LAD) and a leaf area index (LAI) equivalent to a volume filled with an infinite number of infinitely small planar surfaces).

2. DART-RC (Ray Carlo) combines Monte Carlo (MC) and FT methods in order to simulate LiDAR signals (Gastellu-Etchegorry et al., 2016; Yin et al., 2016). 3D landscapes are simulated in the same way as for DART-FT module.

3. DART-Lux is a new module that broadens the application domain of DART to large landscapes through the introduction of a bidirectional MC modeling approach adapted from the physically based and unbiased rendering engine called LuxCoreRender (Georgiev et al., 2012; *LuxCoreRender – Open Source Physically Based Renderer*). It greatly improves the computational efficiency of simulations for large and complex landscapes. For example, the reduction of simulation time and computer memory can be over 100-times. Indeed, this DART mode only tracks radiation that impacts the signal forming the sensor observation.

Landscapes are simulated as the juxtaposition of facets and volumes filled with fluids and turbid medium. Volumes in DART-Lux can be defined independently from the 3D arrays of voxels, unlike DART-FT and RC. Although still under intensive testing, DART-Lux already simulates most RS products of DART-FT and DART-RC, including SIF and LiDAR. Presently, TOA signals are simulated using DART-FT based atmosphere modeling (Wang & Gastellu-Etchegorry, 2021). MC-based modeling of atmosphere thermal radiative transfer, as well as radiative budget are under development.

SIF modeling was initially introduced in DART-FT for vegetation canopies represented explicitly with facets (Gastellu-Etchegorry et al., 2017) and later for canopies simulated with 3D turbid voxels (Regaieg et al., 2020). More recently, SIF modeling was also implemented in DART-Lux, for both facet-based as well as turbid canopies (Regaieg et al., in preparation). As indicated above, compared to the standard DART-FT mode, DART-Lux is much more efficient in terms of computation time and required memory to simulate RS images, including SIF images. However, up to now it does not simulate the landscape RB. Therefore, in this work, we simulated SIF image observations at the spatial resolution of 1m in DART-Lux, whereas the forest RB was simulated in DART-FT at a lower spectral resolution to reduce computational demand.

The leaf radiative transfer model Fluspect-Cx, which was embedded in DART and tested by (Malenovský et al., 2021), simulates additionally to leaf spectral reflectance and transmittance optical properties the forward and backward fluorescence excitation-emission matrices per photosystem (PSI and PSII). Its inputs include contents of foliar pigments, water and dry matter, a structural parameter characterizing the leaf optical thickness, and leaf fluorescence quantum efficiencies *fqe* (*i.e.*, fraction of $APAR_{green}$ emitted as fluorescence) of a dark-adapted leaf, that are in DART referred to as PSI and PSII fluorescence yields. Leaf physiology and local climatology influence *fqe*. However, unlike the SCOPE model, DART does not contain a leaf biochemical model, and therefore cannot simulate the canopy climatic weights that condition leaf *fqe*. Therefore, in DART, *fqe* is an input parameter that can be specified per individual foliage facet, per group of foliage facets, per type of turbid medium, or as a single value for all leaf facets and turbid medium types. Groups of foliage facets can correspond, for instance, to sunlit and shaded leaves (*i.e.*, leaves irradiated by direct sun or not at a certain time), or to sun- and shade-adapted leaves (*i.e.*, leaves that have grown under and adapted to high or low light intensity such that biochemical contents vary), knowing that a sun-adapted leaf can be

momentarily a shaded leaf and vice versa. In this work, forest *fqe* values published in (W. Liu et al., 2019) are used. Although very likely differing from actual values of the study forest sites, these values are sufficiently representative to investigate the impact of forest architecture and different structures (*e.g.*, wood components) on canopy SIF signal and emission. We also note that although sun-adapted and shade-adapted *fqe*'s are considered, the actual light and temperature modulations are not. Consequently, a leaf emitted SIF is given by APAR and *fqe* per leaf adaptation.

2.2. Study sites

Eight deciduous forest sites in the Smithsonian Environmental Research Center (SERC, Edgewater, MD, USA) were selected as the study sites. The stands mainly consist of mixed-species deciduous forests of *Liquidambar styraciflua* and *Liriodendron tulipifera* for the overstory, *and C. tomentos*a, *Quercus alba*, and *F. grandifolia* for the understory (Kamoske et al., 2019; Parker, 1995). Descriptions of forest stands and management characteristics can be found in (Brush et al., 1980, Parker et al., 2001, McMahon et al., 2010). Four forest stand types were selected from the combinations of both canopy development categories ["intermediate" (I) or "mature" (M)] and experimental status categories ["control" (C) or "logged" (L)], and two sites of each type (indexed 1 and 2) were used for this study (Table 1). Therefore, the eight study sites (Figure 1) have different canopy architectures, as illustrated by their height maps (Figure 2) and LAI vertical profiles. The forest plots LI2, LM1, LM2, and, to a lesser extent, LI2, have a larger horizontal heterogeneity than the other plots. These plots also have pronounced heterogeneity, with foliage density being larger (*i.e.*, larger LAI voxel values in DART-FT) in the bottom canopy layers than in the top canopy layers. Table 2 shows the wood area density and the LAI for sun- and shade-adapted leaves (cf. Section III-1). We note that the concept of wood area density does not have an actual physical meaning linking with trunks and branches' surface areas. It is derived from leaf off G-LiHT ALS data, and used to compensate the interception contribution induced by woody part. The presence of a local topography explains why the total ground area (*i.e.*, area based on DEM; Table 2) is larger than the scene area (i.e., $100\,m \times 100\,m$). Leaf chlorophyll a+b and carotenoid contents (µg cm^{-2}) were derived from top of canopy leaf samples collected at SERC in July of 2017 (Campbell et al., 2018), and measured using established protocol described in (Campbell et al., 2007). Pigments were extracted in dimethyl sulfoxide, identified spectro-photometrically at 1-nm resolution

159 using a dual-beam spectrophotometer (Perkin-Elmer; Wellesley, MA, USA) and calculated
160 using absorption coefficients and equations described by (Wellburn, 1994).

161 Biochemical and optical properties of leaves, woody elements and soil properties used in DART
162 are listed in Table 3. The overall LAI of 3-D reconstruction has been validated against field
163 litter-collection measurements in 2012 for various voxel dimensions from 0.5m to 5m.

164

165 Table 1. Study sites' nomenclature and description.

	Abbreviations	Description
Experimental status categories	C (Control)	No known management
	L (Logged)	Selective harvest (~ 50% of basal area)
Canopy development categories	M (Mature)	~125 years-old at time of harvesting
	I (Intermediate)	~70 years old at time of harvesting

166

167 Table 2. Wood area density, LAI (per sun-/shade-adapted leaves) and DEM-derived area for each site.

Parameter/Study site	CI1	CI2	CM1	CM2	LI1	LI2	LM1	LM2
Wood area density ($m^2.m^{-2}$)	0.792	0.863	0.939	0.991	0.665	0.435	0.827	0.615
Sun-adapted LAI ($m^2.m^{-2}$)	2.916	3.093	3.697	3.160	1.964	0.951	1.341	1.920
Shade-adapted LAI ($m^2.m^{-2}$)	2.601	2.847	2.996	3.174	3.181	2.810	3.419	3.559
Area based on DEM (m^2)	12450.7	14475.9	16535.3	11297.9	17628.8	15395.0	17576.3	20142.0

168

169 Table 3. Biochemical and optical properties used in DART modeling of the study sites.

Parameter/Study site	CI1	CI2	CM1	CM2	LI1	LI2	LM1	LM2
Leaf chlorophyll a+b content ($\mu g.cm^{-2}$)	24.307	23.253	20.23	18.146	20.569	23.264	19.619	20.165
Leaf total carotenoid content ($\mu g.cm^{-2}$)	7.06	6.81	6.338	5.852	6.295	6.843	6.156	6.364
Leaf dry matter content ($g.cm^{-2}$)	0.012							
Leaf equivalent water thickness (cm)	0.009							
Leaf fluorescence quantum efficiency	PSI: 0.0053, PSII: shade-adapted: 0.0201, sun-adapted: 0.0154							
Wood optical property	Bark of *Populus tremuloides*							
Soil optical property	Loam-gravelly brown dark soil (Alfisol from the spectra library: http://speclib.jpl.nasa.gov/)							

170

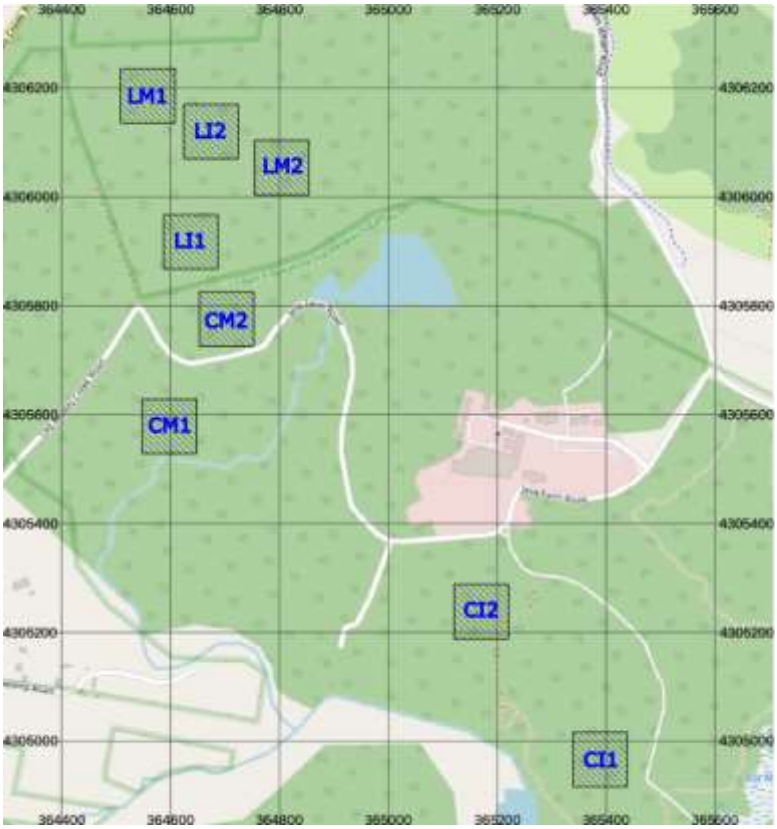

Plot Sites	Latitude	Longitude
CM1	38.8887	-76.5612
CM2	38.8904	-76.5600
CI1	38.8857	-76.5545
CI2	38.8833	-76.5520
LM1	38.8941	-76.5618
LM2	38.8930	-76.5589
LI1	38.8917	-76.5608
LI2	38.8935	-76.5604

171

172 Figure 1. Locations of SERC forest study sites (Edgewater, MD, USA) and G-Liht flight paths.

173

174 **2.3. Creation of 3D forest abstractions from airborne LiDAR acquisitions**

175 The 3D abstractions (mock-ups) of the eight forest sites were derived from 2012 multi-
176 directional and multi-temporal acquisitions by an airborne discrete-return LiDAR scanner
177 (Riegl's VQ480i), which is part of the Goddard's LiDAR, Hyperspectral and Thermal (G-LiHT)
178 Airborne Imager (Cook et al., 2013). The LiDAR acquisitions were taken during two forest
179 growth stages: i) the leaf-off stage (in March) and ii) the leaf-on stage (in June). Each
180 constructed forest mock-up ($100m \times 100m$) corresponds to a 3D array of $1m$-size voxels filled
181 with a turbid medium. The leaf angle distribution varies with height following an ellipsoidal
182 distribution generated by mean leaf incline angle from 10° at the lower canopy to 60° at the
183 upper canopy. In this experiment, we assumed an overall leaf incline angle of 57.3° over the
184 whole canopy, which may induce a slight underestimation of LAI at the upper canopy and over
185 estimation at the lower canopy in scene construction. This assumption has minor influence since
186 the change of incline angle is correlated with sun illumination, where majority of the sunlight
187 is intercepted by the leaves with larger incline angle. Since the objective was to investigate

changes in the diurnal variation of canopy SIF radiance and leaf emissions on 15 June 2017 between 7.00 and 19.00 (local time, with a time step of 1 h), the DART simulated solar zenith angles (SZA) and solar azimuth angles (SAA) were adjusted accordingly, with for example (SZA, SAA) = (76.85°, 109.51°) at 7.00, (15.62°, 5.8°) at 13.00, and (74.33°, 252.4°) at 19.00 of the local time.

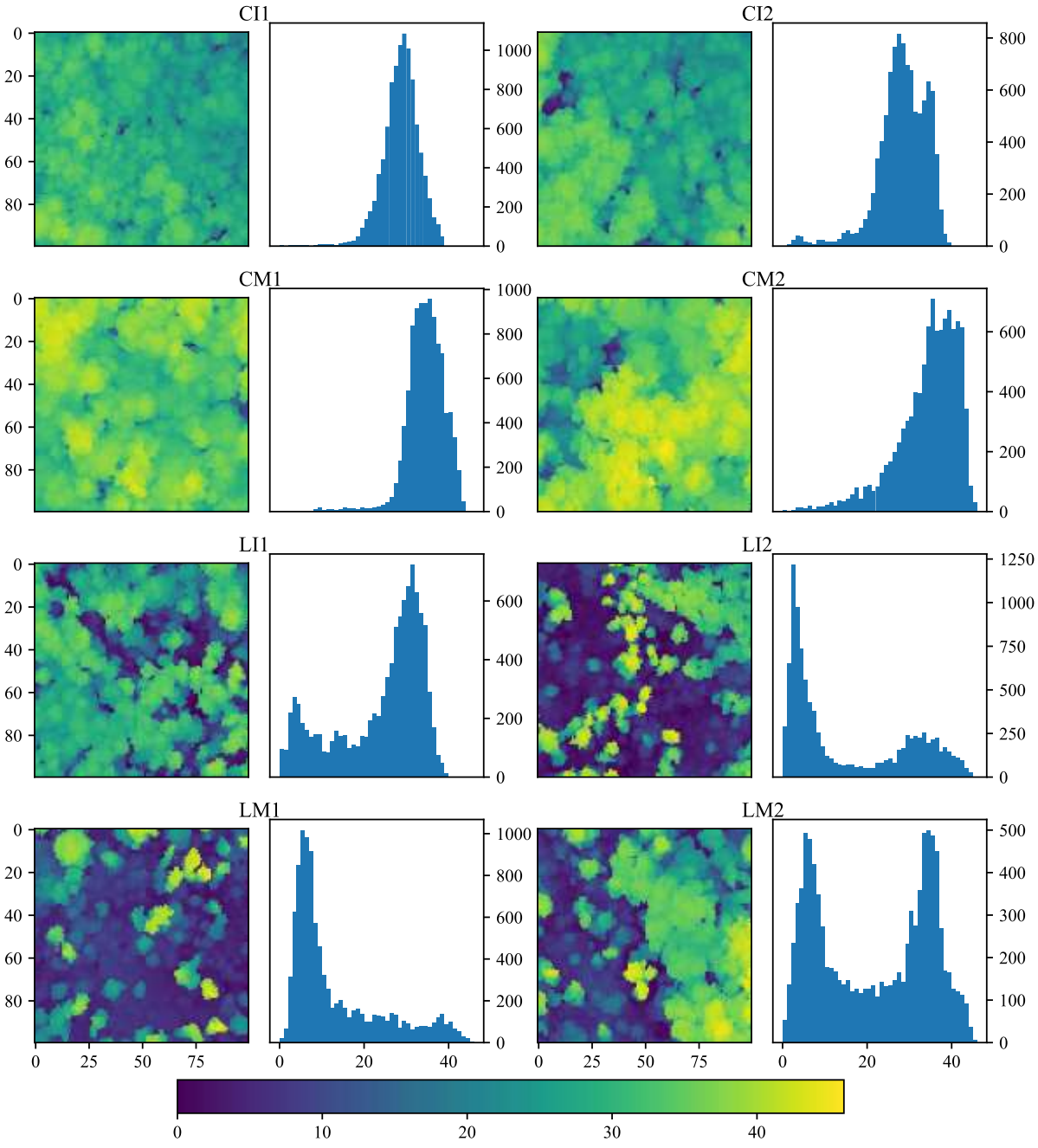

Figure 2. Maps and histograms of forest top-of-canopy height (m) for the eight forest study sites.

196 Table 4. Forest plot mean height and height standard deviation and number of pure bare ground pixels.

Plot	CI1	CI2	CM1	CM2	LI1	LI2	LM1	LM2
Mean Height (m)	28.65	28.34	34.54	34.33	23.80	15.19	13.31	21.75
Height standard deviation (m)	4.37	5.90	4.61	7.32	10.44	14.03	10.88	13.17
Number of pure bare ground pixels (out of 10 000)	2	1	2	4	89	258	8	48

197

198 **2.4. Preprocessing of modeled forest scenes**

199 Leaf biochemical and anatomical properties are adapted to the leaf exposure to sun direct and
200 scattered diffuse radiation (Givnish, 1988; Nobel, 1976). To assess 3D distribution of sun- and
201 shade-adapted foliage in each forest plot, we used DART-FT to compute hourly time series of
202 3D RB in the PAR domain from sunrise to sunset on 15 June 2012, with SZA and SAA as
203 specified in the section 2.3. The diurnal radiation intercepted by foliar elements in each turbid
204 voxel of the 3D plots computed by DART-FT was then used to classify the foliage turbid voxels
205 of each forest plot into sun- and shade-adapted foliage voxel groups. Sun- and shade-adapted leaf
206 classification methods based on thresholds on the intercepted radiation were developed for the
207 DART model for vegetation canopies simulated as facets (Malenovský et al., 2021). Here, in the
208 absence of information on the threshold definition, and for a vegetation canopy simulated as
209 turbid voxels, we chose to simply define classification decision threshold in such a way that the
210 numbers of sun-adapted voxels and shade-adapted voxels were equal. Subsequently, specific *fqe*
211 input values were assigned to the sun-adapted and shade-adapted cells (W. Liu et al., 2019)

212 Since the DART-FT mode was slow and too demanding for computer memory when simulating
213 SIF radiance of the forest plots represented by many voxels ($>10^5$) for 372 spectral bands (Table
214 5), we used the DART-Lux mode instead. As DART-Lux could at that time only simulate the
215 SIF signal of landscapes represented by geometrical facets, a "turbid-to-facet" conversion
216 procedure was designed to transform the forest turbid mock-ups (already classified into sun-
217 adapted and shade-adapted voxels) into forest 3D abstractions with leaf and woody elements
218 being represented with solid facets (cf. Appendix). DART-FT and DART-Lux give nearly
219 equivalent results in terms of canopy reflectance and SIF radiance (cf. Appendix). Small
220 differences may be observed due to the different strategies adopted by the two modes (*i.e.*,
221 discrete ordinates for DART-FT, Bi-directional Monte Carlo for DART-Lux), and also due to

the approximation of turbid volumes by clouds of facets. These differences are supposed to be negligeable compared to the differences caused by the canopy structure.

2.5. Simulated structural complexity

Three structurally different forest abstractions were considered for this study (Figure 3):

1. 3D mock-ups: derived from airborne LiDAR data, with classified sun- and shade-adapted cells as explained in the two previous sections.
2. 1D mock-ups: horizontally homogenized 3D mock-ups having the same heights and vertical profiles of sun- and shade-adapted leaf area density and wood area density but missing the forest horizontal heterogeneity.
3. 0D mock-ups: horizontally and vertically homogenized mock-ups having the mean height of the original 3D canopies, shade-adapted leaves homogeneously distributed in the mock-up bottom half, sun-adapted leaves homogeneously distributed in the mock-up top half, and woody elements homogeneously distributed within the entire scene. Compared to 3D forest mock-ups, 0D mock-ups miss the forest horizontal and vertical heterogeneity, including the simplifying assumption that all sun-adapted leaves are located at the top and all the shade-adapted leaves are located at the bottom of the canopy.

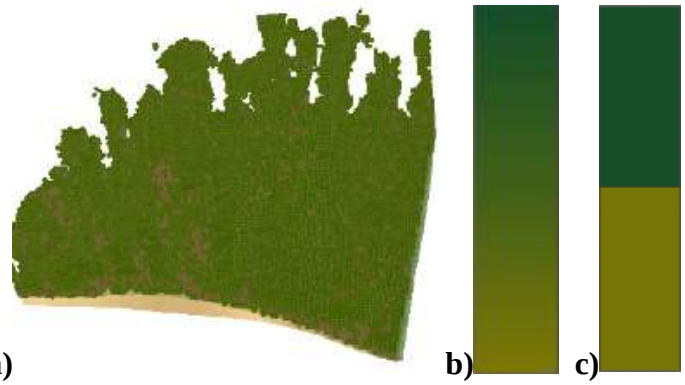

Figure 3: The three types of scene abstractions: a) 3D, b) 1D, c) 0D (top: sun-adapted, bottom: shade-adapted leaves)

2.6. Simulated SIF products

SIF nadir images of a high spectral resolution, from 0.15 nm to 4 nm (Table 5), were simulated with DART-Lux. DART-FT was used to simulate the PAR and SIF radiative budget with a

lower spectral resolution ([400-640 nm] at 20 nm resolution, [640-850] at 10 nm resolution) and 40 discrete directions, in order to limit computational demands.

Table 5. The 372 spectral bands of DART-Lux simulations. They over-sample the O_2B (~687nm) and O_2A (~760nm) oxygen absorption bands, and under-sample the [400-640nm] band (no SIF emission)

Spectral interval (nm)	Spectral resolution (nm)	Number of spectral bands
400-640	4	60
640-641.5	1.5	1
641.5-686.5	1	45
686.5-694	0.15	50
694-694.5	0.5	1
694.5-759.5	1	65
759.5-770	0.15	70
770-770.5	0.5	1
770.5-848.5	1	78
848.5-850	1.5	1

The influence of the canopy 3D architectures on 3D SIF emissions was assessed by comparing the DART-FT RB fluxes (*i.e.*, intercepted, scattered, absorbed and emitted PAR and total SIF radiation) per voxel in the simulated 3D, 1D and 0D mock-ups. Here, the PAR absorbed by leaves ($W.m^{-2}$) informs us on $APAR_{green}$ (the 1st process). $SIF_{emitted}$ ($W.m^{-2}$) is the sum of PSI and PSII emissions by adaxial and abaxial sides of all leaves in the canopy. It depends on the directionality and intensity of the incident PAR relative to leaf orientation, and therefore on $APAR_{green}$ and the local leaf physiology (*e.g.*, leaf sun and shade adaptations). SIF emission yield informs us on the 2nd process. It is defined as:

$$\text{SIF emission yield} = \frac{\text{SIF}_{\text{emitted}}}{\text{APAR}_{\text{green}}}. \quad (1)$$

Since satellite and airborne spectrometers only measure SIF radiation that exits a canopy, the 3rd process is investigated through the so-called SIF escape factor$_{hemi}$:

$$\text{SIF escape factor}_{hemi} = \frac{\text{SIF}_{\text{exitance}}}{\text{SIF}_{\text{emitted}}} \quad (2)$$

where $SIF_{exitance}$ is the total SIF radiation exiting the top of the canopy in all directions of the upper hemisphere. SIF escape $factor_{hemi}$ was computed for the chlorophyll fluorescence peaks located at 640 – 700 nm and 700 – 850 nm spectral regions.

SIF sensors generally measure from a unique viewing direction. Hence, the directional SIF nadir escape factor was also studied:

$$\text{SIF escape factor}_{nadir} = \frac{\pi.\,\text{SIF}_{nadir\ radiance}}{\text{SIF}_{\text{emitted}}} \quad (3)$$

SIF escape $factor_{nadir}$ was also computed for the chlorophyll fluorescence peaks located at 640 – 700 nm and 700 – 850 nm spectral regions.

Finally, the combination of the 2nd and the 3rd processes was in the case of a nadir observation evaluated with the SIF nadir yield (sr^{-1}) (van der Tol et al., 2019):

$$\text{SIF nadir yield} = \frac{\text{SIF}_{\text{nadir radiance}}}{\text{APAR}_{\text{green}}} \quad (4)$$

where $SIF_{\text{nadir radiance}}$ is a SIF flux ($W.m^{-2}.sr^{-1}$), that is for example recorded by an optical remote sensing sensor in the nadir viewing direction.

2.7. Canopy structure error assessment

The impact of forest architecture on diurnal SIF emission and nadir observation was assessed as the relative errors made on SIF quantities that are simulated with mock-ups (*i.e.*, 1D, 0D) with simplified architecture, taking the quantities simulated with the 3D mock-ups as reference.

The influence of forest 3D structure on SIF observation was assessed by comparing the DART-Lux top-of-canopy (TOC) nadir SIF radiance L_v (PSI, PSII and total), of the 3D, 1D and 0D mock-ups of the eight forest sites simulated. Two types of relative errors were computed:

- Per spectral band for a specific time (*e.g.*, 12.00 local time), by computing the relative errors $\boldsymbol{\varepsilon_{SIF,L_v,iD-3D}(\lambda)}$ where $\boldsymbol{i} \in \{\mathbf{0}, \mathbf{1}\}$:

$$\varepsilon_{SIF,L_v,iD-3D}(\lambda) = 100\% \times \frac{SIF_{radiance,iD}(\lambda) - SIF_{radiance,3D}(\lambda)}{SIF_{radiance,3D}(\lambda)} \quad (5)$$

- Per hour from 7.00 to 19.00, by computing mean absolute relative errors (MARE) for the two 640 – 700 nm and 700 – 850 nm spectral regions:

$$MARE_{SIF,L_v,1D-3D}(t) = \frac{1}{\sum_i \Delta\lambda_i} . \sum_i \frac{|SIF_{radiance,1D}(t,\lambda) - SIF_{radiance,3D}(t,\lambda)|}{SIF_{radiance,3D}(t,\lambda)} . \Delta\lambda_i \quad (6)$$

Using 3D plots as reference, the influence of canopy architecture was also assessed for:

- Nadir reflectance ρ:relative errors $\varepsilon_{\rho,0D\text{-}3D}(\lambda)$and $\varepsilon_{\rho,1D\text{-}3D}(\lambda)$ of 0D and 1D plots, as well as $MARE_{\rho,1D\text{-}3D}(t)$ of 1D plots.

- $APAR_{green}$: relative error $\varepsilon_{APAR,1D-3D}(t)$ of 1D plots.

- SIF emission yield: relative error $\varepsilon_{SIF.EY,1D-3D}(t)$ of 1D plots.

- $SIF_{emitted}$: relative error $\varepsilon_{SIF.em,1D-3D}(t)$ of 1D plots.

-SIF escape $factor_{hemi}$ and SIF escape $factor_{nadir}$: relative errors $\varepsilon_{SIF.EF,1D-3D}(t)$ of 1D plots at 640 – 700 nm and 700 – 850 nm spectral regions.

- SIF nadir yield: relative errors $\varepsilon_{SIF.NY,1D-3D}(t)$ of 1D plots at 640 - 700 nm and 700 - 850 nm.

with relative error for a given quantity Q equal to $\varepsilon_{Q,1D-3D}(t) = 100\% \times \frac{Q_{1D}(t) - Q_{3D}(t)}{Q_{3D}(t)}$.

2.8. Influence of canopy wood on SIF emission and measurements

Although they do not intrinsically emit fluorescence, woody elements impact the RB and SIF observations through their interaction with PAR and SIF. They give rise to two major effects. i) Shading effect: woody elements shade foliar elements, which lowers leaf irradiance and subsequently SIF emission. ii) Blocking effect: woody elements intercept the emitted SIF radiation, preventing it from escaping the canopy. These two effects are not independent, due to sky radiation and multiple scattering and re-absorption mechanisms in the canopy. For example, the same woody element can shade a leaf element and block its SIF radiation.

DART simulations were used to quantify the influence of woody elements on SIF observation, and to separate the shading and blocking effects of woody elements for the CM1 and LM2 sites. For that, theoretical "no wood" (NW) scenes were constructed by removing cells corresponding to woody elements from the original "with wood" 3D mock-ups (W). It allowed us to compare

the DART-Lux top-of-canopy (TOC) nadir SIF radiance (PSI, PSII and total) of the (W) and (NW) abstractions, and to compute two types of relative error:

- Per spectral band for a specific time (*e.g.*, 12.00 local time):

$$\varepsilon_{SIF,L_v,NW-W}(\lambda) = 100\% \times \frac{SIF_{radiance,NW}(\lambda) - SIF_{radiance,W}(\lambda)}{SIF_{radiance,W}(\lambda)} \quad (7)$$

- Per hour from 7.00 to 19.00, by computing mean absolute relative errors for the 640 – 700 nm and 700 – 850 nm spectral regions:

$$MARE_{SIF,L_v,NW-W}(t) = \frac{1}{\sum_i \Delta\lambda_i} . \sum_i \frac{|SIF_{radiance,NW}(t,\lambda) - SIF_{radiance,W}(t,\lambda)|}{SIF_{radiance,W}(t,\lambda)} . \Delta\lambda_i \quad (8)$$

Using W plots as reference, the influence of woody elements was assessed for:

- $\mathrm{APAR}_{\mathrm{green}}$ (shading effect): relative error $\varepsilon_{APAR,NW-W}(t)$ NW.

- SIF nadir escape factor $\mathrm{SIF}_{nadir\ EF}$ (blocking effect): relative error $\varepsilon_{SIF.NEF,NW-W}(t)$ of NW plots, where:

$$\mathrm{SIF}_{nadir\ EF} = \frac{\pi\ .\ \mathrm{SIF}_{\mathrm{nadir\ radiance}}}{\mathrm{SIF}_{\mathrm{emitted}}} \quad (9)$$

With the relative error for a given quantity Q equal to:

$$\varepsilon_{Q,NW-W}(t) = 100\% \times \frac{Q_{NW}\ (t) - Q_W(t)}{Q_W(t)} \quad (10)$$

3. Results

3.1. General influence of forest abstractions on SIF nadir observations

Figure 4 shows the PSI, PSII and total SIF nadir radiance of the 8 forest plots simulated with 3D, 1D and 0D mock-ups at 12.00 (SZA = 21.050°, SAA = 47.256°). $\varepsilon_{SIF,L_v,0D-3D}(\lambda)$ and $\varepsilon_{SIF,L_v,1D-3D}(\lambda)$ quantify the relative errors associated with the 0D and 1D forest plots. For all plots, the 1D mock-ups give the largest nadir total SIF, PSI and PSII radiance. $\varepsilon_{SIF,L_v,1D-3D}$ illustrates the influence of the forest horizontal heterogeneity on radiation propagation in forest, since the canopy horizontal heterogeneity is the only difference between 3D and 1D mock-ups. These larger values of 1D SIF radiance can be explained by the fact that the top layers of 1D

330 plots intercept more radiation than the top layers of 3D plots (i.e., clumping effect), which gives
331 rise to larger SIF emission by canopy layers that tend to contribute most to the canopy SIF
332 radiance. Also, the ground is more visible in 3D plots than 1D plots, whereas the ground has no
333 SIF emission. The order of magnitude of the difference between the radiance of 1D and 3D
334 mockups is similar for all investigated forest sites.

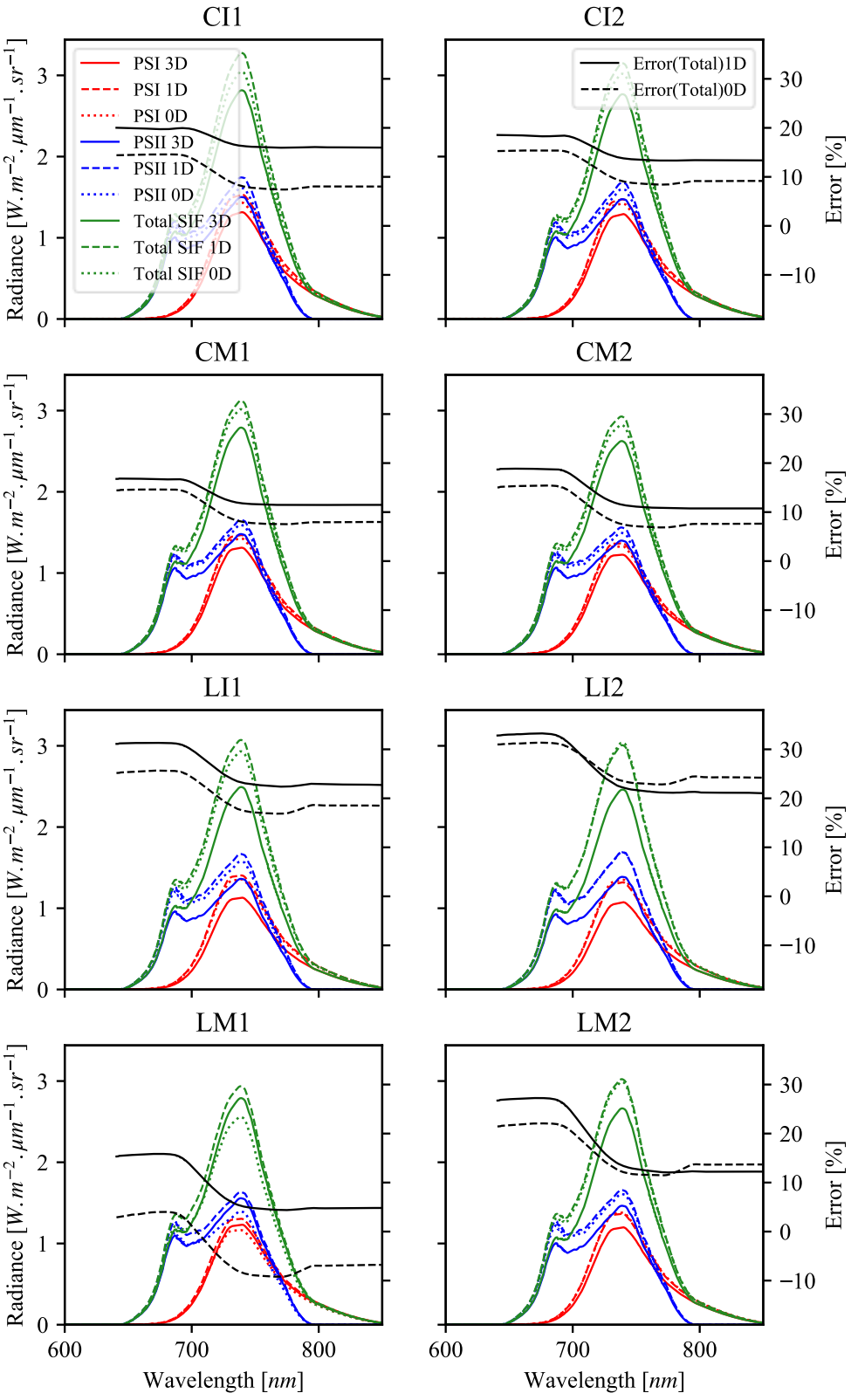

Figure 4. PSI, PSII and total SIF nadir radiance of the eight sites simulated with 3D, 1D and 0D abstractions, at 12.00 local time (SZA = 21.050°, SAA = 47.256°).

SIF radiance values of 0D and 1D forest mock-ups differ due to differences in the leaf and wood vertical distributions, which vary greatly among the sites (except for LI2 and LM2). In general, nadir SIF radiance relative differences $\varepsilon_{SIF,L_v,0D-1D}(\lambda)$ between 0D and 1D plots are much smaller than $\varepsilon_{SIF,L_v,1D-3D}(\lambda)$ between 1D and 3D plots, except for LM1.It means that forest horizontal heterogeneity has a larger influence on SIF radiance than forest vertical heterogeneity. SIF radiance was always smaller for 0D mock-ups than for 1D mockups. This is mostly explained by the homogenized vertical distribution of both foliar and woody elements in the 0D abstractions compared to 1D abstractions. For example, in CI1, CI2, CM1 and CM2, leaf density is higher in upper canopy layers (Figure 14), foliar homogenization increases the density of foliar elements in the canopy bottom layers, which increases the canopy shading and blocking effects. For LI2, the situation is different because leaf density is highest in the lower canopy layers. Therefore, foliar homogenization increases leaf density in the canopy upper layers, which decreases the canopy shading and blocking effects. These trends are also influenced by the vertical distribution of woody elements.

The relative difference $\varepsilon_{SIF,L_v,0D-3D}(\lambda)$ between the radiance of 0D and 3D mock-ups is driven by horizontal and vertical heterogeneity. The inequality $\varepsilon_{SIF,L_v,0D-3D}(\lambda) < \varepsilon_{SIF,L_v,1D-3D}(\lambda)$ indicates that vertical and horizontal heterogeneities have an opposite effect on canopy SIF radiance in our simulations. While the horizontal heterogeneity tends to decrease canopy SIF nadir radiance, the vertical heterogeneity tends to increase it. LM1 is an exception. Its 0D SIF radiance is lower than its 3D SIF radiance in the NIR domain. It means that its vertical heterogeneity imposes a larger influence on SIF nadir radiance than its horizontal heterogeneity, which is consistent with the fact that LM1 is the only plot where the density of woody and foliar elements is very dense in the lower canopy layers.

Figure 5 shows the diurnal evolution of $MARE_{SIF,L_v,1D-3D}(t)$ (*i.e.*, relative error of total nadir SIF radiance of 1D plots compared to 3D plots) at 640 - 700 nm and 700 - 850 nm. This quantity is mostly influenced by the forest horizontal heterogeneity. It appears symmetrically distributed between the morning and the afternoon hours, with a dip appearing always at local noon. It is the largest around 8.00 and 18.00, reaching up to 55%, and the smallest at 13.00 (local solar noon), with values between 10% and 20%. It is usually larger at 640 - 700 nm than at 700 - 850 nm, where shading effects are dampened by prevailing multiple scattering events. This diurnal variation can be explained by the shadow effects associated with changing solar zenith angle

and associated variability in the proportions of direct sun and diffuse atmospheric radiation. In the early morning, it starts increasing because shadow effects are increasing due to the increase of the direct sun proportion in total irradiance. Later in the morning, it starts decreasing because shadow effects decrease due to the decrease of solar zenith angle, reaching a minimum at solar noon. A symmetrical behavior starts in the second half of the day.

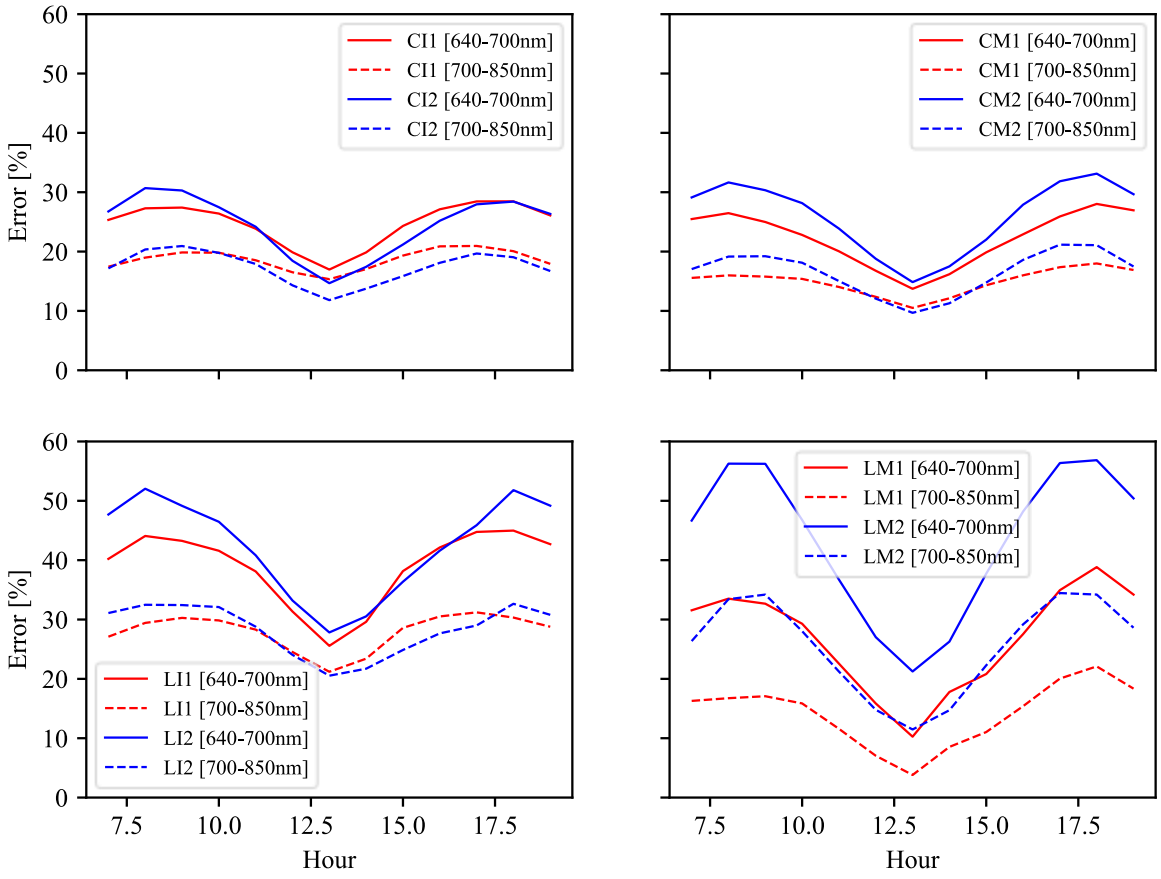

Figure 5. Diurnal evolution of the total nadir SIF radiance relative error $MARE_{SIF,L,1D-3D}(t)$ between 1D and 3D mock-ups at 640 – 700 nm and 700 – 850 nm.

Figure 6 shows the canopy nadir reflectance of the 8 forest plots simulated with 3D, 1D and 0D mock-ups at 12.00 (SZA = 21.050°, SAA = 47.256°). $\varepsilon_{\rho,0D-3D}(\lambda)$ and $\varepsilon_{\rho,1D-3D}(\lambda)$ quantify the of 0D and 1D abstractions compared to 3D abstraction. All curves have the expected local spectral peak around the O_2-A absorption band at 760nm. As for the SIF radiance (Figure 4), the total reflectance of 3D plots is the smallest compared to the 1D and 0D plots, except for LM1 where the 0D plot has a slightly lower reflectance than the 3D plot above 700nm.

Therefore, as for SIF radiance, the horizontal heterogeneity tends to decrease the nadir reflectance.

The influence of the vertical heterogeneity of the plots on their reflectance is not as clear as for SIF radiance. By contrast to the relative errors on the SIF radiance, the relative errors on the total reflectance of the 1D and 0D forest plots are similar. This stresses two points. 1) As for SIF, the forest vertical heterogeneity plays a lesser role than the forest horizontal heterogeneity. 2) The vertical heterogeneity plays a larger role for canopy SIF radiance than for canopy radiance that contains radiance due to the scattering of solar radiation. Also, these relative errors tend to higher for wavelengths under 700nm. Indeed, the 1D and 0D abstractions of the forest cover neglect the shadow effects due to direct and diffuse radiation and canopy structure. Multiple scattering being smaller at wavelengths lower than 700nm, shadowing effects are larger in these wavelengths. The diurnal evolutions of the relative error $MARE_{\rho,1D-3D}(t)$ in nadir reflectance of 1D plots at 640-700 nm and 700-850 nm (Figure 7) have shapes and orders of magnitude similar to those of SIF radiance $MARE_{SIF,L,1D-3D}$ (Figure 5), except for LI2 at 640 - 700nm, where the relative error is higher for SIF radiance.

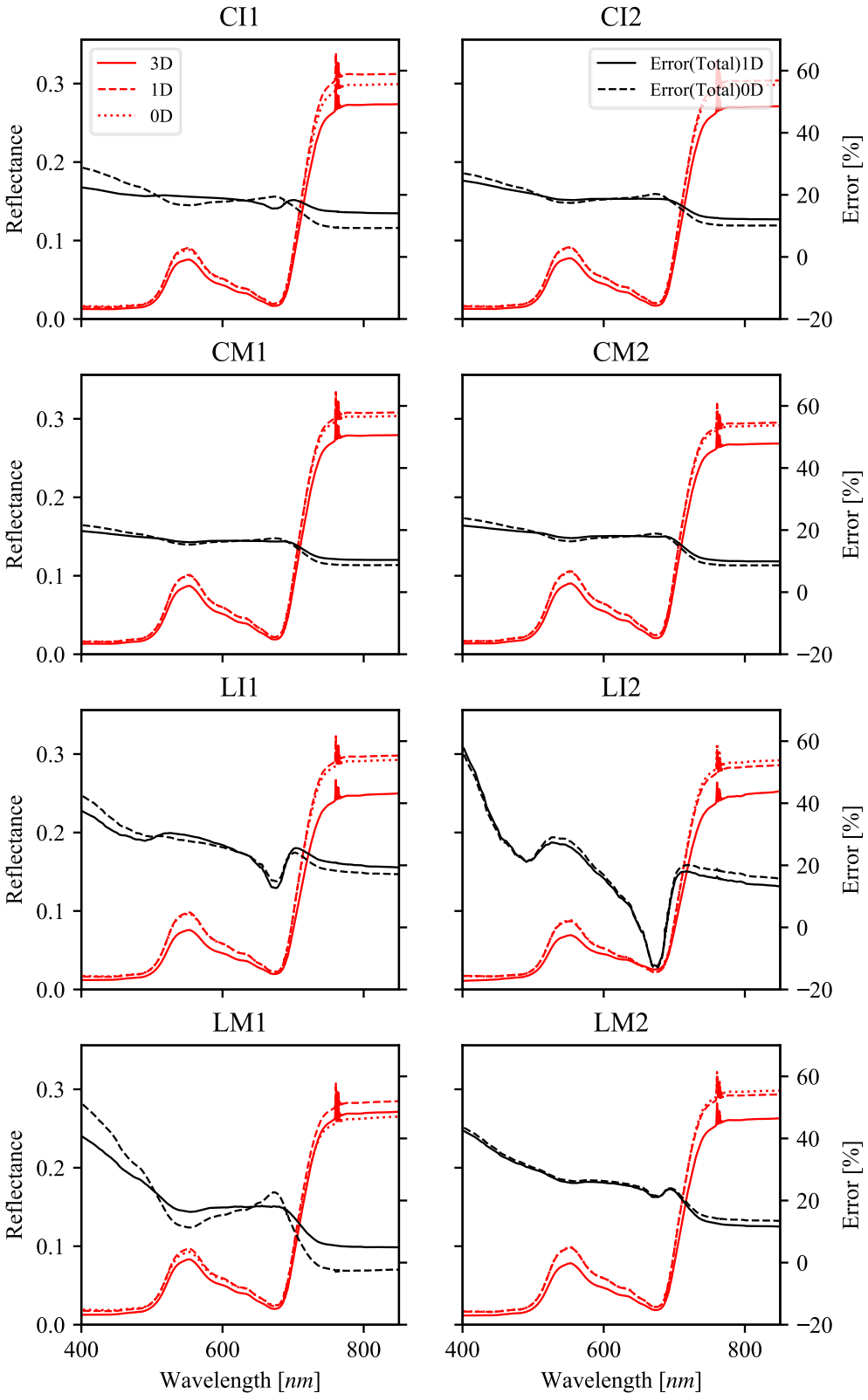

Figure 6: Canopy nadir reflectance of the eight study sites simulated with 3D, 1D and 0D mock-ups, at 12.00 local time (SZA = 21.050°, SAA = 47.256°). $\varepsilon_{\rho,1D-3D}(\lambda)$

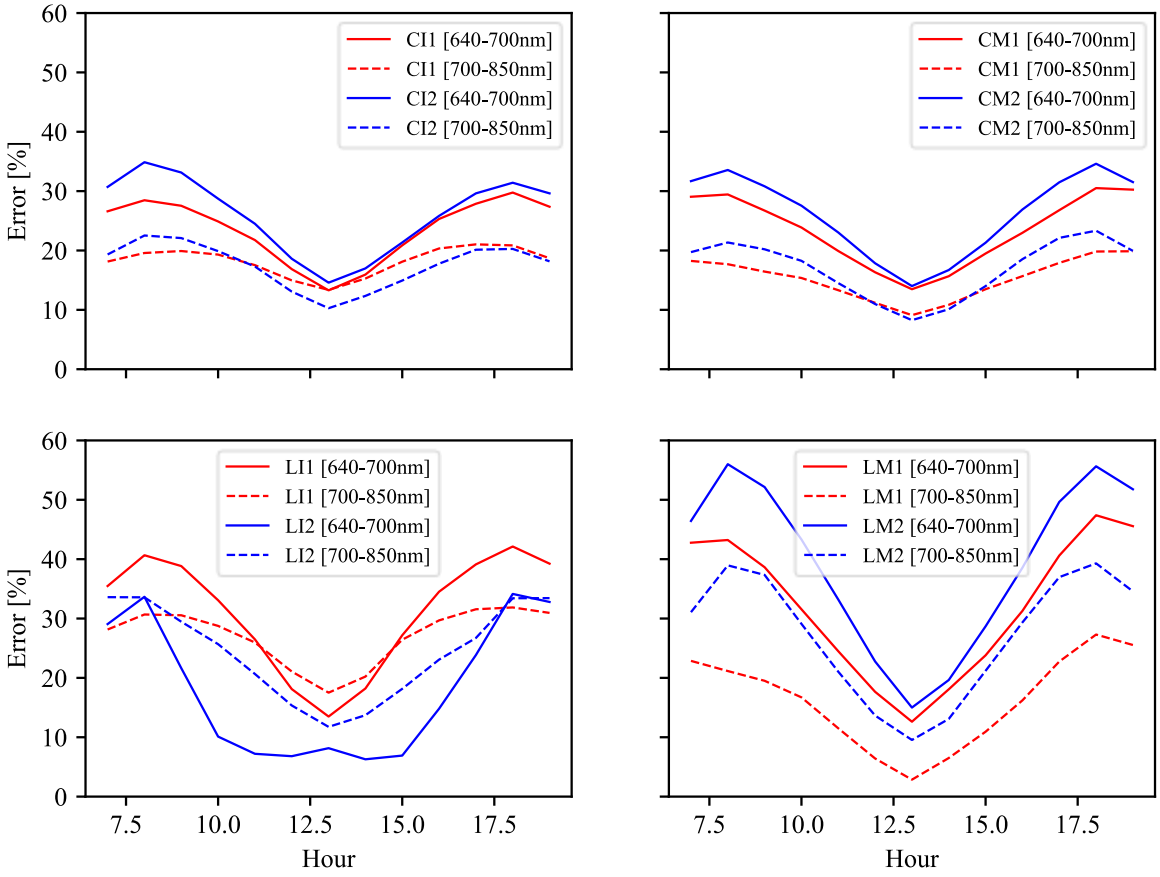

Figure 7: Diurnal evolution of canopy nadir reflectance relative error $MARE_{\rho,1D-3D}$ at 640-700 nm and 700-850 nm due to differences in horizontal heterogeneity in 1D and 3D mock-ups.

3.2. Impact of forest 3D structure on $APAR_{green}$ (1st process)

Figure 8 shows the diurnal PAR absorbed by green leaves ($APAR_{green}$) in the eight 3D and 1D forest mock-ups, and their associated relative error $\varepsilon_{APAR,1D-3D}(t)$. The 3D mock-ups have smaller $APAR_{green}$ than the 1D mock-ups. This is consistent with the larger reflectance of 1D mock-ups compared to the 3D mock-ups, due to the horizontal heterogeneity of the forest plots. $\varepsilon_{APAR,1D-3D}(t)$ is usually smaller than 5%, with a maximum of 10% for LI2 before noon. It is smaller than the relative difference of nadir SIF radiance between 3D and 1D forest abstractions (Figure 5). This indicates that even though the $APAR_{green}$ diurnal changes play an important role, they are not the only cause responsible for the relative difference in the nadir SIF radiance.

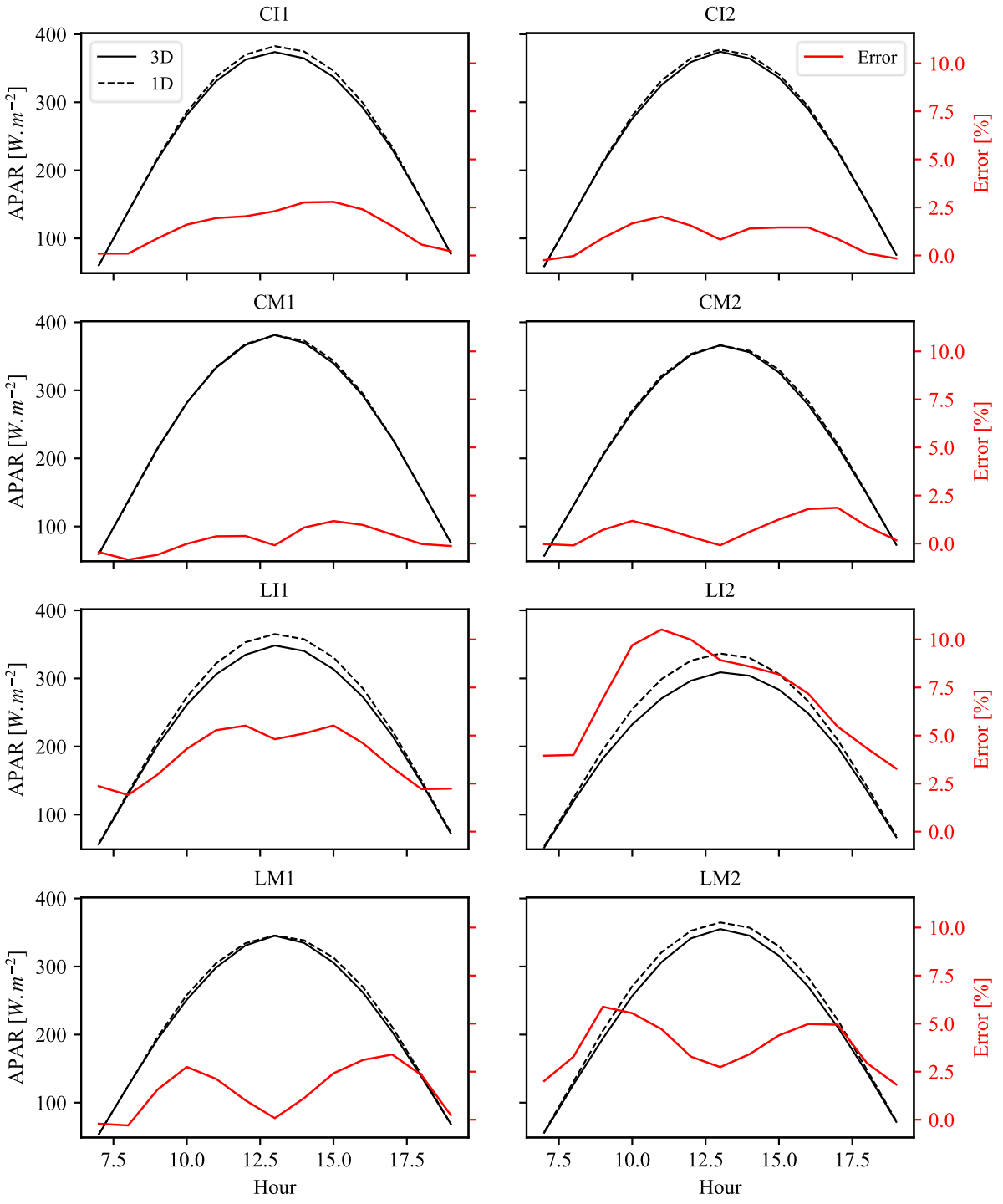

Figure 8. Diurnal PAR absorbed by green leaves ($APAR_{green}$) in 3D and 1D forest abstractions of the eight study sites, and their associated relative error $\varepsilon_{APAR,1D-3D}(t)$ triggered by changes in horizontal heterogeneity of the forest abstractions.

3.3. Impact of forest 3D structure on leaf SIF emission yield (2nd process)

Figure 9 shows the diurnal total SIF emission yield for 3D and 1D mock-ups and the associated diurnal relative error $\varepsilon_{SIF.EY,1D-3D}(t)$ due to horizontal heterogeneity differences. Relative errors are similar and small for all plots. They reveal that in our simulations the impact of forest 3D architecture on SIF emission yield in our simulations is of a less importance. The almost constant diurnal response due to our modeling assumption of constant leaf SIF properties throughout the day.

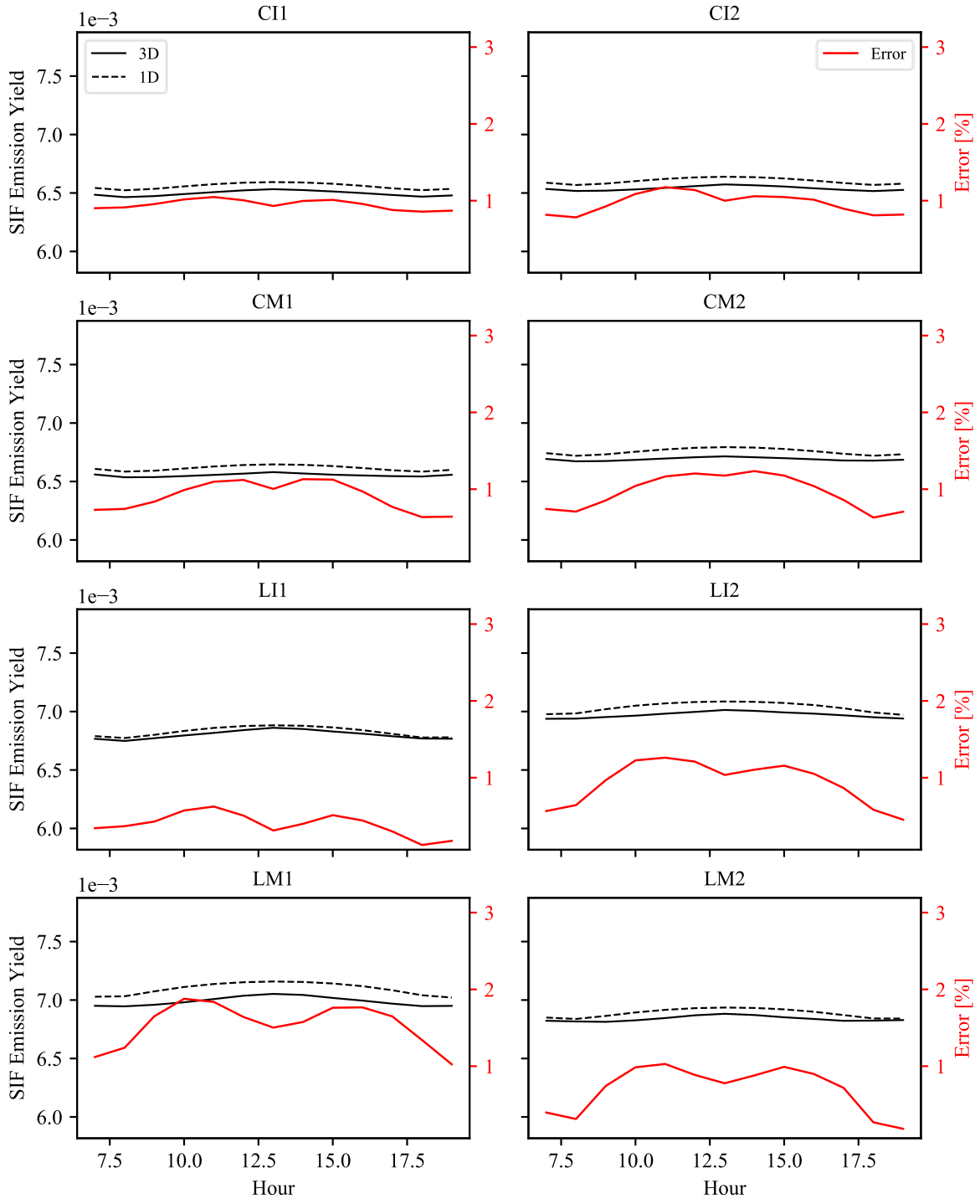

Figure 9. Diurnal SIF emission yield of the 3D and 1D forest mock-ups and relative errors $\varepsilon_{SIF.EY,1D-3D}(t)$

Since SIF emission yield in our simulations is hardly affected by the forest 3D architecture, the diurnal behavior of the DART-FT simulated leaf SIF emission (Figure 10) is understandably very similar to that of $APAR_{green}$ (Figure 8). The relative error $\varepsilon_{SIF.em,1D-3D}(t)$ computed

441 between the 3D and 1D forest abstractions (Figure 10) gathers the combined errors related to
442 both the 1st and the 2nd processes, without being a simple addition of their relative errors.
443 Figure 11 plots the vertical profiles of LAI, and SIF emission in 3D and 1D plots. The LAI of
444 a layer i located between $[i\ m, (i+1)\ m]$ is the total foliar area of this layer divided by the
445 scene area. It shows that the overestimation of the SIF emission in 1D plots compared to 3D
446 plots mainly occurs in the canopy top layers, *i.e.*, $\mathrm{SIF}_{\mathrm{emitted,1D}} > \mathrm{SIF}_{\mathrm{emitted,3D}}$ in these layers.
447 Also, SIF emission is underestimated in the lower layers of 1D plots. Indeed, in 3D forest mock-
448 ups, the forest horizontal heterogeneity leads to better illumination of the lower layers.
449

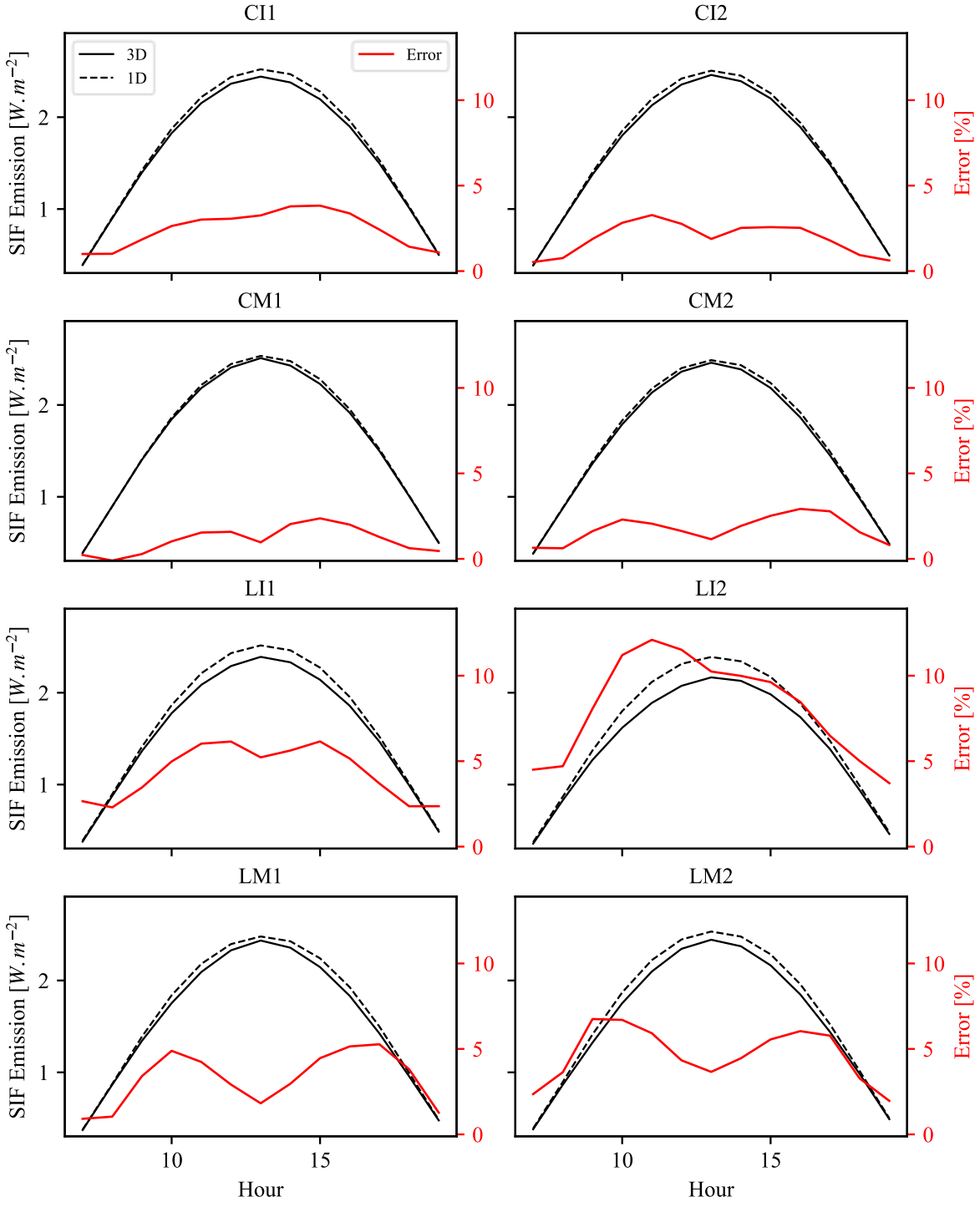

Figure 10. Diurnal leaf SIF emissions for the 3D and 1D forest abstractions and their associated relative errors $\varepsilon_{SIF.em,1D-3D}(t)$.

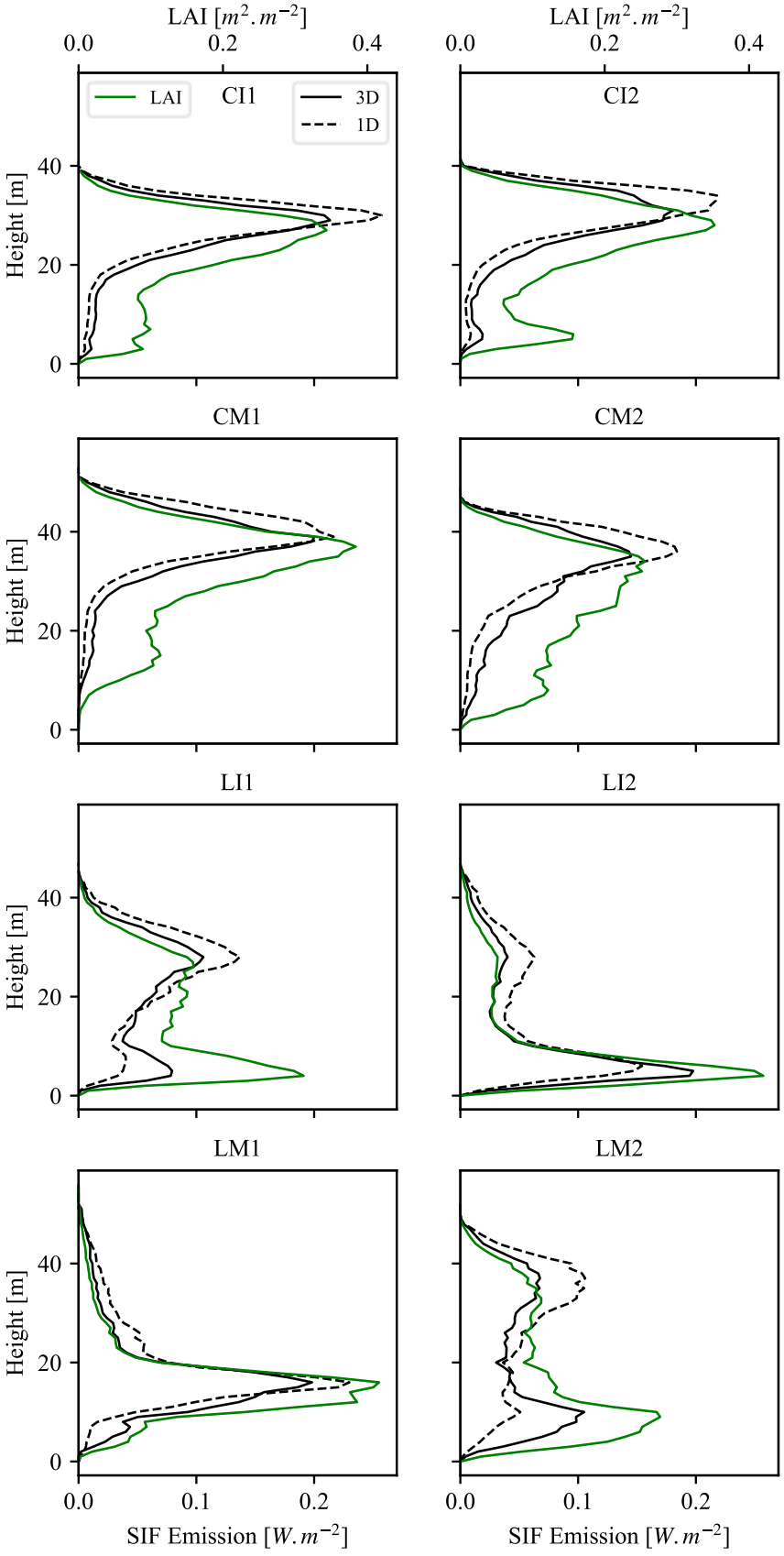

Figure 11. Vertical profiles of LAI and leaf SIF emission at 12.00 (local time).

3.4. Impact of forest 3D structure on SIF escape factor (3rd process)

Figure 12 and Figure 13 show the diurnal SIF escape factor$_{hemi}$ and SIF escape factor$_{nadir}$ of 3D and 1D plots at 640 - 700 nm and 700 nm - 850 nm, and their relative errors $\varepsilon_{SIF.EF,1D-3D}(t)$ and $\varepsilon_{SIF.EFnadir,1D-3D}(t)$ are larger (*e.g.*, > 50% for LM2) than for APAR$_{green}$ (Figure 8) and leaf SIF emission (Figure 10). Therefore, the 3rd process is more affected by forest 3D structure than the first two processes. The SIF escape factor is systematically overestimated in 1D plots. It is larger at 700 nm - 850 nm than at 640 - 700 nm, due to more important multiple scattering mechanisms, which results in lower relative errors at 700 nm - 850 nm than at 640 - 700 nm.

The SIF photons that cannot escape the canopy are absorbed by the canopy elements (i.e., leaves, woody elements, ground). The overestimation of the SIF escape factor of 1D plots compared to 3D plots is also reflected by a higher absorption of SIF photons in 3D plots (Table 6, Table 7). We can note that the ground absorption is greatly underestimated in 1D forest abstractions. Again, this is explained by the forest horizontal heterogeneity.

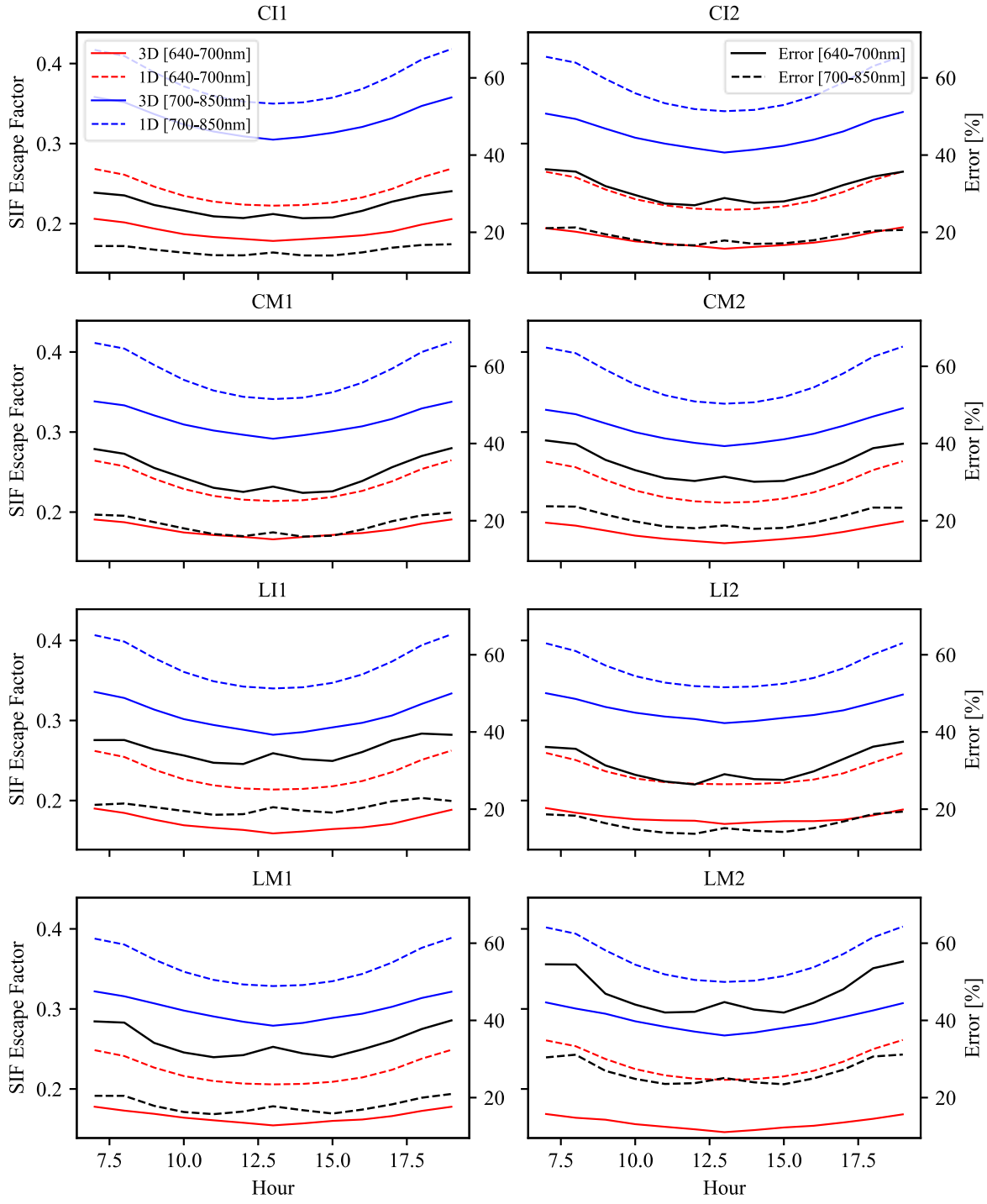

Figure 12. Diurnal SIF escape factor$_{hemi}$ of the 3D and 1D plots and their associated relative errors.

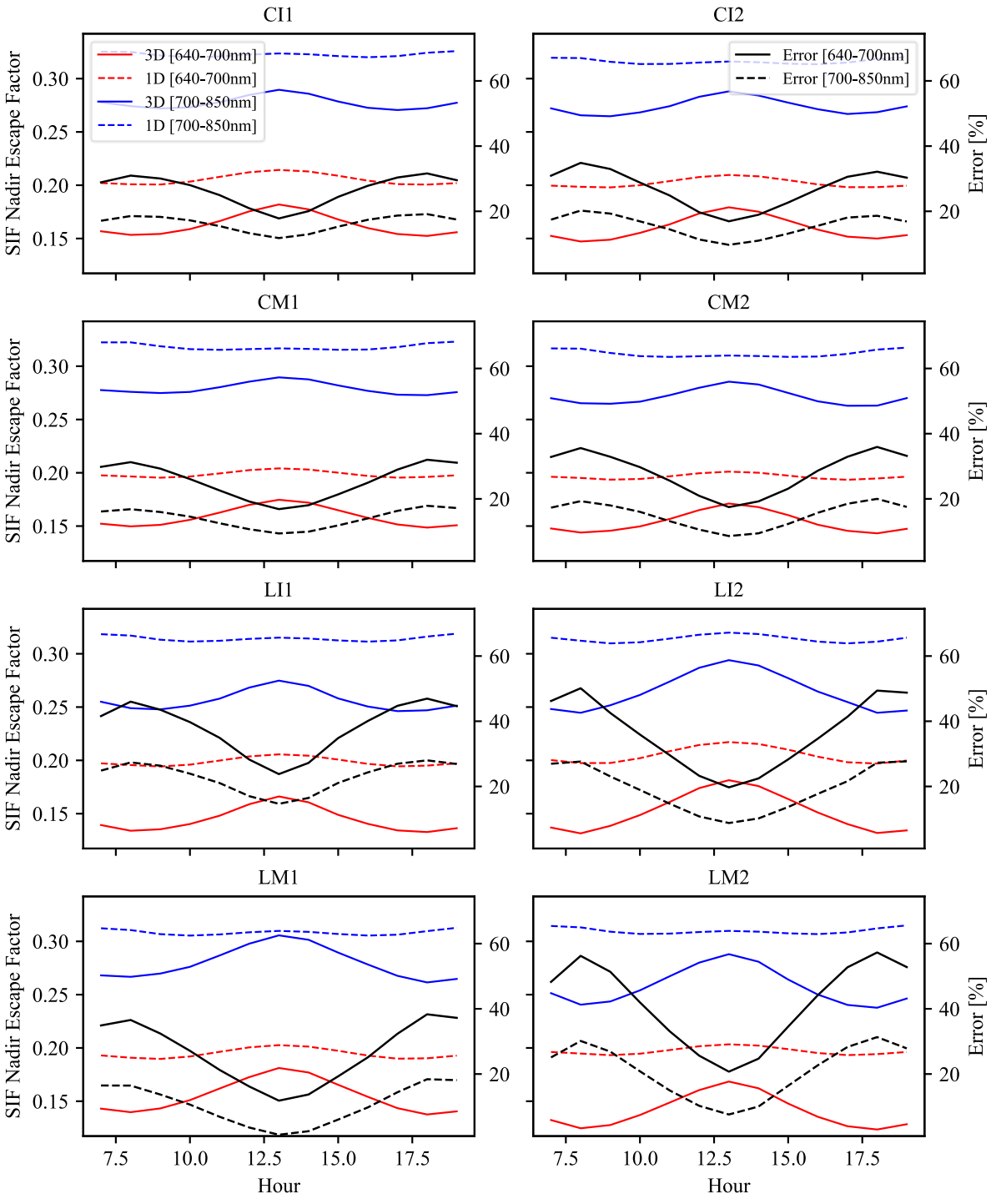

Figure 13: Diurnal SIF escape factor$_{nadir}$ of the 3D and 1D plots and their associated relative errors.

Figure 14 shows the vertical profiles of LAI, woody elements (defined similarly as the vertical profile of LAI), and SIF absorption in 3D and 1D plots. The vertical profiles of SIF absorption

478 show that in 1D forest abstractions, absorption is overestimated in the top layers and
479 underestimated in the bottom layers as for the leaf SIF emission profiles (Figure 11).

480

481 Table 6. SIF absorption by the ground and vegetation (leaves and wood) (640-700nm) at 12pm

Plot	CI1	CI2	CM1	CM2	LI1	LI2	LM1	LM2
Fraction of emitted SIF absorbed by "Ground" (3D)	0,0310	0,0290	0,0230	0,0272	0,0463	0,0704	0,0486	0,0449
Fraction of emitted SIF absorbed by "Ground" (1D)	0,0216	0,0180	0,0130	0,0160	0,0301	0,0584	0,0329	0,0274
Relative difference (%)	-30,28	-38,19	-43,40	-41,38	-35,14	-17,12	-32,44	-38,97
Fraction of emitted SIF absorbed by "Leaves + Wood" (3D)	0,7765	0,7838	0,7903	0,7912	0,7757	0,7352	0,7636	0,7843
Fraction of emitted SIF absorbed by "Leaves + Wood" (1D)	0,7512	0,7545	0,7616	0,7613	0,7461	0,7073	0,7462	0,7492
Relative difference (%)	-3,26	-3,74	-3,63	-3,78	-3,81	-3,79	-2,28	-4,47
Absorption fraction (3D)	0,8075	0,8129	0,8133	0,8184	0,8220	0,8056	0,8123	0,8291
Absorption fraction (1D)	0,7728	0,7725	0,7746	0,7772	0,7762	0,7657	0,7791	0,7766
Relative difference (%)	-4,30	-4,97	-4,76	-5,03	-5,57	-4,95	-4,09	-6,34

482

483 Table 7. SIF absorption by the ground and vegetation (leaves and wood) (700-850nm) at 12pm.

Plot	CI1	CI2	CM1	CM2	LI1	LI2	LM1	LM2
Fraction of emitted SIF absorbed by "Ground" (3D)	0,0905	0,0842	0,0683	0,0768	0,1249	0,1741	0,1282	0,1249
Fraction of emitted SIF absorbed by "Ground" (1D)	0,0716	0,0593	0,0440	0,0502	0,0941	0,1640	0,0952	0,0887
Relative difference (%)	-20,96	-29,52	-35,50	-34,62	-24,68	-5,78	-25,71	-28,95
Fraction of emitted SIF absorbed by "Leaves + Wood" (3D)	0,6194	0,6369	0,6543	0,6600	0,6062	0,5265	0,5897	0,6185
Fraction of emitted SIF absorbed by "Leaves + Wood" (1D)	0,6133	0,6257	0,6453	0,6482	0,5991	0,5098	0,6037	0,6057
Relative difference (%)	-0,98	-1,77	-1,39	-1,79	-1,16	-3,19	2,38	-2,08
Absorption fraction (3D)	0,7099	0,7211	0,7226	0,7369	0,7311	0,7006	0,7179	0,7434
Absorption fraction (1D)	0,6849	0,6850	0,6893	0,6985	0,6932	0,6738	0,6989	0,6944
Relative difference (%)	-3,53	-5,01	-4,61	-5,21	-5,18	-3,83	-2,64	-6,59

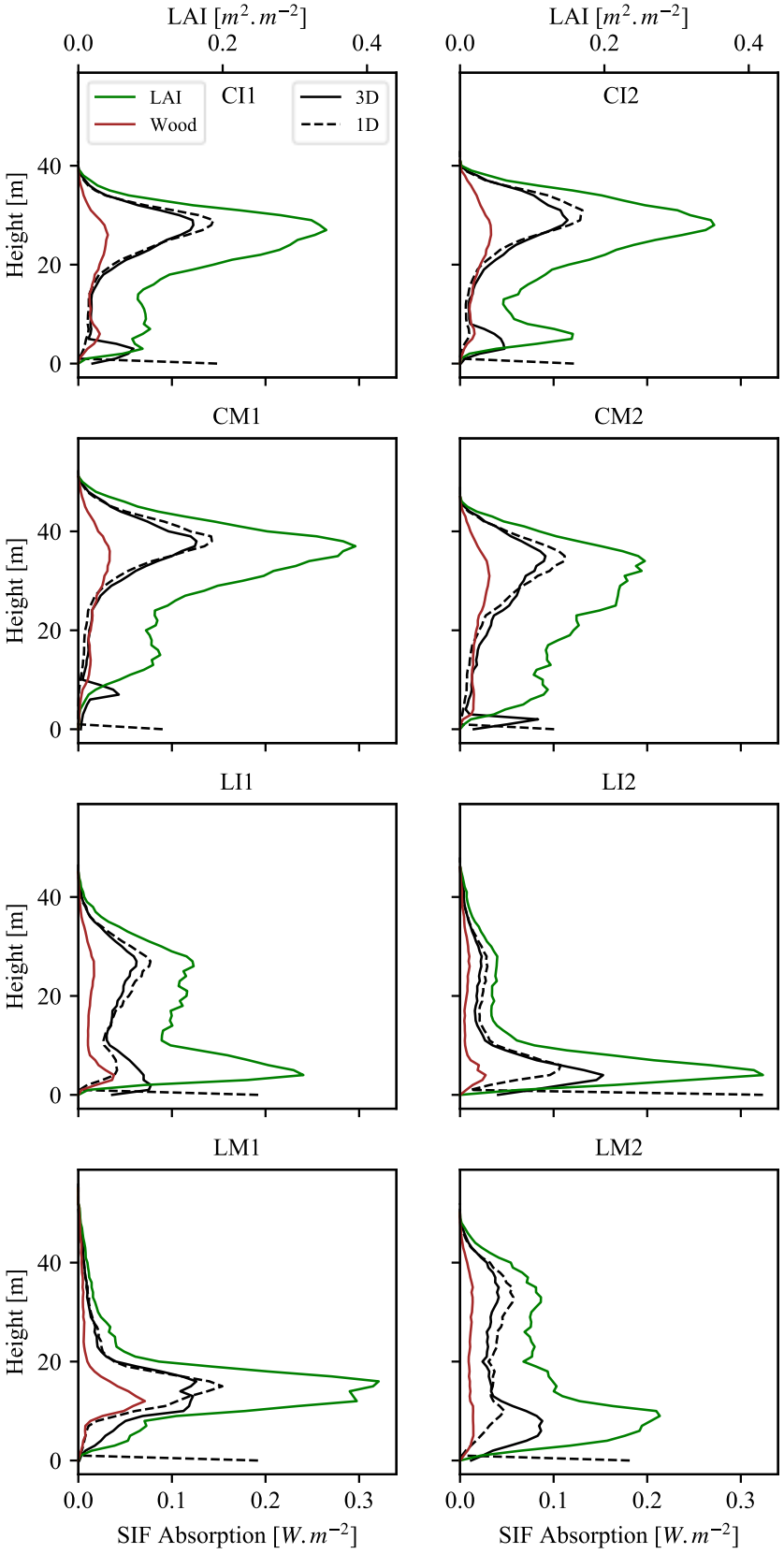

Figure 14.Vertical profiles of LAI, woody elements and SIF absorption in 3D and 1D forest abstractions, at 12.00 (local time).

3.5. Impact of forest 3D structure on SIF nadir yield (2nd and 3rd processes)

Figure 15 shows diurnal values of SIF nadir yield for 3D and 1D forest plots and their relative error $\varepsilon_{SIF.NY,1D-3D}(t)$. SIF nadir yield informs on the potential of nadir viewing remote sensing instruments to observe leaf SIF emission. The diurnal evolution of $\varepsilon_{SIF.NY,1D-3D}$ is similar to the diurnal evolution of total nadir SIF radiance relative error $MARE_{SIF,L_v,1D-3D}$ (Figure 5): larger errors occur in early morning around 8:00 and late afternoon around 18:00, with minimal errors at noon. SIF yield of 1D plots is always overestimated. Also, errors are larger at 640 nm - 700 nm than at 700 - 850 nm. This is due to the lower impact of multiple scattering at 640 - 700 nm than at 700 - 850 nm and therefore the larger impact of shadowing effects at 640 - 700 nm.

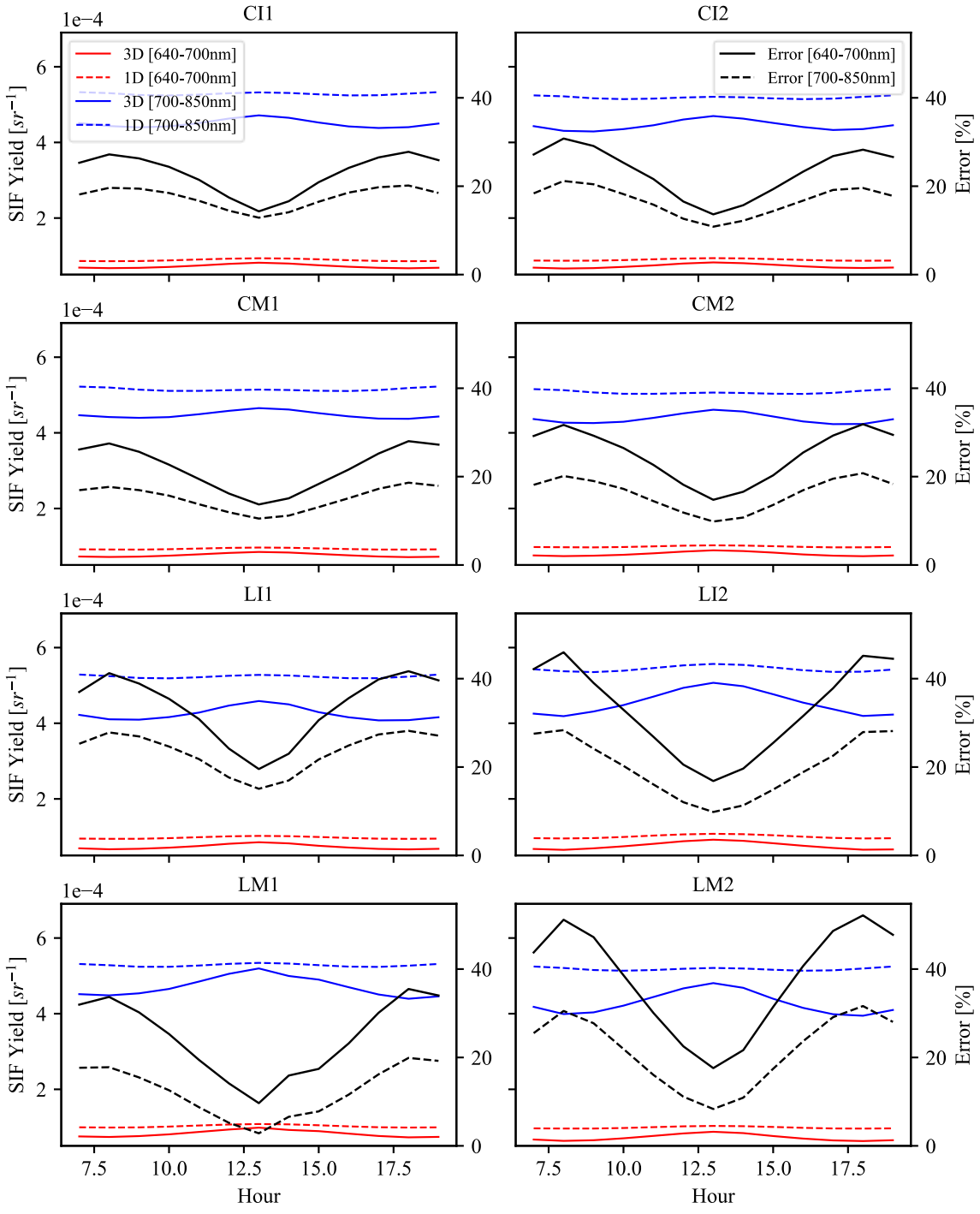

Figure 15. Diurnal SIF nadir yield of 3D and 1D plots and relative errors at 640 - 700 nm and 700 - 850 nm.

3.6. Influence of woody elements

Figure 16 illustrates the impact of woody elements (*i.e.*, branches and trunks) on the canopy SIF signal. It shows PSI, PSII and total SIF nadir spectral radiance at 12.00 of local time for CM1 and LM1 3D plots simulated with (W) and without (NW) woody elements, and also the

associated relative errors $\varepsilon_{SIF,L,NW-W}(\lambda)$ for the total SIF nadir radiance. SIF radiance is significantly higher if wood is neglected in DART simulations, especially in the near-infrared domain. $\varepsilon_{SIF,L_v,NW-W}(\lambda)$ is larger (≈25%) at wavelengths above 750nm, and smaller at wavelengths smaller than 680nm. This is explained by the fact that there is more multiple scattering at these wavelengths, which in turn increases the probability of interception of SIF radiation by woody elements.

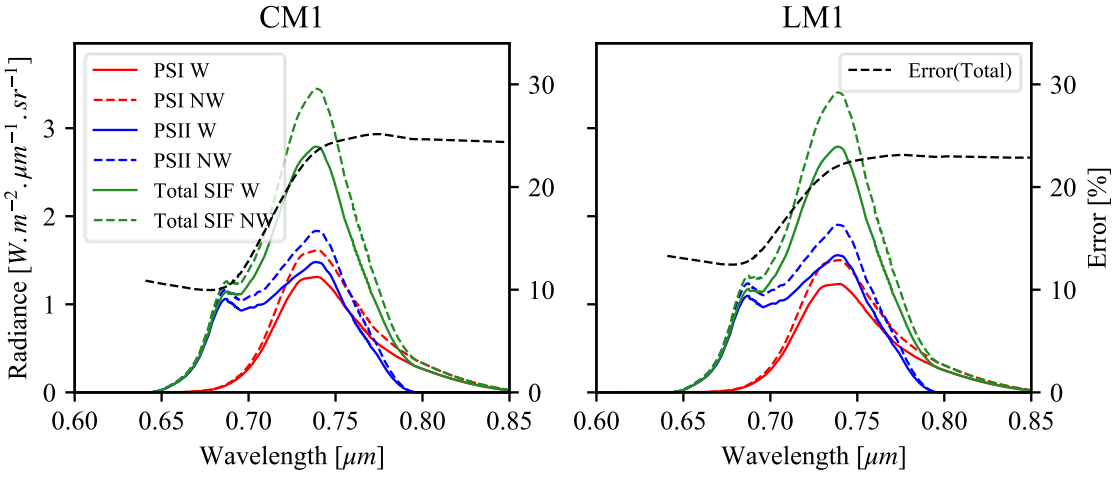

Figure 16. PSI, PSII and total SIF nadir spectral radiance and error $\varepsilon_{SIF,L_v,NW\text{-}W}(\lambda)$ of 3D CM1 and LM1 plots simulated with (W) and without (NW) woody elements at 12.00 (local time)

The diurnal relative error of the SIF total nadir radiance for CM1 and LM1 3D plots simulated without woody elements, compared to presence of woody elements, varies over the course of the day (Figure 17). It is lowest at solar noon for LM1 and relatively stable for CM1. The time variability for LM1 is explained by the fact that its leaf and wood densities are in the canopy upper layers, which increases the influence of horizontal heterogeneity, and consequently the occurrence of smaller errors at noon. Conversely, for CM1, the leaf and wood densities are larger at lower tree heights, which leads to smaller horizontal heterogeneity effects, including smaller shadow effects.

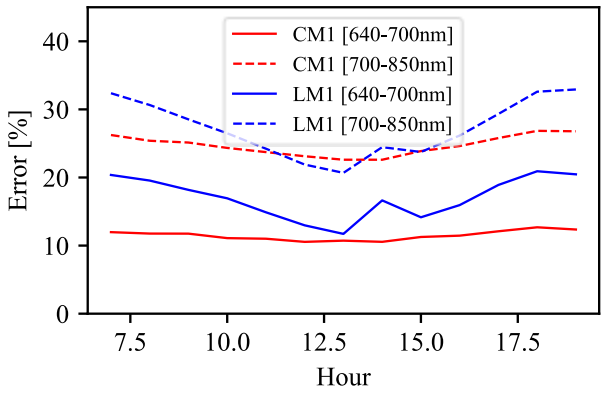

Figure 17. Diurnal relative error of total nadir SIF radiance $MARE_{SIF,L_v,NW-W}(t)$ of the CM1 and LM1 3D forest plots simulated without woody elements. 640 – 700 nm and 700 – 850 nm.

The influence of woody elements on the remotely sensed SIF signal can be split into shading and blocking effects. These effects are not independent. The shading effect corresponds to the shading of leaves by woody elements during the direct sun and atmosphere illumination of the forest scene. It limits the absorption of PAR by chlorophylls and consequently decreases leaf SIF emission (*i.e.*, 1st process). The blocking effect corresponds to the interception (*i.e.*, absorption and scattering) by woody elements of SIF radiation from its leaf emission to the exit of the forest canopy along the viewing direction of the remote sensing sensor. Figure 18 illustrates the magnitude of the shading effect. It shows the DART simulated diurnal $APAR_{green}(t)$ and the associated relative error $\varepsilon_{APAR,NW-W}(t)$, for the CM1 and LM1 3D plots with and without woody elements. $APAR_{green}$ is always larger for the plots without wood, as expected. The relative error associated to the shading effect greatly varies over the selected day. It is minimal at solar midday, when trunks and branches are blocking the least amount of direct solar radiation, and largest in early morning and late afternoon when trunks and branches are blocking a larger part of direct PAR. Figure 19 illustrates the blocking effect. It shows the diurnal SIF nadir escape factor at [400nm-700nm] and [700nm-850nm] for the CM1 and LM1 3D plots simulated with (W) and without (NW) woody elements, and the associated relative error $\varepsilon_{SIF.NEF,NW-W}(t)$. This relative error is nearly constant over the day, conversely to the relative error on the canopy $APAR_{green}$. Indeed, as a first approximation $SIF_{nadir\ EF}$ corresponds to a quantity that is relatively constant: the sum of the canopy "direct – direct" and "diffuse – direct" transmittance (Vermote et al., 1997) weighted by a normalized vertical distribution of leaf SIF emitted radiation. The "diffuse – direct" transmittance is much smaller at [640-700nm] than at [700nm-850nm] because vegetation absorbs much more at [640-700nm] than at [700nm-850nm]. Since the blocking effect of wood is more pronounced for oblique

directions, it has a higher impact on the "diffuse – direct" than on the "direct – direct" transmittance. This explains that $\varepsilon_{SIF.NEF,NW-W}(t)$ is smaller at [640-700nm] than at [700nm-850nm].

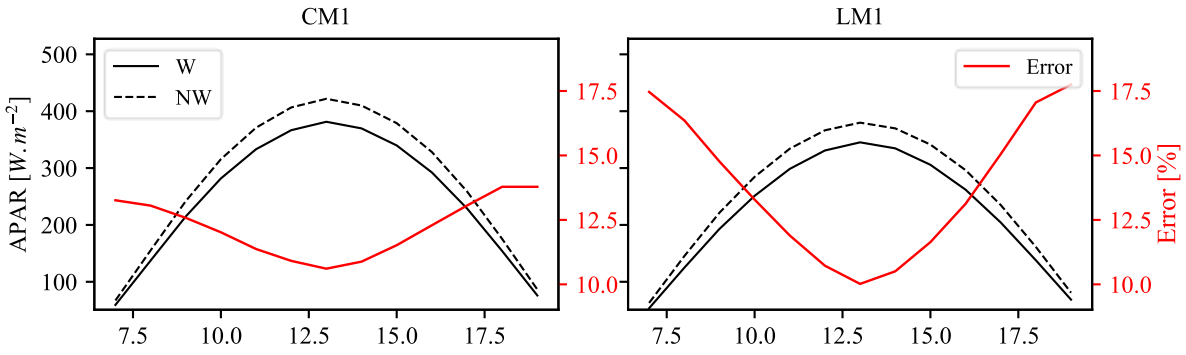

Figure 18. Diurnal $APAR_{green}$ of CM1 and LM1 3D forest plots with (Wood) and without (No Wood) woody elements and their associated relative errors $\varepsilon_{APAR,NW-W}(t)$.

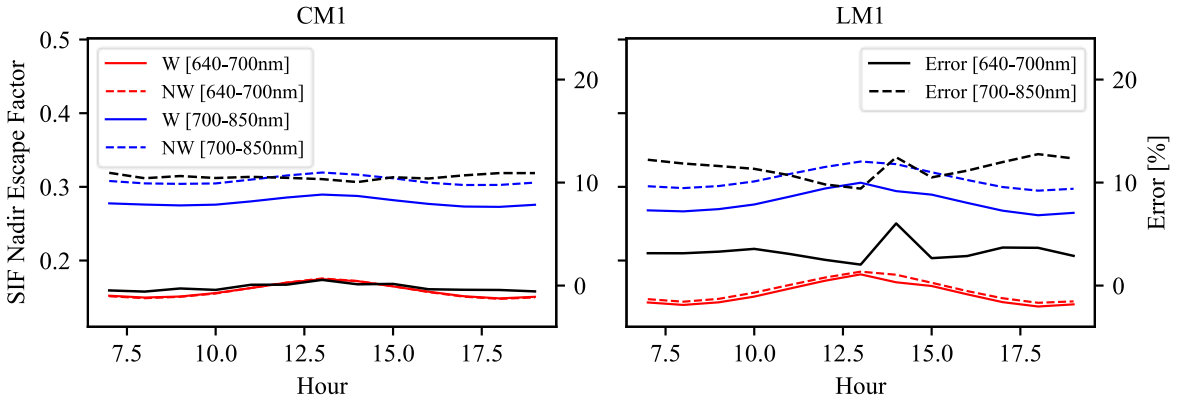

Figure 19. Diurnal SIF nadir escape factor over [640nm-700nm] and [700nm-850nm] of CM1 and LM1 3D plots simulated with (W) and without (NW) woody elements and associated relative error $\varepsilon_{SIF.NEF,NW-W}(t)$.

4. Discussion

4.1. 3D structure of the forest study sites

The comparison of DART simulated SIF and non SIF radiometric quantities of 1D and 3D abstractions of the studied forest plots highlights the influence of the forest architecture, and especially the forest horizontal heterogeneity, on these quantities: $APAR_{green}$ ($\varepsilon_{APAR,1D-3D}(t)$: Figure 8), SIF emitted ($\varepsilon_{SIF.em,1D-3D}(t)$: Figure 10), $SIF_{nadir\ yield}$ ($\varepsilon_{SIF.NY,1D-3D}(t)$: Figure 15), canopy SIF exitance and escape factor ($\varepsilon_{SIF.EF,1D-3D}(t)$: Figure 12), SIF nadir yield ($\varepsilon_{SIF.NY,1D-3D}(t)$: Figure 15) and reflectance (Figure 6). Braghiere et al. (2021) found that the

SIF modeling was improved by introducing a clumping index (Nilson, 1971; Pinty et al., 2006) to replicate the behavior of structurally complex 3D canopies in the 1D model CliMA-Land (based on the mSCOPE model (Yang et al., 2017)). In this study, simulating the SIF signal while neglecting the forest horizontal heterogeneity can lead to very large relative errors, especially for logged "L" forest sites where they can reach 60%. For example, the error on SIF radiance $MARE_{SIF,L_v,1D-3D}(t)$ is higher for the logged "L" forest sites (Figure 5). This is consistent with the fact that these forest sites have a higher horizontal heterogeneity, with a higher canopy height variability and a higher number of pure bare ground pixels, as shown in Table 4 and in the height maps (Figure 2). Generally, the horizontal heterogeneity tends to decrease the SIF signal that escapes the forest canopy. The vertical heterogeneity appeared to have an opposite effect in most cases. These points are further discussed below.

4.2. Effect of 3D architecture on the three processes driving SIF generation

Several sensitivity analysis studies based on radiative transfer modeling were carried out to assess the impact of some structural parameters on the SIF such as leaf density, leaf angular distribution and fractional vegetation cover (Tong et al., 2021; Zeng et al., 2020), the contribution of understory (Hornero et al., 2021), clumping and woody elements impacts (Malenovský et al., 2021). In this study, we assessed the impact of canopy heterogeneity on SIF and processes driving its generation. High relative errors in nadir SIF radiance were observed for the 8 forest plots due to neglecting the 3D forest architecture, in particular, the horizontal heterogeneity. Errors were maximal in the hours of the day with lowest PAR having the larger shading effects. They were higher than 50% in the most heterogeneous plots (LI2 and LM2) and at [640-700nm] where shading effects are higher due to the lower importance of multiple scattering in the canopy. The errors in the canopy SIF radiance where forest horizontal architecture was neglected (*i.e.*, 1D forest plots) can be explained by two processes that drive the SIF signal generation.

1) $APAR_{green}$ is overestimated if the forest horizontal architecture is neglected. It leads to an overestimation of the SIF emitted by leaves. This overestimation of SIF emission mainly occurs in the upper canopy layers. This is mainly due to the fact that in the forest 1D abstractions, the leaves of the top layers are homogeneously distributed, whereas in actual 3D forests, they can be greatly clumped at two levels: they are grouped within distinct tree

crowns, and also, they tend to be clumped within each tree crown. Combined, these effects result in upper layers of 1D plots that are more efficiently illuminated than in 3D plots, which explains higher SIF emission in 1D plots than in 3D plots. However, in the bottom layers, the SIF emission of 1D plots is underestimated. Indeed, the roughness of the actual canopy causes a better penetration of light to the bottom layers of the 3D plots, compared to the associated 1D plots, where the top layers of the canopy shade more efficiently the light. This is illustrated by Figure 11: the profile of SIF emission is similar to the profile of LAI with a higher $\frac{\mathrm{SIF_{emitted}}}{\mathrm{LAI}}$ value in the top layers. This means that the SIF emission per leaf area unit is higher for the top layers because leaves in the top layers are able to capture more light than the leaves in the bottom layers.

2) The emitted SIF radiation has a higher ability to escape from the canopy in the 1D abstractions of the forest plots both for the upward nadir direction (*cf.* SIF yield in Figure 15), and for the upper hemisphere (*cf.*, SIF escape factor$_{hemi}$ in Figure 12). It corresponds to an underestimation of the total absorption fraction of SIF in all 1D abstractions of the 8 forest plots (Table 6, Table 7). This underestimation of SIF absorption is rather large for the ground, and larger for [640-700nm] (*i.e.*, between -17 and -43% for [640-700nm], between -5% and -35% for [700-850nm]) and rather small for "Leaf + Wood" (i.e., between -2 and -4% for [640-700nm], between -1 and -3% for [700-850nm]). LM1 has a slightly different behavior: in its 1D abstraction, the absorption of "Leaf + Wood" is slightly overestimated for [700-850nm] (*i.e.*, around 2%). Part of the underestimation of SIF absorption by the ground for 1D plots is due to the smaller area of the ground in the 1D plot compared to the 3D plot where topography is simulated (Table 2).

The vertical profiles of SIF emission (Figure 11) and absorption (Figure 14) of the 1D plots show that emission and absorption are both overestimated in the top layers and underestimated in the bottom layers. A main particularity for the absorption profile is the influence of the ground. It shows sharp peaks at 0 m height for 1D simulations. For the 3D abstractions of the forest plots, the height of the ground is variable. Therefore, ground absorption peaks appear in the bottom for the “C” plots. These peaks are not visible in “L” plots, because of important absorption of the leaves and woody elements in the bottom part of the canopies.

4.3. Influence of 3D architecture on the canopy reflectance.

As a first approximation, SIF emission can be considered as the reflection of radiation at a different wavelength from that of the incident radiation. Therefore, it makes sense to find similar errors for SIF radiance $MARE_{SIF,L_v,1D-3D}(t)$ and canopy reflectance $MARE_{\rho,1D-3D}(t)$. However, SIF has some particularities that may differ from reflectance. Indeed, the SIF emission only comes from leaf elements. Other components of the canopy (*i.e.*, woody elements and ground) do not emit SIF radiation, even though they contribute indirectly by scattering SIF radiation emitted by foliar elements. On the other hand, all elements of the canopy can contribute directly to the canopy radiance. Since bare ground does not directly contribute to the SIF radiance of forest plots, pure bare ground pixels have SIF radiance values close to zero. A nadir viewing sensor cannot see the bare ground in 1D plots, conversely to 3D plots. Hence, $MARE_{SIF,L_v,1D-3D}$ tends to be larger than $MARE_{\rho,1D-3D}$ because for canopy reflectance, pure bare ground pixels and vegetation pixels have values of the same order of magnitude. This explains that for LI2, the SIF radiance errors (Figure 5) are notably larger than the reflectance errors (Figure 7). Indeed, compared to the other sites (cf. Table 4), the LI2 site has the particularity to have the largest surface of ground without vegetation cover. Therefore, its $MARE_{SIF,L_v,1D-3D}$ tends to be large, especially if the ground reflectance is high. Multiple scattering explains that SIF radiance errors are larger in 640 – 700nm than in 700-850nm domain. Indeed, in the 700 – 850nm, the shadowing effects due to the canopy structure are attenuated by the important multiple scattering in this spectral domain. It is also the case for canopy reflectance in most cases expect for LI1 (in the middle of the day) and LI2 (Figure 7). This is because we only consider the 640 – 700nm spectral region and not all the 400 – 700nm for the comparison with SIF. Indeed, In Figure 6, we see that for these plots, $\varepsilon_{\rho,1D-3D}(\lambda)$ has a local minimum around 680nm, and even a sign change for LI2.

4.4. Influence of woody elements

Although woody elements do not generate SIF emission, their interaction with the photosynthetically active light and with SIF radiation emitted by leaves can highly impact the SIF signal, as shown in (Malenovský et al., 2021). We studied their influence on the SIF signal by comparing the SIF signal of forest plots that was simulated without and with woody elements. For that, we removed the woody elements from the 3D abstractions of the CM1 and LM1 plots. It appeared that the plots without woody elements had a higher simulated SIF radiance,

662 especially in the 700-850 nm spectral domain where multiple scattering is highly influenced by
663 the presence of woody elements. The influence of woody elements is smaller in the 640 – 700
664 nm spectral domain. The shading effect of woody elements on SIF emission leads to a lower
665 $APAR_{green}$ (Figure 18) and therefore triggering less SIF emission. It was shown to be more
666 important than the blocking effect of woody elements (Figure 19), especially for oblique solar
667 directions and at 640-700 nm.

668

669 **5. Concluding remarks**

670 This study investigated the potential effect of the forest 3D architecture on diurnal nadir SIF
671 RS observations and SIF emissions inside the canopy. We studied the following three processes
672 responsible for modulation of the canopy SIF signal: i) the attenuation of incident PAR in the
673 canopy, ii) the leaf SIF emission efficiency, and iii) the attenuation of the SIF between its place
674 of emission and its observation above the canopy. The potential impact of woody elements on
675 the SIF signal of forest stands was also investigated. Eight study sites, located within the
676 temperate deciduous forest in the Smithsonian Environmental Research Center, were modeled
677 using the DART-FT and DART-Lux radiative transfer modes and the effects of their forest
678 architecture were assessed by comparing SIF quantities of the sites simulated as 3D, 1D and
679 0D scenes.

680 Although several general trends common to all sites were clearly identified, some results
681 were of the site-specific nature due to structural differences in canopy horizontal and vertical
682 heterogeneity. Results revealed that the horizontal heterogeneity of forests had a larger
683 influence than the canopy vertical heterogeneity. Therefore, for a correct modeling of remotely
684 sensed SIF signals of spatially heterogeneous canopies, one must consider the full 3D
685 architecture of forests and not only their vertical heterogeneity as being assumed in 1D RTMs.

686 Studying the propagation of SIF radiation within the canopy through quantitative
687 parameters, such as the SIF escape factor and the nadir SIF yield, is essential for linking the
688 SIF RS observation to the canopy foliage SIF emission. Three key indicators were able to
689 explain most of the differences between the nadir SIF signal of canopies simulated as 3D and
690 1D landscapes. The SIF escape factor (ε_{1D-3D} up to 40%) was shown to be the most indicative
691 parameter, followed by the attenuation of incident PAR and consequently reduction of
692 $fAPAR_{green}$ (ε_{1D-3D} less than 5%), and the SIF emission yield (ε_{1D-3D} less than 2%) induced
693 by different *fqe* values assigned to the sun- and shade-adapted leaves. Our results indicated that

694 the influence of forest architecture on SIF escape factor and nadir SIF yield values (ε up to 40%)
695 varies in time, with differences in forest stand structure and per spectral domain, with ε being
696 always greater for the wavelength range of 640 – 700 nm than for the range of 700 – 850 nm.
697 The presence of woody elements inside DART-simulated forest scenes appeared to have
698 a relatively large influence on the canopy SIF radiance through the two effects: i) a shading of
699 photosynthetically active foliage and ii) a blocking (obstruction) of SIF radiation. The relative
700 error associated with the neglection of wood existence ranged between 10% and 35%,
701 depending on analyzed spectral domain and forest site, where the relative errors for the shading
702 effect were ranging between 10 and 20%, and for the blocking effect between 0 and 10%.
703 Although this work underlines the usefulness of 3D RTMs for investigating physical
704 bases linking RS SIF observations with SIF emitted inside a forest canopy, there are several
705 modeling aspects that should be reconsidered and improved in the follow-up work. For example,
706 leaf SIF emission properties were assumed to be constant throughout the day, *i.e.*, the actual
707 modulation of SIF emission by local environmental conditions (*e.g.*, leaf temperature, air
708 humidity, etc.) was not considered. Remediation of this strong assumption requires inclusion of
709 a full canopy energy balance in the DART modeling scheme, that would allow to account for
710 crucial environmental parameters of radiative (*i.e.*, visible, near infrared and thermal infrared
711 radiation budgets) as well as non-radiative processes (*e.g.*, photosynthesis). This is currently
712 possible only by coupling DART with a 1D energy budget model like SCOPE. The development
713 of a 3D energy balance modeling, based on DART radiation budget computations, is on the list
714 of our future works. Three major DART-Lux modeling works, partly completed, will also be very
715 helpful for rapid simulations of SIF over larger landscapes: SIF and thermal emission of
716 vegetation simulated as turbid medium, and 3D radiative budget, including SIF emission.
717

718 **Acknowledgements**

719 This work was funded as the “Fluo3D” project by the TOSCA program of the French National
720 Space Agency (Centre National d'Etudes Spatiales), with financial support from the CNRS
721 through the 80|Prime program.). The authors are grateful to the Australian Research Council
722 Future Fellowship ‘Bridging Scales in Remote Sensing of Vegetation Stress’ (FT160100477)
723 for support of Z. Malenovský, to W. Liu from Fujian Agriculture and Forestry University for
724 providing leaf fluorescence quantum efficiencies for forests, to Geoffrey G. Parker from SERC
725 for providing the geolocations and management categories of the selected study sites and to

Petya K. Campbell from NASA Goddard Space Flight Center and University of Maryland for providing leaf biochemical properties measured for the selected SERC forest species and her contribution to the improvement of the manuscript.

Appendix 1: Conversion of turbid voxels into triangles clouds.

Each turbid cell of a forest mock-ups is converted to a linear combination of a few 3D objects (i.e., made of facets) among N cell objects whose LAI is LAI_n, with $n \in [1\ \ N]$. Accuracy on the simulated LAI is 10^{-2} with N = 16 with LAI_n equal to 0.01, 0.02, 0.05, 0.1, 0.2, 0.3, 0.4, 0.5, 1, 1.5, 2, 2.5, 3, 3.5, 4, and 4.5. The area of a facet in each cell object is 5.10^{-5} m^2 if $LAI_n \leq 2$, and 10^{-4} m^2 if $LAI_n > 2$.

The algorithm of the conversion method is based on the value of LAI_{cell} of the turbid cell to convert:

* Scene $LAI_{cell} < 1$: the turbid cell is replaced by two 3D cell objects at most:
  - 1st cell object (i.e., cell object with the larger LAI): it can be only enlarged. Its enlargement is 5% at most. If it should be 5% to get the exact LAI of the turbid cell, then a 2nd cell is introduced.
  - 2nd cell object: it can be enlarged or shrunk.
* Scene $LAI_{cell} > 1$: the turbid cell is replaced by three cell objects cells at most:
  - 1st cell object: it cannot be scaled. If precision $< 10^{-2}$, then a 2nd cell is used.
  - 2nd cell object: it can be only enlarged, by 5% at most. A 3rd cell is used if a larger enlargement is needed.
  - 3rd cell object: it can be enlarged or shrunk.

Examples of replacement of a turbid cell (LAI_{cell}) by up to 3 3D cell objects:

- $LAI_{cell} = 0.92$ (Figure 20). Replacing it by a cell object of LAI = 1, (*i.e.*, shrinking it by a factor 0.96) would create 2 cm wide empty spaces at the cell borders. Therefore, it was instead replaced by a cell object of LAI=0.5 and a cell object of LAI = 0.4 enlarged by a factor 1.025. (*i.e.*, $0.92 \approx 0.5 + 0.4 \times 1.025^2$).
- $LAI_{cell} = 0.23$ ($\approx 0.2 + 0.02 \times 1.2247^2$) $\Rightarrow$ 2 cell objects: $LAI_n = 0.2$, $LAI_n = 0.02$ scaled by 1.2247
- $LAI_{cell} = 0.48$ ($\approx 0.4 + 0.1 \times 0.8944^2$) $\Rightarrow$ 2 cell objects: $LAI_n = 0.4$, $LAI_n = 0.1$ shrunk by 0.8944

- LAI_{cell} = 0.93 ($\approx 0.5 + 0.4 \times 1.0368^2$) $\Rightarrow$ 2 cell objects: LAI_n=0.5, LAI_n=0.4 scaled by 1.0368
- LAI_{cell} = 0.64 ($\approx 0.5 + 0.1 + 0.05 \times 0.8944$) $\Rightarrow$ 3 cell objects: LAI_n = 0.5, LAI_n= 0.1, LAI_n= 0.05 shrunk by 0.8944.

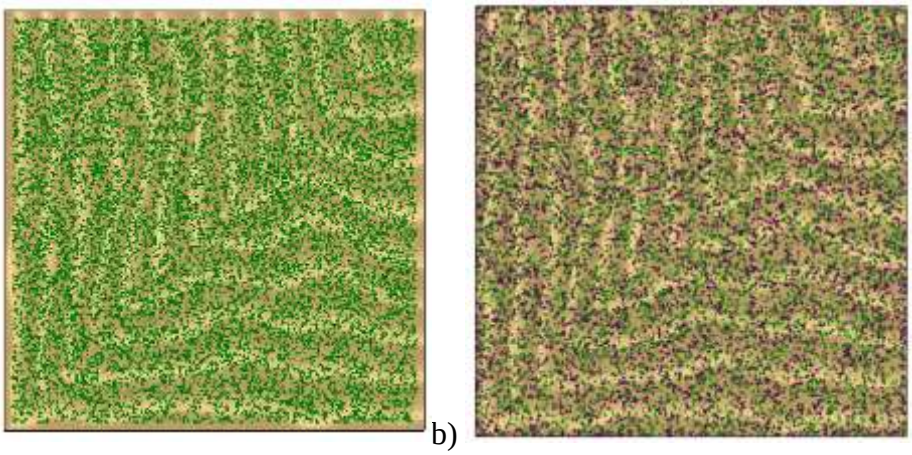

a) b)

Figure 20. Top view of a turbid cell of LAI = 0.92 simulated with N cell objects. a) N=1: cell object of LAI = 1 is shrunk by a factor 0.96, resulting in empty space along the borders of the cell. b) N=2: 3D object of LAI = 0.5 (green) + 3D object of LAI = 0.4 enlarged by a factor 1.025 (purple).

This conversion method ensures that the mock-up is represented by a finite number of 3D objects (i.e., 16x3 = 48). It also avoids the appearance of holes due to shrinking the 3D objects, and large exceeding of voxel limits due to the enlargement of 3D objects. M = 3 samples of each cell object are randomly used to introduce a random variability in the mock-ups. Also, a random rotation of 0°, 90°, 180° or 270° relative to the vertical axis ensures more randomness of the simulated cell.

Appendix 2: Equivalence between DART-FT and DART-Lux simulations

Our work combines DART-FT simulations of radiative budget and DART-Lux simulations of scene radiance / reflectance. Therefore, the consistency of these two DART modes is an essential point. Relative differences of DART-FT and DART-Lux can be as small as 10^{-5} depending on their modeling parameters of each mode. For example, the number of discrete directions for DART-FT, and the number of samples per pixel for DART-Lux. Here, this similarity is illustrated

through the comparison of the reflectance and SIF radiance of LM1, using model parameters hat were used in our work. Figure 21 indicates that MARE is equal to 1.3% for scene reflectance, 2.1% for PSI radiance, and 1.72% for PSII radiance.

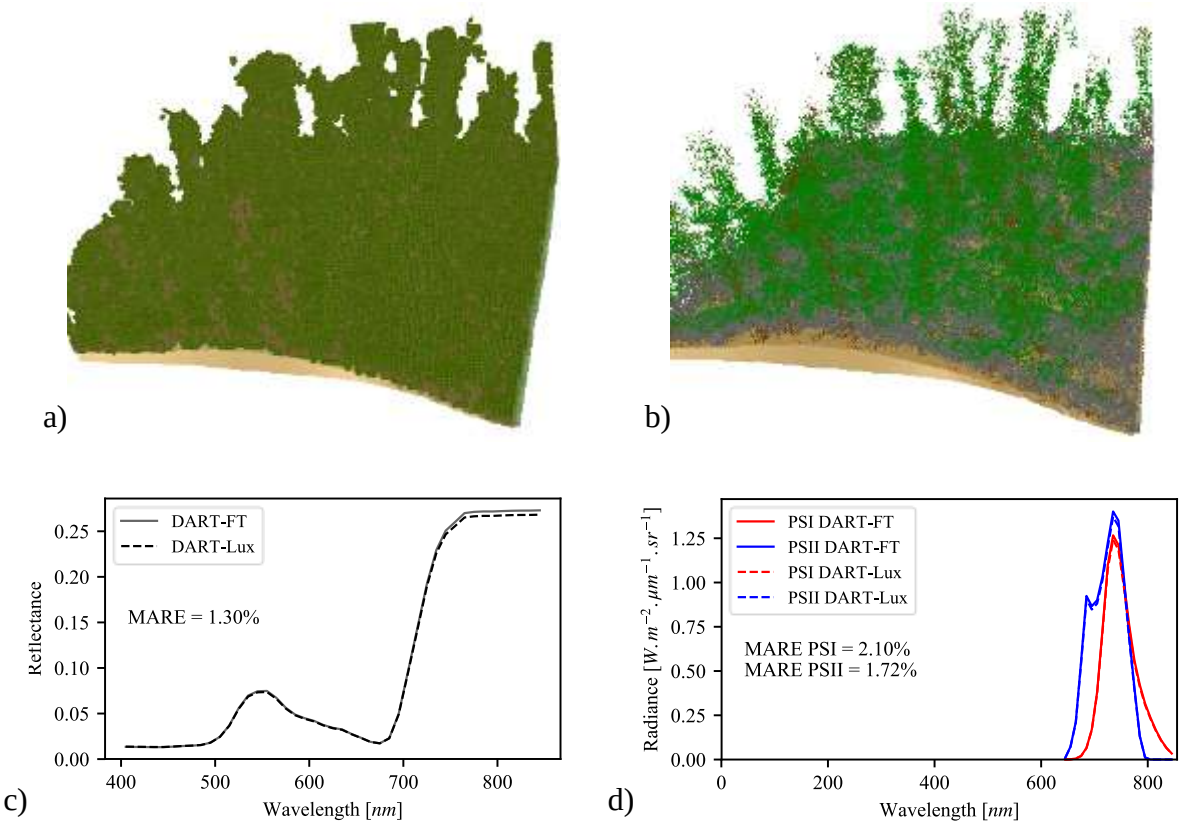

Figure 21: Comparison of DART-FT (turbid voxels) and DART-Lux (turbid voxels transformed to triangles) for a 10m x 10m subscene of CI1. a) LM1 turbid mock-up. b) LM1 triangles cloud mock-up (after conversion). Green: sun-adapted leaves, Grey: shade-adapted leaves, Brown: woody elements. c) DART-FT and DART-Lux scene reflectance. d) Scene PSI and PSII radiance simulated by DART-FT and DART-Lux.

References

Ač, A., Malenovský, Z., Olejníčková, J., Gallé, A., Rascher, U., & Mohammed, G. (2015). Meta-analysis assessing potential of steady-state chlorophyll fluorescence for remote sensing detection of plant water, temperature and nitrogen stress. *Remote Sensing of Environment*, *168*, 420–436. https://doi.org/10.1016/j.rse.2015.07.022

Baker, N. R. (2008). Chlorophyll Fluorescence: A Probe of Photosynthesis In Vivo. *Annual Review of Plant Biology*, *59*(1), 89–113. https://doi.org/10.1146/annurev.arplant.59.032607.092759

Braghiere, R. K., Wang, Y., Doughty, R., Sousa, D., Magney, T., Widlowski, J.-L., Longo, M., Bloom, A. A., Worden, J., Gentine, P., & Frankenberg, C. (2021). Accounting for canopy structure improves hyperspectral radiative transfer and sun-induced chlorophyll fluorescence representations in a new generation Earth System model. *Remote Sensing of Environment*, *261*, 112497. https://doi.org/10.1016/j.rse.2021.112497

Brede, B., Verrelst, J., Gastellu-Etchegorry, J.-P., Clevers, J. G. P. W., Goudzwaard, L., den Ouden, J., Verbesselt, J., & Herold, M. (2020). Assessment of Workflow Feature Selection on Forest LAI Prediction with Sentinel-2A MSI, Landsat 7 ETM+ and Landsat 8 OLI. *Remote Sensing*, *12*(6), Article 6. https://doi.org/10.3390/rs12060915

Campbell, P. K. E., Huemmrich, K. F., Middleton, E. M., Ward, L. A., Julitta, T., Daughtry, C. S. T., Burkart, A., Russ, A. L., & Kustas, W. P. (2019). Diurnal and Seasonal Variations in Chlorophyll Fluorescence Associated with Photosynthesis at Leaf and Canopy Scales. *Remote Sensing*, *11*(5), Article 5. https://doi.org/10.3390/rs11050488

Campbell, P. K. E., Middleton, E. M., McMurtrey, J. E., Corp, L. A., & Chappelle, E. W. (2007). Assessment of vegetation stress using reflectance or fluorescence measurements. *Journal of Environmental Quality*, *36*(3), 832–845. https://doi.org/10.2134/jeq2005.0396

Campbell, P. K. E., Ward, L. A., Huemmrich, K. F., & Middleton, E. (2018). Diurnal and seasonal dynamics in chlorophyll fluorescence, xanthophyll cycle and photosynthetic function, at leaf and canopy scales. *AGU Fall Meeting Abstracts*, *33*. http://adsabs.harvard.edu/abs/2018AGUFM.B33C..07C

819 Cook, B. D., Corp, L. A., Nelson, R. F., Middleton, E. M., Morton, D. C., McCorkel, J. T.,
820 Masek, J. G., Ranson, K. J., Ly, V., & Montesano, P. M. (2013). NASA Goddard's
821 LiDAR, Hyperspectral and Thermal (G-LiHT) Airborne Imager. *Remote Sensing*,
822 *5*(8), Article 8. https://doi.org/10.3390/rs5084045

823 Damm, A., Guanter, L., Paul-Limages, E., Tol, C. van der, Hueni, A., Buchmann, N., Eugster,
824 W., Ammann, C., & Schaepman, M. E. (2015). Far-red sun-induced chlorophyll
825 fluorescence shows ecosystem - specific relationships to gross primary production: An
826 assessment based on observational and modeling approaches. *Remote Sensing of*
827 *Environment*, *166*, 91–105. https://doi.org/10.1016/j.rse.2015.06.004

828 Drusch, M., Moreno, J., Bello, U. D., Franco, R., Goulas, Y., Huth, A., Kraft, S., Middleton,
829 E. M., Miglietta, F., Mohammed, G., Nedbal, L., Rascher, U., Schüttemeyer, D., &
830 Verhoef, W. (2017). The FLuorescence EXplorer Mission Concept—ESA's Earth
831 Explorer 8. *IEEE Transactions on Geoscience and Remote Sensing*, *55*(3), 1273–1284.
832 https://doi.org/10.1109/TGRS.2016.2621820

833 Fournier, A., Daumard, F., Champagne, S., Ounis, A., Goulas, Y., & Moya, I. (2012). Effect
834 of canopy structure on sun-induced chlorophyll fluorescence. *ISPRS Journal of*
835 *Photogrammetry and Remote Sensing*, *68*, 112–120.
836 https://doi.org/10.1016/j.isprsjprs.2012.01.003

837 Gastellu-Etchegorry, J.-P., Demarez, V., Pinel, V., & Zagolski, F. (1996). Modeling radiative
838 transfer in heterogeneous 3-D vegetation canopies. *Remote Sensing of Environment*,
839 *58*(2), 131–156. https://doi.org/10.1016/0034-4257(95)00253-7

840 Gastellu-Etchegorry, J.-P., Lauret, N., Yin, T., Landier, L., Kallel, A., Malenovský, Z., Bitar,
841 A. A., Aval, J., Benhmida, S., Qi, J., Medjdoub, G., Guilleux, J., Chavanon, E., Cook,
842 B., Morton, D., Chrysoulakis, N., & Mitraka, Z. (2017). DART: Recent Advances in
843 Remote Sensing Data Modeling With Atmosphere, Polarization, and Chlorophyll
844 Fluorescence. *IEEE Journal of Selected Topics in Applied Earth Observations and*
845 *Remote Sensing*, *10*(6), 2640–2649. https://doi.org/10.1109/JSTARS.2017.2685528

846 Gastellu-Etchegorry, J.-P., Yin, T., Lauret, N., Cajgfinger, T., Gregoire, T., Grau, E., Feret, J.-
847 B., Lopes, M., Guilleux, J., Dedieu, G., Malenovský, Z., Cook, B. D., Morton, D.,
848 Rubio, J., Durrieu, S., Cazanave, G., Martin, E., & Ristorcelli, T. (2015). Discrete
849 Anisotropic Radiative Transfer (DART 5) for Modeling Airborne and Satellite

Spectroradiometer and LIDAR Acquisitions of Natural and Urban Landscapes. *Remote Sensing*, *7*(2), Article 2. https://doi.org/10.3390/rs70201667

Gastellu-Etchegorry, J.-P., Yin, T., Lauret, N., Grau, E., Rubio, J., Cook, B. D., Morton, D. C., & Sun, G. (2016). Simulation of satellite, airborne and terrestrial LiDAR with DART (I): Waveform simulation with quasi-Monte Carlo ray tracing. *Remote Sensing of Environment*, *184*, 418–435. https://doi.org/10.1016/j.rse.2016.07.010

Georgiev, I., Křivánek, J., Davidovič, T., & Slusallek, P. (2012). Light transport simulation with vertex connection and merging. *ACM Transactions on Graphics*, *31*(6), 192:1-192:10. https://doi.org/10.1145/2366145.2366211

Givnish, T. J. (1988). Adaptation to Sun and Shade: A Whole-Plant Perspective. *Functional Plant Biology*, *15*(2), 63–92. https://doi.org/10.1071/pp9880063

Guanter, L., Zhang, Y., Jung, M., Joiner, J., Voigt, M., Berry, J. A., Frankenberg, C., Huete, A. R., Zarco-Tejada, P., Lee, J.-E., Moran, M. S., Ponce-Campos, G., Beer, C., Camps-Valls, G., Buchmann, N., Gianelle, D., Klumpp, K., Cescatti, A., Baker, J. M., & Griffis, T. J. (2014). Global and time-resolved monitoring of crop photosynthesis with chlorophyll fluorescence. *Proceedings of the National Academy of Sciences*, *111*(14), E1327–E1333. https://doi.org/10.1073/pnas.1320008111

Hernández-Clemente, R., North, P. R. J., Hornero, A., & Zarco-Tejada, P. J. (2017). Assessing the effects of forest health on sun-induced chlorophyll fluorescence using the FluorFLIGHT 3-D radiative transfer model to account for forest structure. *Remote Sensing of Environment*, *193*, 165–179. https://doi.org/10.1016/j.rse.2017.02.012

Hornero, A., North, P. R. J., Zarco-Tejada, P. J., Rascher, U., Martín, M. P., Migliavacca, M., & Hernandez-Clemente, R. (2021). Assessing the contribution of understory sun-induced chlorophyll fluorescence through 3-D radiative transfer modelling and field data. *Remote Sensing of Environment*, *253*, 112195. https://doi.org/10.1016/j.rse.2020.112195

Kallel, A. (2020). FluLCVRT: Reflectance and fluorescence of leaf and canopy modeling based on Monte Carlo vector radiative transfer simulation. *Journal of Quantitative Spectroscopy and Radiative Transfer*, *253*, 107183. https://doi.org/10.1016/j.jqsrt.2020.107183

880 Kamoske, A. G., Dahlin, K. M., Stark, S. C., & Serbin, S. P. (2019). Leaf area density from
881 airborne LiDAR: Comparing sensors and resolutions in a temperate broadleaf forest
882 ecosystem. *Forest Ecology and Management*, *433*, 364–375.
883 https://doi.org/10.1016/j.foreco.2018.11.017

884 Kobayashi, H., & Iwabuchi, H. (2008). A coupled 1-D atmosphere and 3-D canopy radiative
885 transfer model for canopy reflectance, light environment, and photosynthesis
886 simulation in a heterogeneous landscape. *Remote Sensing of Environment*, *112*(1),
887 173–185. https://doi.org/10.1016/j.rse.2007.04.010

888 Liu, W., Atherton, J., Mõttus, M., Gastellu-Etchegorry, J.-P., Malenovský, Z., Raumonen, P.,
889 Åkerblom, M., Mäkipää, R., & Porcar-Castell, A. (2019). Simulating solar-induced
890 chlorophyll fluorescence in a boreal forest stand reconstructed from terrestrial laser
891 scanning measurements. *Remote Sensing of Environment*, *232*, 111274.
892 https://doi.org/10.1016/j.rse.2019.111274

893 Liu, W., Luo, S., Lu, X., Atherton, J., & Gastellu-Etchegorry, J.-P. (2020). Simulation-Based
894 Evaluation of the Estimation Methods of Far-Red Solar-Induced Chlorophyll
895 Fluorescence Escape Probability in Discontinuous Forest Canopies. *Remote Sensing*,
896 *12*(23), Article 23. https://doi.org/10.3390/rs12233962

897 Liu, X., Guanter, L., Liu, L., Damm, A., Malenovský, Z., Rascher, U., Peng, D., Du, S., &
898 Gastellu-Etchegorry, J.-P. (2019). Downscaling of solar-induced chlorophyll
899 fluorescence from canopy level to photosystem level using a random forest model.
900 *Remote Sensing of Environment*, *231*, 110772.
901 https://doi.org/10.1016/j.rse.2018.05.035

902 Liu, Z., Lu, X., An, S., Heskel, M., Yang, H., & Tang, J. (2019). Advantage of multi-band
903 solar-induced chlorophyll fluorescence to derive canopy photosynthesis in a temperate
904 forest. *Agricultural and Forest Meteorology*, *279*, 107691.
905 https://doi.org/10.1016/j.agrformet.2019.107691

906 *LuxCoreRender – Open Source Physically Based Renderer*. (n.d.). Retrieved March 29, 2021,
907 from https://luxcorerender.org/

908 Malenovský, Z., Martin, E., Homolová, L., Gastellu-Etchegorry, J. P., Zurita-Milla, R.,
909 Schaepman, M. E., Polorný, R., Clevers, J. G. P. W., & Cudlín, P. (2008). Influence of

woody elements of a Norway spruce canopy on nadir reflectance simulated by the DART model at very high spatial resolution. *Remote Sensing of Environment*, *112*(1), 1–18. https://doi.org/10.1016/j.rse.2006.02.028

Malenovský, Z., Regaieg, O., Yin, T., Lauret, N., Guilleux, J., Chavanon, E., Duran, N., Janoutová, R., Delavois, A., Meynier, J., Medjdoub, G., Yang, P., Van der Tol, C., Morton, D., Cook, B., & Gastellu-Etchegorry, J. P. (2021). Discrete Anisotropic Radiative Transfer Modelling of Solar-induced Chlorophyll Fluorescence: Structural Impacts in Geometrically Explicit Vegetation Canopies. *Remote Sensing of Environment*.

Meroni, M., Rossini, M., Guanter, L., Alonso, L., Rascher, U., Colombo, R., & Moreno, J. (2009). Remote sensing of solar-induced chlorophyll fluorescence: Review of methods and applications. *Remote Sensing of Environment*, *113*(10), 2037–2051. https://doi.org/10.1016/j.rse.2009.05.003

Migliavacca, M., Perez-Priego, O., Rossini, M., El-Madany, T. S., Moreno, G., Tol, C. van der, Rascher, U., Berninger, A., Bessenbacher, V., Burkart, A., Carrara, A., Fava, F., Guan, J.-H., Hammer, T. W., Henkel, K., Juarez-Alcalde, E., Julitta, T., Kolle, O., Martín, M. P., … Reichstein, M. (2017). Plant functional traits and canopy structure control the relationship between photosynthetic CO2 uptake and far-red sun-induced fluorescence in a Mediterranean grassland under different nutrient availability. *New Phytologist*, *214*(3), 1078–1091. https://doi.org/10.1111/nph.14437

Mohammed, G. H., Colombo, R., Middleton, E. M., Rascher, U., van der Tol, C., Nedbal, L., Goulas, Y., Pérez-Priego, O., Damm, A., Meroni, M., Joiner, J., Cogliati, S., Verhoef, W., Malenovský, Z., Gastellu-Etchegorry, J.-P., Miller, J. R., Guanter, L., Moreno, J., Moya, I., … Zarco-Tejada, P. J. (2019). Remote sensing of solar-induced chlorophyll fluorescence (SIF) in vegetation: 50 years of progress. *Remote Sensing of Environment*, *231*, 111177. https://doi.org/10.1016/j.rse.2019.04.030

Nilson, T. (1971). A theoretical analysis of the frequency of gaps in plant stands. *Agricultural Meteorology*, *8*, 25–38. https://doi.org/10.1016/0002-1571(71)90092-6

Nobel, P. S. (1976). Photosynthetic Rates of Sun versus Shade Leaves of Hyptis emoryi Torr. *Plant Physiology*, *58*(2), 218–223. https://doi.org/10.1104/pp.58.2.218

940 North, P. R. J. (1996). Three-dimensional forest light interaction model using a Monte Carlo
941 method. *IEEE Transactions on Geoscience and Remote Sensing*, *34*(4), 946–956.
942 https://doi.org/10.1109/36.508411

943 Parker, G. G. (1995). Structure and microclimate of forest canopies. *Forest Canopies.*, 73–
944 106.

945 Pinty, B., Lavergne, T., Dickinson, R. E., Widlowski, J.-L., Gobron, N., & Verstraete, M. M.
946 (2006). Simplifying the interaction of land surfaces with radiation for relating remote
947 sensing products to climate models. *Journal of Geophysical Research: Atmospheres*,
948 *111*(D2). https://doi.org/10.1029/2005JD005952

949 Regaieg, O., Wang, Y., Malenovský, Z., Yin, T., Kallel, A., Duran, N., Delavois, A., Qi, J.,
950 Chavanon, E., Lauret, N., Guilleux, J., Cook, B., Morton, D., & Gastellu-Etchegorry,
951 J. P. (2020). Simulation of Solar-Induced Chlorophyll Fluorescence from 3D Canopies
952 with the Dart Model. *IGARSS 2020 - 2020 IEEE International Geoscience and*
953 *Remote Sensing Symposium*, 4846–4849.
954 https://doi.org/10.1109/IGARSS39084.2020.9323616

955 Rossini, M., Nedbal, L., Guanter, L., Ač, A., Alonso, L., Burkart, A., Cogliati, S., Colombo,
956 R., Damm, A., Drusch, M., Hanus, J., Janoutova, R., Julitta, T., Kokkalis, P., Moreno,
957 J., Novotny, J., Panigada, C., Pinto, F., Schickling, A., … Rascher, U. (2015). Red and
958 far red Sun-induced chlorophyll fluorescence as a measure of plant photosynthesis.
959 *Geophysical Research Letters*, *42*(6), 1632–1639.
960 https://doi.org/10.1002/2014GL062943

961 Sakai, Y., Kobayashi, H., & Kato, T. (2020). FLiES-SIF version 1.0: Three-dimensional
962 radiative transfer model for estimating solar induced fluorescence. *Geoscientific*
963 *Model Development*, *13*(9), 4041–4066. https://doi.org/10.5194/gmd-13-4041-2020

964 Tong, C., Bao, Y., Zhao, F., Fan, C., Li, Z., & Huang, Q. (2021). Evaluation of the FluorWPS
965 Model and Study of the Parameter Sensitivity for Simulating Solar-Induced
966 Chlorophyll Fluorescence. *Remote Sensing*, *13*(6), Article 6.
967 https://doi.org/10.3390/rs13061091

968 van der Tol, C., Verhoef, W., Timmermans, J., Verhoef, A., & Su, Z. (2009). An integrated
969 model of soil-canopy spectral radiances, photosynthesis, fluorescence, temperature

and energy balance. *Biogeosciences*, *6*(12), 3109–3129. https://doi.org/10.5194/bg-6-3109-2009

van der Tol, C., Vilfan, N., Dauwe, D., Cendrero-Mateo, M. P., & Yang, P. (2019). The scattering and re-absorption of red and near-infrared chlorophyll fluorescence in the models Fluspect and SCOPE. *Remote Sensing of Environment*, *232*, 111292. https://doi.org/10.1016/j.rse.2019.111292

Verhoef, W. (1984). Light scattering by leaf layers with application to canopy reflectance modeling: The SAIL model. *Remote Sensing of Environment*, *16*(2), 125–141. https://doi.org/10.1016/0034-4257(84)90057-9

Vermote, E., Tanré, D., Deuze, J., Herman, M., & Morcette, J.-J. (1997). Second Simulation of the Satellite Signal in the Solar Spectrum, 6S: An overview. *IEEE Trans. Geosci. Remote. Sens.* https://doi.org/10.1109/36.581987

Verrelst, J., Malenovsky, Z., Tol, C. van der, Camps-Valls, G., Gastellu-Etchegorry, J.-P., Lewis, P., North, P., & Moreno, J. (2019). Quantifying Vegetation Biophysical Variables from Imaging Spectroscopy Data: A Review on Retrieval Methods. *Surveys in Geophysics*, *40*(3), 589–629. https://doi.org/10.1007/s10712-018-9478-y

Verrelst, J., Rivera, J. P., van der Tol, C., Magnani, F., Mohammed, G., & Moreno, J. (2015). Global sensitivity analysis of the SCOPE model: What drives simulated canopy-leaving sun-induced fluorescence? *Remote Sensing of Environment*, *166*, 8–21. https://doi.org/10.1016/j.rse.2015.06.002

Verrelst, J., van der Tol, C., Magnani, F., Sabater, N., Rivera, J. P., Mohammed, G., & Moreno, J. (2016). Evaluating the predictive power of sun-induced chlorophyll fluorescence to estimate net photosynthesis of vegetation canopies: A SCOPE modeling study. *Remote Sensing of Environment*, *176*, 139–151. https://doi.org/10.1016/j.rse.2016.01.018

Vilfan, N., van der Tol, C., Muller, O., Rascher, U., & Verhoef, W. (2016). Fluspect-B: A model for leaf fluorescence, reflectance and transmittance spectra. *Remote Sensing of Environment*, *186*, 596–615. https://doi.org/10.1016/j.rse.2016.09.017

Vilfan, N., Van der Tol, C., Yang, P., Wyber, R., Malenovský, Z., Robinson, S. A., & Verhoef, W. (2018). Extending Fluspect to simulate xanthophyll driven leaf

reflectance dynamics. *Remote Sensing of Environment*, *211*, 345–356. https://doi.org/10.1016/j.rse.2018.04.012

Wang, Y., & Gastellu-Etchegorry, J.-P. (2021). Accurate and fast simulation of remote sensing images at top of atmosphere with DART-Lux. *Remote Sensing of Environment*, *256*, 112311. https://doi.org/10.1016/j.rse.2021.112311

Wellburn, A. R. (1994). The Spectral Determination of Chlorophylls a and b, as well as Total Carotenoids, Using Various Solvents with Spectrophotometers of Different Resolution. *Journal of Plant Physiology*, *144*(3), 307–313. https://doi.org/10.1016/S0176-1617(11)81192-2

Yang, P., van der Tol, C., Campbell, P. K. E., & Middleton, E. M. (2021). Unraveling the physical and physiological basis for the solar- induced chlorophyll fluorescence and photosynthesis relationship using continuous leaf and canopy measurements of a corn crop. *Biogeosciences*, *18*(2), 441–465. https://doi.org/10.5194/bg-18-441-2021

Yang, P., Verhoef, W., & van der Tol, C. (2017). The mSCOPE model: A simple adaptation to the SCOPE model to describe reflectance, fluorescence and photosynthesis of vertically heterogeneous canopies. *Remote Sensing of Environment*, *201*, 1–11. https://doi.org/10.1016/j.rse.2017.08.029

Yin, T., Gastellu-Etchegorry, J.-P., Lauret, N., Grau, E., & Rubio, J. (2013). A new approach of direction discretization and oversampling for 3D anisotropic radiative transfer modeling. *Remote Sensing of Environment*, *135*, 213–223. https://doi.org/10.1016/j.rse.2013.03.030

Yin, T., Lauret, N., & Gastellu-Etchegorry, J.-P. (2015). Simulating images of passive sensors with finite field of view by coupling 3-D radiative transfer model and sensor perspective projection. *Remote Sensing of Environment*, *162*, 169–185. https://doi.org/10.1016/j.rse.2015.02.020

Yin, T., Lauret, N., & Gastellu-Etchegorry, J.-P. (2016). Simulation of satellite, airborne and terrestrial LiDAR with DART (II): ALS and TLS multi-pulse acquisitions, photon counting, and solar noise. *Remote Sensing of Environment*, *184*, 454–468. https://doi.org/10.1016/j.rse.2016.07.009

Zeng, Y., Badgley, G., Chen, M., Li, J., Anderegg, L. D. L., Kornfeld, A., Liu, Q., Xu, B., Yang, B., Yan, K., & Berry, J. A. (2020). A radiative transfer model for solar induced fluorescence using spectral invariants theory. *Remote Sensing of Environment*, *240*, 111678. https://doi.org/10.1016/j.rse.2020.111678

Zhang, Z., Zhang, Y., Porcar-Castell, A., Joiner, J., Guanter, L., Yang, X., Migliavacca, M., Ju, W., Sun, Z., Chen, S., Martini, D., Zhang, Q., Li, Z., Cleverly, J., Wang, H., & Goulas, Y. (2020). Reduction of structural impacts and distinction of photosynthetic pathways in a global estimation of GPP from space-borne solar-induced chlorophyll fluorescence. *Remote Sensing of Environment*, *240*, 111722. https://doi.org/10.1016/j.rse.2020.111722

Zhang, Z., Zhang, Y., Zhang, Q., Chen, J. M., Porcar-Castell, A., Guanter, L., Wu, Y., Zhang, X., Wang, H., Ding, D., & Li, Z. (2020). Assessing bi-directional effects on the diurnal cycle of measured solar-induced chlorophyll fluorescence in crop canopies. *Agricultural and Forest Meteorology*, *295*, 108147. https://doi.org/10.1016/j.agrformet.2020.108147

Zhao, F., Dai, X., Verhoef, W., Guo, Y., van der Tol, C., Li, Y., & Huang, Y. (2016). FluorWPS: A Monte Carlo ray-tracing model to compute sun-induced chlorophyll fluorescence of three-dimensional canopy. *Remote Sensing of Environment*, *187*, 385–399. https://doi.org/10.1016/j.rse.2016.10.036

Zhao, F., Li, Y., Dai, X., Verhoef, W., Guo, Y., Shang, H., Gu, X., Huang, Y., Yu, T., & Huang, J. (2015). Simulated impact of sensor field of view and distance on field measurements of bidirectional reflectance factors for row crops. *Remote Sensing of Environment*, *156*, 129–142. https://doi.org/10.1016/j.rse.2014.09.011

4.3 Conclusion

In this chapter, the impact of forest structure on SIF emission and observation was studied using realistic mock-ups derived from LiDAR. Results showed that neglecting the forest structure can lead to an overestimation of SIF radiance by up to 50% notably for oblique sun directions. The impact of vegetation structure was higher on the propagation of SIF within the canopy than on the PAR absorption and SIF emission. Results also showed that SIF radiance is overestimated if woody elements are neglected. This overestimation is more due to the shadowing effect than to the blocking effects of the woody elements. As already mentioned, this study was conducted after conversion of turbid voxels to quasi turbid medium because at that time, the turbid medium was not implemented yet in DART-Lux. The comparison of the turbid and the quasi-turbid representation showed that the turbid has a longer computation time but a lower Monte Carlo noise for the same number of samples. Should the work be redone, the quasi-turbid representation of vegetation would probably be used again.

Chapter 5

Thermal emission and radiative budget modeling in DART-Lux

Photosynthetically active vegetation continuously exchanges matter and energy with its environment via biochemical reactions and heat transfer processes. Energy exchanges can be separated into non-radiative (*e.g.*, sensible and latent heat exchanges) and radiative exchanges that consist in receiving energy through the absorption of incident radiation from the sun directly or after being scattered by the atmosphere and through the radiation emitted by the atmosphere and all the surrounding materials such as soil, woody elements, etc. and lose energy by emitting thermal radiation. The net absorbed radiation is therefore the difference between absorbed and emitted energy. Radiative energy exchanges are an important component of the energy balance of vegetation. Therefore, modeling the radiation budget including thermal emission is essential. The first section of this chapter presents the modeling of thermal emission and the second section presents the modeling of the radiative budget in DART-Lux.

5.1 Thermal emission modeling

5.1.1 Theoretical background

Thermal emission is an energy emission in the form of electromagnetic radiation from any material having a temperature T higher that the absolute zero (*i.e.*, $T > 0$ K) due to the movement of molecules and atoms in the material.

The Planck law gives the spectral distribution of isotropic radiance emitted by a blackbody (*i.e.*, an ideal body that absorbs all the incident electromagnetic radiation) at temperature T (K):

$$L_B(\lambda, T) = \frac{2.h.c^2}{\lambda^5} . \frac{1}{e^{\frac{hc}{\lambda.k.T}} - 1} \ (W.m^{-2}.m^{-1}.sr^{-1}) \tag{5.1}$$

where λ is the wavelength in m, $h = 6.626\,070\,15 \times 10^{-34}$ J.s is the Planck's constant, $c = 2.997\,924\,58 \times 10^{8}\ m.s^{-1}$ (in vacuum) is the speed of light, and $k = 1{,}380\,649 \times 10^{-23}$ J.K^{-1} is the Boltzmann constant.

The exitance of a Blackbody over the whole spectrum results from the integration of the Planck's law over the whole spectrum, and over the hemisphere ($\times \pi$ for an isotropic radiance). It is given by the Stefan-Boltzmann law:

$$\begin{aligned} M_B(T) \quad &= \pi . \int_0^{+\infty} \frac{2.h.c^2}{\lambda^5} . \frac{1}{e^{\frac{hc}{\lambda.k.T}} - 1} \, d\lambda \\ &= \sigma . T^4 \ \ (W.m^{-2}) \end{aligned} \tag{5.2}$$

where $\sigma = \frac{2.\pi^5.k^4}{15.h^3.c^2} \approx 5.670374419 \times 10^{-8}\ W.m^{-2}.K^{-4}$

Real bodies are not perfect emitters, the emitted radiance is scaled by their spectral emissivity:

$$L(\lambda, T) = \varepsilon(\lambda) . L_B(\lambda, T) \tag{5.3}$$

For a spectral band $(\lambda, \Delta\lambda)$, the emitted radiance is computed as the average of the emitted radiance over this band:

$$L_{\lambda,\Delta\lambda}(T) = \frac{1}{\Delta\lambda} \int_{\lambda-\frac{\Delta\lambda}{2}}^{\lambda+\frac{\Delta\lambda}{2}} \varepsilon(\lambda) . L_B(\lambda, T) \, d\lambda = \frac{\varepsilon_{\Delta\lambda}}{\Delta\lambda} \int_{\lambda-\frac{\Delta\lambda}{2}}^{\lambda+\frac{\Delta\lambda}{2}} L_B(\lambda, T) d\lambda \tag{5.4}$$

where $\varepsilon_{\Delta\lambda}$ is the emissivity over the band $(\lambda, \Delta\lambda)$.

The brightness temperature T_B of an observed emitting body having a thermodynamic temperature T and an emissivity $\varepsilon(\lambda)$ is the thermodynamic temperature a black body should have in order to have the radiance $L(\lambda, T)$ of the emitting body at the wavelength λ. It is computed using the inverse function of the Planck law:

$$T_B(\lambda) = L_B^{-1}(L(\lambda, T), \lambda) = \frac{h.c}{k.\lambda.\ln\left(1 + \frac{2.h.c^2}{\lambda^5.\varepsilon(\lambda).L_B(\lambda, T)}\right)} \tag{5.5}$$

If the emitting body is a blackbody, its brightness temperature is equal to its thermodynamic temperature for every wavelength. Otherwise, it is less than or equal to its thermodynamic temperature and is wavelength dependent.

For a spectral band $(\lambda, \Delta\lambda)$, instead of a single wavelength, the brightness temperature is:

$$T_B(\lambda, \Delta\lambda) = L_B^{-1}\left(L_{\lambda,\Delta\lambda}(T), \lambda_{eq}\right) \tag{5.6}$$

with λ_{eq} the wavelength between λ-$\frac{\Delta\lambda}{2}$ and λ+$\frac{\Delta\lambda}{2}$ for which the Planck function is equal to the average of the Planck function on the spectral band $(\lambda, \Delta\lambda)$ for the temperature T. According to the mean value theorem, λ_{eq} exists. It is defined as:

$$L_B\left(\lambda_{eq}, T\right) = \frac{1}{\Delta\lambda}.\int_{\lambda-\frac{\Delta\lambda}{2}}^{\lambda+\frac{\Delta\lambda}{2}} L_B(\lambda, T)d\lambda \tag{5.7}$$

5.1.2 Thermal emission for facets

From the point of view of the modelling of radiative transfer, the thermal emission of facets corresponds to the consideration of the emitting facets as light sources. This functionality is already implemented in the LuxCoreRender software. However, it is limited to single face emitters, and to constant radiance per object.

In a first step, the single face emitting facet has been adapted to create a double face emitting facet. This is done by sampling the whole sphere instead of the upper hemisphere when sampling an emission direction, and by making the material emit when it is hit by a ray from the upper or the lower side.

In a second step, other methods have been introduced in order to simulate more realistic temperature distributions than constant temperature per object.

Simulation and importation of 3D temperature distribution

a) Illumination

The illumination method is used in DART-FT to simulate a more or less realistic 3D temperature distribution based on the illumination of surfaces. The idea is that the most illuminated surfaces tend to have higher temperature and vice versa. This is an approximation since the temperature of a surface depends on many other parameters such as its heat capacity and its heat exchanges through conduction and convection; its estimation requires the computation of the full energy balance. However, the illumination method is a first approximation. It requires to specify the range of temperature ($T_{mean}, \Delta T$) per type of element (e.g., wall with specific orientation). The first order irradiance (i.e., direct sun and atmosphere radiation) is used to distribute the temperature: the most illuminated surfaces are assigned the maximal temperature, the least illuminated surfaces are assigned the least temperature and intermediately illuminated surfaces are assigned intermediate temperature values.

In DART-Lux, the illumination method differs from DART-FT: rays are not sent from the source (i.e., sun and atmosphere) but from so-called emitting points in the scene elements of which the temperature must be computed. Therefore, for facets, the illumination method starts with the determination of emitting points in the scene elements. This is done by computing the intersection of each facet with a 3D regular grid. Then, scene facets are virtually segmented into sub-polygons, and the centroid of each sub-polygon (Figure 5-1) is treated as an emitting point. Any triangle that does not intersect the grid because it is too small is assigned an emitting point that is the centroid of this triangle.

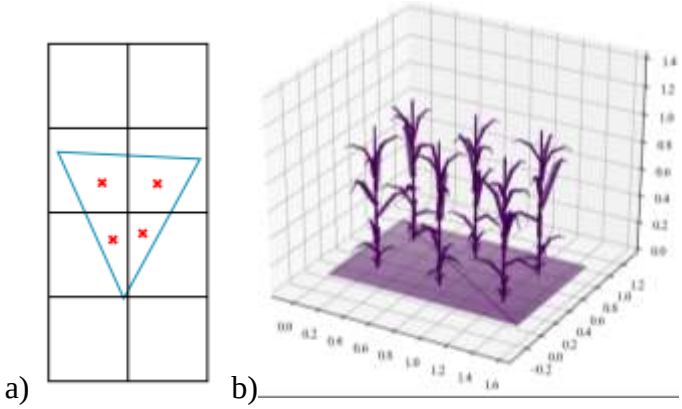

Figure 5-1: Points sampling method for a single triangle (a) and a maize scene (b)

Then, the irradiance (Figure 5-2) of the centroid of each facet, on the two sides of the facet, is computed using direct sun irradiance and atmosphere diffuse irradiance defined by a SKYL value. This order 1 irradiance $E_{P,1}$ at each centroid P is:

$$E_{P,1} = E_{P,dir,1} + E_{P,diff,1} \tag{5.8}$$

With $E_{P,dir,1}$ the direct order 1 irradiance computed by tracing a ray for the point P in the sun direction. If the ray is not intercepted, $E_{P,dir,1}=E_{sun}.|\Omega_s.\vec{n}|$, ($E_{sun}$ is the sun irradiance for a surface perpendicular to the sun direction Ω_s and $\vec{n}$ is the surface normal, if $\Omega_s.\vec{n} > 0$, the top face is illuminated, otherwise the bottom face is illuminated). If the ray is intercepted, $E_{P,dir} = 0$.

The incident diffuse radiation at a point P is:

$$E_{P,diff,1} = \int_{2\pi} L_{P,1}(\Omega_i).|\Omega_i.\vec{n}|.d\Omega \tag{5.9}$$

with $L_{P,1}(\Omega_i)$ the order 1 diffuse radiance incident to the point P.

$E_{P,diff,1}$ is estimated using a Monte Carlo estimator $\hat{E}_{P,diff,1}$ with N sampled directions Ω_i:

$$\hat{E}_{P,diff,1} = \frac{1}{N}.\sum_{i=1}^{N}\frac{L_{P,1}(\Omega_i).|\Omega_i.\vec{n}|}{p(\Omega_i)} \tag{5.10}$$

The PDF for sampling a direction $p(\Omega_i)$ verifies $\int_{2\pi} p(\Omega_i).d\Omega=1$. The importance sampling is used. It requires that $p(\Omega_i)$ has a similar shape to the integrand $f(\Omega_i)=L_{P,1}(\Omega_i).|\Omega_i.\vec{n}|$

Taking $p(\Omega_i)=c.|\Omega_i.\vec{n}|$ with $c \in \mathbb{R}$ (cosine distribution) leads to $c=\frac{1}{\pi}$, and Eq (5.10) becomes:

$$\hat{E}_{P,diff,1} = \frac{\pi}{N}.\sum_{i=1}^{N} L_{P,1}(\Omega_i) \tag{5.11}$$

$\hat{E}_{P,diff,1}$ is unbiased. Its expected value is equal to the real value $E_{P,diff,1}$ (cf. Appendix 5-1).

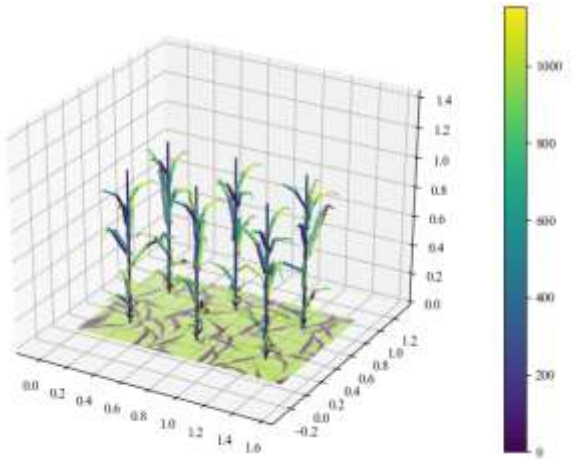

Figure 5-2: Local irradiance computed over the maize scene

Once the local irradiance is computed, a temperature T_P is assigned for each irradiance value E_P (Figure 5-3), using the user-defined temperature properties ($T_{mean}, \Delta T$) and the relationship:

$$T_P^4 = a.E_P + b \tag{5.12}$$

This relationship is chosen because for a surface at the thermal equilibrium with temperature T and receiving an energy flux E, T^4 increases linearly with E.

a and b are compute such that $T_{max}^4 = a.E_{max} + b$ and $T_{min}^4 = a.E_{min} + b$:

$$a = \frac{T_{max}^4 - T_{min}^4}{E_{max} - E_{min}} \tag{5.13}$$

$$b = T_{max}^4 - a.E_{max} \tag{5.14}$$

Therefore:

$$T_P = \left(\frac{T_{max}^4 - T_{min}^4}{E_{max} - E_{min}}.(E_P - E_{max}) + T_{max}^4\right)^{\frac{1}{4}} \tag{5.15}$$

We note from Eq (5.15) that if E_{max}, E_{min} and E_P are multiplied by a factor α, the expression of T_P remains the same. Hence, the absolute value of BOA irradiance E_{BOA} used in the illumination step is not important. Therefore, any dummy value can be used and there is no need compute the real BOA irradiance or to perform a multispectral illumination.

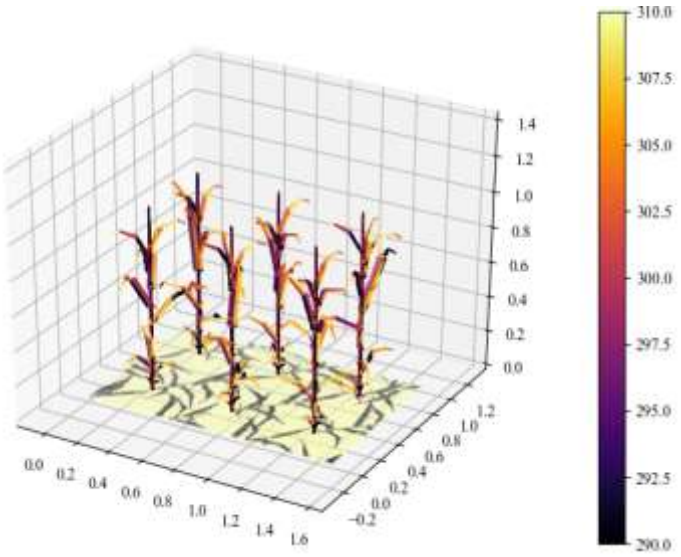

Figure 5-3: Temperature distribution computed over the maize scene

Once the temperature distribution is computed, the radiative transfer simulation starts.

b) Sunlit and shaded temperatures

For some applications including SIF emission, one need to know the thermodynamic temperature of sunlit (T_{su}) and shaded (T_{sh}) parts for each type of element of the scene, and to use them in a radiative transfer model. This possibility was introduced in DART-Lux based on the illumination method described in the previous section.

A sunlit fraction is computed at each point, as the ratio between the order 1 local irradiance, and the local irradiance the point would receive if it was totally sunlit:

$$f_{sunlit} = \frac{E_P}{\frac{E_{dir,BOA}}{\cos(\theta_s)}.|\Omega_l.\Omega_s| + E_{diff,BOA}} \tag{5.16}$$

The emitted radiance by this point is then:

$$L_{\lambda,\Delta\lambda}(T_{su}, T_{sh}, f_{sunlit}) = f_{sunlit}.L_{\lambda,\Delta\lambda}(T_{su}) + (1 - f_{sunlit}).L_{\lambda,\Delta\lambda}(T_{sh}) \tag{5.17}$$

c) Imported SCOPE temperature profiles

Some 1D models that compute the full energy balance such as SCOPE provide 1D temperature profiles for sunlit and shaded leaves. The temperature profiles provided by SCOPE are function of the height within the canopy for shaded leaves $T_{sh}(z)$ and the leaf zenith angle, azimuth angle and height within the canopy for sunlit leaves $T_{su}(z, \theta_l, \varphi_l)$. DART-Lux can import these

Some 1D models of canopy energy balance simulate 1D temperature profiles for leaves. The SCOPE model simulates a 1D temperature profile for sunlit leaves and another one for shaded leaves. The temperature profiles from SCOPE are function of the height in the canopy for shaded leaves $T_{sh}(z)$ and on the leaf zenith angle, the azimuth angle and the height in the canopy for sunlit leaves $T_{su}(z, \theta_l, \varphi_l)$. DART-Lux was adapted to import these temperature profiles and to simulate radiative transfer with them. To this end, the sunlit fraction f_{sunlit} is computed using Eq (5.16) and the emitted radiance is computed using Eq (5.17), the temperatures T_{sh} and T_{su} being interpolated from the imported SCOPE temperature profiles according to the height of the centroid for T_{sh}, and according to the height of the centroid and the zenith and azimuth angles of the normal vector of the facet for T_{su}.

d) Importation of 3D temperature distribution

DART-Lux was adapted to import any 3D temperature distribution. The approach relies on a division of the scene into "voxels" at any 3D resolution and on the assignation of the corresponding temperature to all scene elements inside each voxel. 3D temperature distributions can be provided by other models like fire models (*e.g.*, Y. Liu et al. 2019). In addition, 2D temperature distributions, for example derived from the inversion of remote sensing images, can also be imported.

Radiative transfer simulation

Once the temperature distribution is computed and/or imported, the radiative transfer simulation starts. The temperature distribution methods provide discrete temperature values for points distributed over the scene or for virtual voxels. This is done only for the central scene and not for the eventual repeated scenes (*i.e.*, duplications of the scene of interest in order to simulate its neighborhood). However, in reality, any point in the scene can emit if sampled or intercepted by a ray, including points outside the central scene (i.e., scene of interest). Therefore, to compute the emitted radiance of any point M in the scene, its corresponding point in the central scene M_c is computed first using a horizontal shift. If the temperature is defined using a temperature profile, the temperature of the voxel containing M_c is assigned to M. Otherwise, the nearest point to M_c with an assigned temperature is searched over the scene (Figure 5-3) and its temperature is assigned to M. The search operation is optimized using a Bounding Volume Hierarchy (BVH) structure implementation from LuxCoreRender.

5.1.3 Thermal emission for volumes

The modeling of thermal emission of volumes filled with homogeneous fluids or turbid medium has been designed and implemented into DART-Lux.

Volumes with spatially constant temperature

Let us consider a volume homogenously filled with a fluid or turbid medium at constant thermodynamic temperature T, and a ray sent from the sensor (Figure 5-4) that enters the volume at a point A. Then, the order 1 thermal emission of the volume is computed.

For a volume filled with a fluid, the radiance emitted by an elementary layer of the volume of height dz and seen by the sensor is:

$$dL = \sigma_t . dz . L_{\lambda,\Delta\lambda}(T) . e^{-\sigma_t . z} \tag{5.18}$$

with $\sigma_t . dz$ the area of emitting particles in the layer dz per horizontal surface unit, $L_{\lambda,\Delta\lambda}(T)$ the emitted particle radiance and $e^{-\sigma_t . z}$ the transmittance between the layer dz and point A.

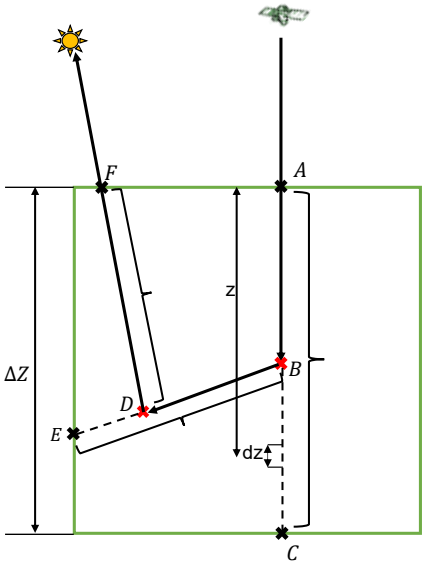

Figure 5-4: Schematic representation of the volume thermal emission

For a volume filled with turbid medium:

$$dL = G(\Omega_v) . u_l . dz . L_{\lambda,\Delta\lambda}(T) . e^{-G(\Omega_v) . u_l . z} \tag{5.19}$$

with $G(\Omega_v) . u_l . dz$ the effective area of emitting leaves in the layer dz per horizontal surface unit, $L_{\lambda,\Delta\lambda}(T)$ the emitted leaf radiance and $e^{-G(\Omega_v) . u_l . z}$ the transmittance between the layer dz and point A.

By integrating over the segment $[AC]$ (*i.e.*, whole volume), we get the radiance L_{order1} emitted along this segment at order 1 and seen by the sensor. For a volume filled with a fluid, we get:

$$L_{order1} = \int_{\Delta Z} dL \quad = \int_0^{\Delta Z} \sigma_t . L_{\lambda,\Delta\lambda}(T) . e^{-\sigma_t . z} . dz \tag{5.20}$$

$$= L_{\lambda,\Delta\lambda}(T) . (1 - e^{-\sigma_t . \Delta Z})$$

Similarly, for a volume filled with turbid medium:

$$L_{order1} = L_{\lambda,\Delta\lambda}(T) . (1 - e^{-G(\Omega_v) . u_l . \Delta Z}) \tag{5.21}$$

Multiple order emission is simulated as successive order 1 emission whenever the ray sent from the sensor is intercepted at a point B. Then, a scattering direction $\overrightarrow{BE}$ is sampled, with E being the interception of the scattering direction and the edge of the volume. The emission along the segment $[BE]$ seen at B is computed using Eq (5.20) or (5.21) and scattered at B towards the sensor. Then, a travel distance is sampled over $\overrightarrow{BE}$. If the sampling leads to an interception in point D within the volume, a new scattering direction $\overrightarrow{DF}$ is sampled, and the emission along $[DF]$ seen at D is computed and scattered towards B, and so on until a sampled travel distance is outside the volume, or until the specified maximal scattering order is reached.

Illumination method and sunlit fraction for volumes

For a horizontally infinite homogeneous turbid medium, as for SCOPE, the sunlit and shaded fractions of leaves are computed statistically using the Beer law. For a layer at height z inside a canopy of height ΔZ, we have:

$$f_{sunlit}^{layer}(z) = e^{-G(\Omega_s) . u_l . \frac{\Delta Z - z}{\cos\theta_s}} = \frac{E_{dir}(z)}{E_{dir,BOA}} \tag{5.22}$$

This definition is extended to compute the average fraction of sunlit leaves in a turbid cell:

$$\bar{f}_{sunlit}^{cell} = \frac{1}{E_{BOA} . \Delta Z} \int_0^{\Delta Z} E(z) . dz \tag{5.23}$$

The computation of the integral in Eq (5.23) would require to divide the cell into smaller layers and to compute the irradiance at each layer, which would be very computationally expensive.

Instead, an approximation is made by assuming that the cell is inside an infinite homogeneous layer of the same height as the cell. Then, $\bar{f}_{sunlit}^{cell}$ becomes:

$$\bar{f}_{sunlit}^{cell} \approx \frac{1}{\Delta Z}\int_0^{\Delta Z} e^{-G(\Omega_s).u_l.\frac{\Delta Z - z}{cos\,\theta_s}}.dz \tag{5.24}$$

According to the mean value theorem, there exists a height z_{eq} such that:

$$e^{-G(\Omega_s).u_l.\frac{\Delta Z - z_{eq}}{\cos\theta_s}} = \frac{1}{\Delta z}.\int_0^{\Delta z} e^{-G(\Omega_s).u_l.\frac{\Delta Z - z}{\cos\theta_s}}.dz \tag{5.25}$$

Thus, the irradiance at the height z_{eq} is approximately equal to the mean irradiance over the cell, and therefore:

$$\bar{f}_{sunlit} \approx \frac{E(z_{eq})}{E_{BOA}} \tag{5.26}$$

$E(z_{eq})$ is also used for assigning a temperature to the cell.

Volumes with spatially variable temperatures

The illumination method for temperature distribution for volumes gives a 3D temperature array. A 3D temperature array can also be imported directly. However, a volume is not necessarily contained by a single cell. The same volume can then have different temperatures if it is contained in more than one cell. DART-Lux has been adapted to manage these volumes.

Let us consider a homogenous cell filled with turbid medium, of height H. It is divided into 2 layers, the bottom layer of height h has a temperature T_1 and the top layer of height $H - h$ has a temperature T_2. For a ray coming from the sensor from at the nadir direction for example, entering the volume, a distance is randomly sampled inside the volume. The PDF $p(l)$ for sampling this distance is proportional to the Beer law and verifies the following normalization equality:

$$\int_0^H p(l).dl = 1 \tag{5.27}$$

Therefore (c.f. Appendix 5-2),

$$p(l) = \frac{G(\Omega).u_l.e^{-G(\Omega).u_l.l}}{1 - e^{-G(\Omega).u_l.H}} \tag{5.28}$$

By sampling a distance l according to this PDF, the obtained distance is between 0 and H. If $l < H - h$, the observed radiance is computed assuming that the volume has a constant temperature T_2, otherwise, the observed radiance is computed assuming that the volume has a constant temperature T_1. In Appendix 5-2, we show that the expected value of order 1 radiance computed using this sampling technique is equal to the true value of observed order 1 radiance. Since the multiple order emission is treated as successive order 1 emissions, this method allows one to simulate thermal emission observations for homogeneous volumes.

5.1.4 Results

Six scene examples are shown below to assess the accuracy of the developed modeling and to illustrate some potential uses:

Synthetic scene (Facets)

The thermal emission modeling and the temperature determination method using illumination are first assessed by comparison with DART-FT. Figure 5-5 shows the brightness temperatures images simulated using DART-FT (CT = 5 min 45 s, RAM = 1.9 GB) and DART-Lux (CT = 24 s, RAM = 1.2 GB) for the same synthetic scene made of facets only with three trees and a house whose roof has four parts. The average image radiance is 14.134 $W.m^{-2}.\mu m^{-1}.sr^{-1}$ for DART-FT and 14.119 $W.m^{-2}.\mu m^{-1}.sr^{-1}$ for DART-Lux. The DART-FT image has many pixels with extreme values at the level of the trees caused by discretization effects. The scene is 20 × 20 m² and the spatial resolution is 5 cm. The temperature distribution is determined using the illumination method with direct illumination only. In both DART-FT and DART-Lux images, we note that sunlit ground has a higher temperature than shaded ground. Also, the four parts of the roof give four different signals because they receive different direct illumination, depending on their orientation relatively to the solar direction.

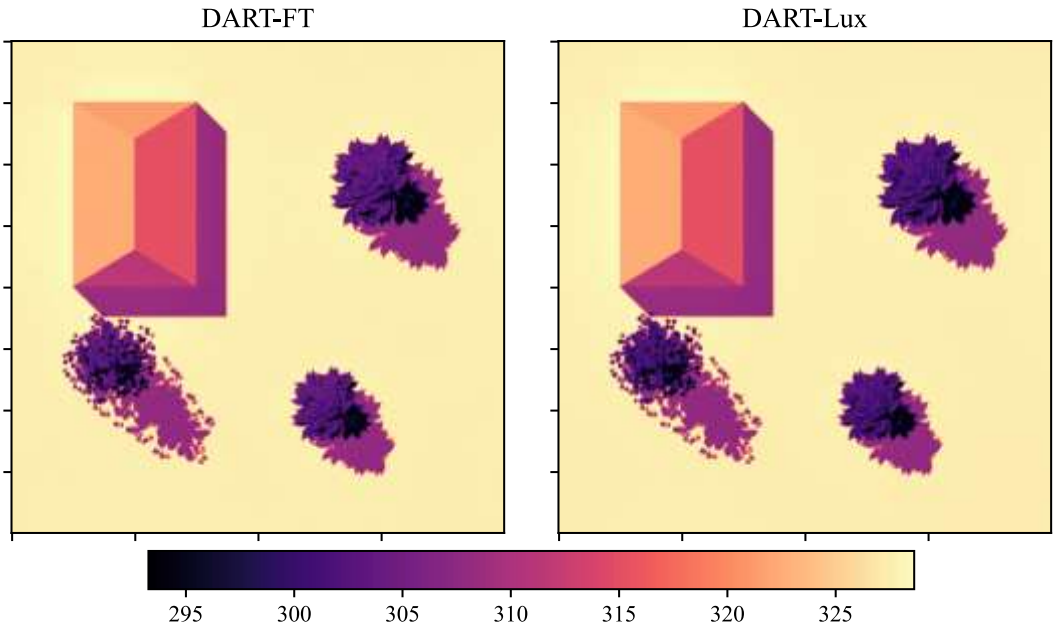

Figure 5-5: Nadir brightness temperature (K) images simulated by DART-FT and DART-Lux for a simple synthetic scene at 10 µm.

Turbid volume

Thermal emission modeling in volumes is assessed by comparison with DART-FT for a simple turbid volume on top on a non-emitting and a non-reflective ground. The turbid volume has a LAI = 1, a spherical LAD, a thermodynamic temperature equal to 290 K, and leaf reflectance and transmittance both equal to 0.06 (*i.e.*, 0.88 emissivity). Figure 5-6 shows the comparison of simulated radiance between DART-FT (CT = 1 min 2 s) and DART-Lux (CT = 8 s) between 8 and 14 µm.

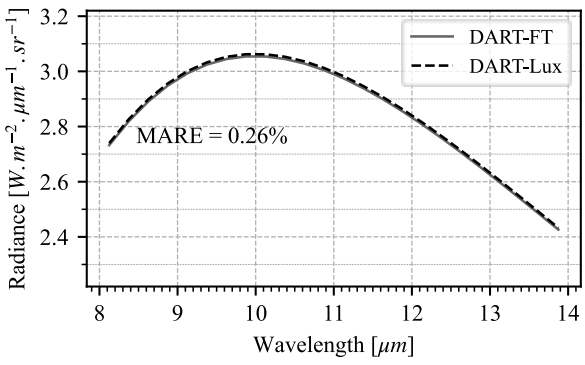

Figure 5-6: Radiance comparison between DART-FT and DART-Lux for a simple turbid plot

Realistic urban scene: Brienne district (Toulouse)

Figure 5-7 shows a brightness temperature image of the Brienne district in Toulouse, simulated using DART-FT (CT = 1 h 30 min, RAM = 23.25 GB) and DART-Lux (8 min 32 s, RAM = 33.58 GB) at 10 µm wavelength. The scene is 750 × 1400 m² and the spatial resolution is 1 m. The temperature distribution is computed illumination (direct only) with a mesh grid resolution of 0.5 m in DART-Lux and an illumination step of 0.5 in DART-FT. The average image radiance is 10.340 $W.m^{-2}.\mu m^{-1}.sr^{-1}$ for DART-FT and 10.360 $W.m^{-2}.\mu m^{-1}.sr^{-1}$ for DART-Lux. Extreme values pixel are observed in the DART-FT image. For a more accurate DART-FT simulation, more discretization parameters are required which would increase computation time and memory requirements.

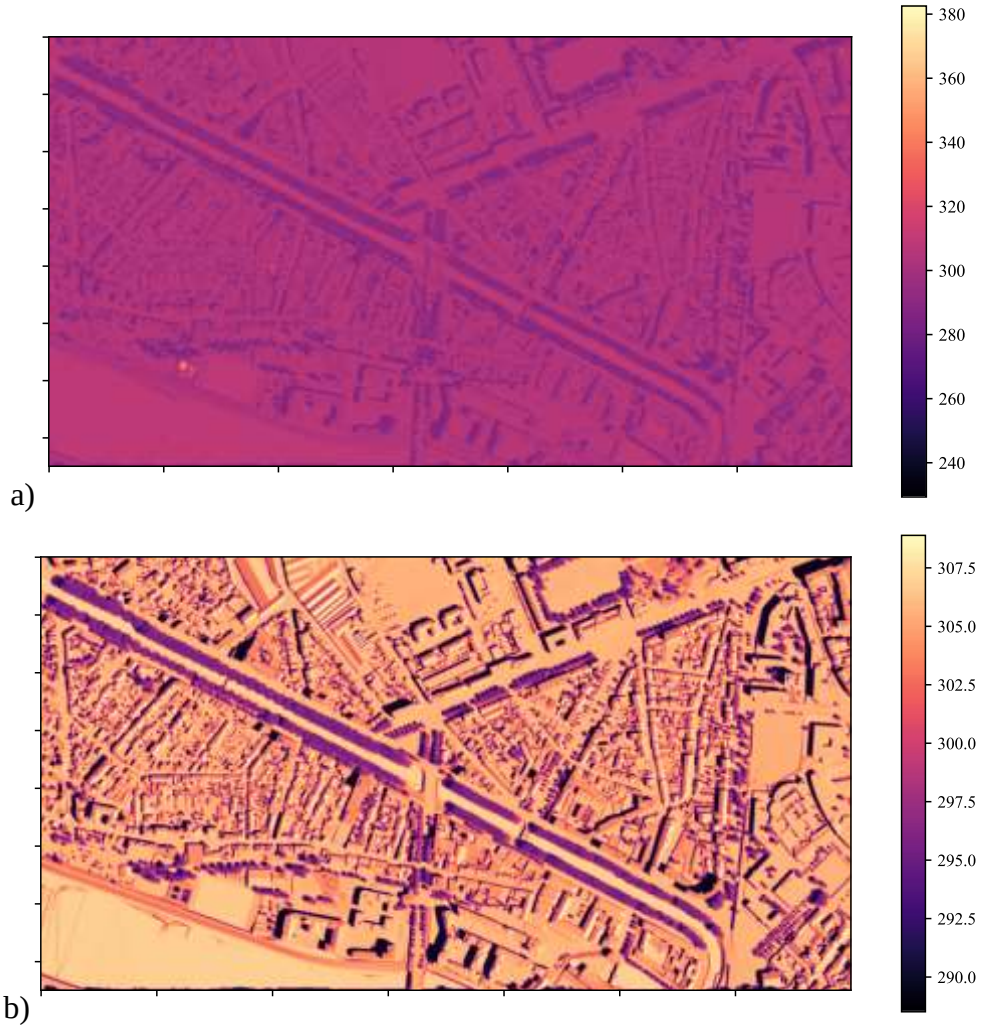

Figure 5-7: Nadir brightness temperature (K) images at 10 µm of the Brienne district, Toulouse (750 × 1400 m², 1 m resolution) simulated by DART-FT (a) and DART-Lux (b)

Realistic forest scene: SERC forest

Figure 5-8 shows an airborne brightness temperature image taken by the NASA's GLiHT thermal infrared imager (spectral range [8 – 14 µm]) over the SERC forest (Maryland, USA), and its corresponding image simulated with DART-Lux. The mock-up is a 3D distibution of voxels derived from the GLiHT airborne LiDAR measurements. It is 600 × 600 m² large with 0.5 m voxel dimension. In the absence of a measurements of 3D temeprature distribution, the temperature was distibuted using the illumination with a priori minimal and maximal temperature values for vegetation and ground, and a priori emissivities. To mimic the airborne image, the modeling of a pushbroom camera was introduced into DART-Lux. It was used to simulate this image. Although only approximate input parameters were used, the simulated images shows some visual similarities with the real image.This simulation cannot be run with DART-FT due to large computational requirements.

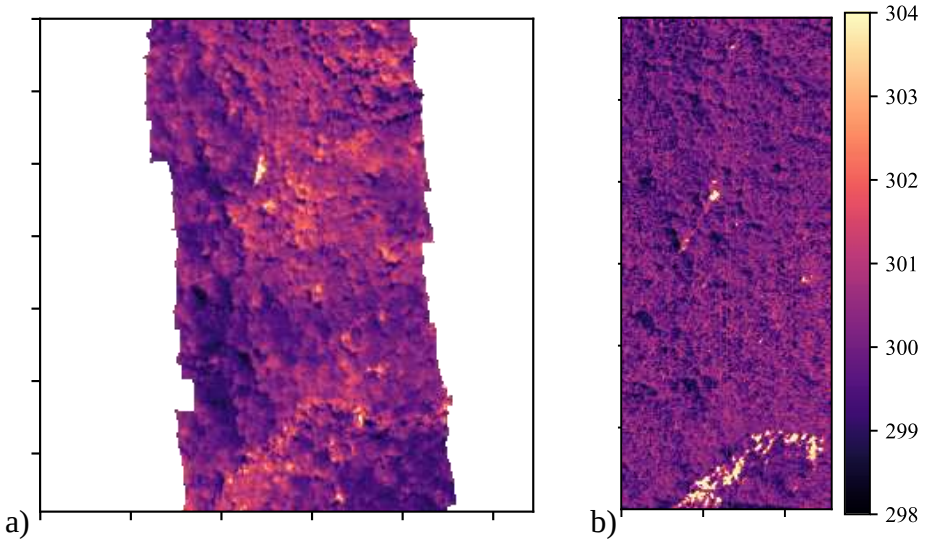

Figure 5-8: Brightness temperature (K) image (8 – 14 µm) over the SERC forest a) GLiHT image b) DART-Lux simulated image

Realistic maize field

Figure 5-9 shows images of a maize field in Auzeville, France, used in the frame of the calibration of the future TRISHNA satellite mission. They were acquired using a thermal camera (7.7 – 13 µm) at different positions. Figure 5-9 also shows the corresponding DART-Lux images. In these simulations, the mock-up was constructed respecting the real field

geometry and a single 3D maize plant object assumed to be representative. No LAI calibration was done. Leaves emissivity were measured from sample leaves from the field and temperature was distributed using the illumination method, with a priori temperature values because no temperature measurements were performed on the leaves. This is not a fully relevant comparison with field measurements, however, visual similarities with the simulated images can be observed.

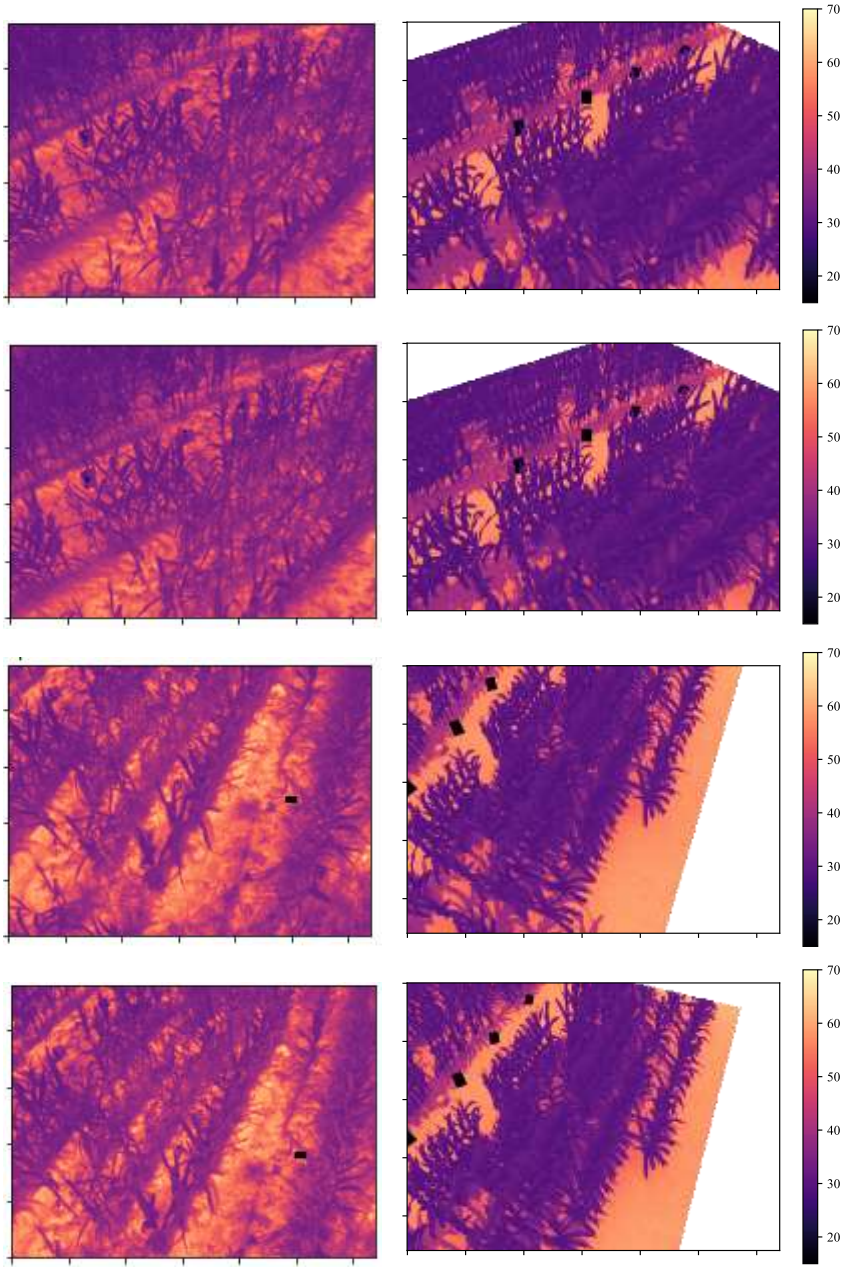

Figure 5-9: Thermal camera images (7.7 – 13 µm) of a maize field (left) and corresponding DART-Lux simulations (°C)

Fire simulation

DART-Lux is also able to simulate fire simulation using volumes filled with fluids. As an example of fire application to DART-lux, we simulated an open vegetation fire scene, generated using the physical fire model FDS (McGrattan et al., 2013), which is part of the set of validation simulation of FDS (Case 064). It is based on measurements of a 1-ha experimental homogeneous grassland fire conducted in Australia (Mell et al., 2007). The scene is simulated using the latest FDS version to date (FDS6) and provides at 25 cm spatial resolution for several time steps 3D distribution of temperature, gas molar fraction for CO2, CO, H2O and soot volume fraction. The scene is input to DART using the DAO tool to load fluids as voxels and the temperature is included using a 3D temperature file created from the FDS output scene.

The simulated fire image is for a Middle Infra-Red (MIR) camera, the agema 550, which has a narrow spectral band located at 3.9 µm. This spectral band is often used in fire monitoring. Figure 5-10 show nadir image simulated by DART-Lux, 50s after the ignition of the fire. During the experiment, only visible images were collected, so no image-to-image comparison is possible. Flames show brightness temperatures in an expected range in field scale propagating fire (>600K (Paugam et al., 2013)).

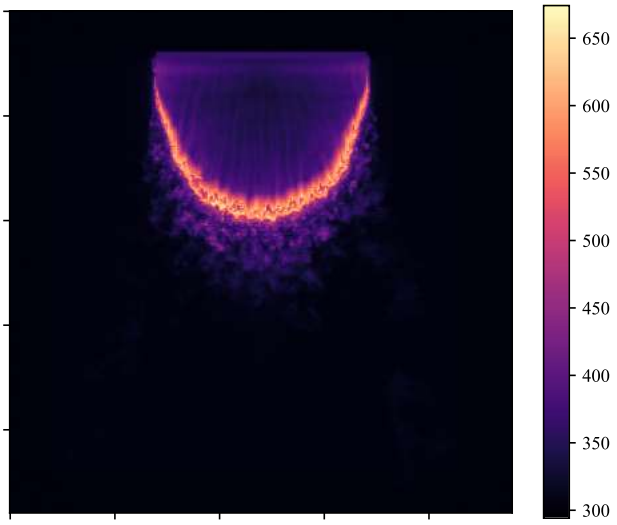

Figure 5-10: Nadir brightness temperature (K) image of a fire over a vegetated scene. (Courtesy of Ronan Paugam)

5.2 Radiative budget modeling in DART-Lux

DART-Lux uses the bi-directional path tracing algorithm to estimate sensor-level radiance using Monte Carlo integration techniques. It only computes end-to-end (*i.e.*, light source to sensor) radiance contribution of sampled light paths. Hence, this method does not provide information about the amount and the fate of radiation (*i.e.*, interception, scattering, absorption) at each vertex of these light paths. Therefore, unlike DART-FT, the simulation of images by DART-Lux is not adapted to the simultaneous simulation of the radiative budget.

An alternative method was developed to overcome this limitation. It takes advantage of the efficient bi-directional radiance computation method of DART-Lux to have an estimation of the local radiative budget at a number of points distributed over the scene. Then, all the different radiative budget products (per facet, per voxel) are derived: 3D radiative budget per type of scene element, including vertical profiles and total radiative budget per type of scene element. These radiative budget products are well adapted to the simulation of photosynthesis of 3D plants. For example, they provide information on the radiation that is absorbed chlorophylls. This method is developed for scene elements simulated as facets and as volumes.

5.2.1 Scene elements simulated as facets

Eq (5.11) introduced in the illumination method for distributing temperature in the scene presented in Section 0 is used to estimate the local order 1 irradiance for a point P of the scene. This equation can be extended to compute the row vector spectral irradiance $\hat{E}_{\lambda,P,n}$ of order n:

$$\hat{E}_{\lambda,P,n} = \frac{\pi}{N}.\sum_{i=1}^{N} L_{\lambda,P,n}(\Omega_i) \tag{5.29}$$

with $L_{\lambda,P,n}(\Omega_i)$ the row vector of order n spectral radiance incident to the point P.

Having estimated the local incident spectral radiation, the scattered $E_{\lambda,P,scat}$ and absorbed $E_{\lambda,P,abs}$ spectral radiation vectors can be deduced:

$$\hat{E}_{\lambda,P,scat} = \begin{cases} \hat{E}_{\lambda,P,n} * \rho_\lambda \text{ (backward scattering)} \\ \hat{E}_{\lambda,P,n} * \tau_\lambda \text{ (forward scattering)} \end{cases} \tag{5.30}$$

$$\hat{E}_{\lambda,P,abs} = \hat{E}_{\lambda,P,scat} * (1 - \omega_\lambda) \tag{5.31}$$

with ρ_λ and τ_λ the hemispherical spectral reflectance and transmittance vectors respectively at the point P and the spectral band $(\lambda, \Delta\lambda)$, and $\omega_\lambda = \rho_\lambda + \tau_\lambda$ the single scattering albedo, $(*)$ is the vector element-wise product operator.

In presence of SIF emission, it is also deduced as the product of the vector of spectral irradiance by the corresponding excitation emission fluorescence matrix:

$$\hat{E}_{\lambda,P,\text{SIF}} = \begin{cases} \hat{E}_{\lambda,P,n} \times M_{PSx,backward} \text{ (backward SIF)} \\ \hat{E}_{\lambda,P,n} \times M_{PSx,forward} \text{ (forward SIF)} \end{cases} \quad (5.32)$$

with $(\times)$ the ordinary matrix product operator.

The thermally emitted radiation is computed directly from the local temperature T:

$$E_{\lambda,P,emis} = \pi . L_{\lambda,\Delta\lambda}(T) \quad (5.33)$$

5.2.2 Scene elements simulated as volumes

The bi-directional Monte Carlo rendering method previously presented for volumes allows one to simulate images of scenes containing these volumes. It allows one to sample light paths and to evaluate the contribution of these paths to the radiance observed by the sensor. It does not provide information about the intercepted, scattered, absorbed radiation along these paths. A method to compute these quantities for volumes was developed.

A volume acquires radiative energy from ingoing radiation from its boundaries $E_{V,in}$ and from emission $E_{V,emis}$, and loses the radiative energy that exits through its boundaries $E_{V,out}$ and by absorption $E_{V,abs}$. The energy conservation principle states:

$$E_{V,in} + E_{V,emis} = E_{V,out} + E_{V,abs} \quad (5.34)$$

The method used for computing facets radiative budget can also be used to compute the incident radiation of the two sides of the boundary surfaces of volumes and therefore it allows to compute the estimations of the spectral ingoing $\hat{E}_{\lambda,V,in}$ and outgoing $\hat{E}_{\lambda,V,out}$ radiation vectors.

In presence of thermal emission, the spectral emission $E_{\lambda,V,emis}$ can be computed knowing the spectral emitted radiance $L_{\lambda,\Delta\lambda}$ and the total area of leaves A_l inside the volume for turbid volumes. For each spectral band $(\lambda, \Delta\lambda)$:

$$E_{\lambda,V,emis} = 2.\pi . A_l . L_{\lambda,\Delta\lambda} \quad (5.35)$$

For a fluid volume of total volume V:

$$E_{\lambda,V,emis} = 4.\pi.V.\sigma_{t,\Delta\lambda} * L_{\Delta\lambda} \tag{5.36}$$

Therefore, the absorbed radiation can be estimated, and consequently the estimations of intercepted radiation $\hat{E}_{\lambda,V,int}$ and the scattered radiation $\hat{E}_{\lambda,V,scat}$ can be deduced knowing the spectral single scattering albedo ω_λ.

$$\hat{E}_{\lambda,V,abs} = \hat{E}_{\lambda,V,in} - \hat{E}_{\lambda,V,out} + E_{\lambda,V,emis} \tag{5.37}$$

$$\hat{E}_{\lambda,V,int} = \frac{\hat{E}_{\lambda,V,abs}}{1-\omega_\lambda} \tag{5.38}$$

$$\hat{E}_{\lambda,V,scat} = \hat{E}_{\lambda,V,int} \times \omega_\lambda \tag{5.39}$$

Where $\div$ is the vector element-wise division operator.

We note from Eq (5.38) that if for a given spectral band $(\lambda_i, \Delta\lambda_i)$, $E_{\lambda_i,V,abs} = 0$, and therefore $\omega_{\lambda_i} = 1$, it is impossible to compute and $\hat{E}_{\lambda_i,V,int}$ and therefore $\hat{E}_{\lambda_i,V,scat}$. In case ω_{λ_i} is close to 1, $E_{\lambda_i,V,abs}$ is small compared to $E_{\lambda_i,V,in}$ and $E_{\lambda_i,V,out}$ and this causes high variance of $\hat{E}_{\lambda_i,V,abs}$, $\hat{E}_{\lambda_i,V,int}$ and $\hat{E}_{\lambda_i,V,scat}$ (c.f. Appendix 5-3).

In presence of SIF emission, the spectral emission E_{emis} can be estimated using the fluorescence excitation emission matrix $M_{PSx} = M_{PSx,backward} + M_{PSx,forward}$:

$$\hat{E}_{\lambda,V,emis} = \hat{E}_{\lambda,V,int} \times M_{PSx} \tag{5.40}$$

Therefore, Eq (5.34) gives:

$$\hat{E}_{\lambda,V,in} - \hat{E}_{\lambda,V,out} = \hat{E}_{\lambda,V,int} * (1-\omega_\lambda) + \hat{E}_{\lambda,V,int} \times M_{PSx} \tag{5.41}$$

And consequently

$$\hat{E}_{\lambda,V,int} = (\hat{E}_{\lambda,V,in} - \hat{E}_{\lambda,V,out}) \times (I - diag(\omega_\lambda) - M_{PSx})^{-1} \tag{5.42}$$

Where I is the identity matrix and $(.)^{-1}$ is the matrix inversion operator.

5.2.3 Results

Scene elements simulated as facets

Figure 5-11 shows a radiative budget product (intercepted radiation per facet) of a maize field computed using DART-Lux and compared DART-FT. The results provided by the two modes are similar. However, computation time is longer for DART-Lux (1 min 39 s) compared to DART-FT (54 s). From, the intercepted radiation, the scattered and absorbed radiation as well as the SIF emission (only for SIF emission bands) can be derived (Figure 5-14). The emitted thermal radiation is computed independently and directly from the local temperature (Figure 5-14).

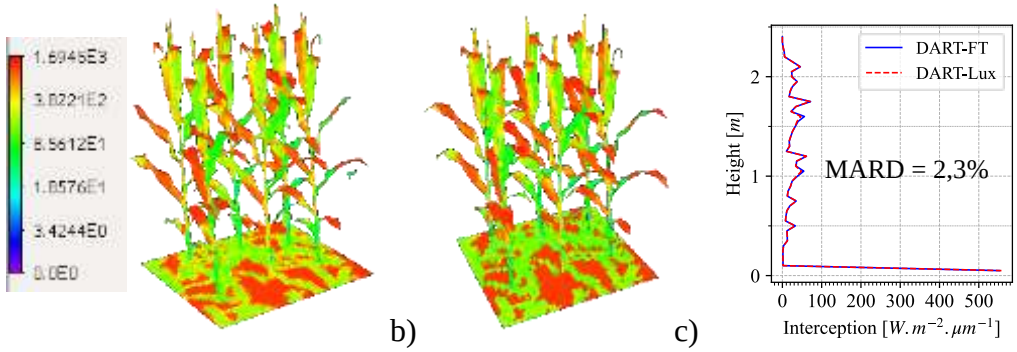

a) b) c)

Figure 5-11: Intercepted radiation ($W.m^{-2}.\mu m^{-2}$) for a visible band in of a maize field computed using a) DART-FT b) DART-Lux c) vertical profile comparison

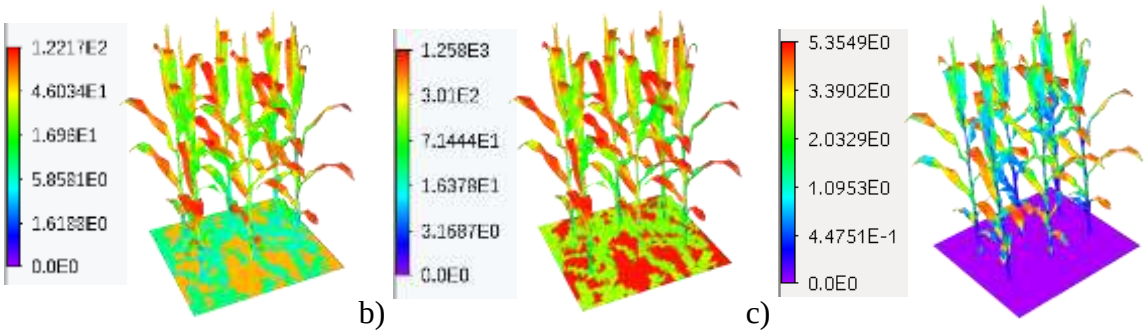

a) b) c)

Figure 5-12: a) Scattered radiation, b) absorbed radiation and c) SIF emission ($W.m^{-2}.\mu m^{-2}$) per facet computed by DART-Lux.

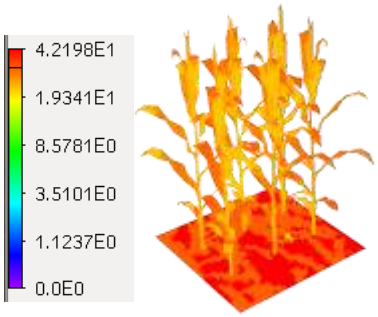

Figure 5-13: Emitted thermal radiation ($W.m^{-2}.\mu m^{-2}$) computed by DART-Lux

Scene elements simulated as turbid

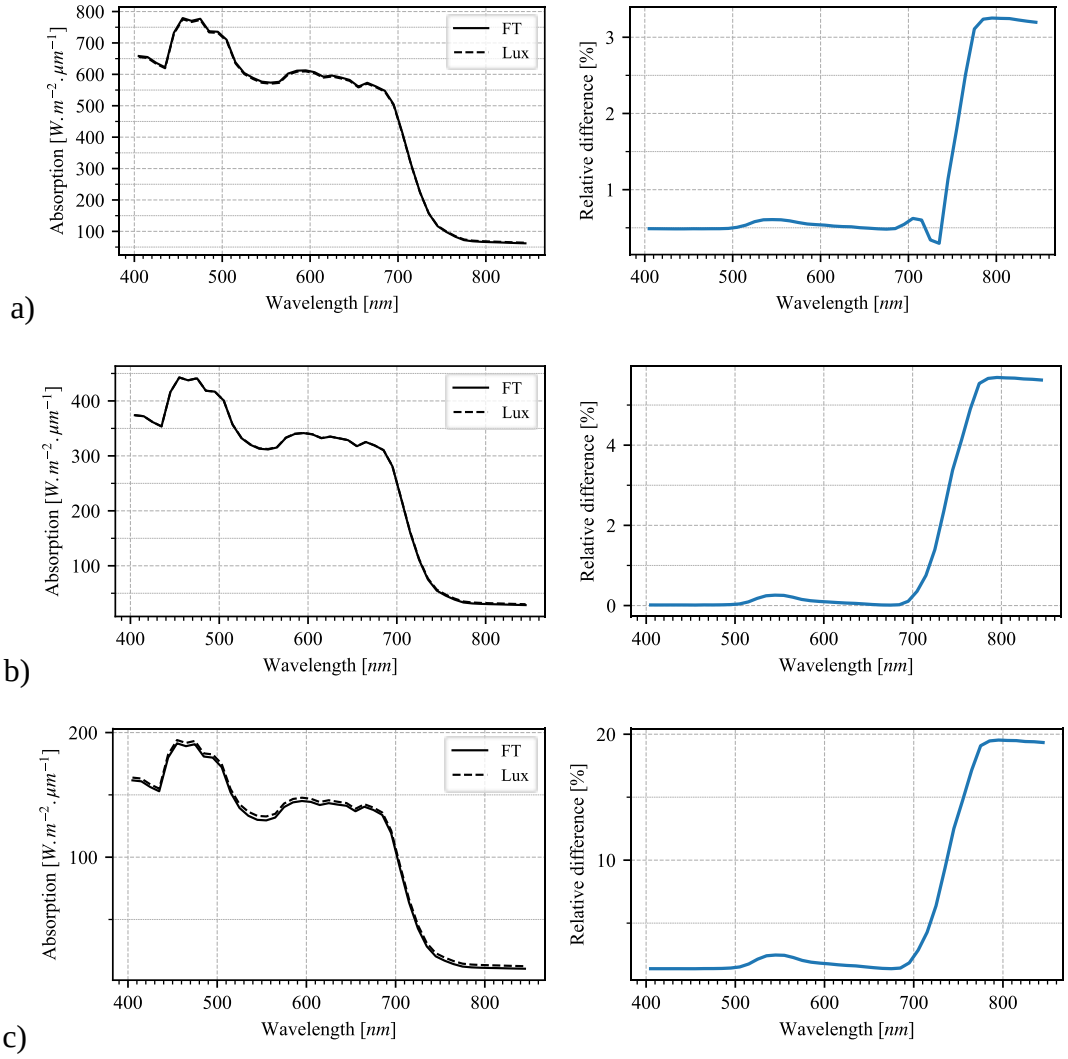

Figure 5-14: Absorbed radiation of a turbid plot computed by DART-Lux compared to DART-FT a) LAI = 1, b) LAI = 0.5, c) LAI = 0.2

Figure 5-14 shows a radiative budget product (absorbed radiation) of a turbid plot computed by DART-Lux and compared to DART-FT for different LAI values. As mentioned in Section 2255.2.2, the estimation of absorbed radiation is less accurate (*i.e.*, higher relative difference with DART-FT considered here as reference) for high values of single scattering albedo, *i.e.*, for near infrared bands. Moreover, the smaller the LAI value is, is the small is the absorption and the less accurate is its estimation by DART-Lux.

Although the absorption estimation is not accurate in the near infrared, we can get a good estimation of the emitted SIF as shown because it is only due to absorption in the visible domain

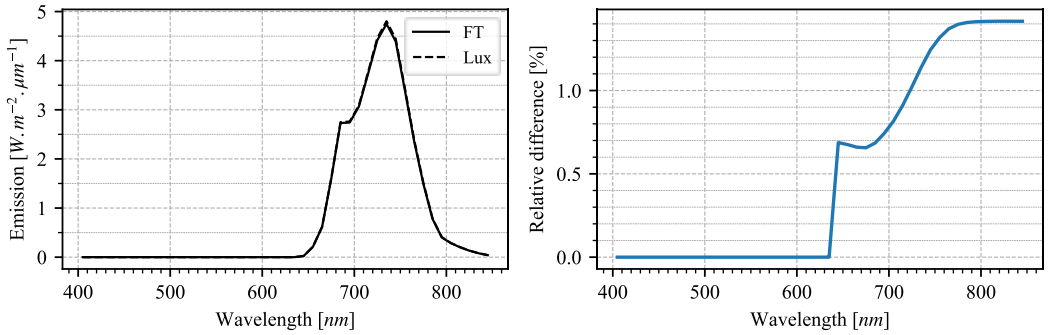

Figure 5-15: Emitted SIF of a turbid plot computed by DART-Lux compared to DART-FT (LAI = 0.5)

5.2.4 Discussion

The developed method takes advantage of the efficiency of DART-Lux for computing radiance images to compute the radiative budget products. It allows DART-Lux to compute most of the radiative budget components already available in DART-FT. The only case where it cannot provide results is for volumes and for spectral bands with a high single scattering albedo. However, this method is not optimal for computing the radiative budget. Indeed, the local incident radiation at each point is computed independently from the others, leading to many repetitive computations. To reduce these repetitive computations, the same light sub-paths are stored and used for all the points. This slightly improves the performance, but it is still less efficient than the forward model DART-FT.

However, it offers some advantages: 1) it is highly flexible: the user can choose to compute the radiative budget only for regions or scene elements of interest, with consideration of all the other scene elements. Therefore, in the case where the elements of interest are much smaller than the total scene, it can be more efficient than DART-FT. For instance, if one is interested

in having the SIF emission of one of the six maize plants shown in Figure 5-12, it is possible to compute it independently of the other plants (Figure 5-16) and the computation time in this case become 16 s compared to 1 min 39 s for the total scene and 54 s for DART-FT. 2) it highly parallelizable: radiative budget of different elements of the same scene can be computed independently and parallelly on several machines. 3) It can benefit from a future use of Graphics Processing Units (GPUs) for accelerating the ray tracing.

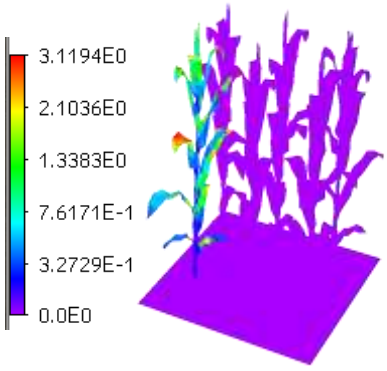

Figure 5-16: SIF emission ($W.m^{-2}.\mu m^{-2}$) of one of the six maize plants

5.3 Conclusion

In this chapter, we introduced the thermal emission and radiative budget modeling in DART-Lux due to their importance in the energy balance modeling. The thermal emission modeling was introduced for scene elements simulated as facets or volumes, and allowed to simulate efficiently large-scale thermal infrared images. The radiative budget modeling is usually less efficient than DART-FT. However, it is flexible and can be efficient if the radiative budget of only a limited part of the scene is needed. It can probably be improved in the future, notably through the use of GPUs.

Appendix 5-1: Expected value of $\widehat{E}_{P,diff,1}$

$$\mathbb{E}[\hat{E}_{P,diff,1}] = \frac{\pi}{N}.\sum_{i=1}^{N}\mathbb{E}[L_{P,1}(\Omega_i)]$$

$$= \frac{\pi}{N}.\sum_{i=1}^{N}\int_{2\pi} L_{P,1}(\Omega_i).\frac{|\Omega.\vec{n}|}{\pi}.d\Omega$$

$$= \int_{2\pi} L_{P,1}(\Omega_i).\frac{|\Omega.\vec{n}|}{\pi}.d\Omega$$

$$= E_{P,diff,1}$$

Appendix 5-2:

We have $p(l) = c.e^{-G(\Omega).u_l.l}$ and $\int_0^H p(l).dl = 1$.

Then, $c = \frac{1}{\int_0^H e^{-G(\Omega).u_l.l}.dl} = \frac{G(\Omega).u_l}{1-e^{-G(\Omega).u_l.H}}$

Therefore, $p(l) = \frac{G(\Omega).u_l.e^{-G(\Omega).u_l.l}}{1-e^{-G(\Omega).u_l.H}}$

The CDF of $p(l)$ is: $P(l) = \int_0^l \frac{G(\Omega).u_l.e^{-G(\Omega).u_l.x}}{1-e^{-G(\Omega).u_l.H}}.dx = \frac{1-e^{-G(\Omega).u_l.l}}{1-e^{-G(\Omega).u_l.H}}$

To sample a distance l from $p(l)$ using a random number ξ: $P(l) = \frac{1-e^{-G(\Omega).u_l.l}}{1-e^{-G(\Omega).u_l.H}} = \xi$

Then, $l = \frac{-\ln\left(1-\xi\left(1-e^{-G(\Omega).u_l.H}\right)\right)}{G(\Omega).u_l}$

The order 1 radiance observed by the sensor in this configuration is:

$$L_{order1}(T_1,T_2) = \int_0^H G(\Omega).u_l.L_{\lambda,\Delta\lambda}\big(T(z)\big).e^{-G(\Omega).u_l.z}.dz$$

$$= \int_0^h G(\Omega).u_l.L_{\lambda,\Delta\lambda}\big(T(z)\big).e^{-G(\Omega).u_l.z}.dz + \int_h^H G(\Omega).u_l.L_{\lambda,\Delta\lambda}\big(T(z)\big).e^{-G(\Omega).u_l.z}.dz$$

$$= L_{\lambda,\Delta\lambda}(T_1)(1-e^{-G(\Omega).u_l.h}) + L_{\lambda,\Delta\lambda}(T_1)(e^{-G(\Omega).u_l.H} - e^{-G(\Omega).u_l.h})$$

The expected order 1 radiance computed using the sampling technique:

$$E[\hat{L}] = \int_0^H L_{order1}\big(T(z)\big).p(z).dz$$

$$= \int_0^H L_{\lambda,\Delta\lambda}(T(z)).\big[1-e^{-G(\Omega).u_l.H}\big].\frac{G(\Omega).u_l.e^{-G(\Omega).u_l.z}}{1-e^{-G(\Omega).u_l.H}}.dz$$

$$= L_{\lambda,\Delta\lambda}(T_1).\int_0^h G(\Omega).u_l.e^{-G(\Omega).u_l.z}.dz + L_{\lambda,\Delta\lambda}(T_2).\int_h^H G(\Omega).u_l.e^{-G(\Omega).u_l.z}.dz$$

$$= L_{\lambda,\Delta\lambda}(T_1)(1-e^{-G(\Omega).u_l.h}) + L_{\lambda,\Delta\lambda}(T_1)(e^{-G(\Omega).u_l.H} - e^{-G(\Omega).u_l.h})$$

$$= L_{order1}(T_1, T_2)$$

Appendix 5-3: Variance of volume radiative budget components

Variance of $\hat{E}_{abs}$:

$$var\big(\hat{E}_{\lambda_i,V,abs}\big) = var\big(\hat{E}_{\lambda_i,V,in} - \hat{E}_{\lambda_i,V,out} + E_{\lambda_i,V,emis}\big)$$

$$= var\big(\hat{E}_{\lambda_i,V,in}\big) + var\big(-\hat{E}_{\lambda_i,V,out}\big) + var\big(E_{\lambda_i,V,emis}\big)$$

$$= var\big(\hat{E}_{\lambda_i,V,in}\big) + var\big(\hat{E}_{\lambda_i,V,out}\big)$$

Therefore, if $E_{\lambda_i,V,abs} \ll E_{\lambda_i,V,in}$ and $E_{\lambda_i,V,abs} \ll E_{\lambda_i,V,out}$, $var\big(\hat{E}_{\lambda_i,V,abs}\big)$ becomes very high compared to the real value $E_{\lambda_i,V,abs}$.

Variance of $\hat{E}_{\lambda_i,V,int}$:

$$var\left(\hat{E}_{\lambda_i,V,int}\right) = var\left(\frac{\hat{E}_{\lambda_i,V,abs}}{1-\omega_{\lambda_i}}\right)$$

$$= \frac{1}{\left(1-\omega_{\lambda_i}\right)^2}\left(var\left(\hat{E}_{\lambda_i,V,in}\right) + var\left(\hat{E}_{\lambda_i,Vout}\right)\right)$$

Therefore, $var\left(\hat{E}_{\lambda_i,V,int}\right) \to +\infty$ if $\omega \to 1$

Variance of $\hat{E}_{\lambda_i,V,scat}$:

$$var\left(\hat{E}_{\lambda_i,V,scat}\right) = var\left(\omega_{\lambda_i}.\hat{E}_{\lambda_i,V,int}\right)$$

$$= \left(\frac{\omega_{\lambda_i}}{1-\omega_{\lambda_i}}\right)^2.\left(var\left(\hat{E}_{\lambda_i,V,in}\right) + var\left(\hat{E}_{\lambda_i,V,out}\right)\right)$$

Therefore, $var\left(\hat{E}_{\lambda_i,V,scat}\right) \to +\infty$ if $\omega_{\lambda_i} \to 1$

Appendix 5-4: Nomenclature

Symbol	Description	Unit
$\hat{E}_{\lambda,P,abs}$	Estimator of absorbed radiation at point P	$W.m^{-2}.\mu m^{-1}$
$\hat{E}_{\lambda,P,n}$	Estimator of incident radiation at point P (order n)	$W.m^{-2}.\mu m^{-1}$
$\hat{E}_{\lambda,P,scat}$	Estimator of scattered radiation at point P	$W.m^{-2}.\mu m^{-1}$
$\hat{E}_{\lambda,P,\mathrm{SIF}}$	Estimator of SIF emission at point P	$W.m^{-2}.\mu m^{-1}$
$\hat{E}_{\lambda,V,abs}$	Estimator of scattered radiation at point P	$W.m^{-2}.\mu m^{-1}$
$\hat{E}_{\lambda,V,emis}$	Estimator of emitted radiation in a volume V	$W.m^{-2}.\mu m^{-1}$
$\hat{E}_{\lambda,V,int}$	Estimator of intercepted radiation in a volume V	$W.m^{-2}.\mu m^{-1}$
$\hat{E}_{\lambda,V,scat}$	Estimator of scattered radiation in a volume V	$W.m^{-2}.\mu m^{-1}$
E_{BOA}	Bottom of atmosphere irradiance	$W.m^{-2}.\mu m^{-1}$
$E_{P,1}$	First order irradiance at point P	$W.m^{-2}.\mu m^{-1}$
$E_{P,diff,1}$	First order diffuse irradiance at point P	$W.m^{-2}.\mu m^{-1}$

$E_{P,dir,1}$	First order direct irradiance at point P	$W.m^{-2}.\mu m^{-1}$
$E_{V,in}$	Ingoing radiation to volume V	$W.m^{-2}.\mu m^{-1}$
$E_{V,out}$	Outgoing radiation from volume V	$W.m^{-2}.\mu m^{-1}$
$E_{\lambda,P,emis}$	Emitted radiation at point P	$W.m^{-2}.\mu m^{-1}$
$E_{\lambda,V,emis}$	Emitted radiation at volume V	$W.m^{-2}.\mu m^{-1}$
f_{sunlit}	Fraction of sunlit leaves	-
$L_B(\lambda,T)$	Black body of temperature T emitted radiance at wavelength λ	$W.m^{-2}.\mu m^{-1}.sr^{-1}$
L_{order1}	Order 1 emitted radiance of a volume	$W.m^{-2}.\mu m^{-1}.sr^{-1}$
$L_{\lambda,\Delta\lambda}(T)$	Emitted radiance of an object of temperature T at the spectral band $(\lambda,\Delta\lambda)$	$W.m^{-2}.\mu m^{-1}.sr^{-1}$
$L_\lambda(T)$	Emitted radiance of an object of temperature T at wavelength λ	$W.m^{-2}.\mu m^{-1}.sr^{-1}$
$M_B(T)$	Black body object of temperature T thermal emission exitance	$W.m^{-2}$
T	Thermodynamic temperature	K
T_B	Brightness temperature	K
T_P	Thermodynamic temperature at point P	K
λ_{eq}	Equivalent wavelength	μm

Conclusions and perspectives

This thesis was driven by the need for a comprehensive SIF model in order to link the SIF observations to the photosystem level instantaneous photosynthetic activity and to enable a better understanding and interpretation of these observations with the purpose of monitoring the photosynthesis process at different spatial and temporal scales. This is crucial for addressing some of the most imperious challenges such as climate change and the need to provide food for the increasing world population under the constraints of water scarcity and the increasing frequency of extreme weather conditions.

DART is one of the most comprehensive radiative transfer models for RS applications. Since 2017, its initial flux tracking mode (DART-FT) simulates SIF by upscaling leaf-level SIF simulated by Fluspect for canopies simulated as facets, and can provide SIF radiation budget and TOA and BOA RS observations of these canopies. Faced with the difficulty of having a complete SIF measurements dataset for a relevant comparison with a SIF radiative transfer model, we went through model-to-model comparison to assess the accuracy of the DART-FT SIF modeling. DART-FT gave results in agreement with the "reference" SIF model SCOPE/mSCOPE (1D) for horizontally homogeneous scenes and for different configurations, by approximating the turbid medium used in SCOPE with a quasi-turbid medium (*i.e.*, a cloud of facets randomly distributed). Then, DART-FT was extended to simulate SIF for vegetation represented as 3D turbid medium. This statistical representation of vegetation is widely used in RS radiative transfer models, especially for simulating large landscapes. For example, it can be useful for reducing the computational requirements for scenes simulated with a very large number of facets, or if the explicit 3D representation with facets of the simulated scene is not available (*e.g.*, only a 3D array of LAI is available). DART-FT SIF modelling for quasi-turbid medium and for turbid medium appeared to closely match. This is a kind of validation for DART-FT SIF modelling for turbid medium because DART-FT SIF modelling for quasi turbid medium has already been validated with SCOPE model.

However, the need for simulating SIF large for landscapes (e.g., a few square kilometers) driven by the advancements in the reconstruction methods of large 3D mock-ups and also the upcoming SIF satellite mission FLEX which will have a spatial resolution of 300 m, cannot be satisfied with DART-FT. Indeed, DART-FT cannot simulate large landscapes with reasonable computational resources because it tracks all radiation all over the scene which is convenient if the radiative budget of the whole scene is required, but it is not optimal for simulating images. For this reason, a more efficient mode called DART-Lux is developed. It uses a Monte Carlo bi-directional path tracing algorithm implementation from the open-source rendering engine LuxCoreRender adapted for RS applications and included in the DART framework. It can greatly decrease computation time and memory usage especially for large and complex scenes. Therefore, DART-Lux is well adapted to the simulation of large scenes. This highlights the interest to introduce the modeling of SIF and thermal emission in DART-Lux. The simulation of images in DART-Lux was extended to SIF images simulation by adapting the SIF emission equation to the bi-directional path tracing algorithm. The 3D turbid medium modeling of vegetation was also introduced, including the SIF. DART-Lux SIF modeling was assessed by comparison to DART-FT: the two modes provided results in close agreement. Computational requirements are usually much less important for DART-Lux, especially for large and complex scenes. The gain in computation time decreases if the number of spectral bands increases.

The introduction of SIF in DART-Lux allowed one to simulate SIF observations for large and complex scenes that were not possible to simulate using DART-FT. It was applied to eight realistic forest plots to evaluate the impact of the 3D structure on SIF observation by comparing 3D SIF simulations to their equivalent 1D simulations. For nadir radiance, we had large relative difference that could reach 50% especially for oblique sun directions. DART-FT radiative budget products obtained with low spectral resolution allowed one to analyze these differences. They are explained by two major reasons: 1) the canopy represented in 3D absorbs less PAR and therefore emits less SIF than 1D canopies due to clumping and shadowing effects. 2) the emitted SIF within the canopy escapes more easily from 1D canopies than from 3D canopies. Similarly, the neglect of woody elements in 3D canopies leads to an overestimation of SIF: the presence of wood elements reduces the PAR absorption by the leaves (shadowing effect) and prevents a fraction of the emitted SIF from escaping the canopy (blocking effect).

An accurate simulation of SIF requires the consideration of local meteorological parameters that influence the fluorescence quantum efficiency and therefore SIF emission. Therefore, a

simulation of the full energy budget is required including all the energy exchanges of the vegetation with its environment whether they are made via radiative or non-radiative processes. From the radiation point of view, it is essential to evaluate the energy gain of the vegetation by the incident solar radiation, and the energy loss by thermal emission. Therefore, we have introduced the modeling of the radiative budget and thermal emission in DART-Lux. Thermal emission modeling proved to be very efficient and accurate by comparison with DART-FT. Although the radiative budget modeling using the bi-directional path tracing method is less efficient than the discrete ordinates method (*i.e.*, DART-FT) for most scenes, its flexibility offers advantages. Indeed, it allows one to get the radiative budget for a set of sub-zones in the simulated scene, and this radiative budget can be calculated per type of scene element. Future improvements, notably the use of GPU acceleration, can make the implemented method more and more useful.

The remaining step towards the development of a comprehensive SIF model is the consideration of non-radiative energy exchange processes. These processes include photosynthesis, heat conduction, turbulence, etc. A 1D/ 3D energy model, called DART-EB (Energy Budget), is being developed by the DART team. In addition to the radiative energy exchanges (thermal emission, radiation budget) computed by DART, DART-EB simulates non-radiative processes. Starting from an initial guess of local temperature, the energy exchanges are computed. Obviously, the energy balance condition (*i.e.*, energy gains equal to energy loss) is not verified. Then, an iterative approach starts and local temperatures are adjusted at each iteration until convergence. (*i.e.*, reaching the energy balance). DART-EB will allow to assess the 3D temperature distribution and the multiplicative factors η that scale the dark-adapted leaf-level SIF emission to give steady state SIF as function of the leaf photosynthetic rate. In addition to SIF observations, thermal images will also be more accurately simulated using this physically-based approach. This is important in the frame of the preparation of the upcoming satellite missions with high spatial resolution thermal infrared sensors on-board (*i.e.*, TRISHNA mission of CNES / ISRO and LSTM mission of ESA).

Conclusions et perspectives

Cette thèse a été motivée par le besoin d'un modèle SIF complet afin de relier les observations SIF à l'activité photosynthétique instantanée au niveau du photosystème et de permettre une meilleure compréhension et interprétation de ces observations dans le but de suivre le processus de photosynthèse à différentes échelles spatiales et temporelles. Ceci est crucial pour répondre à certains des défis les plus impérieux tels que le changement climatique et la nécessité de fournir de la nourriture à une population mondiale croissante sous les contraintes de la rareté de l'eau et de la fréquence croissante des conditions météorologiques extrêmes.

DART est l'un des modèles de transfert radiatif les plus complets pour les applications de télédétection. Depuis 2017, son mode de suivi de flux initial (DART-FT) simule la SIF en mettant à l'échelle la SIF au niveau des feuilles simulé par Fluspect pour les canopées simulées sous forme de facettes, et peut fournir un bilan radiatif de SIF et des observations de télédections en TOA et en BOA de ces couverts. Face à la difficulté d'avoir un jeu de données complet de mesures SIF pour une comparaison pertinente avec un modèle de transfert radiatif SIF, nous sommes passés par une comparaison modèle à modèle pour évaluer la précision de la modélisation DART-FT SIF. DART-FT a donné des résultats en accord avec le modèle SIF "de référence" SCOPE/mSCOPE (1D) pour des scènes homogènes horizontalement et pour différentes configurations, en rapprochant le milieu turbide utilisé dans SCOPE avec un milieu quasi turbide (*i.e.*, un nuage de facettes réparties aléatoirement). Ensuite, DART-FT a été étendu pour simuler la SIF pour la végétation représentée sous forme de milieu turbide 3D. Cette représentation statistique de la végétation est largement utilisée dans les modèles de transfert radiatif pour la télédétection, surtout pour simuler des paysages larges. Par exemple, elle peut être utile pour réduire les besoins en ressources de calcul pour des scènes simulées avec un très grand nombre de facettes, ou si la représentation 3D explicite avec des facettes de la scène simulée n'est pas disponible (*e.g.*, seule une distribution 3D de LAI est disponible). La

modélisation de SIF de DART-FT pour le milieu quasi-turbide et pour le milieu turbide montrent une correspondance étroite. Il s'agit d'une sorte de validation pour la modélisation DART-FT SIF pour milieu turbide car la modélisation DART-FT SIF pour milieu quasi turbide a déjà été validée avec le modèle SCOPE

Cependant, le besoin de simuler la SIF pour des grands paysages (*e.g.*, quelques kilomètres carrés) porté par les progrès des méthodes de reconstruction de grandes maquettes 3D et également la prochaine mission satellite SIF FLEX qui aura une résolution spatiale de 300 m, ne peut pas être satisfait par DART-FT. En effet, DART-FT ne peut pas simuler de grands paysages avec des ressources de calcul raisonnables parce qu'il suit tous les rayons sur toute la scène, ce qui est pratique si le bilan radiatif de toute la scène est requis, mais ce n'est pas optimal pour la simulation d'images. Pour cette raison, un mode plus efficace appelé DART-Lux est développé. Il utilise une implémentation d'algorithme de traçage de chemin bidirectionnel Monte Carlo à partir du moteur de rendu open source LuxCoreRender adaptée aux applications RS et incluse dans le framework de DART. Il peut généralement réduire le temps de calcul et le besoin en mémoire, en particulier pour les scènes volumineuses et complexes. Par conséquent, DART-Lux est bien adapté à la simulation de grandes scènes. Ceci met en évidence l'intérêt d'introduire la modélisation du SIF et de l'émission thermique dans DART-Lux. La simulation d'images par DART-Lux a été étendue à la simulation d'images SIF en adaptant l'équation d'émission SIF à l'algorithme de traçage de chemin bidirectionnel. La modélisation 3D du milieu turbide de la végétation a également été introduite, y compris la SIF. DART-Lux SIF a été évalué par comparaison avec DART-FT : les deux modes ont fourni des résultats en accord étroit. Les exigences de calcul sont généralement beaucoup moins importantes pour DART-Lux, en particulier pour les scènes volumineuses et complexes. Le gain en temps de calcul diminue si le nombre de bandes spectrales augmente.

L'introduction de la SIF dans DART-Lux a permis de simuler des observations SIF pour des scènes larges et complexes qu'il n'était pas possible de simuler avec DART-FT. Il a été appliqué à huit maquettes forestières réalistes pour évaluer l'impact de la structure 3D sur l'observation SIF en comparant des simulations SIF 3D à leurs simulations 1D équivalentes. Pour la luminance au nadir, nous avons eu une grande différence relative qui pouvait atteindre 50%, en particulier pour les directions solaires obliques. Les produits de bilan radiatif DART-FT obtenus avec une faible résolution spectrale ont permis d'analyser ces différences. Elles s'expliquent par deux raisons principales : 1) la canopée représentée en 3D absorbe moins de

PAR et émet donc moins de SIF que les canopées 1D en raison des effets d'agglutination et d'ombrage. 2) la SIF émise dans la canopée s'échappe plus facilement des canopées 1D que des canopées 3D. De même, la négligence des éléments ligneux dans les canopées 3D conduit à une surestimation de la SIF : la présence d'éléments ligneux réduit l'absorption du PAR par les feuilles (effet d'ombrage) et empêche une fraction de la SIF émis de s'échapper de la canopée (effet de blocage).

Une simulation précise de la SIF nécessite la prise en compte des paramètres météorologiques locaux qui influencent l'efficacité quantique de la fluorescence et donc l'émission de SIF. Il faut donc simuler le bilan énergétique complet incluant tous les échanges énergétiques de la végétation avec son environnement qu'ils se fassent par des processus radiatifs ou non radiatifs. Du point de vue du rayonnement, il est essentiel d'évaluer le gain d'énergie de la végétation par le rayonnement solaire incident, et la perte d'énergie par émission thermique. Par conséquent, nous avons introduit la modélisation du bilan radiatif et de l'émission thermique dans DART-Lux. La modélisation des émissions thermiques s'est avérée très efficace et précise par rapport à DART-FT. Bien que la modélisation du bilan radiatif utilisant la méthode de traçage de chemin bidirectionnel soit moins efficace que la méthode des ordonnées discrètes (*i.e.*, DART-FT) pour la plupart des scènes, sa flexibilité offre des avantages. En effet, elle permet d'obtenir le bilan radiatif pour un ensemble de sous-zones de la scène simulée, et ce bilan radiatif peut être calculé par type d'élément de scène. Des améliorations futures, notamment l'utilisation de l'accélération GPU, peuvent rendre la méthode implémentée de plus en plus utile.

L'étape restante vers le développement d'un modèle SIF complet est la prise en compte des processus d'échange d'énergie non radiatifs. Ces processus incluent la photosynthèse, la conduction thermique, la turbulence, etc. Un modèle énergétique 1D/3D, appelé DART-EB (Energy Budget), est en cours de développement par l'équipe DART. En plus des échanges d'énergie radiative (émission thermique, bilan radiatif) calculés par DART, DART-EB simule des processus non radiatifs. A partir d'une estimation initiale de la température locale, les échanges d'énergie sont calculés. De toute évidence, la condition de bilan énergétique (*i.e.*, des gains d'énergie égaux à la perte d'énergie) n'est pas vérifiée. Ensuite, une approche itérative démarre et les températures locales sont ajustées à chaque itération jusqu'à convergence. (*i.e.*, atteindre l'équilibre énergétique). DART-EB permettra d'évaluer la distribution de température 3D et les facteurs multiplicatifs η qui pondèrent l'émission de SIF au niveau des feuilles

adaptées à l'obscurité pour donner la SIF à l'état d'équilibre en fonction du taux de photosynthèse des feuilles. En plus des observations SIF, les images thermiques seront également simulées avec plus de précision à l'aide de cette approche basée sur la physique. Ceci est important dans le cadre de la préparation des prochaines missions satellites avec des capteurs infrarouges thermiques à haute résolution spatiale embarqués (*i.e.*, la mission TRISHNA du CNES / ISRO et la mission LSTM de l'ESA).

Bibliography

Ač, A., Malenovský, Z., Olejníčková, J., Gallé, A., Rascher, U., & Mohammed, G. (2015). Meta-analysis assessing potential of steady-state chlorophyll fluorescence for remote sensing detection of plant water, temperature and nitrogen stress. *Remote Sensing of Environment, 168*, 420–436. https://doi.org/10.1016/j.rse.2015.07.022

Antyufeev, V. S., & Marshak, A. L. (1990). Monte Carlo method and transport equation in plant canopies. *Remote Sensing of Environment*, *31*(3), 183–191. https://doi.org/10.1016/0034-4257(90)90088-4

Baker, N. R. (2008). Chlorophyll Fluorescence: A Probe of Photosynthesis In Vivo. *Annual Review of Plant Biology*, *59*(1), 89–113. https://doi.org/10.1146/annurev.arplant.59.032607.092759

Brewster, D. (1834). XIX. On the Colours of Natural Bodies. *Earth and Environmental Science Transactions of The Royal Society of Edinburgh*, *12*(2), 538–545. https://doi.org/10.1017/S0080456800031203

Campbell, P. K. E., Huemmrich, K. F., Middleton, E. M., Ward, L. A., Julitta, T., Daughtry, C. S. T., Burkart, A., Russ, A. L., & Kustas, W. P. (2019). Diurnal and Seasonal Variations in Chlorophyll Fluorescence Associated with Photosynthesis at Leaf and Canopy Scales. *Remote Sensing*, *11*(5), Article 5. https://doi.org/10.3390/rs11050488

Campbell, P. K. E., Middleton, E. M., Corp, L. A., & Kim, M. S. (2008). Contribution of chlorophyll fluorescence to the apparent vegetation reflectance. *Science of The Total Environment*, *404*(2), 433–439. https://doi.org/10.1016/j.scitotenv.2007.11.004

Cogato, A., Meggio, F., De Antoni Migliorati, M., & Marinello, F. (2019). Extreme Weather Events in Agriculture: A Systematic Review. *Sustainability*, *11*(9), Article 9. https://doi.org/10.3390/su11092547

Cogliati, S., Rossini, M., Julitta, T., Meroni, M., Schickling, A., Burkart, A., Pinto, F., Rascher, U., & Colombo, R. (2015). Continuous and long-term measurements of reflectance and sun-induced chlorophyll fluorescence by using novel automated field spectroscopy systems. *Remote Sensing of Environment*, *164*, 270–281. https://doi.org/10.1016/j.rse.2015.03.027

Costa, J. M., Grant, O. M., & Chaves, M. M. (2013). Thermography to explore plant–environment interactions. *Journal of Experimental Botany*, *64*(13), 3937–3949. https://doi.org/10.1093/jxb/ert029

Dence, T. P. (2013). A Brief Look into the Lambert W Function. *Applied Mathematics*, *4*(6), Article 6. https://doi.org/10.4236/am.2013.46122

Disney, M. I., Lewis, P., & North, P. R. J. (2000). Monte Carlo ray tracing in optical canopy reflectance modelling. *Remote Sensing Reviews*, *18*(2–4), 163–196. https://doi.org/10.1080/02757250009532389

Drusch, M., Moreno, J., Bello, U. D., Franco, R., Goulas, Y., Huth, A., Kraft, S., Middleton, E. M., Miglietta, F., Mohammed, G., Nedbal, L., Rascher, U., Schüttemeyer, D., & Verhoef, W. (2017). The FLuorescence EXplorer Mission Concept—ESA's Earth Explorer 8. *IEEE Transactions on Geoscience and Remote Sensing*, *55*(3), 1273–1284. https://doi.org/10.1109/TGRS.2016.2621820

Fournier, A., Daumard, F., Champagne, S., Ounis, A., Goulas, Y., & Moya, I. (2012). Effect of canopy structure on sun-induced chlorophyll fluorescence. *ISPRS Journal of Photogrammetry and Remote Sensing*, *68*, 112–120. https://doi.org/10.1016/j.isprsjprs.2012.01.003

Frankenberg, C., Butz, A., & Toon, G. C. (2011). Disentangling chlorophyll fluorescence from atmospheric scattering effects in O2 A-band spectra of reflected sun-light. *Geophysical Research Letters*, *38*(3). https://doi.org/10.1029/2010GL045896

Gao, S., Huete, A., Kobayashi, H., Doody, T. M., Liu, W., Wang, Y., Zhang, Y., & Lu, X. (2022). Simulation of solar-induced chlorophyll fluorescence in a heterogeneous forest using 3-D radiative transfer modelling and airborne LiDAR. *ISPRS Journal of Photogrammetry and Remote Sensing*, *191*, 1–17. https://doi.org/10.1016/j.isprsjprs.2022.07.004

Gascon, F., Gastellu-Etchegorry, J.-P., & Lefevre, M.-J. (2001). Radiative transfer model for simulating high-resolution satellite images. *IEEE Transactions on Geoscience and Remote Sensing*, *39*(9), 1922–1926. https://doi.org/10.1109/36.951083

Gastellu-Etchegorry, J.-P., Demarez, V., Pinel, V., & Zagolski, F. (1996). Modeling radiative transfer in heterogeneous 3-D vegetation canopies. *Remote Sensing of Environment*, *58*(2), 131–156. https://doi.org/10.1016/0034-4257(95)00253-7

Gastellu-Etchegorry, J.-P., Lauret, N., Yin, T., Landier, L., Kallel, A., Malenovský, Z., Bitar, A. A., Aval, J., Benhmida, S., Qi, J., Medjdoub, G., Guilleux, J., Chavanon, E., Cook, B., Morton, D., Chrysoulakis, N., & Mitraka, Z. (2017). DART: Recent Advances in Remote Sensing Data Modeling With Atmosphere, Polarization, and Chlorophyll Fluorescence. *IEEE Journal of Selected Topics in Applied Earth Observations and Remote Sensing*, *10*(6), 2640–2649. https://doi.org/10.1109/JSTARS.2017.2685528

Gastellu-Etchegorry, J.-P., Martin, E., & Gascon, F. (2004). DART: A 3D model for simulating satellite images and studying surface radiation budget. *International Journal of Remote Sensing*, *25*(1), 73–96. https://doi.org/10.1080/0143116031000115166

Gastellu-Etchegorry, J.-P., Yin, T., Lauret, N., Cajgfinger, T., Gregoire, T., Grau, E., Feret, J.-B., Lopes, M., Guilleux, J., Dedieu, G., Malenovský, Z., Cook, B. D., Morton, D., Rubio, J., Durrieu, S., Cazanave, G., Martin, E., & Ristorcelli, T. (2015). Discrete Anisotropic Radiative Transfer (DART 5) for Modeling Airborne and Satellite Spectroradiometer and LIDAR Acquisitions of Natural and Urban Landscapes. *Remote Sensing*, *7*(2), Article 2. https://doi.org/10.3390/rs70201667

Gerhards, M., Schlerf, M., Mallick, K., & Udelhoven, T. (2019). Challenges and Future Perspectives of Multi-/Hyperspectral Thermal Infrared Remote Sensing for Crop Water-Stress Detection: A Review. *Remote Sensing*, *11*(10), Article 10. https://doi.org/10.3390/rs11101240

Gobron, N., Pinty, B., Verstraete, M. M., & Govaerts, Y. (1997). A semidiscrete model for the scattering of light by vegetation. *Journal of Geophysical Research: Atmospheres*, *102*(D8), 9431–9446. https://doi.org/10.1029/96JD04013

Guanter, L., Frankenberg, C., Dudhia, A., Lewis, P. E., Gómez-Dans, J., Kuze, A., Suto, H., & Grainger, R. G. (2012). Retrieval and global assessment of terrestrial chlorophyll fluorescence from GOSAT space measurements. *Remote Sensing of Environment*, *121*, 236–251. https://doi.org/10.1016/j.rse.2012.02.006

Guanter, L., Zhang, Y., Jung, M., Joiner, J., Voigt, M., Berry, J. A., Frankenberg, C., Huete, A. R., Zarco-Tejada, P., Lee, J.-E., Moran, M. S., Ponce-Campos, G., Beer, C., Camps-Valls, G., Buchmann, N., Gianelle, D., Klumpp, K., Cescatti, A., Baker, J. M., & Griffis, T. J. (2014). Global and time-resolved monitoring of crop photosynthesis with chlorophyll fluorescence. *Proceedings of the National Academy of Sciences*, *111*(14), E1327–E1333. https://doi.org/10.1073/pnas.1320008111

Guillevic, P. C., Gastellu-Etchegorry, J.-P., Demarty, J., & Prévot, L. (2003). Thermal infrared radiative transfer within three-dimensional vegetation covers. *Journal of Geophysical Research: Atmospheres*, *108*(D8). https://doi.org/10.1029/2002JD002247

Hernández-Clemente, R., North, P. R. J., Hornero, A., & Zarco-Tejada, P. J. (2017). Assessing the effects of forest health on sun-induced chlorophyll fluorescence using the FluorFLIGHT 3-D radiative transfer model to account for forest structure. *Remote Sensing of Environment*, *193*, 165–179. https://doi.org/10.1016/j.rse.2017.02.012

Jabłoński, A. (1935). Über den Mechanismus der Photolumineszenz von Farbstoffphosphoren. *Zeitschrift für Physik*, *94*(1), 38–46. https://doi.org/10.1007/BF01330795

Jacquemoud, S., & Baret, F. (1990). PROSPECT: A model of leaf optical properties spectra. *Remote Sensing of Environment*, *34*(2), 75–91. https://doi.org/10.1016/0034-4257(90)90100-Z

Kallel, A. (2020a). Two-scale Monte Carlo ray tracing for canopy-leaf vector radiative transfer coupling. *Journal of Quantitative Spectroscopy and Radiative Transfer*, *243*, 106815. https://doi.org/10.1016/j.jqsrt.2019.106815

Kallel, A. (2020b). FluLCVRT: Reflectance and fluorescence of leaf and canopy modeling based on Monte Carlo vector radiative transfer simulation. *Journal of Quantitative Spectroscopy and Radiative Transfer*, *253*, 107183. https://doi.org/10.1016/j.jqsrt.2020.107183

Kallel, A., & Nilson, T. (2013). Revisiting the vegetation hot spot modeling: Case of Poisson/Binomial leaf distributions. *Remote Sensing of Environment*, *130*, 188–204. https://doi.org/10.1016/j.rse.2012.11.018

Kautsky, H., Appel, W., & Amann, H. (1960). Chlorophyll fluorescence and carbon assimilation. Part XIII. The fluorescence and the photochemistry of plants. *Biochemische Zeitschrift*, *332*, 277–292.

Kautsky, H., & Hirsch, A. (1931). Neue Versuche zur Kohlensäureassimilation. *Naturwissenschaften*, *19*(48), 964–964. https://doi.org/10.1007/BF01516164

Kautsky, H., & Zedlitz, W. (1941). Fluoreszenzkurven von Chloroplasten-Grana. *Naturwissenschaften*, *29*(7), 101–102. https://doi.org/10.1007/BF01468767

Kobayashi, H., & Iwabuchi, H. (2008). A coupled 1-D atmosphere and 3-D canopy radiative transfer model for canopy reflectance, light environment, and photosynthesis simulation in a heterogeneous landscape. *Remote Sensing of Environment*, *112*(1), 173–185. https://doi.org/10.1016/j.rse.2007.04.010

Kuusk, A. (1985). The hot-spot effect of a uniform vegetative cover. *Soviet Journal of Remote Sensing*, *3*, 645–658.

Lichtman, J. W., & Conchello, J.-A. (2005). Fluorescence microscopy. *Nature Methods*, *2*(12), Article 12. https://doi.org/10.1038/nmeth817

Liu, X., Guanter, L., Liu, L., Damm, A., Malenovský, Z., Rascher, U., Peng, D., Du, S., & Gastellu-Etchegorry, J.-P. (2019). Downscaling of solar-induced chlorophyll fluorescence from canopy level to photosystem level using a random forest model. *Remote Sensing of Environment*, *231*, 110772. https://doi.org/10.1016/j.rse.2018.05.035

Liu, Y., Kochanski, A., Baker, K. R., Mell, W., Linn, R., Paugam, R., Mandel, J., Fournier, A., Jenkins, M. A., Goodrick, S., Achtemeier, G., Zhao, F., Ottmar, R., French, N. H. F., Larkin, N., Brown, T., Hudak, A., Dickinson, M., Potter, B., … McNamara, D. (2019). Fire behaviour and smoke modelling: Model improvement and measurement needs for next-generation smoke research and forecasting systems. *International Journal of Wildland Fire*, *28*(8), 570–588. https://doi.org/10.1071/WF18204

Liu, Z., Lu, X., An, S., Heskel, M., Yang, H., & Tang, J. (2019). Advantage of multi-band solar-induced chlorophyll fluorescence to derive canopy photosynthesis in a temperate forest. *Agricultural and Forest Meteorology*, *279*, 107691. https://doi.org/10.1016/j.agrformet.2019.107691

Malenovský, Z., Regaieg, O., Yin, T., Lauret, N., Guilleux, J., Chavanon, E., Duran, N., Janoutová, R., Delavois, A., Meynier, J., Medjdoub, G., Yang, P., van der Tol, C., Morton, D., Cook, B. D., & Gastellu-Etchegorry, J.-P. (2021). Discrete anisotropic radiative transfer modelling of solar-induced chlorophyll fluorescence: Structural impacts in geometrically explicit vegetation canopies. *Remote Sensing of Environment*, *263*, 112564. https://doi.org/10.1016/j.rse.2021.112564

McAlister, E. D., & Myers, J. (1940). Time Course of Photosynthesis and Fluorescence. *Science*, *92*(2385), 241–243. https://doi.org/10.1126/science.92.2385.241

McGrattan, K. B., McDermott, R. J., Weinschenk, C. G., & Forney, G. P. (2013). Fire Dynamics Simulator, Technical Reference Guide, Sixth Edition. *NIST*. https://www.nist.gov/publications/fire-dynamics-simulator-technical-reference-guide-sixth-edition

Mell, W., Jenkins, M. A., Gould, J., Cheney, P., Mell, W., Jenkins, M. A., Gould, J., & Cheney, P. (2007). A physics-based approach to modelling grassland fires. *International Journal of Wildland Fire*, *16*(1), 1–22. https://doi.org/10.1071/WF06002

Moya, I., Camenen, L., Evain, S., Goulas, Y., Cerovic, Z. G., Latouche, G., Flexas, J., & Ounis, A. (2004). A new instrument for passive remote sensing: 1. Measurements of sunlight-induced chlorophyll fluorescence. *Remote Sensing of Environment*, *91*(2), 186–197. https://doi.org/10.1016/j.rse.2004.02.012

Müller, N. J. C. (1874). Beziehungen zwischen assimilation, absorption und fluoreszenz im chlorophyll des lebenden blattes. *Jahrb Wiss Bo*, *9*, 42–49.

North, P. R. J. (1996). Three-dimensional forest light interaction model using a Monte Carlo method. *IEEE Transactions on Geoscience and Remote Sensing*, *34*(4), 946–956. https://doi.org/10.1109/36.508411

Paugam, R., Wooster, M. J., & Roberts, G. (2013). Use of Handheld Thermal Imager Data for Airborne Mapping of Fire Radiative Power and Energy and Flame Front Rate of

Spread. *IEEE Transactions on Geoscience and Remote Sensing*, *51*(6), 3385–3399. https://doi.org/10.1109/TGRS.2012.2220368

Pedrós, R., Goulas, Y., Jacquemoud, S., Louis, J., & Moya, I. (2010). FluorMODleaf: A new leaf fluorescence emission model based on the PROSPECT model. *Remote Sensing of Environment*, *114*(1), 155–167. https://doi.org/10.1016/j.rse.2009.08.019

Porcar-Castell, A., Tyystjärvi, E., Atherton, J., van der Tol, C., Flexas, J., Pfündel, E. E., Moreno, J., Frankenberg, C., & Berry, J. A. (2014). Linking chlorophyll a fluorescence to photosynthesis for remote sensing applications: Mechanisms and challenges. *Journal of Experimental Botany*, *65*(15), 4065–4095. https://doi.org/10.1093/jxb/eru191

Regaieg, O., Yin, T., Malenovský, Z., Cook, B. D., Morton, D. C., & Gastellu-Etchegorry, J.-P. (2021). Assessing impacts of canopy 3D structure on chlorophyll fluorescence radiance and radiative budget of deciduous forest stands using DART. *Remote Sensing of Environment*, *265*, 112673. https://doi.org/10.1016/j.rse.2021.112673

Rossini, M., Nedbal, L., Guanter, L., Ač, A., Alonso, L., Burkart, A., Cogliati, S., Colombo, R., Damm, A., Drusch, M., Hanus, J., Janoutova, R., Julitta, T., Kokkalis, P., Moreno, J., Novotny, J., Panigada, C., Pinto, F., Schickling, A., … Rascher, U. (2015). Red and far red Sun-induced chlorophyll fluorescence as a measure of plant photosynthesis. *Geophysical Research Letters*, *42*(6), 1632–1639. https://doi.org/10.1002/2014GL062943

Sakai, Y., Kobayashi, H., & Kato, T. (2020). FLiES-SIF version 1.0: Three-dimensional radiative transfer model for estimating solar induced fluorescence. *Geoscientific Model Development*, *13*(9), 4041–4066. https://doi.org/10.5194/gmd-13-4041-2020

Stokes, G. G. (1852). XXX. On the change of refrangibility of light. *Philosophical Transactions of the Royal Society of London*, *142*, 463–562. https://doi.org/10.1098/rstl.1852.0022

Suárez, L., Zarco-Tejada, P. J., Berni, J. A. J., González-Dugo, V., & Fereres, E. (2009). Modelling PRI for water stress detection using radiative transfer models. *Remote Sensing of Environment*, *113*(4), 730–744. https://doi.org/10.1016/j.rse.2008.12.001

Sušila, P., & Nauš, J. (2007). A Monte Carlo study of the chlorophyll fluorescence emission and its effect on the leaf spectral reflectance and transmittance under various conditions. *Photochemical & Photobiological Sciences*, *6*(8), 894–902. https://doi.org/10.1039/B618315H

Valeur, B. (2012a). Characteristics of Fluorescence Emission. In *Molecular Fluorescence* (pp. 53–74). John Wiley & Sons, Ltd. https://doi.org/10.1002/9783527650002.ch3

Valeur, B. (2012b). Introduction. In *Molecular Fluorescence* (pp. 1–30). John Wiley & Sons, Ltd. https://doi.org/10.1002/9783527650002.ch1

van der Tol, C., Verhoef, W., Timmermans, J., Verhoef, A., & Su, Z. (2009). An integrated model of soil-canopy spectral radiances, photosynthesis, fluorescence, temperature and energy balance. *Biogeosciences*, *6*(12), 3109–3129. https://doi.org/10.5194/bg-6-3109-2009

Vilfan, N., van der Tol, C., Muller, O., Rascher, U., & Verhoef, W. (2016). Fluspect-B: A model for leaf fluorescence, reflectance and transmittance spectra. *Remote Sensing of Environment*, *186*, 596–615. https://doi.org/10.1016/j.rse.2016.09.017

Vilfan, N., Van der Tol, C., Yang, P., Wyber, R., Malenovský, Z., Robinson, S. A., & Verhoef, W. (2018). Extending Fluspect to simulate xanthophyll driven leaf reflectance dynamics. *Remote Sensing of Environment*, *211*, 345–356. https://doi.org/10.1016/j.rse.2018.04.012

Wang, Y., & Gastellu-Etchegorry, J.-P. (2021). Accurate and fast simulation of remote sensing images at top of atmosphere with DART-Lux. *Remote Sensing of Environment*, *256*, 112311. https://doi.org/10.1016/j.rse.2021.112311

Wang, Y., Kallel, A., Yang, X., Regaieg, O., Lauret, N., Guilleux, J., Chavanon, E., & Gastellu-Etchegorry, J.-P. (2022). DART-Lux: An unbiased and rapid Monte Carlo radiative transfer method for simulating remote sensing images. *Remote Sensing of Environment*, *274*, 112973. https://doi.org/10.1016/j.rse.2022.112973

Yang, P., van der Tol, C., Campbell, P. K. E., & Middleton, E. M. (2021). Unraveling the physical and physiological basis for the solar- induced chlorophyll fluorescence and photosynthesis relationship using continuous leaf and canopy measurements of a corn crop. *Biogeosciences*, *18*(2), 441–465. https://doi.org/10.5194/bg-18-441-2021

Yang, P., Verhoef, W., & van der Tol, C. (2017). The mSCOPE model: A simple adaptation to the SCOPE model to describe reflectance, fluorescence and photosynthesis of vertically heterogeneous canopies. *Remote Sensing of Environment*, *201*, 1–11. https://doi.org/10.1016/j.rse.2017.08.029

Yang, X., Wang, Y., Yin, T., Wang, C., Lauret, N., Regaieg, O., Xi, X., & Gastellu-Etchegorry, J. P. (2022). Comprehensive LiDAR simulation with efficient physically-based DART-Lux model (I): Theory, novelty, and consistency validation. *Remote Sensing of Environment*, *272*, 112952. https://doi.org/10.1016/j.rse.2022.112952

Yin, T., Cook, B. D., & Morton, D. C. (2022). Three-dimensional estimation of deciduous forest canopy structure and leaf area using multi-directional, leaf-on and leaf-off airborne lidar data. *Agricultural and Forest Meteorology*, *314*, 108781. https://doi.org/10.1016/j.agrformet.2021.108781

Yin, T., Gastellu-Etchegorry, J.-P., Lauret, N., Grau, E., & Rubio, J. (2013). A new approach of direction discretization and oversampling for 3D anisotropic radiative transfer modeling. *Remote Sensing of Environment*, *135*, 213–223. https://doi.org/10.1016/j.rse.2013.03.030

Zhao, F., Dai, X., Verhoef, W., Guo, Y., van der Tol, C., Li, Y., & Huang, Y. (2016). FluorWPS: A Monte Carlo ray-tracing model to compute sun-induced chlorophyll fluorescence of three-dimensional canopy. *Remote Sensing of Environment*, *187*, 385–399. https://doi.org/10.1016/j.rse.2016.10.036

Zhao, F., Li, Y., Dai, X., Verhoef, W., Guo, Y., Shang, H., Gu, X., Huang, Y., Yu, T., & Huang, J. (2015). Simulated impact of sensor field of view and distance on field measurements of bidirectional reflectance factors for row crops. *Remote Sensing of Environment*, *156*, 129–142. https://doi.org/10.1016/j.rse.2014.09.011